Electronic Thesis and Dissertation Repository

6-8-2015 12:00 AM

Monotonic and Cyclic Performance of Spun-Cast Ductile Iron Helical Tapered Piles

Ahmed Fahmy
The University of Western Ontario

Supervisor
Dr. Mohamed Hesham El Naggar
The University of Western Ontario

Graduate Program in Civil and Environmental Engineering
A thesis submitted in partial fulfillment of the requirements for the degree in Doctor of Philosophy
© Ahmed Fahmy 2015

Follow this and additional works at: https://ir.lib.uwo.ca/etd

Part of the Geotechnical Engineering Commons

MONOTONIC AND CYCLIC PERFORMANCE OF SPUN-CAST DUCTILE IRON HELICAL TAPERED PILES

(Thesis format: Integrated-Article)

by

Ahmed <u>Fahmy</u>

Graduate Program in Engineering Science
Department of Civil and Environmental Engineering

A thesis submitted in partial fulfillment
of the requirements for the degree of
Doctor of Philosophy

The School of Graduate and Postdoctoral Studies
The University of Western Ontario
London, Ontario, Canada

ABSTRACT

The performance of a novel piling system is investigated, which involves a spun-cast ductile iron (SCDI) tapered shaft fitted with a lower helical plate. It combines the efficiency of the tapered section, the competitive cost, effectiveness and durability of spun cast ductile iron with a rough surface and the construction advantages of helical piles. The system is installed using a fast, low vibration and reduced noise process. Seven instrumented piles including five SCDI tapered and two steel straight pipes were installed in sand using mechanical torque. The piles were subjected to cyclic and monotonic compression, uplift and lateral load tests. Different loading sequences were adopted to assess the effect of prior cyclic/monotonic loading on the piles' performance. The installation torque was monitored and the resulting capacity-to-torque ratio was compared to the literature reported values. The compaction of the previously disturbed sand from the helix penetration due to the pile taper resulted in superior compressive behavior of the proposed system compared to the straight shaft piles. The tapered piles exhibited higher stiffness at lower displacements compared to the straight shafted piles and the helix increased their uplift resistance. In addition, tapered shafts enhanced the lateral stiffness and the helix provided fixation due to the passive bearing pressures on the helix surfaces, which further improved the lateral performance of the short helical piles. A three dimensional finite element model was established and calibrated using the experimental data. The model was then used to simulate the response of SCDI piles with different configurations when subjected to different loading conditions including axial and lateral as well as combined moment-horizontal loads. Under cyclic loading, the tapered helical piles exhibited better compressive performance while the straight shaft helical piles performed better in uplift loading. The proposed system stiffness remained practically unchanged through the cyclic lateral loading applied in the current study. The monotonic performance of the tapered helical piles in clay was numerically simulated. The results showed an increase in axial and lateral capacity and stiffness of the tapered piles over the straight shaft ones, with greater uplift-to-compressive capacity ratio than in sand.

KEYWORDS: Tapered, helical, field tests, finite element, ductile iron, axial, lateral.

CO-AUTHORSHIP STATEMENT

The work summarized herein was carried out by the author under the supervision of Dr. M. H. El Naggar. That includes all the field and laboratory tests, numerical modelling, analysis of data, results interpretation, thesis writing and results publications.

Chapter 3: Monotonic Compressive Performance of SCDI Helical Tapered Piles in Sand

A version of Chapter 3 was submitted to *The Journal of Geotechnical and Geological Engineering*

Chapter 4: Monotonic Uplift Performance of SCDI Helical Tapered Piles in Sand

An abstract of Chapter 4 was submitted to *The Geotechnical and Structural Engineering Congress 2016*

Chapter 5: Monotonic Uplift Performance of SCDI Helical Tapered Piles in Sand

A version of Chapter 5 was submitted to *The Canadian Geotechnical Conference GEOQuebec 2015*

Chapter 6: Cyclic Axial Performance of SCDI Helical Tapered Piles in Sand

A version of Chapter 6 was submitted to *The Journal of the Deep Foundation Institute*

Chapter 7: Cyclic Lateral Performance of SCDI Helical Tapered Piles in Sand

A version of Chapter 7 was submitted to *The Journal of Geotechnical and Geoenvironmental Engineering*

Chapter 8: Monotonic Axial and Lateral Performance of SCDI Helical Tapered Piles in Clay

A version of Chapter 8 was submitted to *Soils and Foundations Journal*

To the memory of my parents

ACKNOWLEDGMENTS

TABLE OF CONTENTS

LIST OF TABLES

LIST OF FIGURES

LIST OF ABBREVIATIONS AND SYMBOLS

$a, K_2,$ m, t, λ_k	Fitting factors
α	Adhesion factor
A_{helix}	Helix area [m^2]
A_{pi}	Pile cross-sectional area at the considered strain gauge location [m^2]
β	Combined shaft resistance coefficient
c'	Cohesion [kN/m^2]
C_B	Borehole diameter correction
C_R	Drill rod length correction
C_S	Sampler correction
δ	Soil-pile interface angle [Degrees]
D	Borehole diameter [m]
D_{50}	Soil median particle [m]
D_{avg}	Average pile diameter [m]
d_{eff}	Effective shaft diameter [m]
D_{helix}	Helix diameter [m]
δ_{max}	Corresponding displacement to Q_{min} [m]
δ_{min}	Corresponding displacement to Q_{max} [m]
D_r	Relative density [%]
D_{top}	Top pile diameter [m]
E_m	Hammer efficiency
E_{mod}	Modified Young's modulus [kN/m^2]
E_p	Pile material Young's modulus [kN/m^2]
E_s	Soil Young's modulus [kN/m^2]
ε	Strain [%]
F_y	Yield strength [kN/m^2]
G	Shear modulus [kN/m^2]
γ'	Effective unit weight [kN/m^3]
γ_b	Bulk unit weight [kN/m^3]
G_{max}	Maximum shear modulus [kN/m^2]
γ_p	Pile material unit weight [kN/m^3]
G_S	Specific gravity
$\bar{H}$	Normalized applied horizontal force

H_t	Embedment depth of the top helix [m]
φ_{cs}	Critical state angle of internal friction [Degrees]
φ_p	Peak angle of internal friction [Degrees]
$\varphi_{residual}$	Residual angle of internal friction [Degrees]
K	Axial pile stiffness [kN/m]
K_1	System stiffness at the first cycle [kN/m]
K_L	Lateral pile stiffness [kN/m]
K_o	Coefficient of earth pressure at rest
K_p	Coefficient of passive earth pressure
K_s	Coefficient of lateral earth pressure
K_t	Capacity-to-torque ratio [kN/kN.m]
K_{ts}	Tapered coefficient
K_u	Earth pressure coefficient for uplift loading
LL	Liquid limit [Degrees]
$\bar{M}$	Normalized applied moment
N	Number of loading cycles
N'_{60}	Corrected SPT number for field conditions and overburden stresses effect standardized to 60% energy ratio
N_{60}	Corrected SPT number for field conditions standardized to 60% energy ratio
Nc', $N\gamma'$, N_q'	Combined bearing capacity factors taking into account the shape and depth factors
OCR	Overconsolidation ratio
Pa	Atmospheric pressure [kN/m^2]
PI	Plasticity index [Degrees]
PL	Plastic limit [Degrees]
P_u	Ultimate axial capacity [kN]
P_{ub}	Helix bearing capacity [kN]
P_{uL}	Ultimate lateral capacity [kN]
P_{zi}	Measured axial force at strain gauge location [kN]
Q_d	Design load [kN]
Q_{max}	Maximum applied load [kN]
Q_{min}	Minimum applied load [kN]
Q_o	Pile capacity after driving [kN]
q_s	Shaft resistance [kN/m^2]

R_a	Surface roughness [nm]
r_l	Pile radius at which the shear stresses become negligible [m]
r_m	Average pile radius [m]
σ_p'	Apparent preconsolidation pressure [kN/m^2]
S_r	Ratio of pile settlement to diameter at the ultimate load
S_u	Undrained shear strength [kN/m^2]
σ_v	Overburden stresses [kN/m^2]
σ_v'	Effective overburden stresses [kN/m^2]
T	Installation torque [kN.m]
W_c	Water content [%]
ζ	$\ln(r_l/r_m)$
θ	Taper angle [Degrees]
v	Poisson's ratio
v_p	Pile material Poisson's ratio
ψ	Dilation angle [Degrees]

INTRODUCTION

1.1 Overview

The main purpose of pile foundations is to support structures by transferring their loads to deeper and stronger soil or rock layers. Such foundation systems are typically considered in cases of shallow soft deposits or high superstructures loads. Nowadays, the complexity of the supported onshore and offshore structures and the accompanying complex loading conditions has increased the demands for deep foundations and urged the development of newer higher capacity systems.

The common conventional piling systems are shown in Figure 1 - 1. These are installed by driving, drilling, jetting or applied torque. Recently, special piling systems have been developed to provide more efficient, economic and sustainable piling solutions. Examples of the new systems include hollow core micropiles (Abd-Elaziz & El Naggar, 2012), fibre reinforced helical micropiles (El Sharnouby & El Naggar, 2012) and large diameter helical piles (Elsherbiny and El Naggar, 2013; and Elkasabgy and El Naggar, 2015).

In the continuing effort to produce efficient deep foundation options, the present study proposes a novel piling system consisting of a spun-cast ductile iron *SCDI* tapered pile (Seamless-Pole-Inc., 2010) fitted with a lower helical plate to facilitate its installation. A schematic presentation of the proposed system is shown in Figure 1 - 2.

The proposed system configuration combines the axial and lateral resistance efficiency of the tapered section, the competitive cost and durability of spun-cast ductile iron with rough surface, the lightweight and better handling capabilities of the hollow section and the construction advantages of helical piles.

Different pile forms
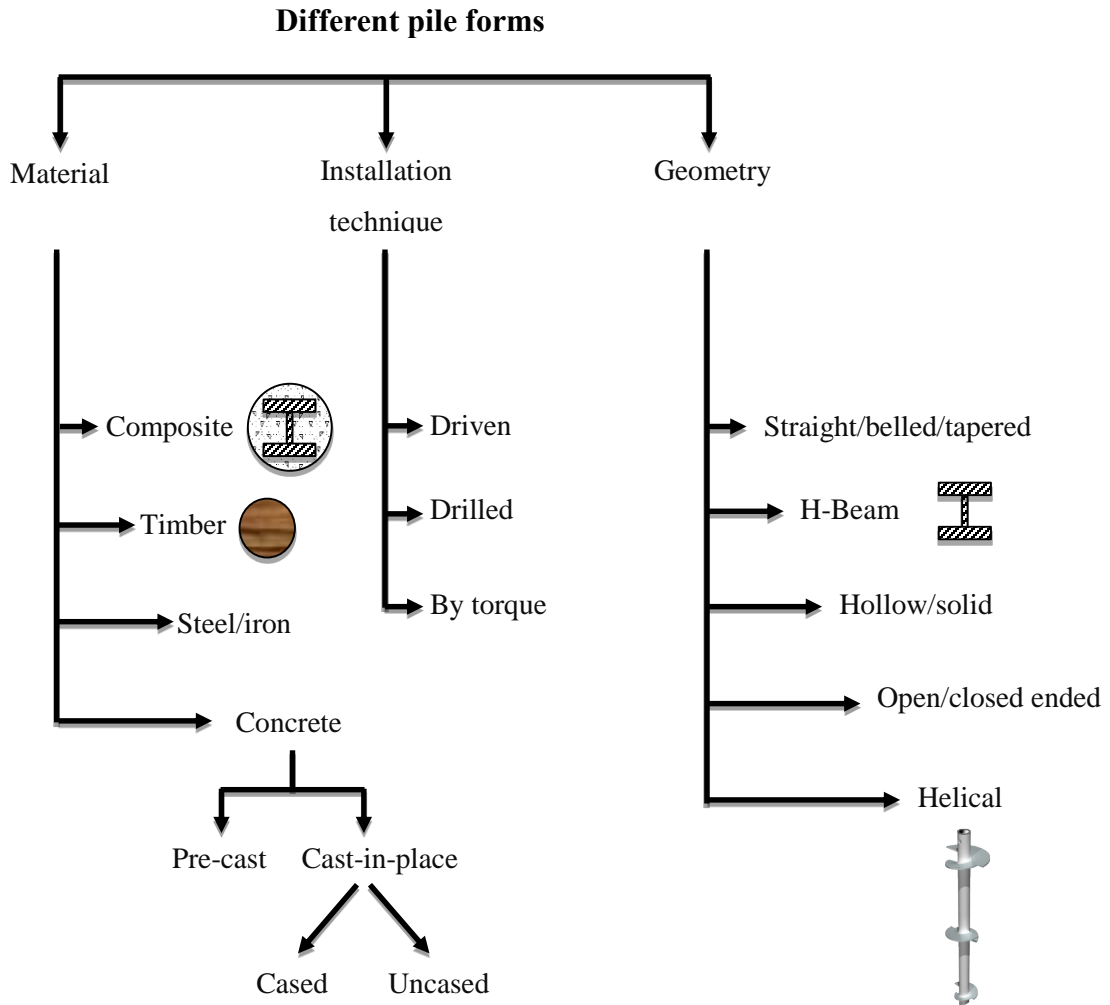
Figure 1 - 1: Common piling methods
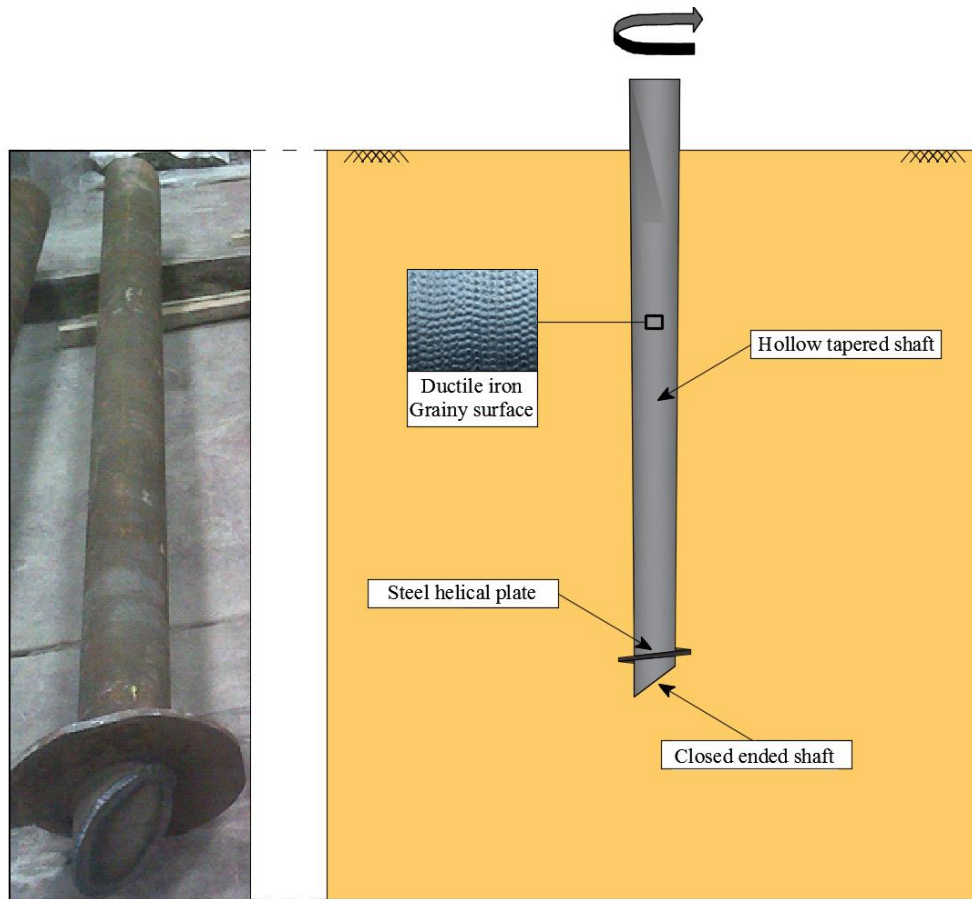
Figure 1 - 2: The proposed piling system configuration

1.2 Research objectives

In order to evaluate the efficiency of the proposed system, the following main objectives were set for this study:

- To investigate the monotonic performance of the proposed novel piling system when embedded in cohesionless and cohesive soils; this includes piles loaded in axial compression, uplift and lateral directions;

- To assess the cyclic compressive, uplift and lateral behavior of the suggested pile in cohesionless soils;

- To quantify the installation effect, to understand the load transfer mechanism and to assess the contribution of the different system components;

- To provide design guidelines for the proposed pile in the above mentioned loading cases, as well as when subjected to combined horizontal-moment loadings.

1.3   Methodology

To fulfill these objectives, a comprehensive investigation program was performed comprising five main stages:

▪ *Literature survey*: An extensive review of the existing literature on piles subjected to different loading conditions and installed in different soil types was performed with special focus on helical and tapered piles. Knowledge of existing system features aided in design of a more efficient and practical hybrid system that combines their advantages and avoids their limitations.

▪ *Pile manufacturing*: During this stage, detailed design of the proposed piling system was carried out. This included selection of the pile's material, consideration of the pile dimensions to maximize the geotechnical capacity and to maintain the structural integrity and the system economy. With help of Seamless Pole Inc. (2010) and the University of Western Ontario Machine Shop, five piles of the proposed configuration were manufactured. In addition, two large diameter straight helical piles were manufactured (contributed by EBS Geostructural Inc., 2014) and tested for comparison purposes.

▪ *Field testing*: The seven full scale piles were instrumented, installed and field tested. The performed tests include cyclic and monotonic compression, uplift and lateral load tests. The piles were tested in different loading sequences to evaluate

the effect of prior loading on the piles' performance. The test results were presented

in load-displacement curves at the pile heads as well as load distribution curves

along the pile shaft. The load displacement curves were used to evaluate the piles

stiffness and capacity, while the load distribution curves were used to evaluate the

load transfer mechanisms.

- *Numerical simulations*: Following the field testing stage, three-dimensional finite

  element FE simulations of the field tests were developed using the commercial

  software package ABAQUS (Hibbitt *et al.*, 2008). Calibration and verification of

  the models against the field test data were first performed for the different loading

  conditions. The effect of the pile geometry and the installation technique were

  identified. In addition, loading cases and soil conditions not tested on site were

  simulated. This includes the performance of single piles in cohesive and cohesion-

  less soil profiles.

1.4   Thesis outline

The presented thesis has been prepared in 'Integrated article' format and comprises nine
chapters. The description of these chapters is summarized below:

Chapter 2 provides a survey of the existing literature on helical (screw) and tapered piles
cyclic and monotonic axial and lateral performance. That includes a review of physical and
finite element models and the available analytical and empirical solutions developed to
predict the behavior of these piling systems.

Chapter 3 reports on the analysis of the field test and numerical modeling results of the
monotonic compressive loading of the *SCDI* helical tapered piles and their performance
compared to that of large diameter straight steel single helix piles in sand. This comprises
both field tests and three dimensional finite element analysis results for piles tested in

different orders. The results are compared to those reported in the literature where applicable.

Chapter 4 presents the field testing and finite element modelling results of the monotonic uplift performance of the proposed system in sand compared to that of large diameter straight steel single helix piles. The results are then compared with those available in the literature as well as those tested in compression presented in Chapter 3.

Chapter 5 addresses the results of the lateral monotonic field tests of the proposed system compared to that of large diameter straight steel single helix piles in sand. This is followed by a summary of the finite element simulation of the system. Design guidelines for piles subjected to combined horizontal-moment loads are given. Again, the results are compared to those available in the literature where applicable.

Chapter 6 presents the results of the cyclic compressive and uplift performance of the proposed system in sand. This includes both field tests and finite element simulations results.

Chapter 7 reports the results of the cyclic lateral performance of the suggested piling system in sand. This includes the results of the carried out field tests and the finite element simulations.

Chapter 8 includes the results of the numerical analysis of single *SCDI* helical tapered piles embedded in a clay profile. The same piles configurations analyzed in Chapters 3 to 7 were considered. This includes monotonic lateral, compression and uplift loading simulations. Design guidelines for piles subjected to combined horizontal-moment loads are also given.

Chapter 9 briefly summarizes the main conclusions drawn from the previous chapters. Suggested recommendations for future research are also presented.

1.5   References

Abd-Elaziz, A. Y. & El Naggar, M. H. 2012. Axial behaviour of hollow core micropiles under monotonic and cyclic loadings. *Geotechnical Testing Journal,* 35(2), 249-260.

EBS 2014. EBS Geostructural Inc. Breslau, ON. (*http://www.ebsgeo.com*/)

Elkasabgy, M. & El Naggar, M.H. 2015. Axial compressive response of large-capacity helical and driven steel piles in cohesive soil. *Canadian Geotechnical Journal*, 52(2), 224-243.

El Sharnouby, M. M. & El Naggar, M. H. 2012. Field investigation of axial monotonic and cyclic performance of reinforced helical pulldown micropiles. *Canadian Geotechnical Journal*, 49(5), 560-573.

Elsherbiny, Z. H. & El Naggar, M. H. 2013. Axial compressive capacity of helical piles from field tests and numerical study. *Canadian Geotechnical Journal*, 50(12), 1191-1203.

Hibbitt, H. D., Karlsson, B. I. & Sorensen, E. P. 2008. ABAQUS Standard user's manual. Pawtucket, R. I.: Hibbitt, Karlsson & Sorensen Inc.

Magnum-Piering 2005. Magnum Piering Inc. (*http://www.magnumpiering.com*/)

Seamless Pole Inc 2010. Ductile iron poles. Birmingham, AL. (*http://www.seamlesspole.com/*

LITERATURE SURVEY

2.1   Introduction

Tapered piles of decreasing circumference with depth have been successfully used for many years as a competent alternative to conventional cylindrical piles. They can be installed by drilling, driving or using torque and can be made of steel, wood, concrete or composite sections. Owing to their geometry, they may provide more than 180% higher axial capacity than conventional straight shafts (Sakr and El Naggar, 2003). In addition, their efficient material distribution leads to greater flexural rigidity at their top, and hence enhances their lateral stiffness and capacity.

Helical piles represent another efficient piling system. The helices facilitate the installation of piles and enhance their axial capacity. Helical piles configurations used in practice nowadays involve the use of one or more helices and fixing them on solid or hollow steel shafts or precast concrete piles (Tomlinson, 1994). Currently, the use of helical piles is gaining wide popularity due to their many advantages including: quick installation process with reduced associated disturbance and soil spoils, the ability to verify the load carrying capacity during installation, the possibility of reusing the piles and suitability for remote locations installations (Perko, 2009). They are employed to support power transmission towers, solar panels, bridges and residential and commercials buildings, etc. In many of these applications, the loading scheme involves static and cyclic compressive, uplift and lateral loading (Elsherbiny and El Naggar, 2013). A typical helical pile configuration is shown in Figure 2 - 1.
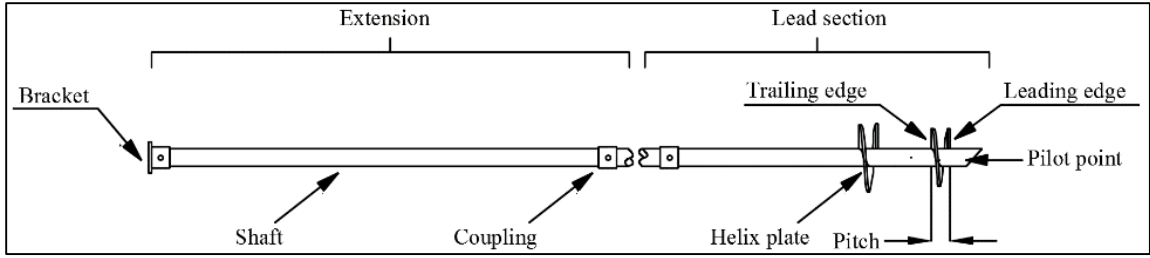
Figure 2 - 1: Typical slender shaft helical pile configuration and terminology - after Perko (2009)

In this study, a novel piling system is suggested, which consists of a spun-cast ductile iron (SCDI) tapered pile (Seamless-Pole-Inc., 2010) fitted with a lower helical plate to facilitate its installation. Because the proposed system combines the advantages of the two well-established deep foundation options, i.e. helical and tapered piles; the relevant literature of both types is presented herein. This includes the axial and lateral performance of both systems under static and cyclic conditions.

2.2 Monotonic axial performance

2.2.1 Helical piles

Helical piles are installed into the ground by employing torque to the pile head. Knowing the installation torque, the axial capacity of helical piles can be predicted using the following equation (Livneh and El Naggar, 2008; Hoyt and Clemence, 1989):

$$P_u = K_t T \tag{2 - 1}$$

Where T is the installation torque, P_u is the ultimate axial capacity and K_t is the capacity-to-torque ratio. Conducting regression analysis of the results of more than 300 pile load tests, Perko (2009) proposed the following expression for K_t:

$$K_t = \frac{\lambda_k}{d_{eff}^{0.92}} \tag{2 - 2}$$

Where d_{eff} is effective shaft diameter and λ_k is a curve fitting factor $=1433$ mm$^{0.92}$/m (22 in$^{0.92}$/ft).

The axial capacity of helical piles depends on several factors including the shaft diameter, the number of helical plates, their diameter and their interspacing.

Generally, there are two methods to evaluate the axial capacity of helical piles: individual bearing and cylindrical shear. At smaller helices inter-spacing, the axial capacity is given by the sum of bottom helix bearing, developed shear stresses along the surface of the inter-helical soil cylinder and the shaft resistance above the top helix (Figure 2 - 2 a). At large interspacing, the individual bearing method is employed. In this method, no interaction between the helices occurs and the axial capacity is given by the sum of the helical plates bearing and the pile shaft resistance as illustrated in Figure 2 - 2 (b). As recommended by the Canadian Foundation Engineering Manual, a minimum interspacing equal to 3 times the largest helix diameter should be kept between the helices to avoid the cylindrical shear failure mode (CGS, 2006).

(a)   (b)
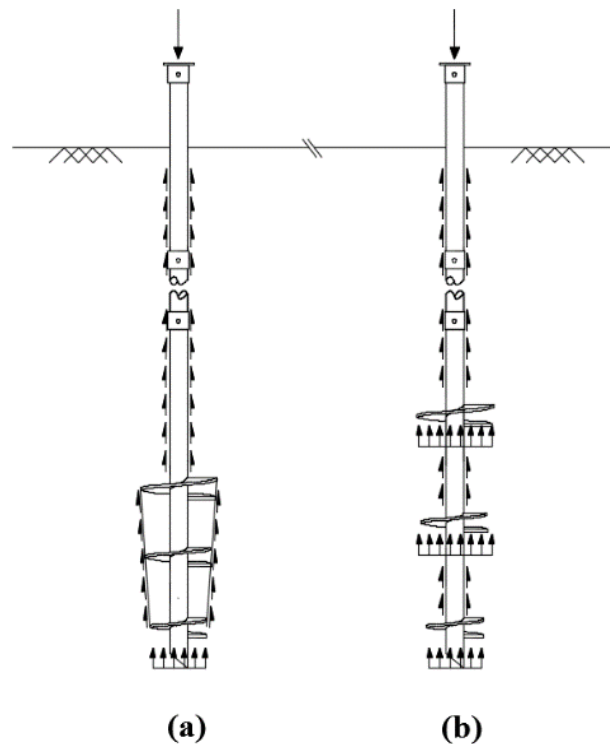
Figure 2 - 2: Schematic presentation of helical piles failure criteria-compression loading (a) Cylindrical shear; (b) Individual bearing - after Perko (2009)

For uplift loading, a minimum pile embedment is required to fully mobilize the top helix bearing resistance. Otherwise, shallow failure conditions may prevail at lower embedment, where shearing of a lifted soil cone above the top helix, as illustrated in Figure 2 - 3, governs the failure.
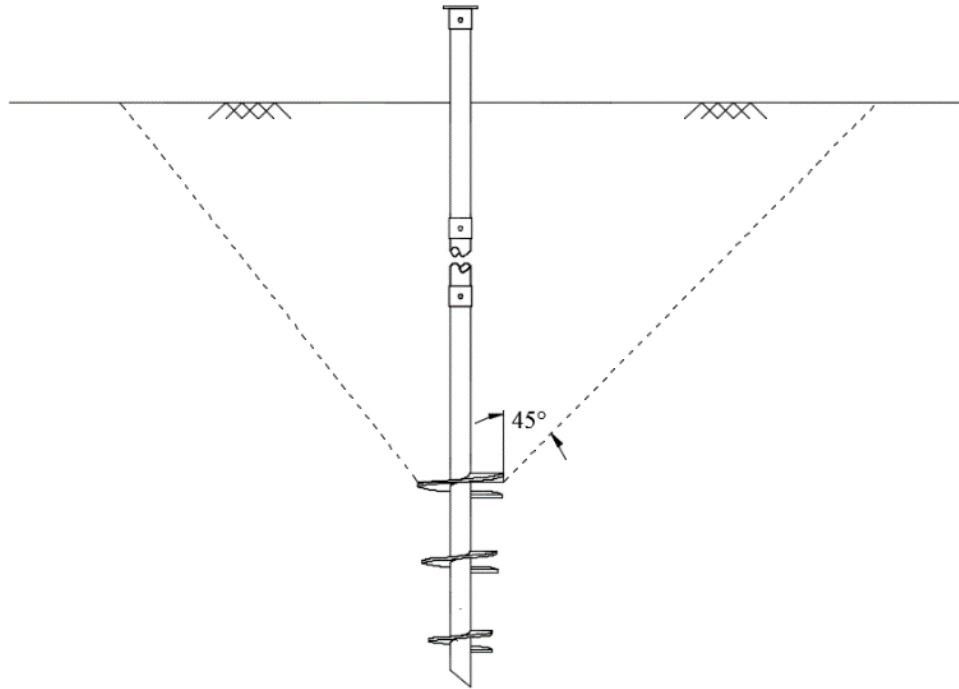
Figure 2 - 3: Shallow failure criteria - uplift loading - after Perko (2009)

Ghaly and Hanna (1992) suggested values of the minimum embedment depth of the top helix H_t as a function of the helix diameter D_{helix}. These values are summarized in Table 2 - 1, which shows that greater embedment is required for coarse grained soils and for denser deposits. Also, greater embedment would be needed in case of higher groundwater tables (i.e. reduced effective weight) (Perko, 2009).

Table 2 - 1: Suggested minimum helical pile embedment (Ghaly and Hanna, 1992)

Soil type	H_t/D_{helix}
Fine grained	5
Loose coarse grained	7
Medium coarse grained	9
Dense coarse grained	11

It should be noted that the installation of helical piles is likely to comprise significant soil shearing and disturbance within the cylindrical installation zone. Higher disturbance is expected for multi-helix piles, especially above the upper helix plate due to the repeated soil penetration and shearing (Tsuha *et al.*, 2012). Zhang (1999) suggested discounting a distance equivalent to one helix diameter from the shaft resistance to account for the soil disturbance/the shadowing effect above the helix in cases of uplift/compression loading. Bagheri and El Naggar (2013) suggested using the residual angle of internal friction of dense sand when calculating the end bearing factor N_q values proposed by Meyerhof (1976). The use of low speed motors to torque down the piles would also minimize the resulting installation disturbance (Perko, 2009). As well, it is recommended to keep the inter-spacing as multiples of the helices pitch, hence forcing all plates to track a single path during installation (Seider, 2004). Furthermore, it was found that for multi-helix piles, the use of tapered helices profile would generally enhance the piles' uplift resistance compared to the cylindrical helices profile (Tsuha *et al.*, 2013).

For the design of helical piles in sand, the values of the earth pressure coefficient K_u suggested in Figure 2 - 4 for different values of angle of internal friction at different depth to diameter ratio can be used for uplift loading (Mitsch and Clemence, 1985). Trofimenkov and Maruipolshii (1965) showed that the compressive to uplift capacity ratio for a single helix pile in sands and clays ranges between 1.3 to 1.5.

It can be generally concluded that helical piles with slender shafts would sustain relatively small compressive loads compared to other greater diameter piles. However, different helical pile systems with large diameter shafts are developed and offer large axial and lateral capacity (Fleming *et al.*, 2009; El Sharnouby and El Naggar, 2012; Elkasabgy and El Naggar, 2013).
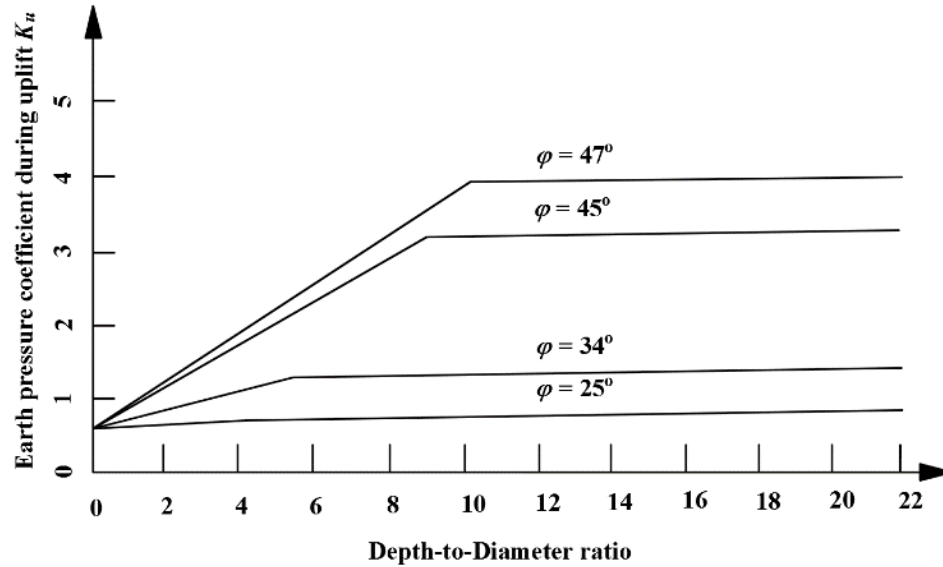
Figure 2 - 4: Variation of the lateral earth pressure coefficients for uplift loading K_u - after Mitch and Clemence (1985)

2.2.2 Tapered piles

Owing to their shape, tapered piles may offer a substantially increased axial capacity reaching up-to 1.5 to 2.5 times the capacities of cylindrical pile of the same average diameter (El Naggar and Sakr, 2000). Wei and El Naggar (1998) found that the pile taper angle increases the efficiency of utilization of the pile material, especially in looser deposits where the additional confining pressure attributed to the pile taper significantly increases the soil stiffness. The resulting ratio between the capacities of tapered piles to straight ones of the same average diameter was up-to 1.37 at confining pressure of 40 kPa (Wei and El Naggar, 1998). This enhancement results from transferring the load to a greater soil volume due to the developed soil arch compared to straight piles (Wei and El Naggar, 1998). In addition, the radial expansion of the soil adjacent to the pile during installation and pile loading results in higher lateral earth pressure and therefore greater frictional resistance compared to the straight shafted piles.

El Naggar and Sakr (2000) proposed the following equation to calculate the developed skin friction q_s along the shaft of tapered piles installed in sands:

$$q_s = K_{ts}K_s\sigma_v'\tan\delta \tag{2 - 3}$$

$$K_{ts} = \frac{\tan(\theta+\delta)\cot(\delta)}{1+2\zeta\tan(\theta)\tan(\theta+\delta)} + \frac{4G\tan(\theta)\tan(\theta+\delta)\cot(\delta)S_r}{(1+2\zeta\tan(\theta)\tan(\theta+\delta))K_s\sigma_v} \tag{2 - 4}$$

where θ is the pile taper angle, σ_v is the overburden stress, K_{ts} is the taper coefficient, K_s is the coefficient of lateral earth pressure, δ is soil-pile interface angle, G is the sand shear modulus, $\zeta = \ln(r_l/r_m)$, r_l is the pile radius at which the shear stresses become negligible, r_m is average pile radius and S_r is the pile settlement as a ratio of its diameter at the ultimate load.

For tapered piles installed in frictional-cohesive soils, K_{ts} can be given by (Khan *et al.*, 2008):

$$K_{ts} = \frac{\tan(\theta+\delta)\cot(\delta)}{1+2\zeta\tan(\theta)\tan(\theta+\delta)} + \frac{4G\tan(\theta)\tan(\theta+\delta)\cot(\delta)S_r}{(1+2\zeta\tan(\theta)\tan(\theta+\delta))K_s\sigma_v}$$
$$+ \frac{C'}{(1+2\zeta\tan(\theta)\tan(\theta+\delta))K_S\sigma_v'\tan(\delta)} \tag{2 - 5}$$

Kurian and Srinivas (1995) numerically investigated the behavior of tapered piles in sand and validated their results with laboratory testing. Their results confirmed the higher efficiency of the compressive capacity of the tapered piles compared to straight ones, where the capacity increases due to the direct bearing on the pile's sides (i.e. higher normal pressure) and consequently the pile side frictional resistance increases (Kurian and Srinivas, 1995). Also, Zhan *et al.* (2012) numerically studied the axial behavior of cast-in-situ 4.0m length tapered piles installed in sands and concluded that a slight increase in shaft taper θ significantly increased the developed shaft stresses even at shallow depths as shown in Figure 2 - 5 (Zhan *et al.*, 2012).
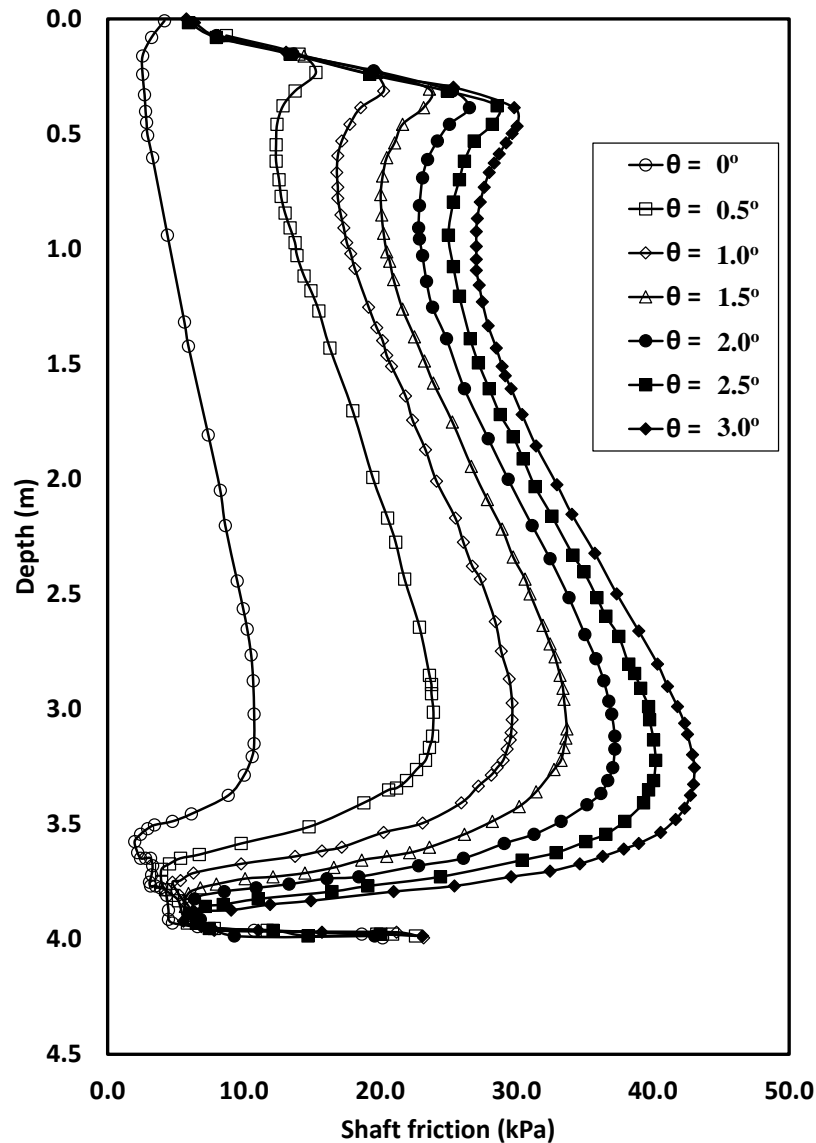
Figure 2 - 5: Developed shaft friction along tapered piles in sand at 2cm displacement - after Zhan *et al.* (2012)

Advantages of tapered piles were also proven by Khan *et al.* (2008) where they showed a capacity increase of 28% to 50% compared to piles of the same volume and average diameter (Khan *et al.*, 2008). Their results showed a stiffer behavior for tapered piles compared to straight ones especially at higher displacements. It was also observed that, unlike straight wall piles, the shaft resistance of piles kept increasing with displacement with no limiting resistance (Kodikara and Moore, 1993).

As shown above, the tapered shaft configuration is generally more efficient in frictional soils whereas the increase of the soil cohesion component reduces the ratio of the tapered to cylindrical pile axial capacity as concluded by Kodikara and Moore (1993). It should be noted that much scarce data exists concerning the performance of tapered in fine grained soils compared to cohesionless soils.

While many studies confirmed the superiority of tapered piles in terms of compressive capacity, this was not the case for their uplift behavior. Generally, less attention was given to their uplift performance (Kodikara and Moore, 1993). El Naggar and Wei (2000b) found that the uplift to compressive capacity ratio of steel tapered piles in sand could be down-to 0.37, with lower ratios for greater taper angle and higher confining pressures. They observed that the uplift behavior of tapered piles is similar to that of straight ones at higher confining pressure (El Naggar and Wei, 2000b).

Kong *et al.* (2013) proposed a concrete tapered pile with enlarged base. While their system yielded an improved uplift capacity compared to the regular tapered and cylindrical piles, conventional belled piles still offers higher uplift resistance (Kong *et al.*, 2013).

In their study, Sakr *et al.* (2005b) studied the uplift performance of FRP tapered piles filled with self consolidated concrete in dense sand using the conventional driving technique as well as a novel toe driving one. They concluded that the pullout capacity of tapered piles were slightly higher than that of straight ones at lower displacements while comparable results were found at greater displacements (Sakr *et al.*, 2005b). Their proposed toe driving technique was found to increase the uplift capacity of the piles thanks to the densification of the soil surrounding the piles as well as avoiding the probable whip effect in case of conventional driving of flexible piles (Sakr *et al.*, 2005b).

Studies have shown that the capacity of driven piles might increase with time. Known as the pile setup phenomena, the pile capacity may increase due to the increase in the soil strength attributed to the dissipation of pore water pressure and stress redistribution (ASCE 20-96, 1997). York *et al.* (1984) studied the performance of driven piles installed in medium dense glacial sands at JFK international airport and observed an increase of 40 to 80% in their capacity with the maximum increase seen after 15 to 25 days of installation.

The setup effect was also reported by Alawneh *et al.* (2009). They suggested that following driving a pile in cohesionless soils, its long term capacity could reach up to 300% of its values upon driving mainly due to the increase in shaft resistance with time (Alawneh *et al.*, 2009). Svinkin (1996) suggested that the pile capacity after a time *t*, Q_t, can be bounded by:

Upper bound value: $Q_t = 1.4Q_o t^{0.1}$ (2 - 6)

Lower bound value: $Q_t = 1.025Q_o t^{0.1}$ (2 - 7)

Where Q_o is the pile capacity right after driving.

2.3   Monotonic lateral performance

2.3.1   Helical piles

When subjected to lateral loads, piles can act either as rigid (short) or flexible (long) depending on their geometry and on the soil stiffness. When the pile has relatively short length with respect to its diameter, it behaves as rigid body, and its lateral capacity is entirely dependent on the soil resistance. Such piles are used to support light weight structures (Perko, 2009).

On the other hand, long piles are flexible, and their lateral resistance is governed by their flexural resistance (Poulos and Davis, 1980). Such piles are ordinarily used to withstand significant lateral loads (Perko, 2009). It can be roughly assumed that piles with slenderness ratio (i.e. length to diameter) greater than 10 are expected to behave as long piles (Perko, 2009).

The lateral resistance of helical piles can be generally estimated using the same techniques adopted for slender piles taking into account the effects of pile installation (Puri *et al.*, 1984). The helix rotation during installation shears the soil surrounding the pile and reduces its strength, with even further disturbance as the number of helices increases (Sakr, 2009). However, for short piles, the presence of helical plates at shallow depths may increase the pile lateral capacity. This was observed by Prasad and Rao (1996) through their

17

experimental investigation of the lateral response of helical piles in clay. They found that the helical pile capacity was 1.2 to 1.5 times that of conventional piles with no helical plates. The increased capacity resulted from the developed bearing/uplift resistance on the front/back half of the helical plates once rotated as well as the frictional resistance on the plates' surfaces contributing to the piles' lateral resistance (Prasad and Rao, 1996).

Helical pile systems with large diameter shafts offer enhanced lateral capacity. El Sharnouby (2012) investigated the lateral performance of steel fibre-reinforced and FRP-steel fibre reinforced helical pulldown micropiles (El Sharnouby, 2012). While the first provided improved system ductility, the latter enhanced the system capacity with 30 to 35% increase in the lateral capacity (compared to the steel fibre-reinforced type) (El Sharnouby, 2012).

2.3.2   Tapered piles

Tapered pile configuration offers higher axial and lateral capacity compared to straight shaft piles with equal average diameter. The increase in axial capacity is attributed to the added frictional resistance owing to the wedging effect during installation as well as soil densification during pile loading. The increase in lateral capacity results from the greater diameter and flexural stiffness of the top portion of the pile, which control the lateral performance of the pile. El Naggar and Wei (1999) experimentally investigated the behavior of steel tapered piles in cohesionless soils at different confining pressures. They found that tapered piles showed generally stiffer response at various load levels with more obvious effect at low confining pressure (El Naggar and Wei, 1999). Their results showed that a taper angle as small as 0.95^o would increase the pile lateral capacity by up to 77% at zero confining pressure. They also noted that the maximum bending moment occurred within the top third of the pile length, i.e. at sections with greater diameter and consequently greater inertia.

Sakr *et al.* (2005a) investigated the lateral performance of FRP composite tapered piles installed using conventional and toe driving techniques. Their results showed, even though composite tapered piles displayed more flexible response compared to the conventional

steel piles, they offered higher lateral resistance compared to toe driven ones. Considering the ultimate load criteria suggested by Prakash and Sharma (1990) where the ultimate load is defined as the value corresponding to 6.25 mm head deflection, (Sakr *et al.*, 2005a) reported that the ultimate capacity of tapered pile could reach up to 200% of the capacity of a cylindrical pile of the same average diameter.

2.4 Cyclic axial performance

The repeated loads imposed by environmental events such as waves, wind or earthquakes can significantly degrade the capacity of piles in sands where failure might occur at loading amplitude as low as 30% of their static capacities for one-way loading, with even lower amplitude for two-way loadings (Chan and Hanna, 1980). The possible degradation results from the accumulation of plastic deformations, the rearrangement of soil particles around the piles and the excess pore pressure development (Poulos, 1981). For two-way loading, degradation of the skin and base resistance would prevail, whereas plastic strain accumulation governs in the case of one way loading, especially in the case of softening behavior along the pile-soil interface (Poulos, 1989).

The decay in pile stiffness/capacity is influenced by the cyclic loading amplitude, where no reduction in the pile resistance would be expected below a threshold loading amplitude (Abdel-Rahman and Achmus, 2011). Suggested values of the threshold cyclic load amplitude for different soil types are summarized in Table 2 - 2, presented as a ratio of the static pile capacity (Schwarz, 2002).

Table 2 - 2: Threshold amplitudes for cyclic loading (Schwarz, 2002)

Soil type	Critical cyclic amplitude to static pile capacity
Sand	0.10~0.40
Silt	0.40~0.60
Normally consolidated Clay	0.30~0.55
Overconsolidated Clay	0.85~1.00

It was observed that materials achieve a resilient state where no further plastic strains accumulate after a limiting number of loading cycles (Brown *et al.*, 2008). This trend is

referred to as the shakedown phenomena. Brown *et al.* (2008) observed that the shakedown phenomenon occurred after 300~1000 loading cycles for piles installed in sands with contact pressure ranging from 100 to 119 kPa (Brown *et al.*, 2008).

2.4.1 Helical piles

Ghaly and Clemence (1998) found that upward creep would be fully recoverable if the cyclic loads are kept within 25% of the pile static capacity. Accordingly, Perko (2009) suggested keeping the applied cyclic loads to helical piles within this limit.

El Naggar and Abdelghany (2007) investigated the cyclic performance of helical piles in clay. They found a minor effect of the cyclic loading on helical pile stiffness. They also observed a reduction of less than 5-10% of the helical piles capacity after being subjected to 15 load cycles.

El Sharnouby and El Naggar (2012) evaluated the effect of static/cyclic loading on the static/cyclic performance of FRP-steel fibre-reinforced helical pulldown micropiles. Small cyclic displacements were observed during the few first loading cycles, with negligible permanent displacements when the piles were previously statically tested to higher loading levels. When applied cyclic loads were higher than the initial static load, the observed shaft degradation was counteracted by the resulting soil stiffening from the lead section (El Sharnouby and El Naggar, 2012). They showed that the application of cyclic loads may increase the axial capacity by up to 15%. Similarly, Jardine and Standing (2012) found that the application of low-level cyclic loads increases the tension capacity of driven piles in sand by up to 20%.

Clemence and Smithling (1984) attributed a possible positive (stiffening) or negative (degrading) effects of cyclic uplift loading of helical anchors to the rate of soil disturbance during installation: for greater installation disturbance, the cyclic loading would densify the soil hence increasing its stiffness; whereas for systems increasing the soil stiffness during installation, the application of cyclic load will loosen the soil and reduces the pile static resistance. They also found that the static post-cyclic capacity of helical anchors is

20

reduced due to the loose soil zone surrounding the anchors developed during the cyclic loading (Clemence and Smithling, 1984).

2.4.2   Tapered piles

The cyclic response of tapered piles received less attention than straight shaft piles. El Naggar and Wei (2000a) suggested limiting the cyclic load amplitude for tapered piles to 25% and 75% of their static uplift and compressive capacity, respectively. Within these limits, tapered piles are expected to show an enhanced performance compared to the cylindrical one (El Naggar and Wei, 2000a). They suggested that keeping the cyclic loading amplitude within these limits would lead to increased pile stiffness with the applied loading cycles due to the densification of the sand surrounding the pile, however, not necessarily in case of dense sand.

2.5   Cyclic lateral performance

When subjected to lateral cyclic loads, the pile-soil system may experience performance degradation with the repetitive loading. Two degradation forms may take place: material degradation and mechanical degradation (Mosikeeran, 1990). While the first results in the change of the soil parameters, the latter reflects the developed plastic deformations in the soil. Combined, these actions would produce greater pile deflections, rotations, developed bending stresses and ultimately lower system resistance. It is generally observed that cyclic loading levels exceeding 70 to 80% of the static system capacity would result in the degradation of the lateral piles resistance, mostly developed within the first few loading cycles (Mosikeeran, 1990). Higher degradation effects and greater developed plastic strains were observed for piles subjected to one-way cyclic load tests than in the case of two-way cyclic load tests (Long and Vanneste, 1994).

Manifested by the pinched hysteretic loops, the soil gapping and the possible soil cave-in processes represent other important phenomena influencing the piles lateral cyclic behavior (Allotey and El Naggar, 2008). Under two-way cyclic loading, a soil gap develops and the effective overburden stresses (hence lateral stresses) at shallow depths might not be

sufficient to close that gap (Mosikeeran, 1990). Following the development of the gap, the sand behind the pile would fall down filling that gap hence creating a looser soil zone behind the pile. As a result of this gapping and cave-in process, a non-symmetric performance would result where stiffer system response governs the firstly loaded side of the pile (El Sharnouby and El Naggar, 2013).

The cave-in and recompression process was also found to reduce the maximum pile bending moment, to move its location to a shallower depth and to increase the dissipation of hysteretic energy (Allotey and El Naggar, 2008). The benefit of the cave-in and recompression are more obvious in case of damaged piles as it further confines the developed hinges along the pile (Allotey and El Naggar, 2008). On the other hand, different results were observed by Guo *et al.* (2014) from their analysis of the lateral performance of H-Piles in sand. They observed that, in case of cyclic lateral loads, the deeper developed gaps would move the location of the maximum bending moment to a deeper location compared to the monotonic case (Guo *et al.*, 2014).

Reese and Van Impe (2001) suggested that during cyclic loading of piles in sand, the void ratio of the soil mass near the ground surface reaches a critical value, implying that cycling of denser soils would degrade it while looser soils would densify during cyclic loading. The stiffening effect was also observed by Verdure *et al.* (2003), who reported that the secant stiffness of piles tested in one-way cyclic load tests is 1.5 to 3 times larger than that of the initial monotonic loading (until reaching the cyclic amplitude level) with the stiffness slightly increasing with loading cycles. After 1000 applied lateral load cycles, Li *et al.* (2010) found no significant axial settlements for centrifuge modelled mono-piles supporting offshore wind turbines. They also suggested that the rate of deflection increases with number of loading cycles and with loading amplitude, where more densification of the surrounding soil takes place.

While several models have been developed to predict the accumulated displacement during cyclic lateral loading of piles in sand (e.g. Little and Briaud, 1988; Lin and Liao, 1999; LeBlanc *et al.*, 2010; Bienen *et al.*, 2012), many of them were found to yield underestimated displacement values (Li *et al.*, 2014).

2.5.1 Helical piles

Abdelghany and El Naggar (2010) investigated the monotonic and cyclic performance of plain and several grouted helical piles alternatives (grouted, reinforced grouted and fibre reinforced grouted). While their results showed a degrading effect for most of the tested piles, the reinforced grouted ones showed the least degradation or a capacity increase after the cyclic loading (Abdelghany and El Naggar, 2010).

Prasad and Rao (1994) found that the pullout capacity of short piles in clay might be reduced in case subjected to cyclic lateral loads depending on the lateral deflection and piles slenderness ratio. They suggested that this reduction might result from the developed gap and the soil strength reduction around the pile (Prasad and Rao, 1994). For that loading condition, they suggested using helical piles where they observed no reduction in their pullout capacity within maximum lateral defections equivalent to 10% of the shaft diameter (Prasad and Rao, 1994). They attributed that to the developed gap for helical pile in sand and the reduced strength soils are confined to a narrow region next to the pile shaft whereas the soil resistance on the periphery of the helices is not altered (Prasad and Rao, 1994).

El Sharnouby (2012) analyzed the performance of steel fibre reinforced and FRP-steel fibre reinforced helical pulldown micropile. He observed that the FRP-steel fibre reinforced helical pulldown micropile had 60-100% stiffer response. When subjected to two-way lateral cyclic loads, both pile types suffered stiffness degradation due to the gap that developed behind the pile, which also resulted in a preferred loading direction offering stiffer response than the other side. Accordingly, he suggested considering the softer side for design purposes. He also found that the application of lateral cyclic loads did not affect the axial performance of the FRP reinforced helical pulldown micropiles (El Sharnouby, 2012).

2.5.2 Tapered piles

To date, very limited studies are available in terms of the analysis of the lateral cyclic performance of tapered piles.

2.6 Summary

This chapter presents a summary of the available literature on the performance of the two well established pile types that form the basis of the proposed piling system in this study: helical piles and tapered piles. The definition of the systems is firstly presented. This was followed by review of the available studies analyzing the axial and lateral performance of single helical and tapered piles at static and cyclic conditions. General design guidelines for both systems were presented. The effects of the piles installation, the change of capacity with time and the possible change in stiffness or strength when subjected to cyclic loads were discussed. The literature survey revealed that a limited number of studies were carried out in order to study the performance of tapered piles in cohesive soils and also when subjected to cyclic lateral loads. Even less attention was given to the uplift performance of tapered piles. Accordingly, further investigation of tapered piles under these conditions is recommended.

2.7   References

Abdelghany, Y. & El Naggar, M. H. Full-scale experimental and numerical analysis of instrumented helical screw piles under axial and lateral monotonic and cyclic loadings-A promising solution for seismic retrofitting. 6th International Engineering and Construction Conference, 2010, Cairo, Egypt. American Society of Civil Engineers.

Abdel-Rahman, K. & Achmus, M. Behavior of foundation piles for offshore wind energy plants under axial cyclic loading. Simulia customer conference, 2011, Barcelona/Spain. 1-13.

Alawneh, A. S., Nusier, O. K. & Awamleh, M. S. 2009. Time dependent capacity increase for driven pile in cohesionless soil. *Jordan Journal of Civil Engineering,* 3(1), 1-31.

Allotey, N. & El Naggar, M. H. 2008. A numerical study into lateral cyclic nonlinear soil-pile response. *Canadian Geotechnical Journal,* 45(9), 1268-1281.

ASCE-20-96 1997. Standard guidelines for the design and installation of pile foundations. American Society of Civil Engineers.

Bagheri, F. & El Naggar, M. H. Effects of the installation disturbance on the behavior of the multi-helix screw anchors in sands. GeoMontreal 2013, Montreal.

Bienen, B., Dührkop, J., Grabe, J., Randolph, M. F. & White, D. J. 2012. Response of piles with wings to monotonic and cyclic lateral loading in sand. *Journal of Geotechnical and Geoenvironmental Engineering,* 138(3), 364-375.

Brown, S. F., Juspi, S. & Yu, H. S. 2008. Experimental observations and theoretical predictions of shakedown in soils under wheel loading. *Advances in Transportation Geotechnics*.

CGS. 2006. *Canadian Foundation Engineering Manual*, 4th edition, Canadian Geotechnical Society.

Chan, S. F. & Hanna, T. H. 1980. Repeated loading on single piles in sand. *Journal of Geotechnical Engineering Division,* 106(GT2), 171-188.

Clemence, S. P. & Smithling, A. P. Dynamic uplift capacity of helical anchors in sand. Proceedings of the 4th Australia-New Zealand conference on geomechanics, 1984. 88-93.

El Naggar, M. H. & Abdelghany, Y. Helical screw piles (HSP) capacity for axial cyclic loadings in cohesive soils. 4th International Conference on Earthquake Geotechnical Engineering, 2007, Thessaloniki, Greece. 25-28.

El Naggar, M. H. & Sakr, M. 2000. Evaluation of axial performance of tapered piles from centrifuge tests. *Canadian Geotechnical Journal,* 37(6), 1295-1308.

El Naggar, M. H. & Wei, J. Q. 2000a. Cyclic response of axially loaded tapered piles. *Geotechnical Testing Journal,* 23(1), 100-115.

El Naggar, M. H. & Wei, J. Q. 2000b. Uplift behaviour of tapered piles established from model tests. *Canadian Geotechnical Journal*, 37(1), 56-74.

El Naggar, M. H. & Wei, J. Q. 1999. Response of tapered piles subjected to lateral loading. *Canadian Geotechnical Journal,* 36(1), 52-71.

El Sharnouby, M. M. 2012. Monotonic and cyclic behaviour of steel fibre-reinforced and FRP-steel fibre-reinforced helical pulldown micropiles. *PhD thesis.* London, Ontario, Canada: The University of Western Ontario.

El Sharnouby, M. M. & El Naggar, M. H. 2012. Axial monotonic and cyclic performance of fibre-reinforced polymer (FRP)-steel fibre-reinforced helical pulldown micropiles (FRP-RHPM). *Canadian Geotechnical Journal,* 49(12), 1378-1392.

El Sharnouby, M. M. & El Naggar, M. H. Lateral static and cyclic behaviour of the composite steel-fibre reinforced helical pulldown micropiles-innovative foundation solutions for seismic applications. 21st Vancouver Geotechnical Society Symposium: Foundation and Lifeline Engineering, 2013, Vancouver.

Elkasabgy, M. & El Naggar, M. H. 2013. Dynamic response of vertically loaded helical and driven steel piles. *Canadian Geotechnical Journal,* 50(5), 521-535.

Elsherbiny, Z. H. & El Naggar, M. H. 2013. Axial compressive capacity of helical piles from field tests and numerical study. *Canadian Geotechnical Journal*, 50(12), 1191-1203.

Fleming, K., Weltman, A., Randolph, M. & Elson, K. 2009. *Piling engineering*, Taylor and Francis Group.

Ghaly, A. & Hanna, A. 1992. Stresses and strains around helical screw anchors in sand. *Soils and Foundations,* 32(4), 27-42.

Ghaly, A. M. & Clemence, S. P. 1998. Pullout performance of inclined helical screw anchors in sand. *Journal of Geotechncial and Geoenvironmental Engineering,* 124(7), 617-627.

Guo, P. X., Xiao, Y. & Kunnath, S. K. 2014. Performance of laterally loaded H-Piles in sand. *Soil Dynamics and Earthquake Engineering,* 67, 316-325.

Hoyt, R. & Clemence, S. Uplift capacity of helical anchors in soil. 12th International Conference on Soil Mechanics and Foundation Engineering, 1989, Rio de Janeiro. 1019-1022.

Jardine, R. J. & Standing, J. R. 2012. Field axial cyclic loading experiments on piles driven in sand. *Soils and Foundations,* 52(4), 723-736.

Khan, M. K., El Naggar, M. H. & Elkasabgy, M. 2008. Compression testing and analysis of drilled concrete tapered piles in cohesive-frictional soil. *Canadian Geotechnical Journal*, 45(3), 377-392.

Kodikara, J. & Moore, I. 1993. Axial response of tapered piles in cohesive frictional ground. *Journal of Geotechnical Engineering,* 119(4), 675-693.

Kong, G. Q., Yang, Q., Liu, H. L. & Liang, R. Y. 2013. Numerical study of a new belled wedge pile type under different loading modes. *European Journal of Environmental and Civil Engineering,* 17(sup1), s65-s82.

Kurian, N. P. & Srinivas, M. 1995. Studies on the behaviour of axially loaded tapered piles by the finite element method. *International Journal for Numerical and Analytical Methods in Geomechanics,* 19(12), 19(12), 869-888.

Leblanc, C., Houlsby, G. T. & Byrne, B. W. 2010. Response of stiff piles in sand to long-term cyclic lateral loading. *Geotechnique,* 60(2), 79-90.

Li, W., Gavin, D. & Doherty, P. Review of design models for lateral cyclic loading of monopoles in sand. Proceedings of the 8th International Conference on Physical Modelling in Geotechnics, 2014. 819-825.

Li, Z., Haigh, S. K. & Bolton, M. D. Centrifuge modelling of mono-pile under cyclic lateral loads. Physical Modelling in Geotechnics, 2010, Zurich. 965-970.

Lin, S-S. & Liao, J-C. 1999. Permanent strains of piles in sand due to cyclic lateral loads. *Journal of Geotechnical and Geoenvironmental Engineering,* 125(9), 798-802.

Little, R. L. & Briaud, J-L. 1988. Full scale cyclic lateral load tests on six single piles in sand. Texas A&M University College Station Department of Civil Engineering.

Livneh, B. & El Naggar, M. H. 2008. Axial load testing and numerical modeling of square shaft helical piles. *Canadian Geotechnical Journal,* 45(8), 1142-1155.

Long, J. H. & Vanneste, G. 1994. Effects of cyclic lateral loads on piles in sand. *ASCE Journal of Geotechnical Engineering,* 120(1), 225-244.

Meyerhof, G. G. 1976. Bearing capacity and settlement of pile foundations. *Journal of the Geotechnical Engineering Division,* 102(3), 195-228.

Mitsch, M. P. & Clemence, S. P. The uplift capacity of helix anchors in sand. In uplift behavior of anchor foundations in soil: Proceedings of a session sponsored by the Geotechnical Engineering Division of the American Society of Civil Engineers in conjunction with the ASCE convention in Detroit, 1985, New York. ASCE, 26-47.

Mosikeeran, T. 1990. Cyclic lateral load behaviour of piles. Report No.500. Auckland, New Zealand.

Perko, H. 2009. *Helical piles: A practical guide to design and installation,* New Jersey, John Willey and Sons Inc.

Poulos, H. G. 1981. Cyclic axial response of single pile. *Journal of Geotechnical Engineering Division,* 107(1), 41-58.

Poulos, H. G. 1989. Cyclic axial loading analysis of piles in sand. *Journal of Geotechnical Engineering,* 115(6), 836-852.

Poulos, H. G. & Davis, E. H. 1980. *Pile foundation analysis and design*, John Wiley and Sons.

Prakash, S. & Sharma, H. D. 1990. *Pile foundation in engineering practice,* New York, John Wiley and Sons.

Prasad, Y. V. S. N. & Rao, S. N. 1994. Pullout behaviour of model pile and helical pile anchors subjected to lateral cyclic loading. *Canadian Geotechnical Journal,* 31(1), 110-119.

Prasad, Y. V. S. N. & Rao, S. N. 1996. Lateral capacity of helical piles in clay. *Journal of Geotechnical Engineering,* 122(11), 938-941.

Puri, V. K., Stephenson, R. W., Dziedzic, E. & Goen, L. 1984. Helical anchor piles under lateral loading. Laterally loaded deep foundations: Analysis and Performance. ASTM STP 835. Edited by J. A. Langer, E. T. Mosley, and C. D. Thompson. American Society for Testing and Materials, 194–213.

Reese, L. C. & Van Impe, W. F. 2001. *Single piles and pile groups under lateral loading,* London, UK, Taylor and Francis group plc.

Sakr, M. Lateral resistance of helical piles in sands. International Foundation Congress and Equipment Expo, 2009, Orlando, Florida, United States. American Society of Civil Engineers, 464-471.

Sakr, M. & El Naggar, M. H. 2003. Centrifuge modeling of tapered piles in sand. *Geotechnical Testing Journal, 26(1), 1-14.*

Sakr, M., El Naggar, M. H. & NEHDI, M. Lateral behaviour of composite tapered piles in dense sand. *Proceedings of the Institution of Civil Engineers-Geotechnical Engineering,* 2005a*,* 158(3). 145-157.

Sakr, M., El Naggar, M. H. & Nehdi, M. 2005b. Uplift performance of FRP tapered piles in dense sand. *International Journal of Physical Modelling in Geotechnics,* 5(2), 01-16.

Schwarz, P. 2002. Beitrag zum Tragverhalten von Verpresspfählen mit kleinem Durchmesser unter axialer zyklischer Belastung. *Lehrstuhl und Prüfamt für Bodenmechanik und Felsmechanik der Technischen Universität München,* 33.

Seamless-Pole-Inc 2010. Ductile iron poles. Birmingham, AL. (*http://www.seamlesspole.com/*)

Seider, G. 2004. Helical foundations: What an engineer needs to know. *Structure Magazine,* 11, 27-28.

Svinkin, M. R. 1996. Setup and relaxation in glacial sand-Discussion. *Journal of Geotechnical Engineering,* 122(4), 319-321.

Tomlinson, M. J. 1994. *Pile design and construction practice*, Taylor and Francis.

Trofimenkov, J. G. & Maruipolshii, L. G. Screw piles used for mast and tower foundations. Proceedings of the 6th International Conference on Soil Mechanics and Foundation Engineering Conference on Soil Mechanics and Foundation Engineering, 1965, Montreal. 328-332.

Tsuha, C. H. C., Aoki, N., Rault, G., Thorel, L. & Garnier, J. 2012. Evaluation of the efficiencies of helical anchor plates in sand by centrifuge model tests. *Canadian Geotechnical Journal,* 49(9), 1102-1114.

Tsuha, C. H. C., Santos, T. C., Rault, G., Thorel, L., & Garnier, J. Influence of multiple helix configuration on the uplift capacity of helical anchors. Proceedings of the 18th International Conference on Soil Mechanics and Geotechnical Engineering, 2013, Paper. No. 2595.

Verdure, L., Garnier, J. & Levacher, D. 2003. Lateral cyclic loading of single piles in sand. *International Journal of Physical Modelling in Geotechnics,* 3(3), 17-28.

Wei, J. & El Naggar, M. H. 1998. Experimental study of axial behaviour of tapered piles. *Canadian Geotechnical Journal*, 35(4), 641-654.

York, D. L., Brusey, W. G., Clemente, F. M. & LAW, S. K. 1994. Setup and relaxation in glacial sand. *Journal of Geotechnical Engineering,* 120(9), 1498-1513.

Zhan, Y-G., Wang, H. & Liu, F-H. 2012. Numerical study on load capacity behavior of tapered pile foundations. *Electronic Journal of Geotechnical Engineering,* 17, 1969-1980.

Zhang, D. J. Y. 1999. Predicting capacity of helical screw piles in Alberta soils. *MSc thesis.* Edmonton, Alberta: University of Alberta.

MONOTONIC COMPRESSIVE PERFORMANCE OF SCDI

HELICAL TAPERED PILES IN SAND

3.1 Introduction

Pile foundations are used to support structures when the ground near the surface cannot provide the required bearing capacity or settlement represents a major concern. Different piles of varying shapes and materials are used in practice, but mostly either driven piles or drilled shafts. However, due to varying construction challenges and ever increasing demands for sustainable practices and cost saving solutions, the construction industry is pursuing foundations that feature efficient construction techniques, innovative pile configurations and novel application of materials.

Owing to their various construction advantages, helical piles are gaining popularity, especially in projects that require fast installation and quick loading of the foundation. Helical piles are typically manufactured with straight steel shafts (pipe or square section) fitted with one or more helices and are installed using mechanical torque (Perko, 2009). Currently use of helical piles have expanded to a wide range of applications such as power transmission towers, bridges and residential and commercials buildings, which involve static and cyclic compressive, uplift and lateral loading (Elsherbiny and El Naggar, 2013). Helical piles of different configurations and wide range of capacity are being developed and used in practice. For example, square shaft helical piles (Livneh and El Naggar, 2008), helical pull down micropiles and fibre reinforced helical pull down micropiles (El Sharnouby and El Naggar 2012 a and b) and large diameter helical piles (Elkasabgy and El Naggar, 2013, 2015).

Helical piles are installed into the ground by applying torque to the pile head. This installation technique produces minimal vibration, noise and soil spoils, which makes it suitable for construction in urban areas. In addition, monitoring the installation torque allows estimating the pile capacity and provides means for quality assurance/control. Given

the installation torque, the axial pile capacity can be predicted using the following equation (Livneh and El Naggar, 2008; Hoyt and Clemence, 1989):

$$P_u = K_t T \tag{3 - 1}$$

where T is the installation torque, P_u is the ultimate axial capacity and K_t is the capacity-to-torque ratio. Perko (2009) conducted regression analysis of the results of more than 300 pile load tests and proposed the following expression for K_t:

$$K_t = \frac{\lambda_k}{d_{eff}^{0.92}} \tag{3 - 2}$$

Where: d_{eff} is effective shaft diameter and λ_k is a curve fitting factor $=1433\text{mm}^{0.92}/\text{m}$ (22 in$^{0.92}$/ft).

For helical piles with a single helix, the capacity is given by the resistance due the helix bearing and the shear resistance along the pile shaft. Helical piles with slender shafts can only sustain relatively small compressive loads, and low lateral loads compared to other greater diameter piles. However, different helical pile systems with large diameter shafts are developed and offer large axial and lateral capacity (Fleming *et al.*, 2009; Abdeghany and El Naggar, 2010; El Sharnouby and El Naggar, 2012b; Elkasabgy and El Naggar, 2013). Additionally, these solutions would enhance the axial capacity of the piles owing to the increased shaft resistance, which significantly contributes to the compressive capacity.

Tapered piles of decreasing circumference with depth have been successfully used for many years as an efficient piling system. Due to their shape, additional shaft frictional resistance is induced and therefore greater axial capacity is reached. The higher compressive capacity of tapered piles compared to conventional cylindrical piles has been long recognized (e.g. Norlund 1963; Zil'berberg and Sherstnev, 1990; Wei and El Naggar, 1998; El Naggar and Sakr, 2000). The tapered configuration could increase the load carrying capacity of the pile by up to 188% compared to conventional straight shafts (Sakr and El Naggar, 2003). Furthermore, the increased sectional diameter at the top provides an increased lateral resistance compared to the regular straight piles. The capacity of tapered piles ranges between 1.5 to 2.5 times the capacities of cylindrical pile of the same average

diameter (El Naggar and Sakr, 2000). Tapered piles can be installed by drilling, driving or using torque and can be made of steel, wood, concrete or composite sections.

Wei and El Naggar (1998) found that the taper angle increases the efficiency of utilization of the pile material, especially in looser deposits where the confining pressure significantly increased the soil stiffness. The increase was attributed to transferring the load to a greater soil volume resulting from the developed soil arch compared to straight piles. In addition, the radial expansion of the soil adjacent to the pile during installation and pile loading results in higher lateral earth pressure hence greater frictional resistance compared to the straight piles. Wei and El Naggar (1998) proposed the following equation to calculate the skin friction q_s along the shaft of tapered piles installed in sands:

$$q_s = K_{ts} \, K_s \sigma_v\text{'}\tan\delta \tag{3 - 3}$$

$$K_{ts} = \frac{\tan(\theta+\delta)\cot(\delta)}{1+2\zeta\tan(\theta)\tan(\theta+\delta)} + \frac{4G\tan(\theta)\tan(\theta+\delta)\cot(\delta)S_r}{(1+2\zeta\tan(\theta)\tan(\theta+\delta))K_s\sigma_v} \tag{3 - 4}$$

where θ is the pile taper angle, σ_v is the overburden stress, K_{ts} is the taper coefficient, K_s is the coefficient of lateral earth pressure, δ is soil-pile interface angle, G is the sand shear modulus, $\zeta = \ln(r_l/r_m)$, r_l is the pile radius at which the shear stresses become negligible, r_m is average pile radius and S_r is the pile settlement as a ratio of its diameter at the ultimate load.

For tapered piles installed in frictional-cohesive soils, K_{ts} can be given by (Khan *et al.*, 2008):

$$K_{ts} = \frac{\tan(\theta+\delta)\cot(\delta)}{1+2\zeta\tan(\theta)\tan(\theta+\delta)} + \frac{4G\tan(\theta)\tan(\theta+\delta)\cot(\delta)S_r}{(1+2\zeta\tan(\theta)\tan(\theta+\delta))K_s\sigma_v}$$
$$+ \frac{C'}{(1+2\zeta\tan(\theta)\tan(\theta+\delta))K_s\sigma_v\text{'}\tan(\delta)} \tag{3 - 5}$$

where C' is the effective cohesion.

Kurian and Srinivas (1995) investigated the compressive behavior of tapered piles in sand numerically and validated their results with laboratory testing. The results confirmed the

efficiency of tapered piles when compared to straight shaft pile capacities. The increase in pile capacity was attributed to the direct bearing on the pile's sides increasing the normal pressure and therefore the side frictional component of the total pile resistance(Kurian and Srinivas, 1995). Interestingly, unlike cylindrical piles, tapered piles shaft resistance continues to develop with increase in pile settlement (Kodikara and Moore, 1993). Also, Zhan et al. (2012) numerically studied the axial behavior of cast-in-situ 4m length tapered piles installed in sands using the software ABAQUS (Hibbitt et al., 2008), and concluded that a slight increase in shaft taper significantly increases the developed shaft stresses even at shallow depths as shown in Figure 3 – 1.

In the current study, an innovative pile system that combines the efficiency of the tapered section and the construction advantage of helical piles is investigated.
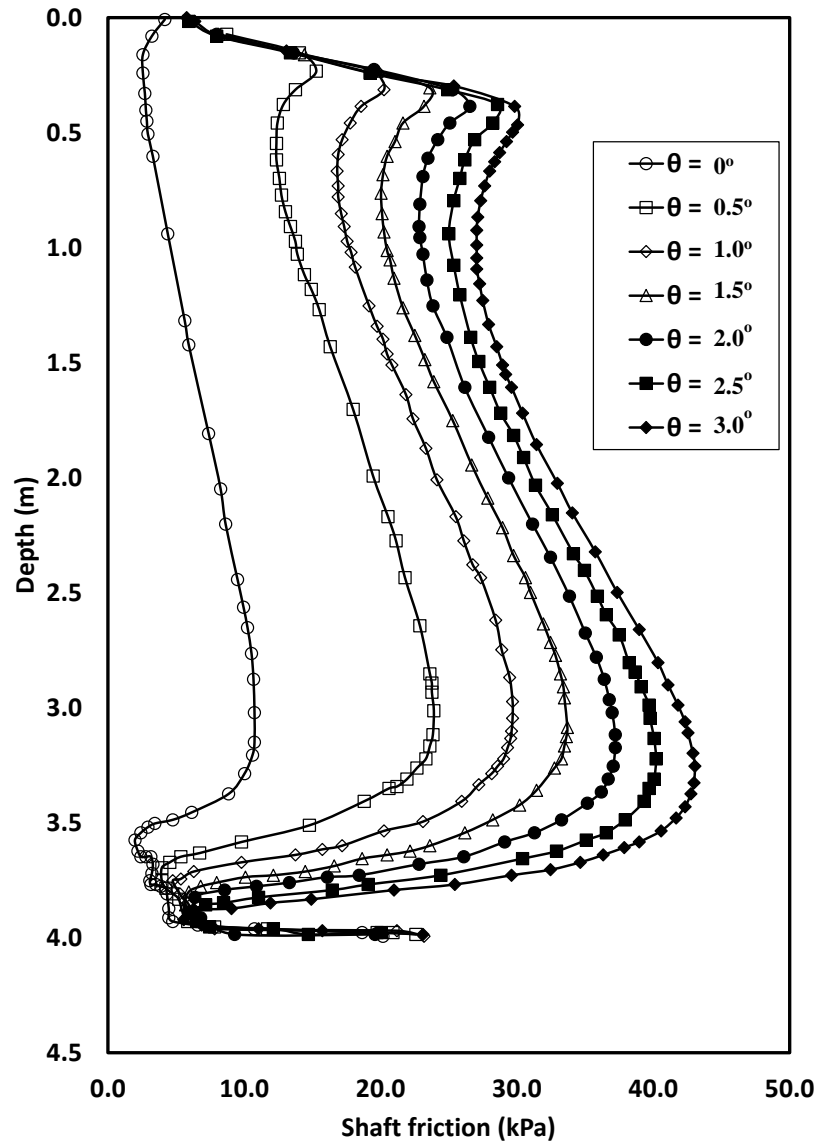
Figure 3 - 1: Developed shaft friction along tapered piles in sand at 2cm displacement (after Zhan *et al.* 2012)

3.2 Objectives and scope of work

The novel piling system investigated in the current study consists of a spun-cast ductile iron tapered pile (Seamless-Pole-Inc., 2010) fitted with a lower helical plate to facilitate its installation. The proposed pile is to be installed using a mechanical torque delivered by a

driving motor holding the pile head. The system configuration and its installation technique offer many advantages compared to the conventional pile types, including:

- Reduced manufacturing costs since the piles are made from molten metal, which eliminates the additional steel rolling costs;

- Fast and environmentally friendly installation process. Low vibration and noise, and no soil spoils during installation making it an apt solution for urban areas;

- Additional frictional resistance along the shaft due to its roughness and hence additional pile axial resistance;

- Increased axial capacity due to the wedging effect during installation as well as soil densification during pile loading;

A comprehensive investigation was conducted in order to assess the feasibility and efficiency of the proposed system. The investigation involved field load tests and numerical analyses to evaluate the axial performance of the proposed pile configuration under compressive monotonic and cyclic loading. In addition, the measurements from the field load tests and the results of the numerical analyses explained the load transfer mechanism of the proposed piles, and a design approach is proposed accordingly.

3.3   Experimental setup

3.3.1   Test piles

Seven hollow section closed ended piles with configurations as shown in Figure 3 - 2 were installed in silty sand soil. Three piles were of configuration A, 2 of configuration B and 2 of configuration C. The piles of configurations A and B were made of ductile iron having a very rough external surface, while those of configuration C were made of steel with conventional (relatively smooth) surface. The wall thickness of all piles was 5.5 mm.
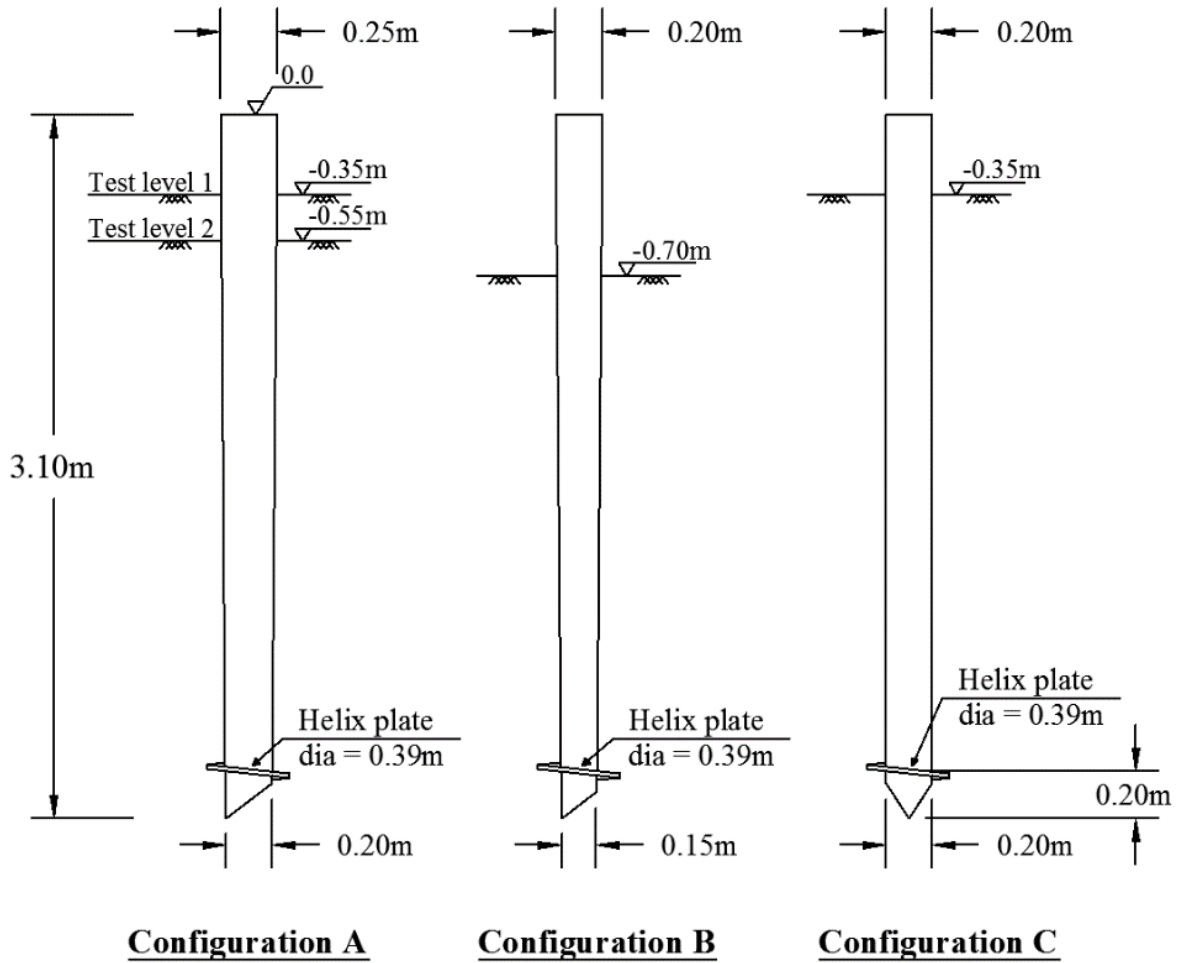
Figure 3 - 2: Tested piles configurations

3.3.2 Instrumentation and test setup

In order to evaluate the load transfer mechanism, each pile was instrumented using eight equally spaced electrical resistance strain gauges mounted at locations as shown in Figure 3 - 3 (a). The strain gauges were fixed on specially machined pockets of 1 mm depth as shown in Figure 3 - 3 (b).
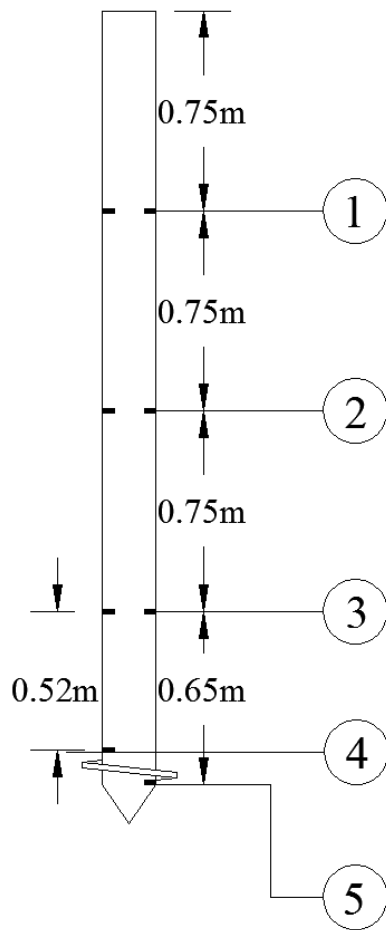
Figure 3 - 3: Strain gauges (a) Locations; (b) Pockets

The lead wires were passed from inside the pile through a small groove to minimize gauge damage during installation. Additionally, four linear variable displacement transducers (LVDTs) were mounted on the corners of the loading plate to monitor the pile head displacement. The applied load was measured using a load cell placed over the pile head. The strain gauges, LVDTs and the load cell were connected to a data acquisition system, which recorded the readings every 1 second. It should be noted that approximately 25% of the installed strain gauges were damaged mainly due to the high frictional stresses developed during pile installation at the soil-pile.

The axial testing setup comprised a main reaction steel beam and two secondary reaction beams as shown in Figure 3 - 4.
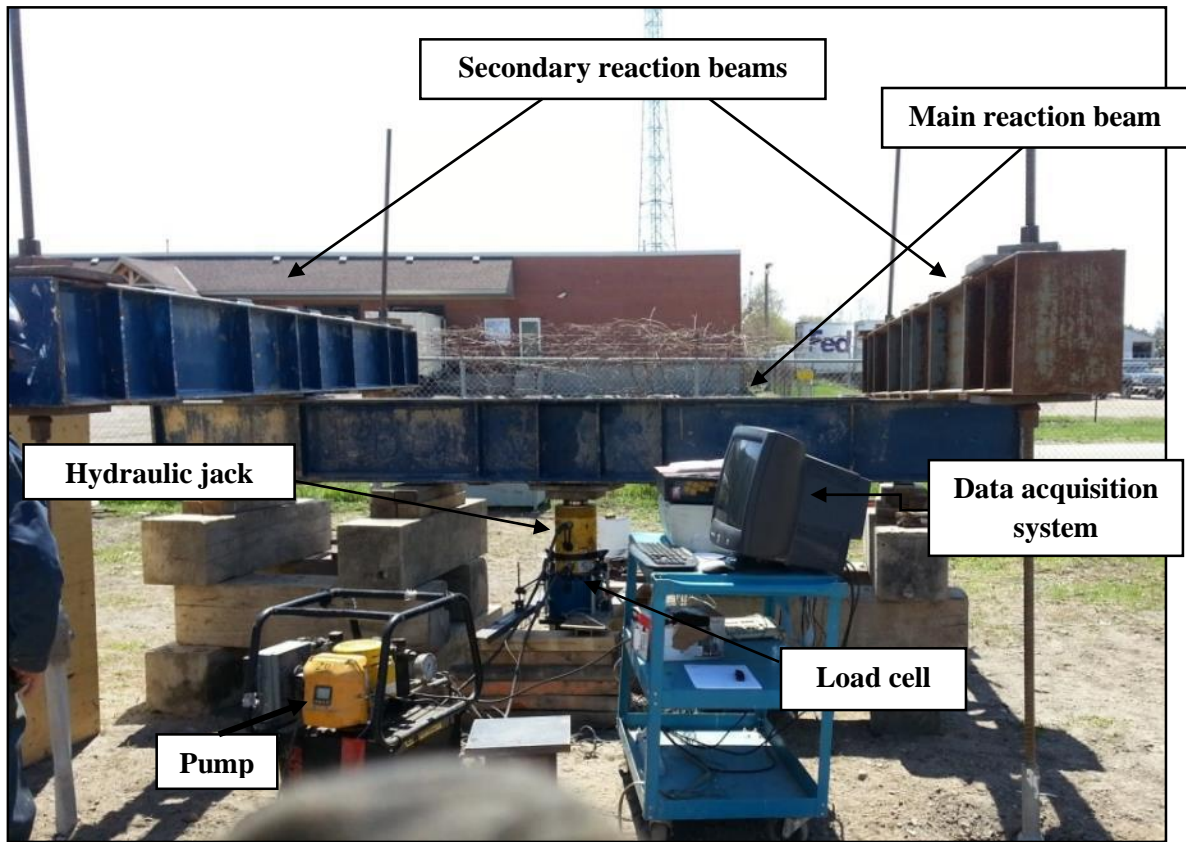
Figure 3 - 4: Test setup - compressive testing

3.3.3 Load test sequence and test procedure

3.3.3.1 Load test sequence

Different load sequences were used to evaluate the effect of cyclic loading on the axial performance of the proposed pile system. The adopted loading sequences are summarized in Table 3 - 1.

Table 3 - 1: Testing sequence

Pile	Configuration	Testing sequence
A1	A	Monotonic compression
A2	A	Monotonic compression
A3	A	Cyclic compression followed by monotonic compression
B1	B	Monotonic compression
B2	B	Cyclic compression followed by monotonic compression
C1	C	Monotonic compression
C2	C	Cyclic compression followed by monotonic compression

Four piles were subjected to monotonic loading to failure, and three piles were subjected to initial cyclic loading followed by monotonic loading to failure. In the cyclic load tests, the piles were initially loaded in four equal increments up to the expected design load then fifteen one-way compression cycles were applied (2 min/full cycle). The cyclic load varied from 70% to 130% of the expected design load. This was followed by an additional fifteen cycles with loads ranging from 55% to 145% of the design load as illustrated in Figure 3 - 5. These load ranges cover the maximum average earthquake peak ground acceleration in Canada (NBCC, 2005).
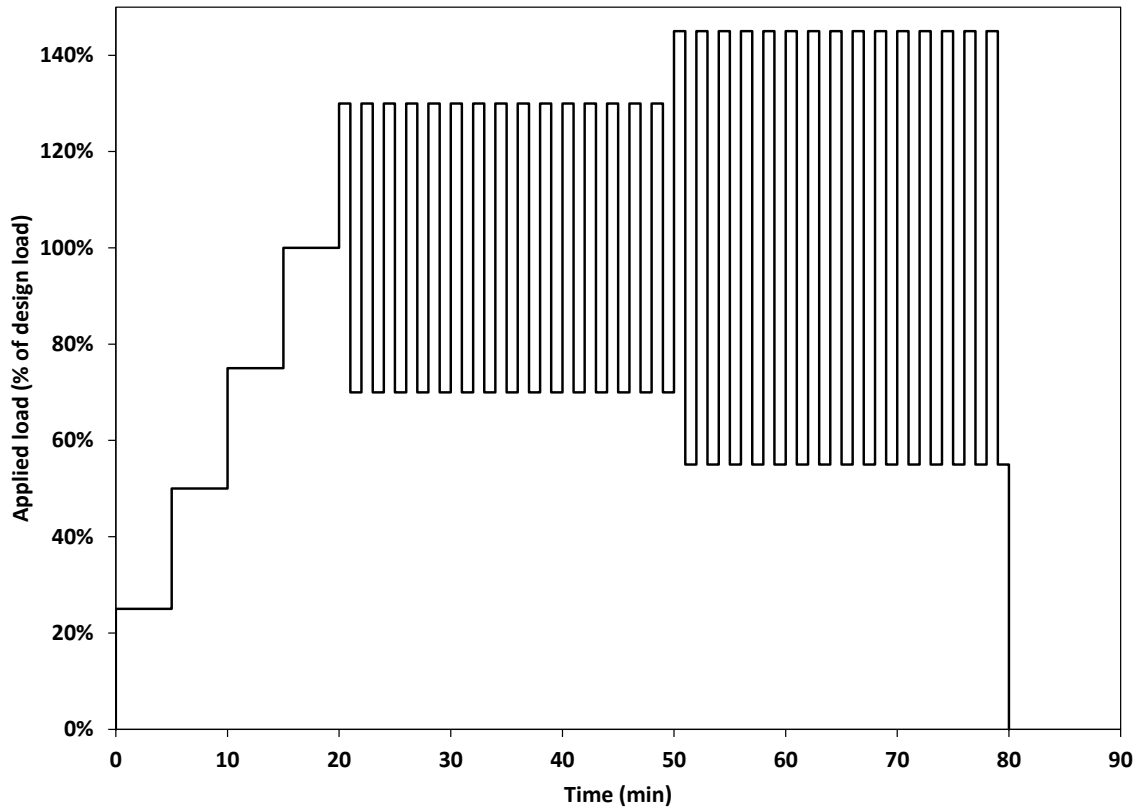
Figure 3 - 5: Axial cyclic loading pattern

3.3.3.2 Testing procedure

The quick maintained static load test procedure was adopted (ASTM D1143, 2007), where the piles were loaded in increments of 5% of their expected ultimate capacity and each load increment was maintained for 5 min. Load increments were added until failure was reached (i.e. no further loading is required to increase the pile penetration). The final load increment was maintained for 15 min. The piles were then unloaded on 4 equal increments, and each load increment was maintained for 5 min. The pile response was monitored for 15 minutes after it was fully unloaded to ensure its full rebound was captured.

3.3.4 Soil parameters

One borehole was drilled in the vicinity of the test piles at the location shown in Figure 3 - 6.
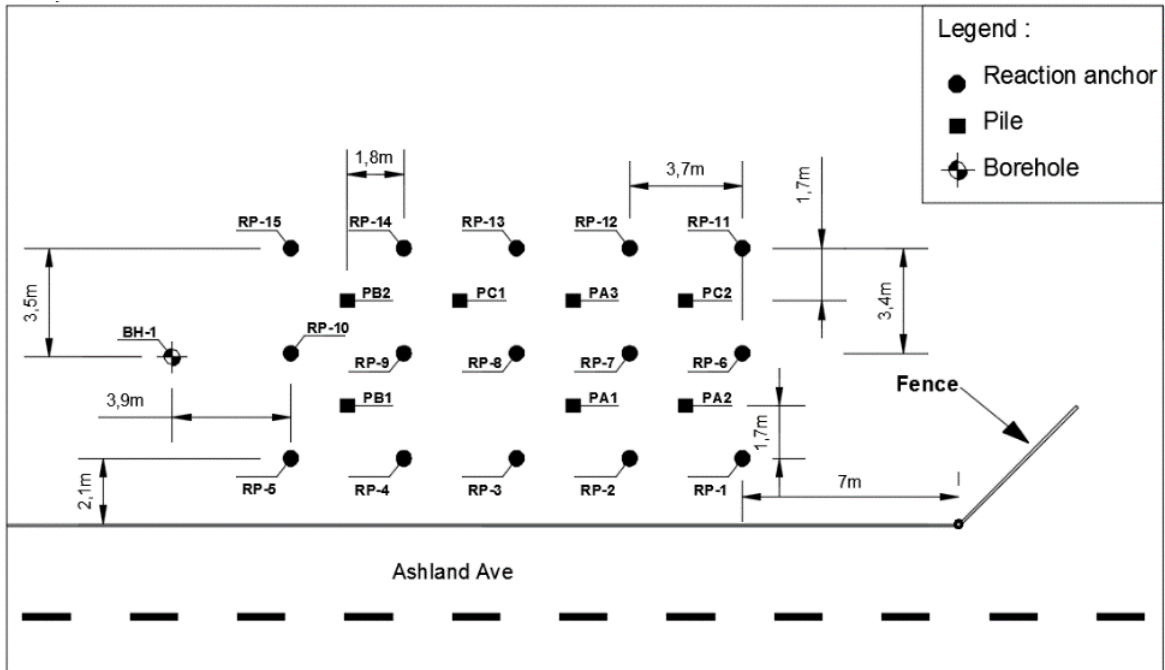
Figure 3 - 6: Site layout showing the drilled borehole location

The borehole log shows that the site is mainly a silty sand layer, which extends from the ground surface to 9.00m below ground surface, followed by a hard silty till, which extends to the end of the borehole (i.e. 11m depth). The details of the soil stratigraphy are as follows:

- A top layer extending down to a 0.5m depth composed of sand with silts. The top soil was mixed with some metallic residues, due to the fact that the testing site is used as a storage area for metallic tanks;

- A 4.5m thick silty sand layer, its color changed from reddish brown along the top 1m to light brown down at its end;

- A thin layer, slightly less than 1m thick, of gravelly sand;

- A 3m thick coarse sand layer with lower silt percentages than previous layers;

- A hard silty till down to the end of the borehole (i.e. 11m depth).

The ground water table was found at 3.5m from the ground surface.

3.3.4.1 Field Tests

Drilling the borehole included carrying out a Standard Penetration Test (SPT) with blow count measurements taken at 0.75m intervals. The values of the relative density, D_r, and the soil stiffness parameters were correlated to the corrected SPT, N_{60}', values standardized to 60% energy ratio. The corrected N_{60}' values can be calculated as (Skempton, 1986):

$$N_{60}= \textbf{Measured number of blows x} \ \frac{C_R C_S C_B E_m}{0.6} \tag{3 - 6}$$

$$N'_{60} = N_{60} \sqrt{\frac{100}{\sigma'_v}} \qquad \textbf{(Liao and Whitmann, 1986)} \tag{3 - 7}$$

where

N_{60} is the corrected value standardized to 60% energy ratio considering the field procedures

N'_{60} is the corrected value considering the overburden pressure effect

σ'_v is the effective overburden stresses

C_S is sampler correction, equal to 1.2 where sampler without liner was used (Skempton, 1986)

C_R is drill rod length correction, equal to 1 at depths greater than 10m and 0.75 for depths less than 4m (Skempton, 1986)

C_B is borehole diameter correction, equal 1.15 for diameter D=200mm (Skempton, 1986)

E_m is hammer efficiency, equal to 0.8 (Bowles, 1996)

The resulting variation of N'_{60} with depth is presented in Figure 3 - 7.
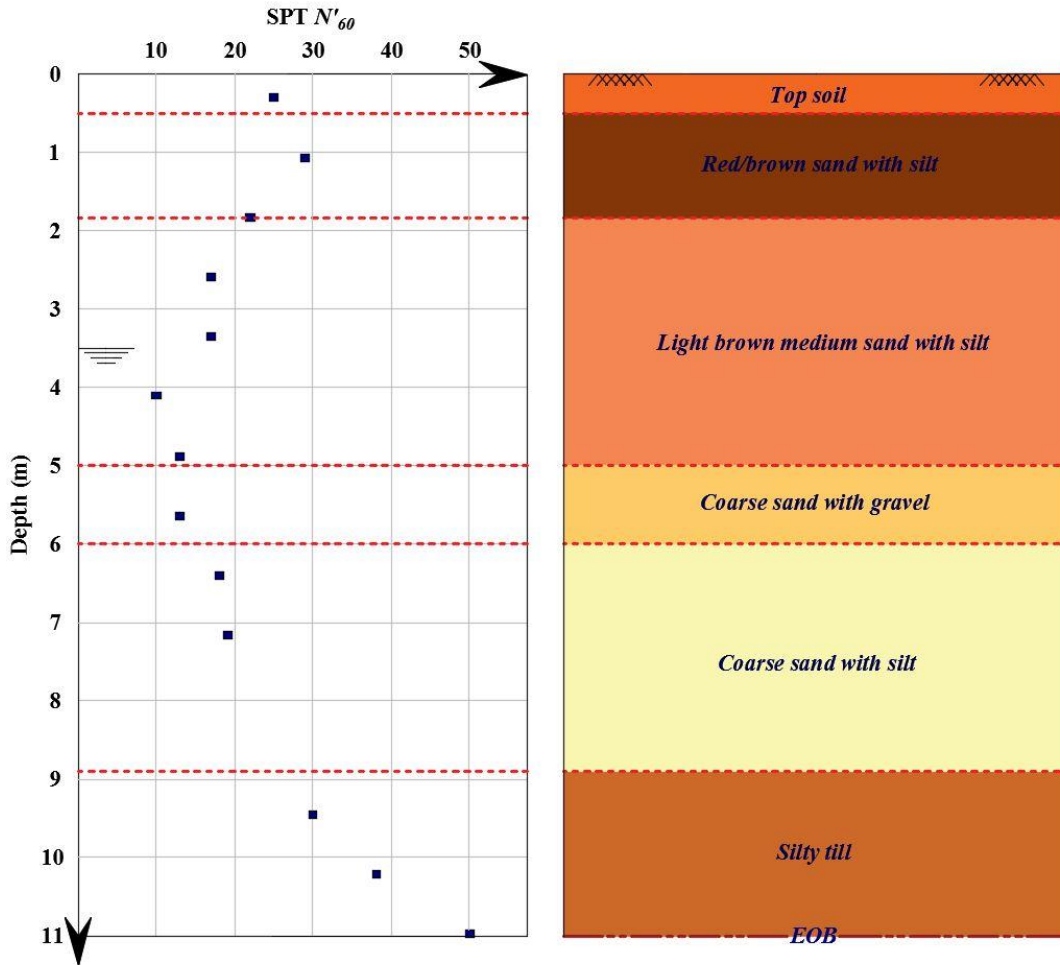
Figure 3 - 7: Variation of SPT N'_{60} with depth

The Sand-cone device (ASTM D1556, 2007) was used to measure the on-site unit weight of the top soil. The soil along the top 0.5m was carefully excavated, followed by two Sand-cone tests performed over the underlying layer. The average measured bulk density was found to be 16.5kN/m^3.

3.3.4.2 Laboratory Testing

Fifteen disturbed samples retrieved from the SPT split-spoon sampler were transported and tested at The University of Western Ontario soils laboratory. The tests included soil

classification, determination of the specific gravity G_S, measurement of water content W_c, direct shear tests and Atterberg limit determination. The representative soil parameters are summarized in Table 3 - 2.

Table 3 - 2: Representative soil parameters

Depth (m) From	Depth (m) To	Peak angle of internal friction φ_p (degrees)	Cohesion C' (kPa)	Specific gravity G_s	Water content W_c (%)	Poisson's ratio ν	E_s (MPa)	Effective unit weight γ' (kN/m³)	Relative density D_r (%)
0	0.5	36							-
0.5	4	38	4	2.71	21	0.3	70	16.5	55

3.3.4.3 Soil Classification and Index Properties

Sieve analyses of the extracted samples at different depths were performed according to ASTM C136 (2006). The resulting gradation curves are shown in Figure 3 - 8.
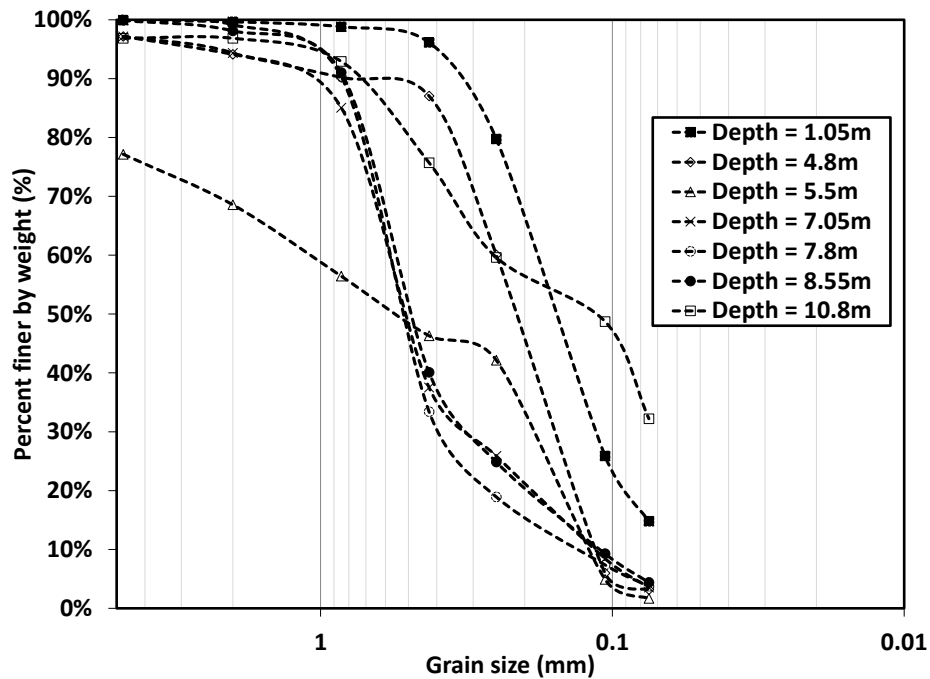
Figure 3 - 8: Grain size distribution for disturbed samples at various depths

44

Given that the tested piles were only 3.1m long, with an even shorter effective embedment depth due to their free length, only soil along the top 4m of the profile were of relevant interest (represented by the sample at 1.05m depth). The classification curve showed only 14.8% fines at that depth and almost 0% Gravel. Atterberg limits of three samples were measured showing average liquid and plastic limits of 25.3% and 21.5% respectively (ASTM D4318, 2010). The top layer can thus be classified as silty sand SM according to the Unified Soil Classification System USCS (ASTM D2487, 2011). The average on-site W_c at the same depth was measured to be 20.5%. Lower percentages of fines were found at deeper layers but then significantly increased at the bottom of the borehole were the percentage of fines at 10.8m depth was found to be 32%. The average measured G_s of two soil samples extracted at depths of 1.05m and 4.8m were found to be 2.71.

3.3.4.4 Soil Shear Strength Parameters

The soil shear strength parameters were measured using a series of direct shear tests (ASTM D3080, 2011) with a horizontal rate of feed of 0.406 mm/min. Samples retrieved at 0.6m and 1.08m depths were tested. The unit weights of the tested soil samples within the direct shear box were set to the field measured unit weight. The resulting variation of shear stresses with normal stresses, vertical displacement and horizontal displacement as well as the residual and peak strength values are shown in Figure 3 - 9. A bilinear shear-normal stress relation was observed with the first section ending at a normal stress of 20 kPa.
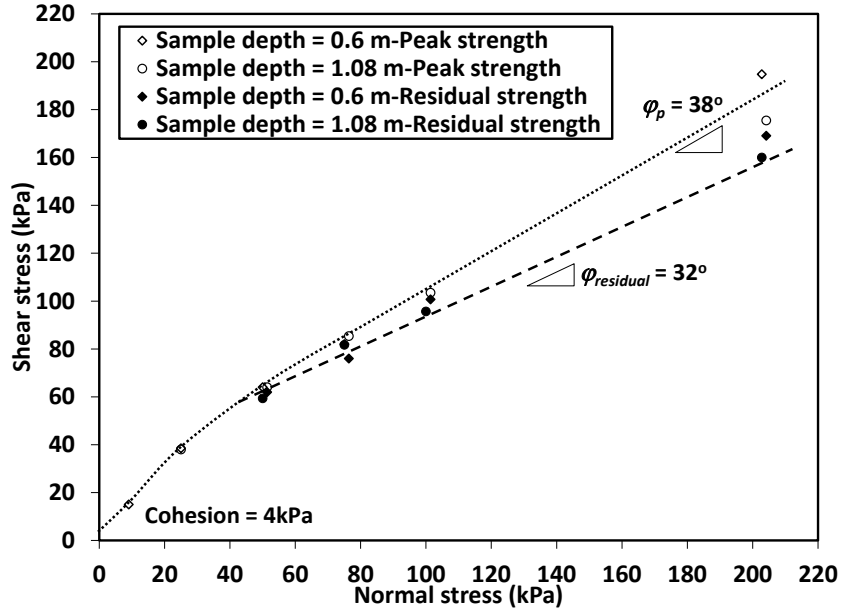
(a)
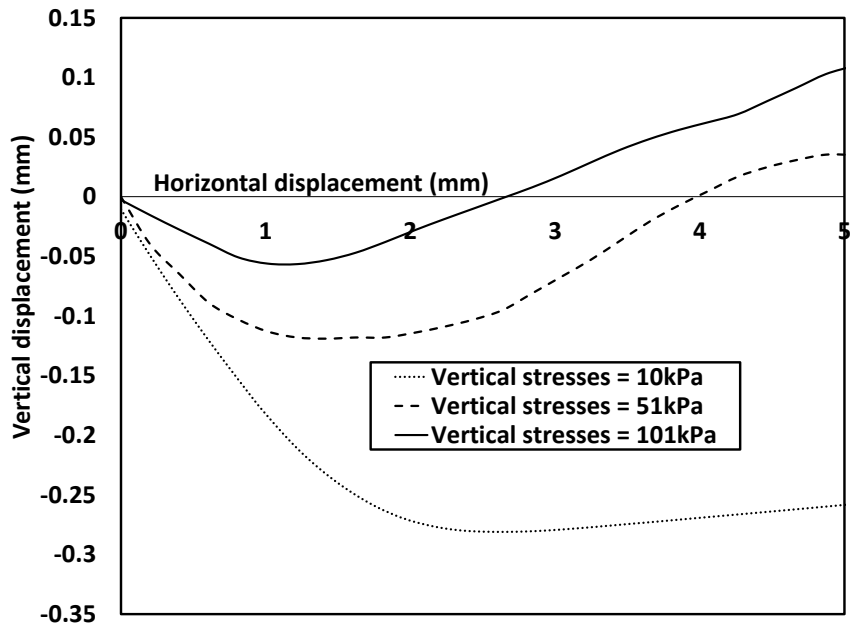
(b)
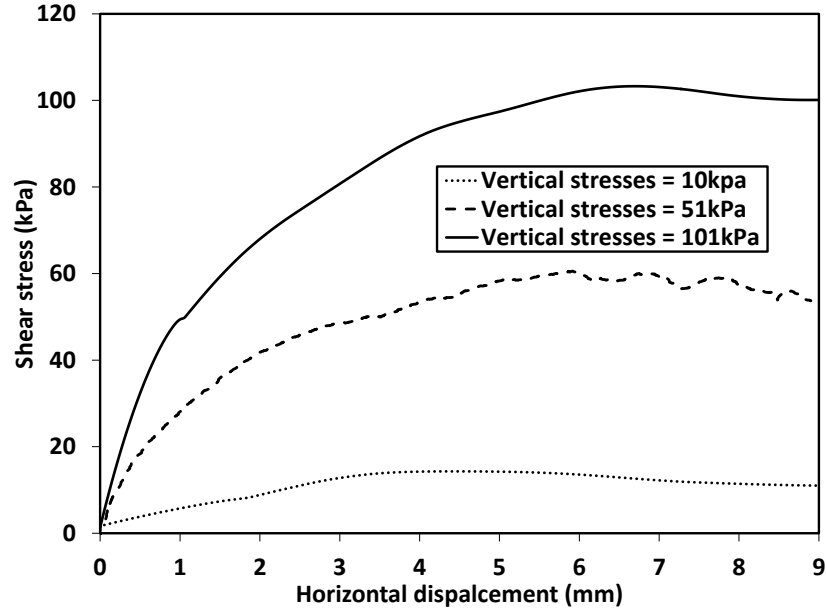
(c)

Figure 3 - 9: Direct shear tests results (a) Shear vs normal stresses; (b) Vertical displacement vs horizontal displacement; (c) Shear stress vs horizontal displacement

From the results shown above, the effective cohesion, c', residual angle of internal friction $\varphi_{residual}$ and peak angle of internal friction φ_p were determined to be 4 kPa, 32° and 38°, respectively. The determined angle of internal friction lies within the upper bound of the relevant range typically found in the literature for the range of the *SPT* number of blows at the location of test specimen, due to the high angularity of the sand particles.

3.3.4.5 Relative Density and Stiffness Parameters

The values of soil relative density, D_r, Young's modulus E_s, and Poisson's ratio v were correlated to the measured SPT values as follow:

The soil D_r was correlated to the results of performed SPT tests using the following equation (Mayne *et al.*, 2002):

$$D_r = 100 \sqrt{\frac{N'_{60}}{60}} \tag{3 - 8}$$

The variation of D_r with depth is shown in Figure 3 - 10 (a), which shows that D_r along the top 4m ranges between 50 to 70%. Considering the angle of internal friction and D_r, the soil deposits along the pile length can be classified as medium dense to dense (Bowles, 1996).

In the absence of undisturbed soil samples, values of the over-consolidation ratio, OCR, are generally correlated to other parameters or test results. The apparent preconsolidation pressure σ_p' for the sand was correlated to N_{60}, i.e.(Mayne, 1992):

$$\sigma_p' = 0.47 \ (N_{60})^m \ Pa \tag{3 - 9}$$

where Pa is the atmospheric pressure *and m* = 0.6 to 0.8 for silty sands to sandy silts (Mayne, 2006).

The calculated OCR with depth considering the above equation and knowing the initial overburden stresses on site is approximately 6 for the top 4 m. This was expected considering the nature of the test site, which was used for storage of heavy steel tanks.

Although several equations have been developed correlating the measured SPT with the soil's E_s, a significant scatter exists between the different correlations (Kulhawy and Mayne, 1990). As a first order estimator, E_s for overconsolidated sand can be correlated to the corrected SPT N_{60}, i.e. (Kulhawy and Mayne, 1990):

$$E_s/Pa = 15N_{60} \tag{3 - 10}$$

The variation of E_s with depth using the above correlation is shown in Figure 3 - 10 (b).
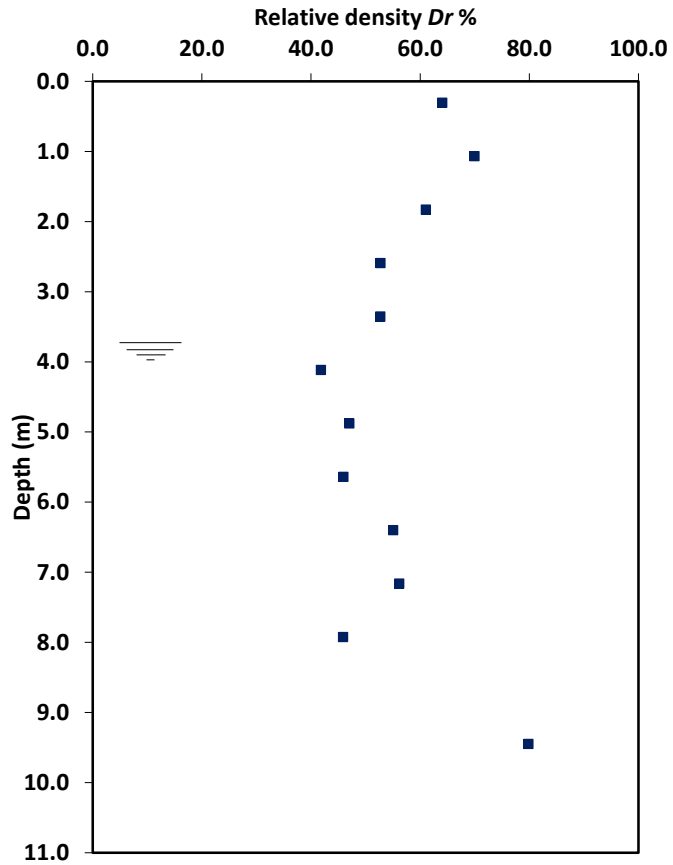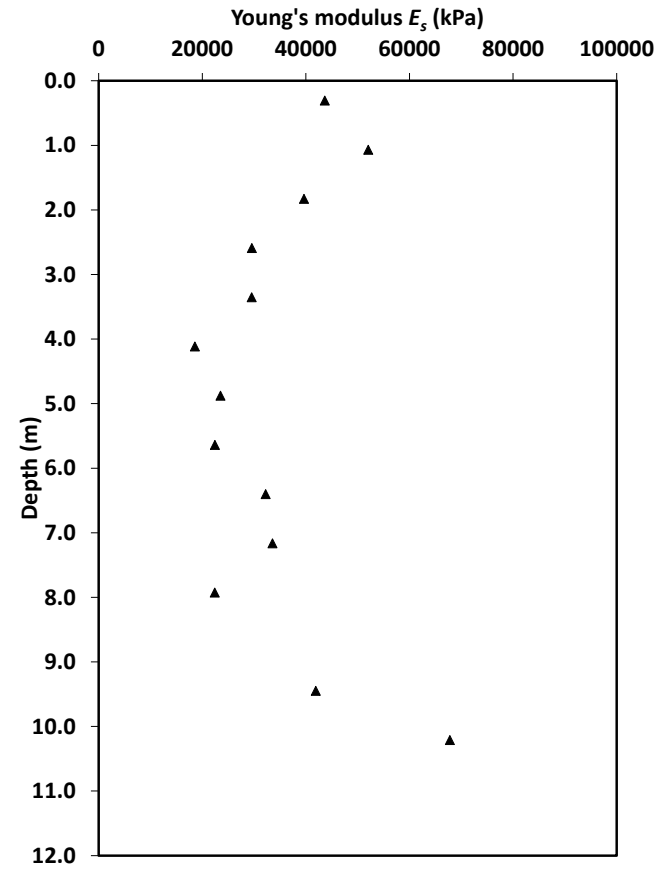
Figure 3 - 10: (a) Variation of the relative density D_r with depth; (b) Variation of the soil Young's modulus with depth using empirical correlations (Kulhawy and Mayne, 1990)

It should be noted, however, that the post–installation values are of main interest to this study. For that, and as a preliminary estimation, the recommended values by Poulos and Davis (1980) for driven piles in sand were considered. They suggested that, while E_s for sand typically varies with depth, it is appropriate for analysis purposes to consider an average modulus value along the pile shaft and greater values below the toe of driven piles (Poulos and Davis, 1980). This is also acceptable considering the relatively short length of the piles in the present study. Average values suggested by Poulos and Davis were in the order of 55~70 MPa for medium dense sand and 70~100 MPa for dense sand layers. Accordingly, an average E_s of 70 MPa was considered for the current soil profile. This value considered in the numerical investigation and calibrated/verified against the field test data as will be discussed later.

The value of ν ranges between 0.2 to 0.4 for loose to dense sands (AASHTO, 2002) hence 0.3 will be considered.

Finally, considering the average OCR of 6 along the first 4m, the average coefficient of earth pressure at rest prior to the pile installation can be given by (Mayne and Kulhawy, 1982)

$$K_{o\text{-}OC} = (1\text{-}Sin\varphi)OCR^{(1\text{-}sin\varphi)} = 0.76 \tag{3 - 11}$$

3.3.5 Installation procedure

To ensure the pile integrity during installation, finite element (FE) models were developed considering the piles configurations and material properties to determine the torque capacity of each pile configuration. The FE models considered the pile to be subjected to a torque applied at its head and full fixation at its toe with no soil along its shaft. This condition represented an upper bound for the shear stresses developed in the pile cross-section due to the installation torque. In reality, gradual transfer of the pile stresses to the soil will be provided by the soil along the soil-pile interface. The calculated maximum (capacity) torque of configurations A, B and C are 58, 32 and 68.5 kN.m, respectively. The lower torque capacity of configuration B piles was expected considering the smaller

50

diameter (lower sectional inertia) as well as the lower Young's modulus and yield strength of cast iron compared to the steel piles (configuration C).

The mechanical torque head used was a Hitachi UH07 rig, and the torque was applied through a specially manufactured steel cap bolted to the pile head as shown in Figure 3 - 11.

(a)

(b)
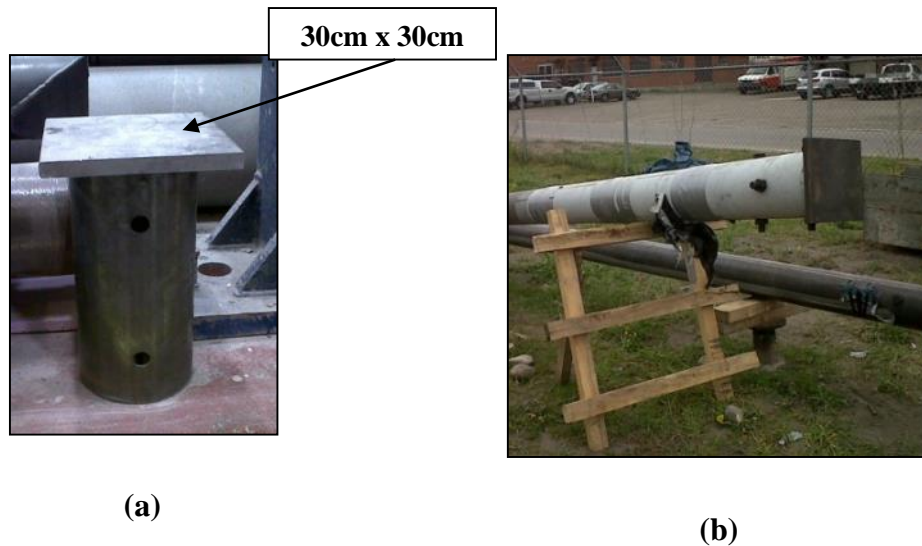
Figure 3 - 11: Setup for pile installation and loading (a) loading cap, (b) cap-pile connection

The applied torque required to overcome the shear resistance at the pile – soil interface was monitored and summarized in Table 3 - 3. It should be noted that prior to the piles installation, the soil along the top 0.3 m to 0.45 m was predrilled to facilitate the pile vertical alignment.

Table 3 - 3: Pile installation torque readings

Depth (m)	Torque (kN.m)						
	PA1	PA2	PA3	PB1	PB2	PC1	PC2
0.0	-	-	-	-	-	-	-
0.3	-	-	-	-	-	-	-
0.6	0.45 m predrilled -0.35 m free length (above ground surface)	0.45 m predrilled -0.55 m free length	0.3m predrilled -0.35 m free length	0.3 m predrilled -0.7 m free length	0.3 m predrilled -0.7 m free length	0.3 m predrilled -0.35m free length	0.3 m predrilled -0.35 m free length
0.9	4.1	NA	6.8	4.1	NA	NA	NA
1.2	6.8	8.1	10.2	8.1	2.0	4.7	3.4
1.5	11.5	12.2	12.9	11.5	4.7	8.1	8.1
1.8	16.3	16.3	16.3	12.9	8.1	1.4	11.5
2.1	24.4	24.4	23.0	16.3	11.5	23.0	13.6
2.4	29.8	30.5	29.2	20.3	16.3	23.7	18.3
2.7	38.0	38.6	37.3	21.0	19.7	20.3	23.0
3.10	40.7	40.7	40.0	20.3	NA	34.6	27.8

Following the installation process, the inclination angle of each pile head with the vertical axis was measured to check the piles verticality. The maximum inclination angle in any direction was found to be less than 2 degrees.

3.4 Results and discussion

3.4.1 Load-displacement curves

The measured load-displacement curves for the different tested piles are shown in Figure 3 - 12 for piles subjected to monotonic loading first, while Figure 3 - 13 presents the measured load-displacement curves for piles subjected to cyclic loading first, followed by monotonic loading to failure.
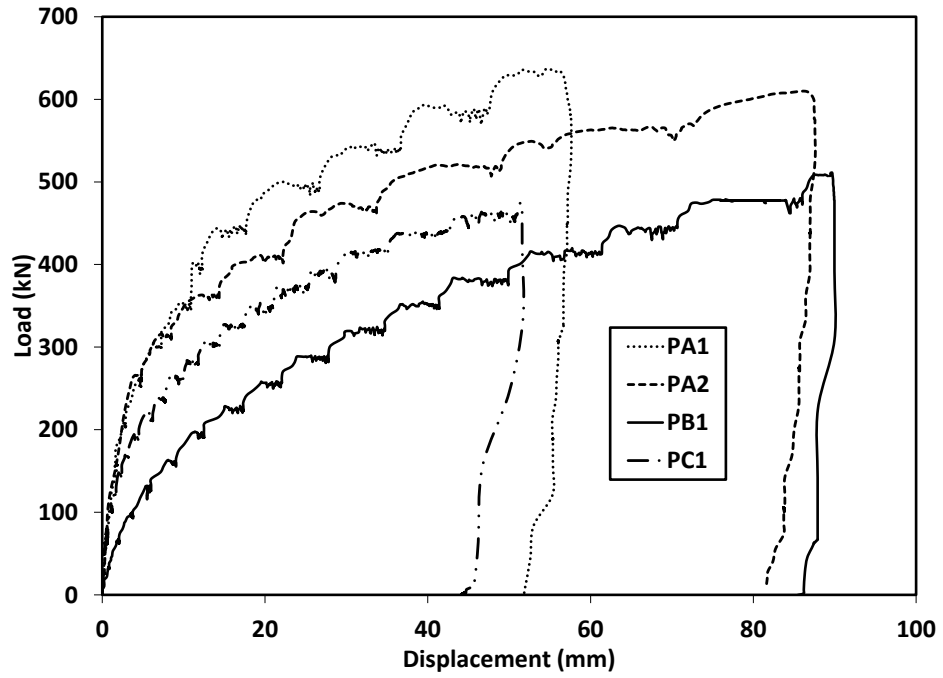
Figure 3 - 12: Load-displacement curve-initial monotonic compression tests
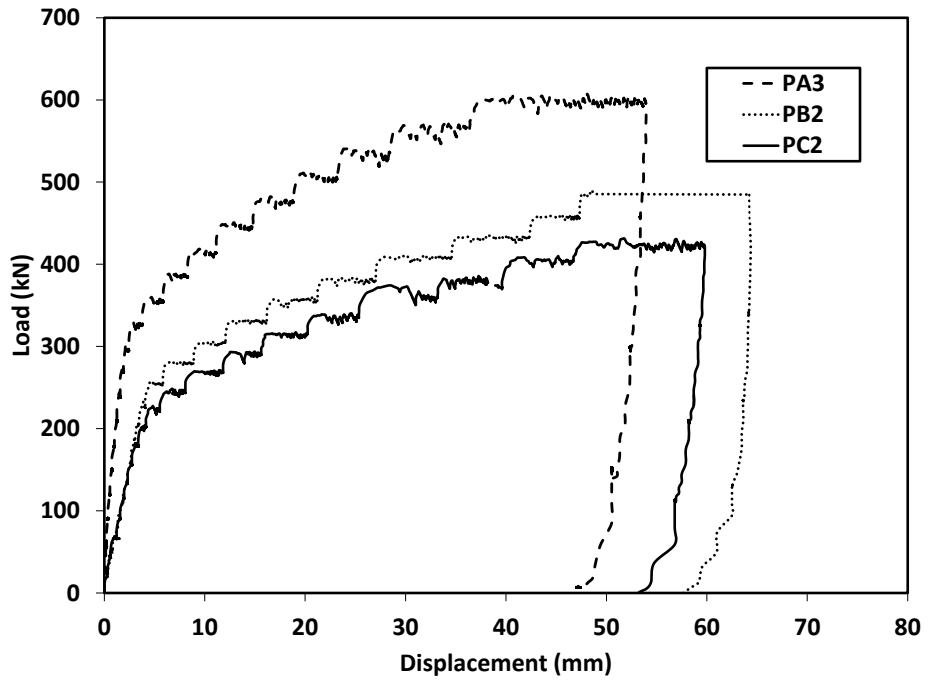
Figure 3 - 13: Load-displacement curve-monotonic compression tests after cyclic loading

It can be noted from Figure 3 - 12 and Figure 3 - 13 that all piles displayed the typical load-displacement curves characterized by an initial linear region, followed by a nonlinear region and finally a linear region that extended to failure or termination of test. It is also noted that piles of configurations A and B exhibited larger stiffness (i.e. slope of the initial linear region) and larger load carrying resistance (maximum load) compared to piles of configuration C.

Comparing the results presented in Figure 3 - 12 and Figure 3 - 13, it is observed that tapered piles subjected to monotonic loading after initial cyclic loading exhibited stiffer response in the initial stage of monotonic loading (i.e. first linear region) up to 50% of the maximum load or even more. This is attributed to re-compacting the soil due the initial cyclic loading, which eliminated any loose soil pockets adjacent to the pile shaft or below the helix.

On the other hand, piles tested monotonically first exhibited stiffer response at higher displacements (i.e. plastic zone) where the load increased with the settlement until the end of the load test. The same behavior was reported by Kodikara and Moore (1993), which was attributed to the increase in the developed frictional resistance along the shaft of tapered piles with the increase in confining pressure associated with cavity expansion due to the taper configuration. However, this was not the case for piles subjected to initial cyclic loading where the pile settlement increased with no increase in the applied load as shown in Figure 3 - 13. This could be attributed to the fact that the soil has already offered maximum unit skin friction (during the cyclic test).

While tapered piles exhibited generally stiffer response, PC1 showed a stiffer behavior than PB1 as shown in Figure 3 - 12. There are various reasons for this observation. First, PB1 had an average diameter of 175 mm while PC1's diameter was 200 mm. Also, PB1 had a greater free standing length (pile segment above ground surface) compared to PC1 (70 cm compared to 35cm) resulting in PB1 bearing on a shallower and less stiff layer therefore developing lower tip/helix resistance. This difference in height would also decrease the shaft resistance of PB1 (less embedded shaft circumference).

The unloading portion of the load displacement curves demonstrated that significant soil plastic strains have occurred due to pile loading as only 3% to 13% of the piles maximum displacements were recovered for different pile configurations.

3.4.2   Pile ultimate capacity

If plunging failure occurs during the load test, the pile ultimate capacity is usually taken as the load that causes plunging. However, in cases where plunging failure is not achieved different criteria are available in the literature that can be used to determine the interpreted failure load from the load-displacement curves. Some failure criteria are represented by settlement limitation at the pile head (e.g. Davisson, 1972; Reese and O'Neil, 1988) and other failure criteria with graphical construction on the load-displacement curve (e.g. Fuller and Hoy, 1970; Butler and Hoy, 1977). The latter methods depend on the actual performance of the pile under the applied load without involving any pile and/or soil property, and tend to be more applicable to variety of pile configurations and soil types. Additionally, the calculated ultimate loads using the first group of methods corresponded to impractically low displacement values, whereas the latter methods yielded ultimate loads that corresponded to pile head displacements around 20~30 mm, which represents an acceptable settlement range for typical construction projects. Therefore, the piles interpreted failure load (ultimate capacity) was defined using the Fuller and Hoy criterion (Fuller and Hoy, 1970), which is also recommended by Prakash and Sharma (1990) for interpretation of enlarged based concrete piles and Frankie piles resembling the studied piles configuration. In this criterion, the pile ultimate capacity is defined as the minimum load for a rate of total settlement of 0.14 mm/kN. The pile ultimate capacity values for the tested piles determined using this criterion are presented in Table 3 - 4.

Table 3 - 4: Piles ultimate static compressive capacity

Pile	Ultimate capacity-Fuller and Hoy (kN)
PA1	450
PA2	400
PA3	500
PB1	260
PB2	330
PC1	315
PC2	270

The superiority of the tapered piles over straight shaft piles can be observed from the results displayed in Table 3 - 4.

For piles with configuration A, the average pile ultimate capacity was more than 34% and 85% higher than those of configuration C (straight shafts) for both cases where piles tested under monotonic loading first, or cyclic loading followed by the monotonic loading respectively. This increase in pile capacity is attributed to the compaction of the soil in the vicinity of the pile shaft during pile installation and loading stages. The soil compaction resulted in an increase of the soil relative density, stiffness and strength along the pile-soil interface, which underscores the main advantage of the proposed system. It compensated for the soil disturbance that occurred during installation of helical piles in sand (Bagheri and El Naggar, 2013), and increased the coefficient of lateral earth pressure, K_s, hence inducing higher frictional resistance component.

The slight difference between the capacity of piles PA1 and PA2 is believed to result from the difference in embedment depth (as shown in Table 3 - 3) as well as the change in ground conditions associated with weather variation during testing. While PA1 was tested in sub-zero temperature, the snow was melting during the testing of PA2 resulting in lower shaft resistance. This will be discussed further in terms of the load transfer established from the strain gauges readings. On the other hand, the results of configurations B and C piles were more comparable for both loading sequences, knowing that configuration B has lower average diameter than configuration C (175 mm compared to 200 mm) and also less embedded depth.

In order to better evaluate the favorable effect of the pile taper on its capacity considering different pile geometries, the piles capacities are compared in terms of unit capacity per volume defined as the pile capacity normalized by the volume of embedded pile material. The normalized unit capacity values are presented in Table 3 - 5.

Table 3 - 5: Ultimate static capacity per unit material volume of the tested piles

Pile	Ultimate Capacity/Pile volume (MN/m^3)
PA1	37.3
PA2	35.6
PA3	41.5
PB1	27.7
PB2	35.1
PC1	26.5
PC2	22.7

The results displayed in Table 3 - 5 confirm the superiority of tapered piles (Configurations A and B) over straight piles for both loading sequences.

3.4.3 Load transfer mechanism

The readings of the strain gauges were used to evaluate the load transfer mechanism. The axial force at different depths P_{zi} was calculated based on the strains measured, as follows:

$$P_{zi} = \varepsilon A_{pi} E_p \tag{3 - 12}$$

where ε is the measured strain, A_{pi} is the cross-sectional area of the pile at the considered strain gauge location, and E_p is the elastic modulus of the pile material.

The load transfer curves (i.e. distribution of axial force along the shaft) are shown in Figure 3 - 14 and Figure 3 - 15 for piles subjected to monotonic loading first, and piles subjected to initial cyclic loading followed by the monotonic loading, respectively. Unfortunately, not all strain gauges continued to function properly and some strain gauges were damaged during installation as mentioned previously. The dashed lines in the load distribution curves, as shown in Figure 3 - 14 (c) and Figure 3 - 15 (a) are extrapolating the observed behavior prior to malfunctioning of the strain gauges.

It is interesting to note that the load transferred through the shaft continued to increase at the same rate as the pile settlement increased for tapered piles. For straight shaft piles, the shaft resistance increased but at a slower rate as the pile settlement increased. On the other hand, the toe resistance component (readings of strain gauge at location 5) tended to display a plateau at around 60 kN for statically tested piles first (as shown for PA2). While analytical solution (i.e. Meyerhof, 1976) would results in almost double this value, the oblique pile tip as well as the shadowing effect around the helix might be the reason for this decreased value hence the end bearing for this configuration would result mainly from the helix plate. However for PA3, and following the bearing layer densification during the initial cyclic tests, this plateau occurred at around 130 kN.

Inspecting Figure 3 - 14 and Figure 3 - 15, it is noted that the initial cyclic loading increased the percentage of the load sustained by the toe resistance due to the compaction of the soil layer beneath the pile toe. This was shown from the strain gauges readings where the percentage of the toe resistance increased from 11% to 22% for PA2 and PA3, respectively. The gauges reading for PC2 showed that approximately 33% of the applied load was carried by the toe resistance. The gauges reading also showed that 57% of the applied load to PA3 was sustained by the shaft friction.

The maximum developed frictional resistance per unit area (i.e. unit friction) for PA1 and PA3 along the pile-soil interface (evaluated as difference in load values at two consecutive strain gauge locations divided by the pile surface area between these two locations) reached 200 kPa and 216 kPa, respectively. To quantitatively evaluate the effect of the pile surface roughness and its effect on the interface behavior, a profilometer was used to scan the pile external surface and to plot longitudinal and radial surface profiles along the pile surface as shown in Figure 3 - 16(c) and (d).
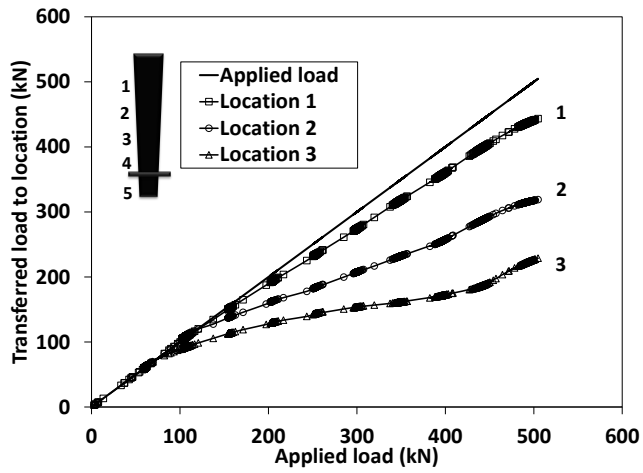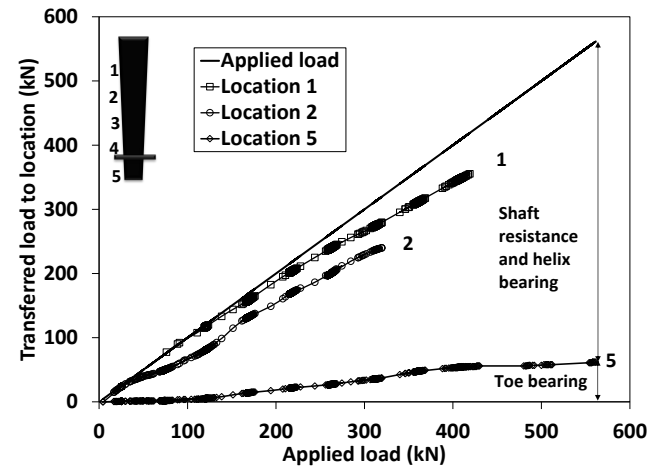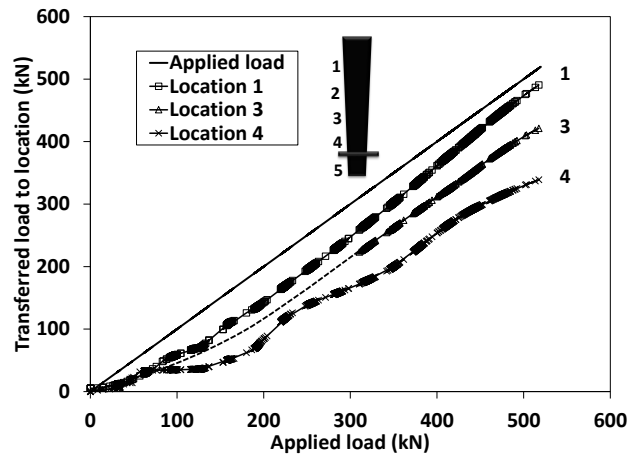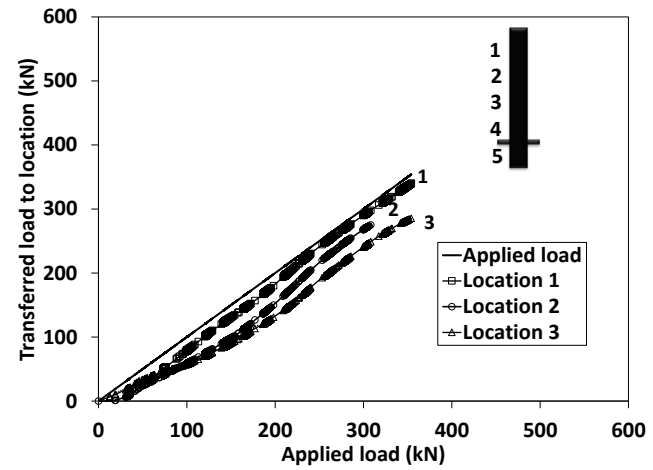
Figure 3 - 14: Variation of measured load at different pile sections: a) PA1; b) PA2; c) PB1; d) PC1

59
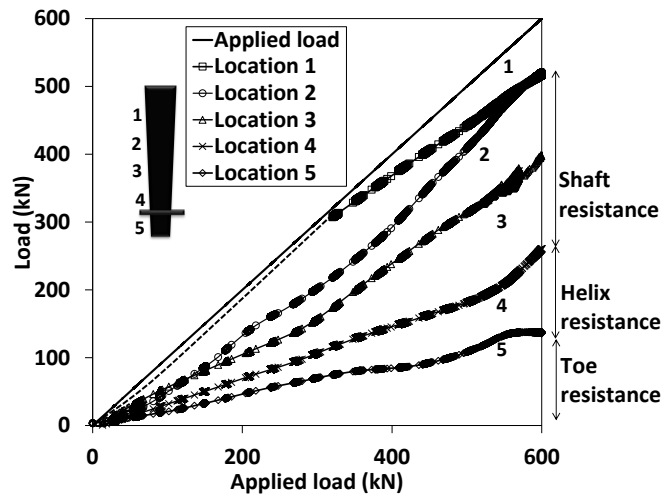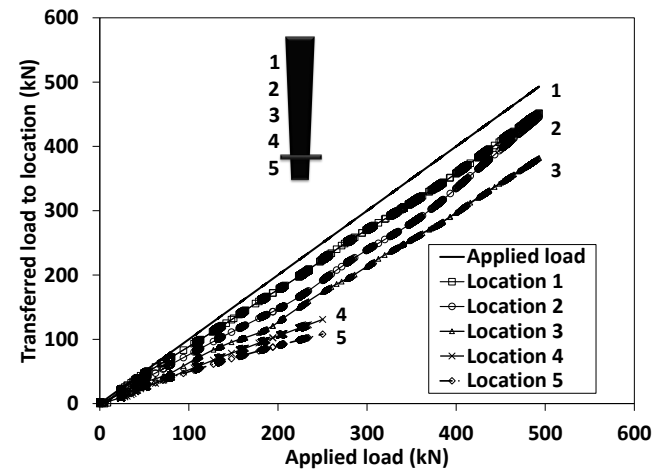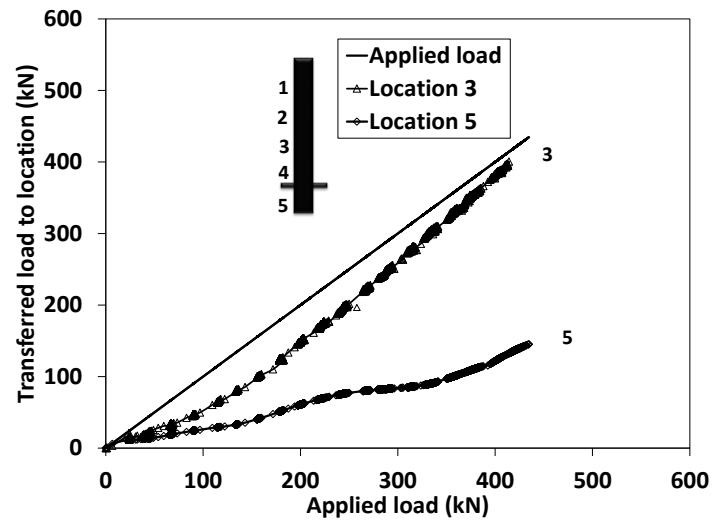
Figure 3 - 15: Variation of measured load at different pile sections: a) PA3; b) PB2; c) PC2

(a)
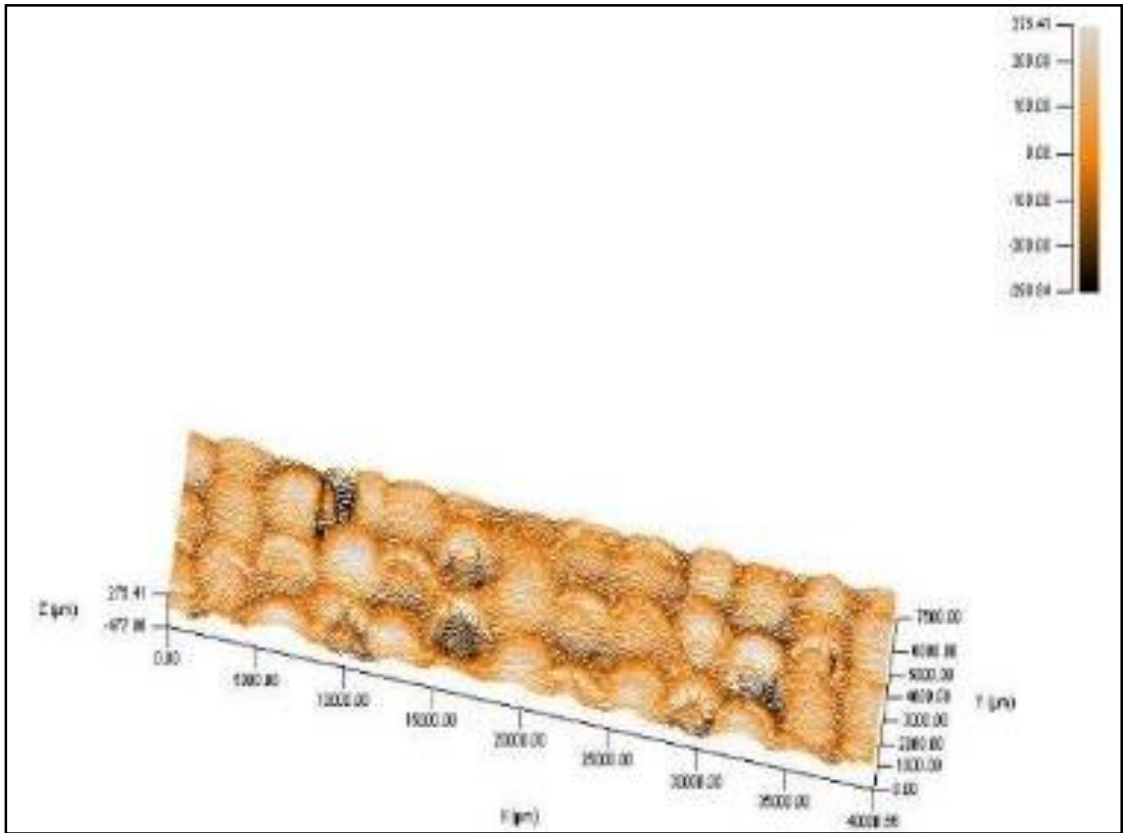
(b)
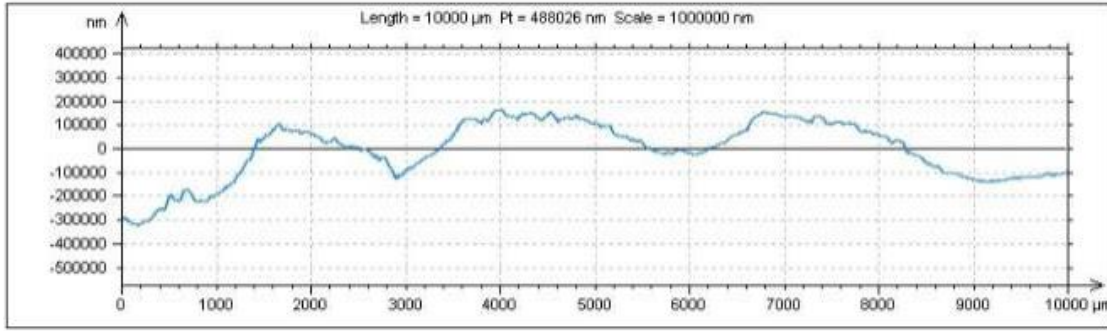
(c)
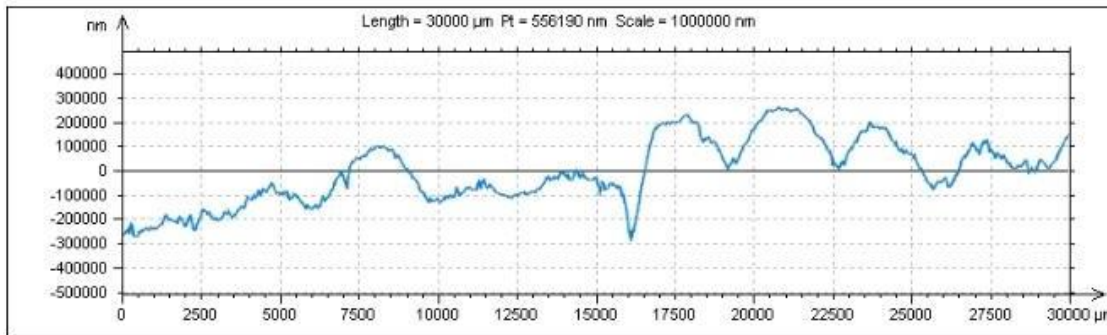
(d)

Figure 3 - 16: Piles external surface –configurations A and B: (a) image of the external surface (After Seamless Pole Inc, 2010); (b) three-dimensional surface scan; (c) surface profile along 100 mm length - longitudinal direction and (d) surface profile along 30 mm length - radial direction

The surface roughness R_a was measured to be 8783nm. Studying the sand-steel interface strength, Lings and Dietz (2005) defined two distinct interface conditions subject to their relative roughness defined as (R_a/D_{50}) where D_{50} is the soil median particle size. For relative roughness values greater than 0.003, dilatant behavior associated with particles rolling. Whereas at lower values, non-dilatant behavior associated with particles sliding would govern (Lings and Dietz, 2005). Considering D_{50} of the top soil (along the pile-soil interface) determined from Figure 3 - 8 and the measured R_a value, the resulting relative roughness is equal to 0.052 hence showing a dilatant behavior along the tapered pile interface. In addition, Dove and Jarrett (2002) showed that, for granular soils in contact with rough surfaces, some passive resistance can be mobilized in case of large asperity spacing and height compared to the soil grain size.

62

The available strain gauges readings of PC1 showed a lower percentage of load carried by the shaft friction and its unit shaft friction was only 55 kPa. Using the β-method recommended by the Canadian Foundation Engineering manual (2006) and considering driven piles in medium dense to dense sand ($\beta = 1$), the maximum developed shaft fiction is equal to 44 kPa. The difference between the calculated and observed values is attributed to the additional cohesive resistance of the soil ($c' = 4$ kPa). The comparison of the values of unit shaft friction for the tapered and cylindrical piles emphasized the advantage of the tapered section in terms of increasing the shaft resistance.

3.4.4 Pile capacity-installation torque correlation

The installation torque was monitored during the installation process. The correlation factor, K_t, of the pile capacity to the installation torque was then calculated using Equation (3 - 1) (i.e. K_t = pile capacity/installation torque). The calculated correlation factor values are compared to the theoretical values determined using Equation (3 - 2) in Table 3 - 6.

Table 3 - 6: Calculated torque factors

Pile	K_t (kN/kN.m)	
	Field calculated values	Calculated values Using Eq.3 - 2
PA1	11.1	9.8
PA2	9.8	9.8
PA3	12.5	9.8
PB1	12.8	12.4
PB2	16.8	12.4
PC1	9.1	10.9
PC2	9.7	10.9

The measured and calculated values of torque are generally in reasonable agreement. However, the observed values for tapered piles tend to be higher than the calculated values, while the calculated values for straight shaft piles are higher than the observed ones. This is due to the fact that Eq. 3 - 2 was developed for helical piles with straight shaft, hence it does not account for the additional capacity due to the pile taper.

3.5 Numerical simulation

To further examine the axial static behavior of the developed pile system, three-dimensional finite element analysis was conducted for the different test piles configurations. The average free lengths of the tested piles were considered as shown in Figure 3 - 2. In addition, two pile configurations, D and E, with dimensions as shown in Figure 3 - 17 were modelled to assess the beneficial effect of the pile taper for longer piles (i.e. higher overburden pressure). All numerical models were developed using the ABAQUS software package (Hibbitt *et al.*, 2008).
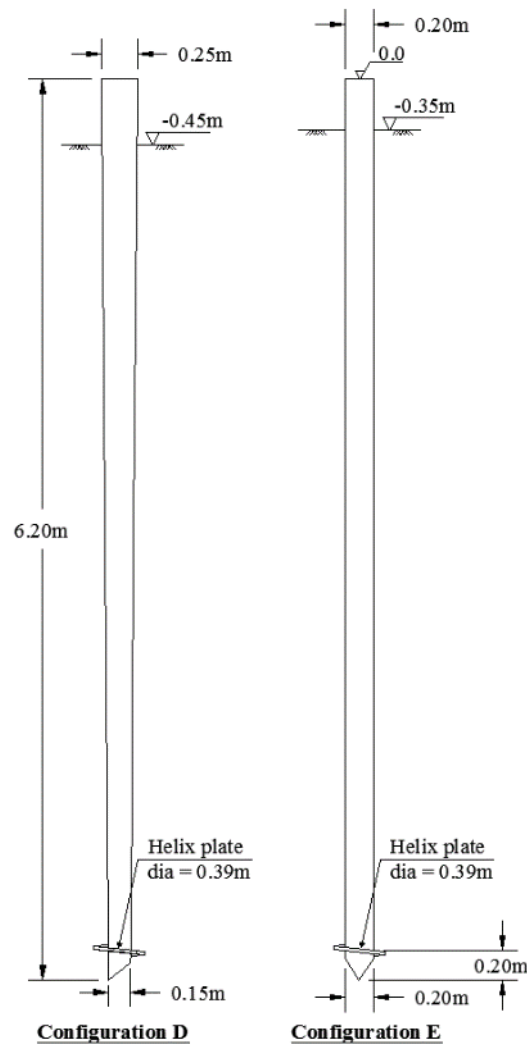
Figure 3 - 17: Piles of configurations D and E geometry

3.5.1 Description of finite element model

The soil-pile system is modeled employing a 3D quarter cylindrical mesh. The pile was placed along the axial z-direction of the model. The helical plates were idealized as planar disk for numerical simplification. Figure 3 - 18 presents the model geometry for a single pile of configuration A subjected to axial loading.
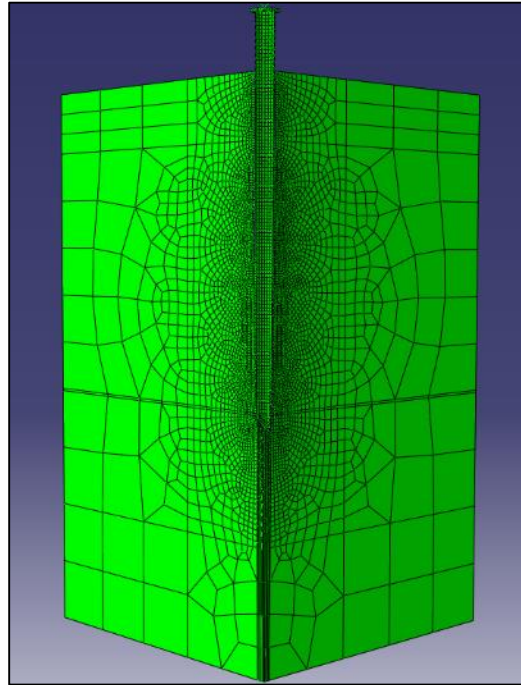
Figure 3 - 18: Finite element model geometry - pile configuration A

The soil medium and the pile were simulated using 8-noded, first order, and reduced integration continuum solid elements (C3D8R) having three active translational degrees of freedom at each node and one integration point located at the centroid. The location of the boundaries was optimized to minimize the effects of the boundary conditions on the results while reducing the computational effort. The radius of the soil cylinder extended 2.5 m (i.e. 10 times the greatest shaft diameter) from the center of the pile shaft. The bottom horizontal boundary was placed at 1.95 m below the pile toe, which is equivalent to 5 helix diameters.

A stress-free boundary was considered for the soil top surface. The translation of the bottom surface of the soil cylinder was restrained in X, Y and Z directions. The vertical

boundaries of the soil were restrained from translating in X (Y) direction and rotating around Y and Z (X and Z) where applicable to simulate the case of a full model. The back of the soil quarter cylinder was restrained from moving X and Y directions (movement along Z direction was allowed). It should be noted that this model was considered instead of the conventional axi-symmetrical analysis because the same model, with different boundary conditions, was used to simulate the lateral performance of the test piles, which will be reported elsewhere.

Mesh refinement at stress/strain concentration zones was necessary to ensure the accuracy of the results. Accordingly, a series of models was developed where the mesh was incrementally refined and the results were compared. When the difference between the results of two consecutive models (i.e. refinements) became less than 2.5%, the most refined model was considered. The elements were most refined along the pile-soil interface and around the helical plate and then their size gradually increased towards the model boundaries. This process resulted in mesh configurations consisting of 37 309/33 267/28 553 elements for pile configurations A/B/C, with maximum elements side dimension ranging from 250 mm/500 mm/330 mm at the model boundaries to 20 mm/17 mm/25 mm at the pile-soil interface. The pile mesh consisted of 1609/869/1451 for configurations A/B/C.

The pile installation process was not explicitly simulated (i.e. wished in place piles were considered). However, the model was calibrated with the field test results and the soil properties following the piles installation as well as the interface characteristics were established accordingly as will be discussed later. The in-situ stress conditions were accounted for in the numerical model as an initial stress through the geostatic equilibrium step**.**

3.5.2   Soil model

The soil is simulated as an elastic-perfectly plastic isotropic continuum. The soil plasticity and failure were modeled using the Mohr-Coulomb yield criterion where values of the

critical state angle of internal friction, φ_{cs}, cohesion yield stress, c' and the dilation angle, ψ. Poisson's ratio, v, and Young's modulus, E_s defined the soil elasticity.

The soil domain was divided into three main sections to allow different soil properties with depth. These sections include: top soil, which had soil properties affected by small overburden pressure and disturbance due to pre-drilling; soil along the pile shaft, which is affected by the re-packing of soil due to the shaft taper (or lack of in case of straight shaft); and soil beneath the helix plate, which experienced high overburden pressure, and compaction in the case of cyclic loading prior to monotonic loading. Average soil parameters were assigned to these sections as shown in Table 3 - 8.

The soil properties employed in the analysis have been calibrated using the field data. Weaker parameters were considered for the top 0.5m to reflect the soil disturbance induced by the initial pre-drilling process. On the contrary, stiffer parameters were considered below the helix plate to account for the soil densification during the installation process.

3.5.3 Pile model

The pile was simulated as linear elastic-perfectly plastic material. The elastic behavior was defined by Poisson's ratio, v_p, and Young's modulus, E_p. The plastic behavior was represented by the yield strength of the pile material. The piles mechanical properties adopted in the model are summarized in Table 3 - 9. Weaker strength parameters were considered for the helix and the base plates (closing the modeled piles end) to accommodate the welding defects observed prior to the piles installation.

3.5.4 Pile-soil interface model

The pile-soil interface was simulated using the penalty-type tangential behavior Coulomb's frictional model. No relative tangential motion occurs until the surface traction reaches a critical shear stress value, which is taken as the lesser of the interface shear strength or a fraction of the interface pressure. Soil-pile interface strength $\tan\delta$ of 0.78 and 0.5 were respectively considered for tapered and straight piles configurations. While the first was

determined by studying the pile surface roughness in comparison to the soil mean particle size as mentioned earlier in this chapter, the latter was considered in accordance to the suggested values by the Canadian Foundation Engineering Manual (2006). Slippage along the soil-pile interface was allowed. Limiting shear stress values along the soil-pile interface of 200 and 80 kPa (as backfigured from field load tests) were set for configurations A and B, respectively. Limiting shear stress of 115 kPa was set for configuration C, as suggested for piles in very dense sands by API recommended practice 2A-WSD (API, 2000). However, as discussed later, this value did not control the behavior because lower shear stress values were developed along the pile-surface interface.

3.5.5   Loading sequence

An initial loading step of geostatic stresses and equilibrium was applied to consider the initial in-situ soil stresses, wishing the pile in. This was followed by displacement controlled analysis for the different cases whereby prescribed displacements were applied at reference points rigidly connected to the top loading plates.

3.5.6   Model calibration and verification

The model properties and configuration were calibrated by comparing the model predictions with observed load-displacement curves during the field load tests. The initial material properties used in the numerical models were the representative soil properties obtained from the boreholes and the laboratory tests as well as the piles material properties as provided by the manufacturers of the steel and ductile cast iron piles. The numerical models were calibrated by adjusting the properties shown in Table 3 - 7 and Table 3 - 8 until a satisfactory match was observed between the calculated and measured responses of piles PA1, PB1 and PC1 as shown in Figure 3 - 19.

Table 3 - 7: Initial soil parameters considered in FE model (before calibration)

Depth (m) From	Depth (m) To	Critical state angle of internal friction φ_{cs} (degrees)	Cohesion C' (kPa)	Dilation angle ψ (degrees)	Poisson's ratio v	Young's modulus E_s (MN/m²)	Effective unit weight γ' (kN/m³)	Earth pressure coefficient K_s
0	0.5	32	4	4	0.3	70	16.5	0.76
0.5	End of model	32		6				

Table 3 - 8: Calibrated soil parameters considered in FE model

Depth (m) From	Depth (m) To	φ_{cs} (degrees) All configurations	C' (kPa) All configurations	ψ (degrees) PA1 and PB1	ψ (degrees) PC1	v All configurations	E_s (MN/m²) PA1	E_s (MN/m²) PB1	E_s (MN/m²) PC1	γ' (kN/m³) All configurations
0	0.5	32	4	4	4	0.3	35	35	35	17
0.5	Helix* level	32	4	6	4	0.3	70	70	60	18
Helix level	End of model	32	4	6	6	0.35	94	73	94	18

Table 3 - 9: Pile mechanical properties considered in FE model

Component	Young's Modulus E_p (kN/m²)	Poisson's ratio v_p	Unit weight γ_p (kN/m³)	Yield strength F_y (MPa)
Shaft- configurations A, B and D	1.69E08	0.28	77	314
Shaft - configurations C and E	2E08	0.28	77	370
Helix and base plates welded connections	2E08	0.28	77	170

*Varies depending on embedded length and pile configuration
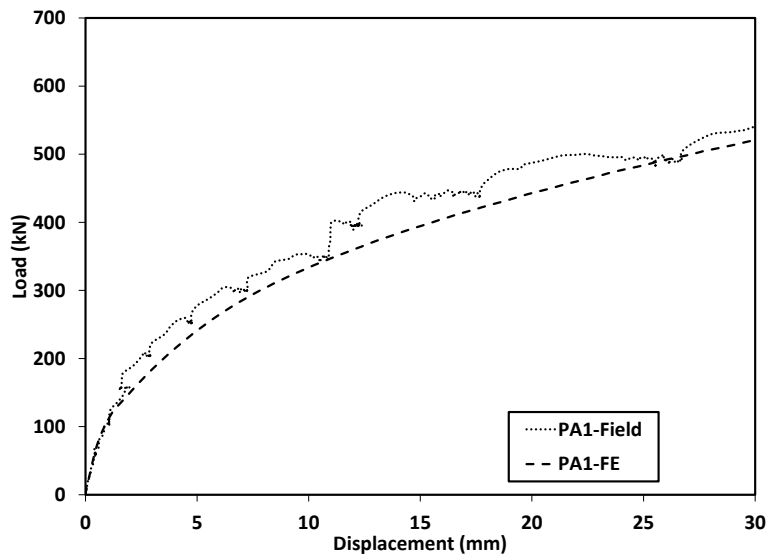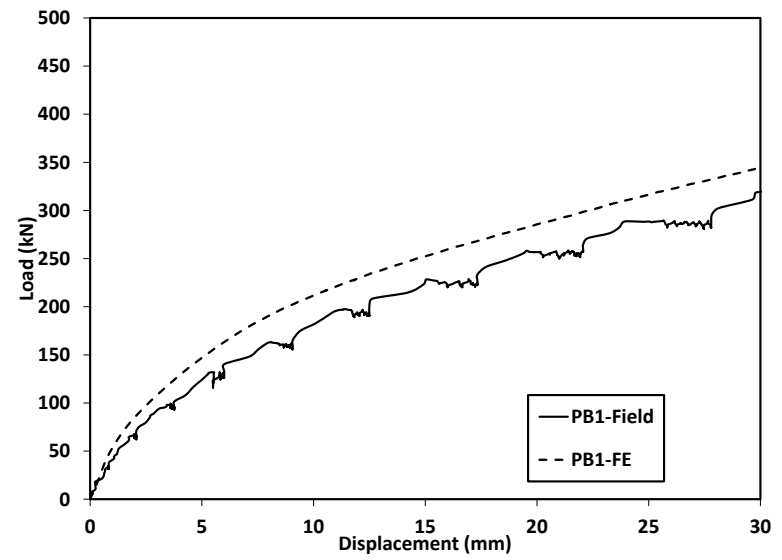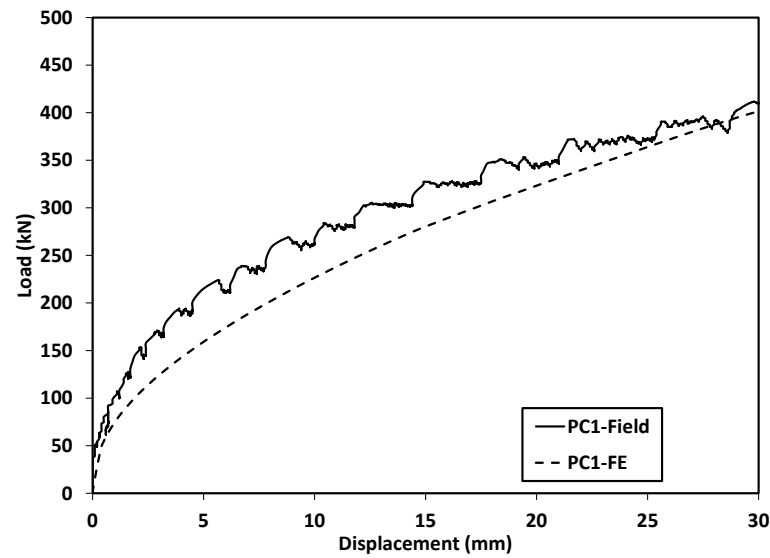
Figure 3 - 19: Comparison of calculated and measured load-displacement curves for calibration: a) PA1; b) PB1; and; c) PC1

In order to verify the ability of the calibrated models to accurately depict the behavior of helical piles under compressive loading, the calibrated model for PA1 was utilized to analyze PA2 considering the same boundary and interface conditions. The same soil and pile properties were also considered except for the soil layer beneath the helix level where its Young's modulus E_s was lowered by 3.5 MPa ($E_{mod} = 90.5$MPa). The lower stiffness was attributed to the difference in embedment depth between PA1 and PA2, as suggested by (Seed and Idriss, 1970):

$$G= 218.82 \, K_2 \, \sigma_o^{,0.5} \tag{3 - 13}$$

$$G= \frac{E}{(1+\upsilon)} \tag{3 - 14}$$

where G is shear modulus and the factor K_2 depends on the sand relative density. For PA1, and considering the calibrated model, the value of K_2 below the pile toe was calculated to be 23.6. Considering this latter value and assuming constant soil relative density and Poisson's ratio as in PA1, the value of E_s was calculated using Equations (3 - 13) and (3 - 14) to be equal to 90.5 MPa for PA2 (considering the difference in the effective overburden pressure due to the difference in the embedment depth). It should be noted that the calculated value of K_2 was lower than the maximum suggested value by Seed and Idriss (1970) for dense sands. This discrepancy, however, would not affect the results since the equation was used to find the variation of G (hence E_s) with depth (from PA1 to PA2) considering the initially calibrated value (for PA1). The numerical predictions were in satisfactory agreement with observed test results as shown in Figure 3 - 20.

In order to investigate the effectiveness of pile taper for higher overburden pressure values (i.e. long piles), the load displacement curves for configurations E and D are compared with those for configurations C and A in Figure 3 - 21.
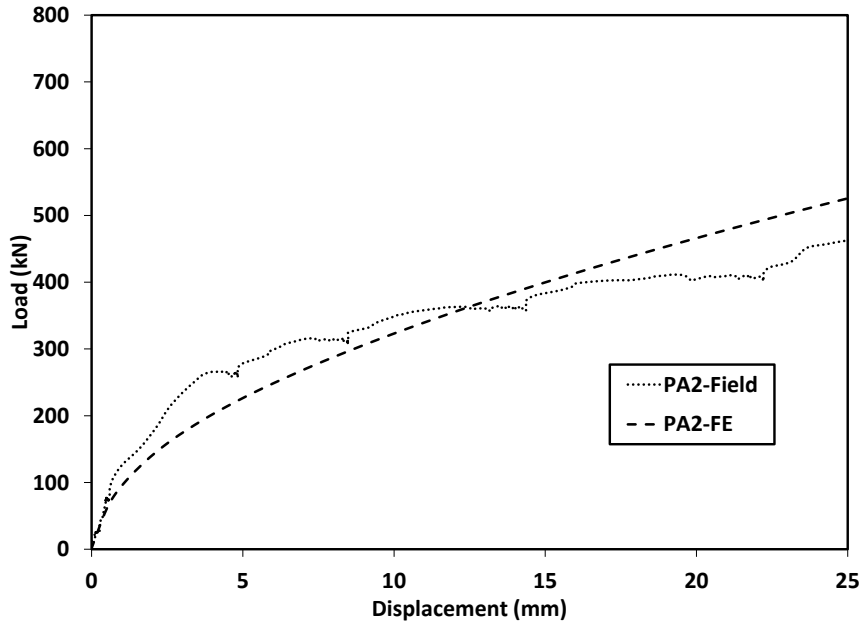
Figure 3 - 20: Comparison of calculated and measured load-displacement curves for validation for PA2
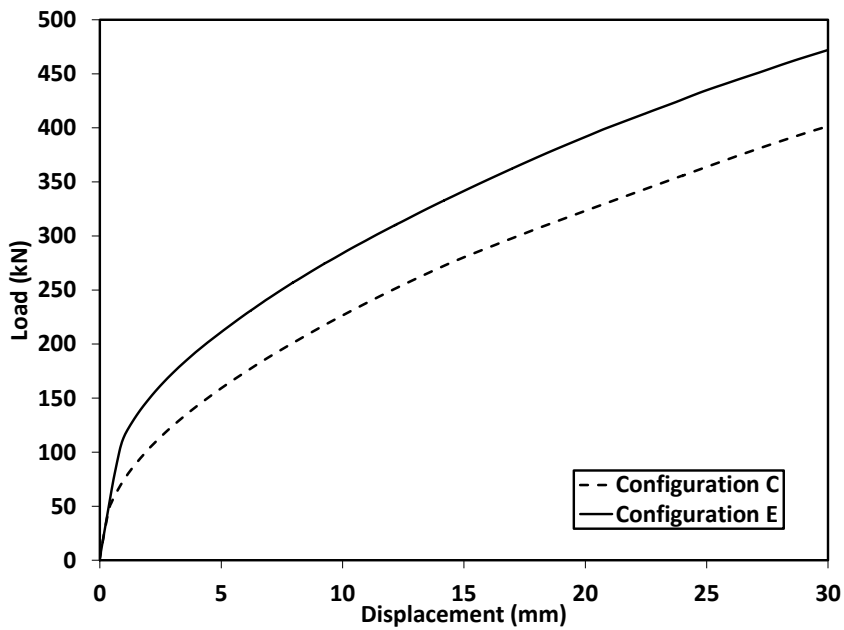
(a)
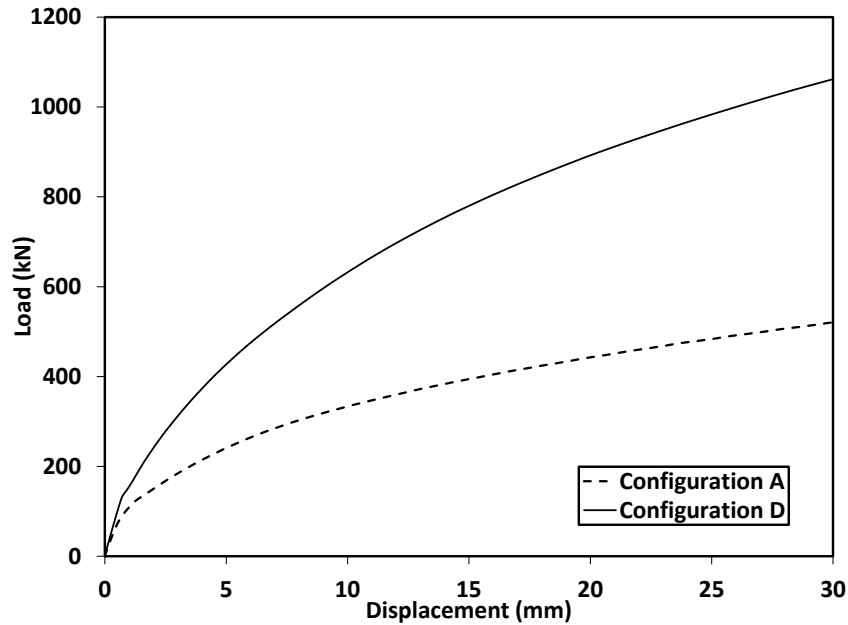
(b)

Figure 3 - 21: Load displacement curves – measured and calculated results: a) Configurations C and E; and b) Configurations A and D

As expected, longer piles exhibited stiffer response and higher maximum load. However, the increases in stiffness and ultimate load for the tapered pile are significantly higher than those for the straight shaft pile, confirming the beneficial effect of the shaft taper. To further illustrate this finding, the Fuller and Hoy (1970) criterion was used to determine the ultimate static capacity considering the calculated load-displacement curves of piles configurations D and E. The ultimate capacity values are 1180 kN and 490 kN for piles D and E, with capacity per unit volume of 50.3 MN/m^3 and 21.5 MN/m^3. Comparing the latter values with those reported in Table 3 - 5 shows that the ultimate capacity per unit volume increased by 38% for the tapered pile while it decreased for straight profile. This demonstrates the benefit of the proposed tapered helical pile for the more realistic pile lengths expected in practical applications, even though the taper angle remained the same. It is expected that larger taper angles would lead to more enhanced performance, as suggested by Eqs. 3 - 3 and 3 - 4.

3.5.7 Soil and interface conditions evaluated from calibration process

The calibration of the numerical model with the field test data involved matching the load-displacement pattern and the frictional resistance from the instrumented pile shaft. The soil and interface properties obtained from the calibration were then deemed to be representative of the pile/soil conditions after pile installation. The values of the lateral earth pressure coefficient, K_s, obtained from the calibration were 2, 1.2 and 0.85 for pile configurations A, B and C, respectively, which demonstrated that the installation process increased the soil confinement. While PA1 and PB1 had the same helix diameter and taper angle, PB1 had a smaller shaft diameter at the helix location (i.e. greater exposed helix shearing area), which resulted in a greater disturbed zone compared to PA1 hence a lower developed K_s value.

The pile installation is expected to disturb the soil adjacent to the pile due to helix rotation and shearing the soil. This effect was observed and reported in other studies (i.e. Bagheri and El Naggar, 2013; Tsuha *et al.*, 2012) where reduced soil parameters were suggested to reflect this disturbance. As shown in Table 3 - 8, the values of peak angle of internal friction and Young's modulus for straight shaft piles dropped by 5% and 14%, respectively. This softening resulted from shearing the soil adjacent to the shaft due to helix rotation, and hence residual/reduced parameters controlled the soil behavior. On the other hand, the numerical model calibration yielded soil strength and stiffness parameters that demonstrated almost full recovery of the soil occurred for piles of configurations A and B (tapered profiles) manifested in full values of limiting strength, peak friction angle φ_p and E_s were developed as shown in Table 3 - 8. This clearly demonstrates the advantage of the tapered shaft for helical piles in re-compacting the disturbed soil adjacent to the pile.

The pile installation also resulted in the compaction of soil beneath the helix/pile toe, and hence increased its Young's modulus to 94, 73 and 94 MPa for configurations A, B and C, respectively. The lower E_s value for PB1 is attributed to two reasons: its smaller embedded length and hence lower overburden pressure; and the helix of pile PB1 was deformed during installation (as noted through visual inspection following the removal of the pile

74

upon the tests completion), hence reducing the bearing area, which was reflected in the numerical model in terms of lower E_p value.

The profiles of shaft friction for the tapered pile PA1 and the straight shaft pile PC1 are presented in Figure 3 - 22 for different displacement levels applied at the pile head.

(a)   (b)
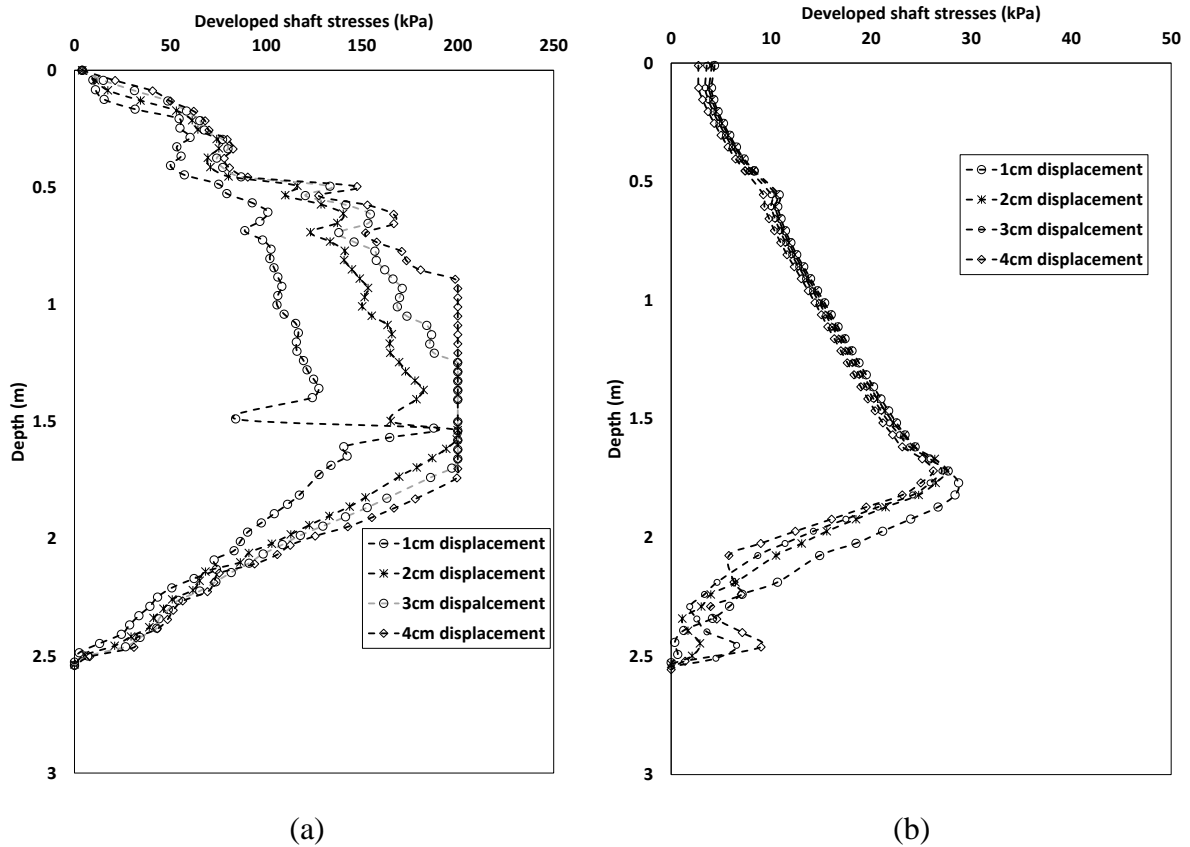
Figure 3 - 22: Shaft friction development with pile displacement: a) PA1; b) PC1

Figure 3 - 22 shows that the shaft friction increased almost linearly from the ground surface until it reaches a maximum. For PA1, the increase in shaft friction was rapid and it reached a maximum of 200 kPa, while the shaft friction of PC1 reached a peak value of 30 kPa. Both piles exhibited a lower shaft friction just above the helix due to the helix shadowing effect. Similar results were reported by Rao *et al.* (1993) and Zhang (1999), and suggested that the shaft friction could not be mobilized along a length of one helix diameter, D_{helix}, above the helix because of the shadowing effect. However, this effect was less significant

for PA1 because the shaft taper resulted in additional compaction of the soil during loading. This is further demonstrated by the increase in shaft friction for PA1 as the pile head displacement increased, while this was not the case for the straight shaft PC1.

The variation of K_{ts} for pile PA1 at 4cm displacement was in good agreement with the values calculated value using Equation (3 - 5) at the same displacement level as shown in Figure 3 - 23.
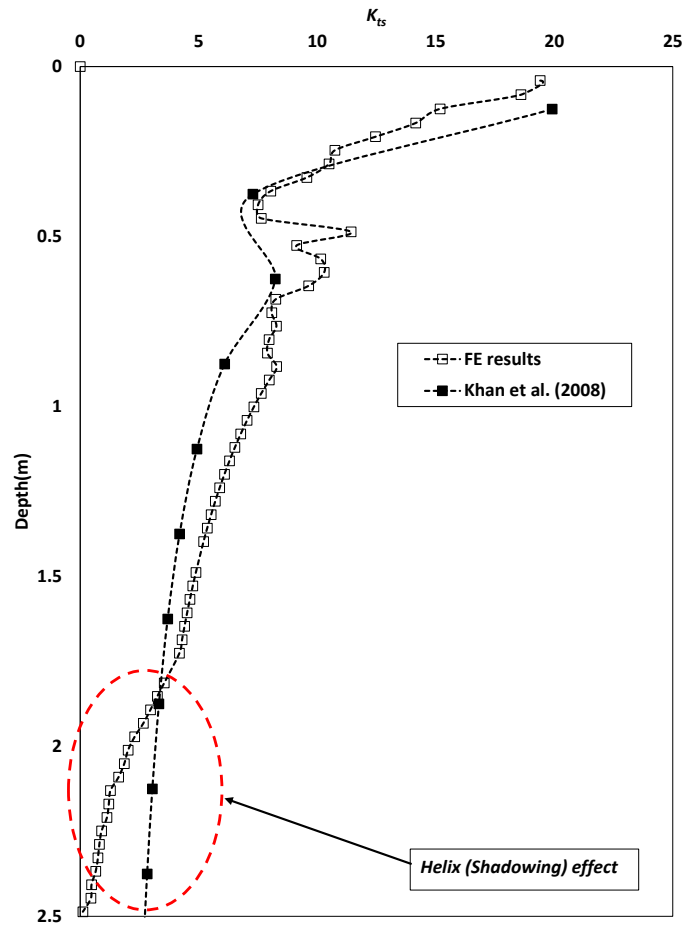
Figure 3 - 23: Variation of the taper coefficient K_{ts} with depth –PA1

The shaft friction profiles for the case of applied displacement of 40 mm at the pile head are shown in Figure 3 - 24 for different pile configurations.
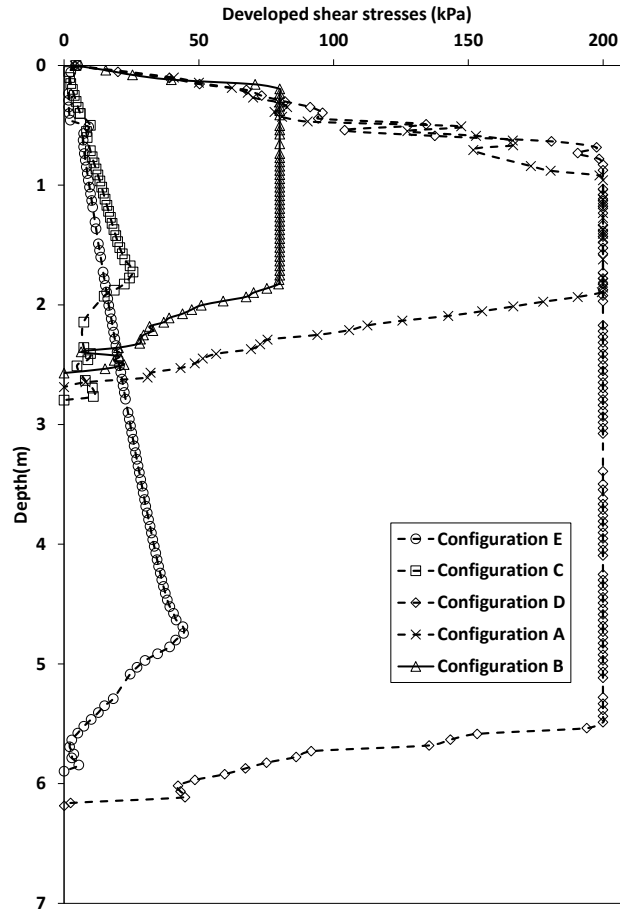
Figure 3 - 24: Variation of developed shear stresses with depth (above the helix)-FE results

The advantage of shaft taper is manifested in the much higher unit shaft friction of tapered piles compared to that of straight shafts. Also, the shadowing effect is clearly evident in the region above the helix, where the shaft friction reduced and diminished near the helix level. This zone extended up to a distance equivalent to 1.9 to 2.3 times the helix diameter above the helix.

To further understand the load transfer mechanism, the calculated soil displacement contours for pile head displacement of 20 mm are shown in Figure 3 - 25.

<div align="center">(a)   (b)   (c)</div>
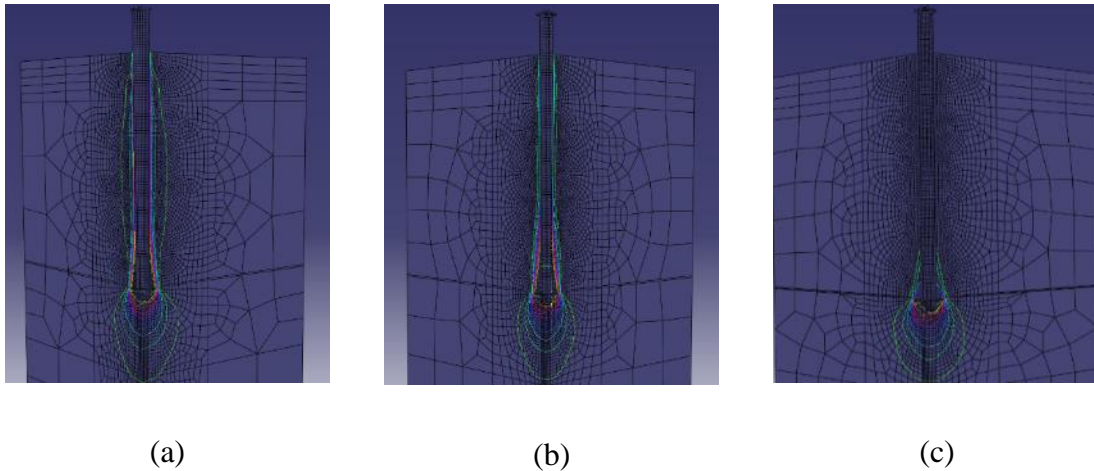
Figure 3 - 25: Soil displacement contours at vertical pile displacement of 2cm, a) configuration A; b) Configuration B; and c) Configuration C

It is noted that the soil displacement contours are concentrated around the helix and pile tip. However, the displacement contours extended to the ground surface for tapered piles (configurations A and B). This demonstrates that the load transfer mechanism for tapered piles involves cavity expansion along the shaft, hence increasing its resistance. Kodikara and Moore (1993) made similar observations. On the other hand, for straight shaft piles (configuration C) slippage takes place at the pile-soil interface when the pile displacement increases and the developed shear stresses at the interface approaches the shear strength. This difference in behavior explains the higher contribution of the shaft resistance for tapered piles compared to the straight ones.

These findings were also confirmed by inspecting the failure progress at higher displacements shown in Figure 3 - 26.
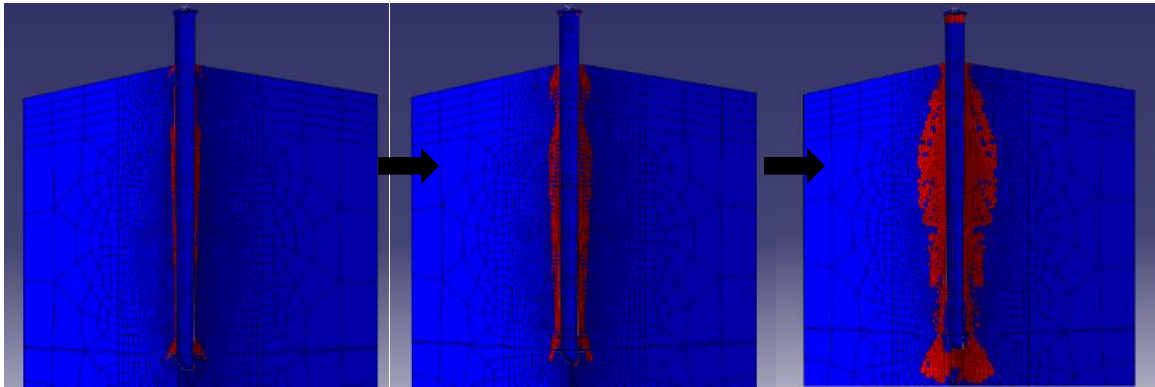
(a)
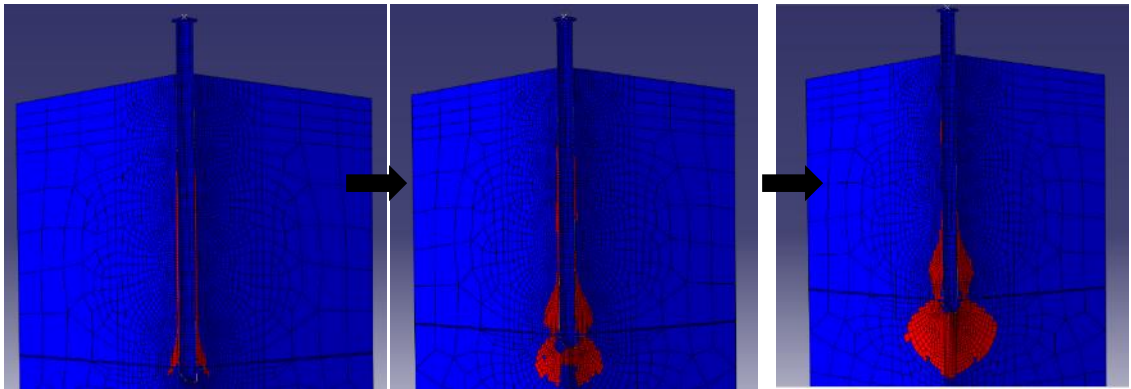
(b)

Figure 3 - 26: Yield progress with loading (a) Configuration A; (b) Configuration C

The soil elements yielded along the tapered pile shaft, but not the straight one. It is interesting to note from that failure progressed along the pile-soil interface and then extended to the bearing area for tapered piles, which shows that the shaft resistance is mobilized first (at small displacement). Furthermore, the yield zone extended radially for configuration A engaging wider soil arch in the vicinity of the pile transferring the load to a greater volume of soil. On the other hand, failure occurred at the pile-soil interface for the straight shaft. This again demonstrates the advantage for tapered helical piles in sand. However, the large capacity of straight helical piles in sand is only achieved at large displacements, which may not be acceptable for the supported structure.

By inspecting Figure 3 - 26, it was also noted that the displacement contours and yield zone below the helix plate extended radially to a distance equal to 1.2~1.3 times the helix diameter. Finally, none of the simulated piles showed any signs of yielding under compressive loading.

3.6   Conclusions

A novel ductile cast iron tapered helical pile system was introduced in this study. A total of seven piles were installed by torque in a silty sand profile and were subjected to static and cyclic compression load tests. The test piles included five tapered helical piles with 2 different average diameters and same taper angle and two straight helical piles. In addition, a numerical investigation was conducted to better understand the performance characteristics of the novel piles. Two different loading sequences were adopted to assess the effect of prior cyclic loading on the pile compressive capacity. The results of the static compressive load tests and their numerical analyses are summarized here. The main conclusions drawn from this study are as follows:

1. The capacity-to-torque ratio for the novel piles was found to be comparable to the available empirical equation proposed by Perko (2009). However, the equation slightly underestimated the capacity of the tapered piles.

2. The tapered piles generally exhibited stiffer response and higher ultimate capacity compared to the straight ones owing to the higher shaft frictional resistance.

3. Initial cyclic loading increased the stiffness of the piles at lower displacements during the following monotonic compressive loading. On the other hand, piles subjected to monotonic compressive loading first showed stiffer response at higher displacements.

4. The results showed higher material efficiency in tapered piles especially at greater pile lengths.

5. The coefficient of lateral earth pressure back-figured from the results was significantly higher for tapered piles (2.0) compared to the straight shafts (0.85). The results demonstrated that the soil along the tapered shaft recovered its stiffness and strength fully, hence erasing the disturbance due to the helix rotation and shearing the soil.

6. The numerical analysis results demonstrated that practical length tapered piles are expected to be even more efficient compared to the straight shaft piles.

7. The analyses showed that tapered helical piles mobilize significant shaft resistance at low displacement, hence eliminating the potential for large displacement that may not be tolerated for the supported structure.

3.7   References

AASHTO. 2002. Standard specifications for highway bridges. *HB-17.* American Association of State and Highway Transportation Officials.

Abdelghany, Y. & El Naggar, M. H. Monotonic and cyclic behavior of helical piles under axial and lateral loading. Proceedings of the Fifth International Conference on Recent Advances in Geotechnical Earthquake Engineering and Soil Dynamics, 2010, San Diego, CA.

API. 2000. Recommended practice for planning, designing and constructing fixed offshore platforms-working stress design. 2A-WSD. American Petroleum Institute.

ASTM C136. 2006. Standard test method for sieve analysis of fine and coarse aggregates. ASTM international.

ASTM D1143. 2007. Standard test method for deep foundations under static axial compressive load. ASTM international.

ASTM D1556. 2007. Standard test method for density and unit weight of soil in place by the sand-cone method. ASTM international.

ASTM D2487. 2011. Standard practice for classification of soils for engineering purposes (Unified Soil Classification System). ASTM international.

ASTM D3080. 2011. Standard test method for direct shear test of soils under consolidated drained conditions. ASTM international.

ASTM D4318. 2010. Standard test methods for liquid limit, plastic limit, and plasticity index of soils. ASTM international.

Bagheri, F. & El Naggar, M. H. Effects of the installation disturbance on the behavior of the multi-helix screw anchors in sands. GeoMontreal, 2013, Montreal.

Bowles, J. 1996. *Foundation analysis and design*, 5th edition, Mc-Graw hill.

Butler, H. D. & Hoy, H. E. 1977. User's manual for the Texas quick load method for foundation load testing. Washington: Federal Highway Administration, Office of Development.

CGS. 2006. *Canadian Foundation Engineering Manual*, 4th edition, Canadian Geotechnical Society.

Davisson, M.T. 1972. High capacity piles. Proceedings of lecture series on innovations in foundation construction, ASCE, Illinois Section, Chicago, 81-112.

Dove, J. E. & Jarrett, J. B. 2002. Behavior of dilative sand interfaces in a geotribology framework. *Journal of Geotechnical and Geoenvironmental Engineering,* 128(1), 25-37.

El Naggar, M. H. & Sakr, M. 2000. Evaluation of axial performance of tapered piles from centrifuge tests. *Canadian Geotechnical Journal,* 37(6), 1295-1308.

El Sharnouby, M. M. & El Naggar, M. H. 2012a. Axial monotonic and cyclic performance of fibre-reinforced polymer (FRP)-steel fibre-reinforced helical pulldown micropiles (FRP-RHPM). *Canadian Geotechnical Journal,* 49(12), 1378-1392.

El Sharnouby, M. M. & El Naggar, M. H. 2012b. Field investigation of axial monotonic and cyclic performance of reinforced helical pulldown micropiles. 49(5), 560-573.

Elkasabgy, M. & El Naggar, M. H. 2013. Dynamic response of vertically loaded helical and driven steel piles. *Canadian Geotechnical Journal,* 50(5), 521-535.

Elkasabgy, M. & El Naggar, M. H. 2015. Axial compressive response of large capacity helical and driven steel piles in cohesive soils. *Canadian Geotechnical Journal,* 52(2), 224-243.

Elsherbiny, Z. H. & El Naggar, M. H. 2013. Axial compressive capacity of helical piles from field tests and numerical study. *Canadian Geotechnical Journal*, 50(12), 1191-1203.

Fleming, K., Weltman, A., Randolph, M. & Elson, K. 2009. *Piling engineering*, Taylor and Francis Group.

Fuller, F. M. & Hoy, H. E. 1970. Pile load tests including quick load test method, conventional methods and interpretations. HRB 333, 78-86.

Hibbitt, H. D., Karlsson, B. I. & Sorensen, E. P. 2008. ABAQUS Standard user's manual. Pawtucket, R. I.: Hibbitt, Karlsson & Sorensen Inc.

Hoyt, R. & Clemence, S. Uplift capacity of helical anchors in soil. 12th International Conference on Soil Mechanics and Foundation Engineering, 1989, Rio de Janeiro. 1019-1022.

Khan, M. K., El Naggar, M. H. & Elkasabgy, M. 2008. Compression testing and *analysis* of drilled concrete tapered piles in cohesive-frictional soil. *Canadian Geotechnical Journal*, 45(3), 377-392.

Kodikara, J. & Moore, I. 1993. Axial response of tapered piles in cohesive frictional ground. *Journal of Geotechnical Engineering,* 119(4), 675-693.

Kulhawy, F. H. & Mayne, P. W. 1990. Manual for estimating soil properties for foundation design. Ithaca, New York: Cornell University.

Kurian, N. P. & Srinivas, M. S. 1995. Studies on the behaviour of axially loaded tapered piles by the finite element method. *International Journal for Numerical and Analytical Methods in Geomechanics*, 19(12), 869-888.

Liao, S. S. C. & Whitman, R. V. 1986. Overburden correction factors for SPT in sand. *Journal of Geotechnical Engineering,* 112(3), 373-377.

Lings, M. L. & Dietz, M. S. 2005. The peak strength of sand-steel interfaces and the role of dilation. *Soils and Foundations,* 45(6), 1-14.

Livneh, B. & El Naggar, M. H. 2008. Axial load testing and numerical modeling of square shaft helical piles. *Canadian Geotechnical Journal,* 45(8), 1142-1155.

Mayne, P. W. In-situ characterization of Piedmont residuum in eastern US. Proc. US-Brazil: Application of Classical Soil Mechanics to Structured Soils, 1992, Belo Horizonte. National Science Foundation/USA, 89-93.

Mayne, P. W. 2006. In-situ test calibrations for evaluating soil parameters. Overview Paper on In-Situ Testing- Singapore Workshop.

Mayne, P. W., CHRISTOPHER, B. & DEJONG, J. 2002. Manual on subsurface investigations— Geotechnical site characterization. Washington, DC.: Federal highway administration, U.S. Department of Transportation.

Mayne, P. W. & Kulhawy, F. H. 1982. Ko-OCR Relationships in Soil. *Journal of the Geotechnical Engineering Division,* 108(6), 851-872.

Meyerhof, G. G. 1976. Bearing capacity and settlement of pile foundations. *Journal of the Geotechnical Engineering Division,* 102(3), 195-228.

NBCC. 2005. *National building code of Canada*, Canadian commission on building and fire codes, and national research council of Canada.

Norlund, R. L. 1963. Bearing capacity of piles in cohesionless soils. *Journal of Soil Mechanics and Foundations Division,* 89(3), 1-36.

Perko, H. 2009. *Helical piles: A practical guide to design and installation,* New Jersey, John Willey and Sons Inc.

Poulos, H. G. & Davis, E. H. 1980. *Pile foundation analysis and design*, John Wiley and Sons.

Prakash, S. & Sharma, H. D. 1990. *Pile foundation in engineering practice,* New York, John Wiley and Sons.

Rao, S. N., Prasad, Y. V. S. N. & Veeresh, C. 1993. Behaviour of embedded model screw anchors in soft clays. *Geotechnique,* 43(4), 605-614.

Reese, L. C. & O'neill, M. W. 1988. Drilled Shafts: Construction and Design. FHWA, Publication No. HI-88-042

Sakr, M. & El Naggar, M. H. 2003. Centrifuge modeling of tapered piles in sand. *Geotechnical Testing Journal,* 26(1), 1-14.

Seamless Pole Inc 2010. Ductile iron poles. Birmingham, AL. (*http://www.seamlesspole.com/)*

Seed, H. B. & Idriss, I. M. 1970. Soil moduli and damping factors for dynamic response analysis. Berkeley, California: Earthquake Engineering Research Centre.

Skempton, A. W. 1986. Standard penetration test procedures and the effects in sands of overburden pressure, relative density, particle size, aging, and over-consolidation. *Geotechnique,* 36(3), 425-447.

Tsuha, C. H. C., Aoki, N., Rault, G., Thorel, L. & Garnier, J. 2012. Evaluation of the efficiencies of helical anchor plates in sand by centrifuge model tests. *Canadian Geotechnical Journal,* 49(9), 1102-1114.

Wei, J. & El Naggar, M. H. 1998. Experimental study of axial behaviour of tapered piles. *Canadian Geotechnical Journal*, 35(4), 641-654.

Zhan, Y.-G., Wang, H. & Liu, F.-C. 2012. Numerical study on load capacity behavior of tapered pile foundations. *Electronic Journal of Geotechnical Engineering* 17, 1969-1980.

Zhang, D. J. Y. 1999. Predicting capacity of helical screw piles in Alberta soils. *MSc thesis.* Edmonton, Alberta: University of Alberta.

Zil'berberg, S. D. & Sherstnev, A. D. 1990. Construction of compaction tapered pile foundation, (from the experience of the Vladspetsstroi Trust). *Soil Mechanics and Foundation Engineering,* 27(3), 96-101.

MONOTONIC UPLIFT PERFORMANCE OF SCDI HELICAL

TAPERED PILES IN SAND

4.1   Introduction and motivation of research

Driven by the need to reduce carbon emissions associated with fossil-based energy production while meeting high electricity demands, the construction of solar farms to harness solar energy has increased exponentially in recent years. In such applications, solar panels are subjected to a complex loading scheme due to wind pressures, including lateral loading, bending moment and suction (uplift) forces. The induced suction pressure from wind could far exceed the applied downward gravitational forces due to the weight of the solar panel and thus becomes the governing design loading condition. Consequently, piles of varying shapes and materials are currently used in practice to sustain uplift loads.

To further enhance the reliability and economic feasibility and to reduce construction time of the solar panels support systems, the construction industry is pursuing foundation systems that feature efficient construction techniques and novel pile configurations and material. In order to address some of these challenges, an innovative pile system is presented in this study, which combines the efficiency of the tapered section, the competitive cost, effectiveness and durability of spun cast ductile iron with rough surface and the construction advantages of helical piles. The performance of spun cast ductile iron helical piles with tapered shaft is examined herein.

Tapered piles have been successfully used for many years as an efficient piling system for applications involving compressive and lateral loading. Owing to their shape, additional shaft frictional resistance is induced and therefore greater axial capacity is mobilized. Similarly, because of the larger section of the tapered pile near the surface, it offers a larger lateral capacity in comparison with straight-shaft piles with equivalent average diameter. While a substantial amount of studies have been conducted on the compressive and lateral capacity of tapered piles (e.g. Zil'berberg and Sherstnev 1990; Wei and El Naggar 1998;

Zhan *et al.* 2012), limited studies on the uplift resistance of tapered piles are available (Kodikara and Moore, 1993).

The experimental results of El Naggar and Wei (2000) demonstrated that the shaft resistance of tapered piles under uplift loading is lower compared to the case of compression loading, but the uplift resistance increased almost linearly with confining pressure They reported that the uplift capacity of the tapered pile was 0.37 to 0.58 of its compressive capacity, and that the tapered piles uplift capacity is lower than that of a straight pile of the same average embedded diameter. Sakr *et al.* (2005) studied the uplift performance of FRP tapered and straight shaft piles installed in dense sand using a toe driving technique. Their results demonstrated that the uplift capacity of the tapered piles was slightly higher than that of the straight ones at lower displacements. However at greater displacements, both piles had comparable uplift capacity. They also reported that the toe driving technique increased the piles uplift capacity, owing to the densification of the sand surrounding the piles (Sakr *et al.*, 2005).

The performance of piles is strongly affected by its loading history. Joshi *et al* (1992) investigated the performance of piles installed in dry sand. The piles were subjected to compression following uplift loads. As presented in Figure 4 - 1, the results demonstrated an initial segment of the load-displacement curve with low stiffness, which extended to approximately 5mm. This was followed by as segment characterized by much higher stiffness. The authors attributed this phenomenon to the formation of a loose pocket of sand below the pile toe during the uplift testing. It should be noted that this behavior was only observed for piles tested in dense sands, but not in medium sands (Joshi *et al.*, 1992). Their results showed that the effect of prior loading was prominent on the toe resistance resulting in a decrease of 16% to 47% of the failure load.
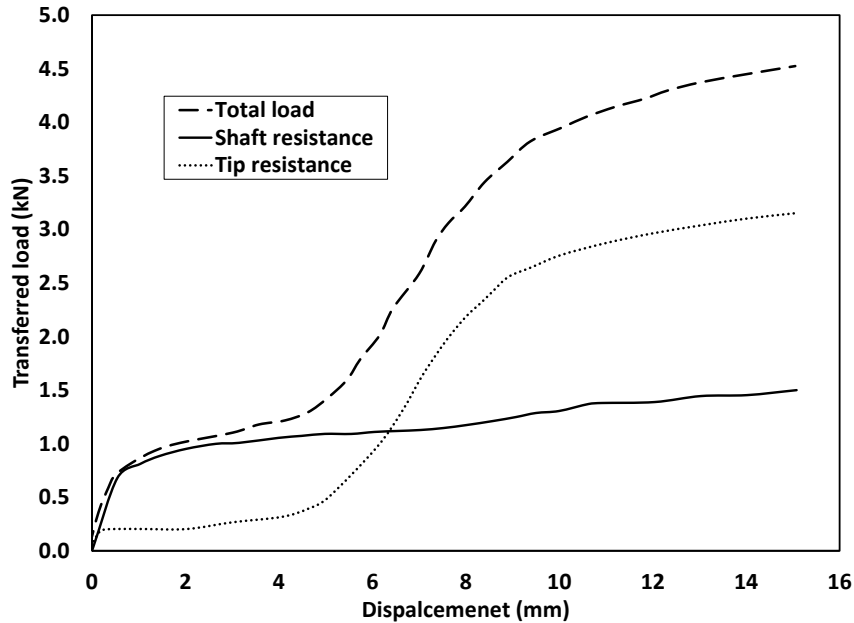
Figure 4 - 1: Load Displacement curves for piles tested under compression after tension in dense sand - after Joshi *et al.* (1992)

Kong *et al.* (2013) proposed a concrete tapered pile with enlarged base that have provided higher uplift capacity than conventional tapered and cylindrical piles, however still lower than the conventional belled piles. The increased uplift capacity was attributed to the larger diameter at the pile toe, which compensated for the smaller diameter near the pile toe due to the pile taper.

Helical piles are fitted with one or more helical plates that help in pile installation by applying torque to the pile head. They offer various construction advantages such as fast installation and low noise and vibration. The capacity of single helix piles is comprised of the soil resistance developed by the helix bearing and the shaft resistance. Trofimenkov and Maruipolshii (1965) reported that the compression-to-uplift capacity of single helix piles installed in sand and clay ranges between 1.4 to 1.5. However, for uplift loading a minimum embedment depth H_t should be provided in order to avoid shallow failures, i.e. failure wedge above top helix extending to the ground surface (Perko, 2009). Ghaly and Hanna (1992) suggested minimum H_t values as function of the helix diameter D_{helix} as presented in Table 4 - 1, which shows greater embedment depths are required for cohesionless soils and with even higher values for denser soil. The variation of the earth

pressure coefficient K_u for uplift loading case is shown in Figure 4 - 2 (Mitsch and Clemence, 1985).

Table 4 - 1: Suggested minimum embedment of helical piles (Ghaly and Hanna, 1992b)

Soil type	Minimum relative embedment (H_t/D_{helix})
Fine grained soils	5
Loose coarse grained soils	7
Medium coarse grained soils	9
Dense coarse grained soils	11
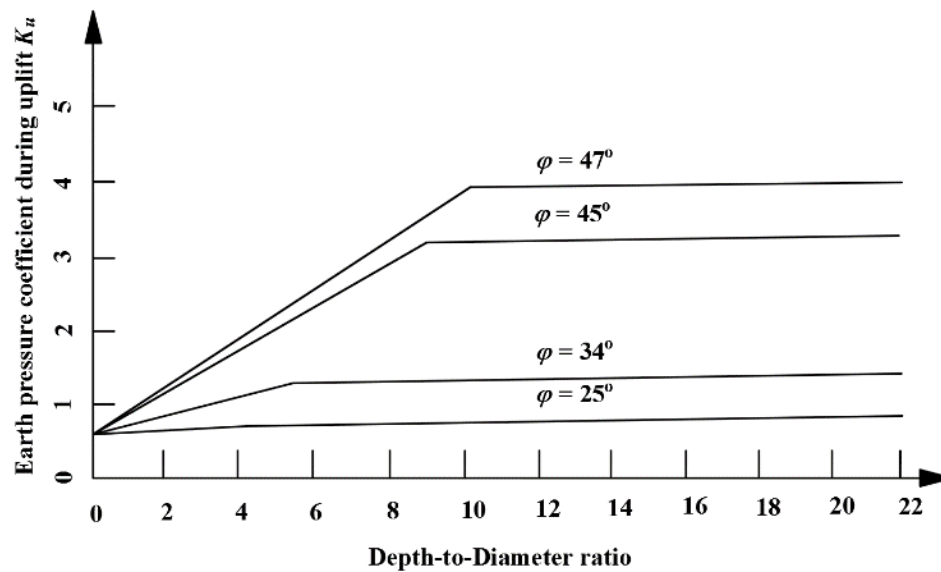
Figure 4 - 2: Variation of the lateral earth pressure coefficients during uplift loading K_u-after Mitch and Clemence (1985)

It should be noted that during the installation of helical piles, significant shearing and disturbance of the soil are likely to occur within the cylindrical installation zone. Greater disturbance may even occur for multi-helix piles, especially above the upper helix plate due to the repeated soil penetration and shearing (Tsuha *et al.*, 2012). Zhang (1999) suggested discounting a distance equal to one helix diameter (D_{helix}) from the shaft resistance in order to account for the soil disturbance/shadowing effects above the helix in

cases of uplift/compression loading. Tsuha *et al.* (2012) suggested lower efficiency of pile capacity for larger helix diameters and denser sand deposits. Bagheri and El Naggar (2013) suggested using the residual angle of internal friction of dense sand when calculating the end bearing factor N_q values proposed by Meyerhof (1976).

The axial capacity of the helical pile can be predicted knowing the installation torque, using an empirical correlation equation (e.g. Livneh and El Naggar, 2008; Hoyt and Clemence, 1989):

$$P_u=K_tT \tag{4 - 1}$$

where T is the installation torque, P_u is the ultimate axial capacity and K_t is the capacity-to-torque ratio. Perko (2009) conducted regression analysis for the results of more than 300 tension and compression pile load tests and proposed the following expression for K_t:

$$K_t= \frac{\lambda_k}{d_{eff}^{0.92}} \tag{4 - 2}$$

where d_{eff} is effective shaft diameter and λ_k =1433mm$^{0.92}$/m (22 in$^{0.92}$/ft) is a curve fitting factor.

While it is a common practice that similar values of K_t are considered for both compression and tension loadings, 10% higher values are generally expected for compression (Perko, 2009).

In the current study, a novel piling system that combines advantages of the tapered configuration and helical pile installation technique is investigated. It consists of a spun-cast ductile iron tapered pile fitted with a lower helical plate to facilitate its installation by means of a mechanical torque applied at the pile head. The proposed pile configuration and installation technique offer several advantages including: fast installation process that produces low vibration and noise, and does not produce soil spoils; enhanced frictional shaft resistance and hence increased pile axial resistance due to its rough surface; higher axial capacity due to the wedging effect during installation because of the tapered shaft; and high durability.

4.2 Objectives and scope of work

A comprehensive investigation program was conducted in order to evaluate the feasibility and efficiency of the proposed system. The investigation involved field load tests of seven piles installed in silty sand and three-dimensional nonlinear finite element analyses to evaluate the performance characteristics of the proposed pile configuration under uplift monotonic loading. The measurements from the field load tests were used to calibrate and verify the numerical models, which were then employed to conduct further analyses to evaluate the load transfer mechanism and to develop an approach for the pile design for uplift loading conditions.

4.3 Experimental setup

4.3.1 Test site soil

A single borehole was drilled to a depth of 11.0 m below the ground surface in the vicinity of the test piles as shown in Figure 4 - 3.
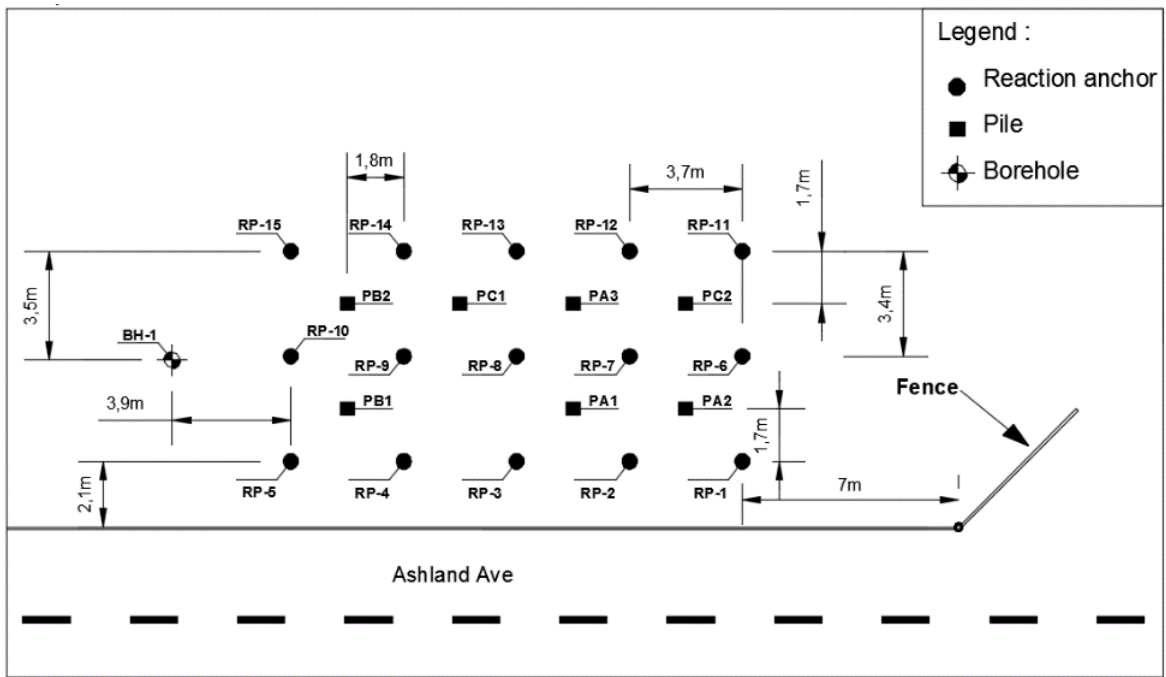
Figure 4 - 3: Site layout showing the drilled borehole location

The borehole log shows that the soil stratigraphy can be described starting from the ground surface in the following sequence: 1) a 0.5m thick layer of silty sand mixed with metallic residues because the testing site was used as a storage area for steel tanks; 2) a 4.5m thick silty sand layer; 3) a 1.0 m thick layer of gravelly sand; 4) a 3m thick layer of coarse sand layer with low percentage of silt; and 5) a hard silty till layer that extended to the end of the borehole.

The ground water table was found at 3.5m from the ground level.

4.3.1.1 Field Tests

The standard penetration test (SPT) was carried out during with blow count measurements taken at 0.75m intervals. The corrected N_{60}' values were determined using the following equation:

N_{60}= Measured number of blows x $\dfrac{C_R C_S C_B E_m}{0.6}$ (Skempton, 1986) (4 - 3)

$N'_{60} = N_{60} \sqrt{\dfrac{100}{\sigma'_v}}$ (Liao and Whitmann, 1986) (4 - 4)

where

N'_{60} is the corrected blow count value considering the field procedures and the overburden pressure effect;

σ'_v is the effective overburden stresses;

C_S is sampler correction, equal to 1.2 for sampler without liner (Skempton, 1986);

C_R is drill rod length correction, equal to 1 at depths greater than 10m and 0.75 for depths less than 4m (Skempton, 1986);

C_B is borehole diameter correction, equal 1.15 for diameter D=200mm (Skempton, 1986);

E_m is hammer efficiency, equal to 0.8 (Bowles, 1996);

The variation of N'_{60} with depth is presented in Figure 4 - 4.

The on-site unit weight of the soil was measured using the sand-cone device (ASTM D1556, 2007). The top 0.5m of soil was excavated first, then two sand-cone tests were performed over the underlying layer. The average measured bulk density was found to be 16.5kN/m³. In addition, correlations with the corrected SPT, N'_{60}, were used to determine the values of the relative density, D_r, and the soil stiffness parameters.
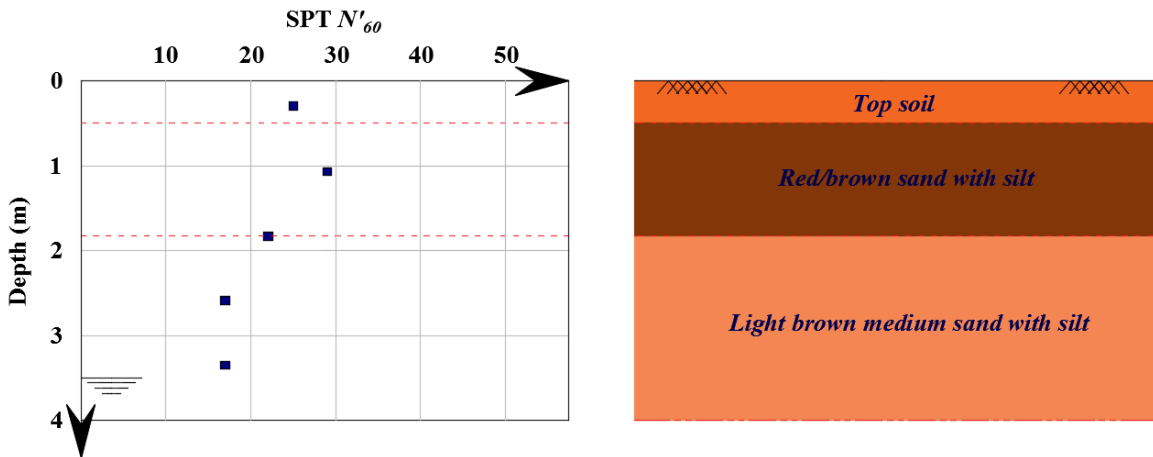
Figure 4 - 4: Variation of SPT N'_{60} with depth

4.3.1.2 Laboratory Testing

Fifteen disturbed samples were retrieved from the split-spoon sampler and were used to conduct several tests at The University of Western Ontario soils laboratory. The performed tests included: measurement of water content W_c, sieve analysis for soil classification; determination of the specific gravity G_S, determination of Atterberg limits; and direct shear tests.

Soil classification and index properties

Sieve analyses were performed for samples retrieved at different depths according to ASTM C136 (2006). The resulting gradation curve is shown in Figure 4 - 5.
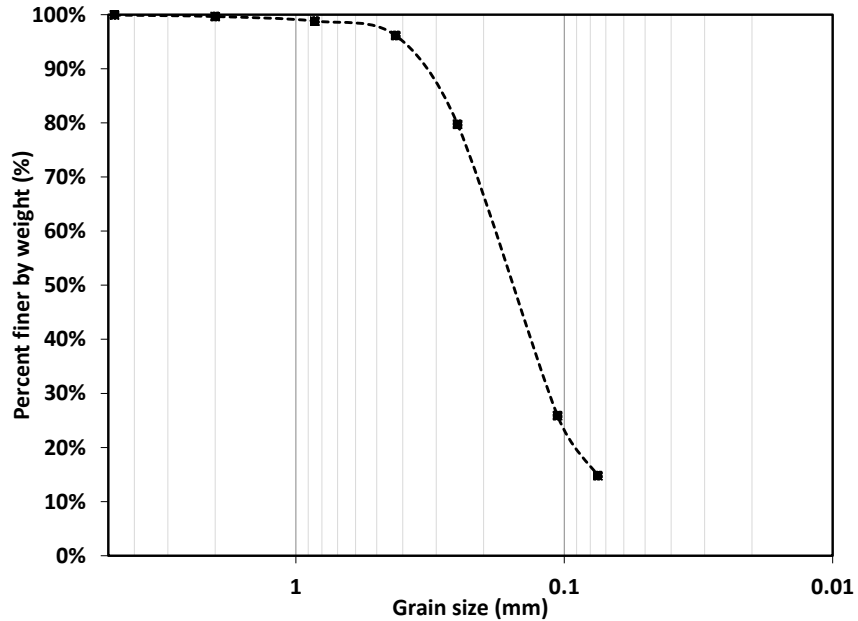
Figure 4 - 5: Grain size distribution for disturbed sample retrieved at 1.05m below the ground surface

The length of the tested piles was only 3.1m, with an even shorter embedded depth due to their free length. Accordingly, only the top 4m of soil was relevant to the piles performance. Thus, the soil sample at 1.05m depth was deemed representative of soil along the pile shaft. The results showed only 14.8% fines at that depth with almost no gravel, with average liquid and plastic limits of 25.3% and 21.5%, respectively (ASTM D4318, 2010). This soil layer was thus classified as silty sand (SM) according to the Unified Soil Classification System USCS (ASTM D2487, 2011). The average on-site W_c was measured to be 20.5% at the same depth. The average of measured G_s of two extracted soil samples at depths of 1.05m and 4.8m was 2.71.

Soil shear strength parameters

A series of direct shear tests (ASTM D3080, 2011) with a horizontal rate of feed of 0.406mm/min were conducted to measure the soil shear strength parameters of samples retrieved at 0.6m and 1.08m depths. The unit weights of the tested samples were set to the field measured unit weight. Figure 4 - 6 shows the resulting variation of shear stresses with normal stresses, vertical displacement and horizontal displacement. The resulting residual

and peak strength values are shown in the same figure. The results showed a bilinear shear-normal stress relation with a change of the chart slope at a normal stress of 20 kPa.
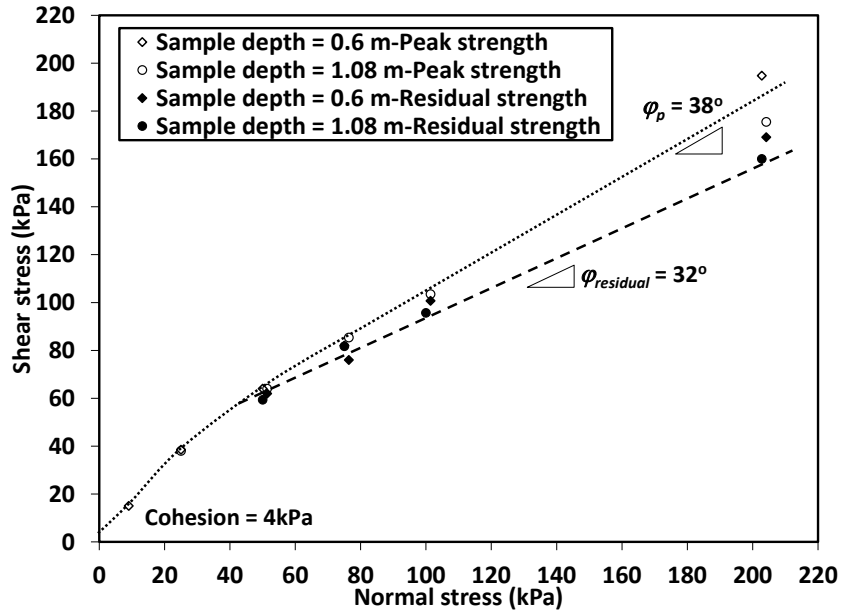
(a)
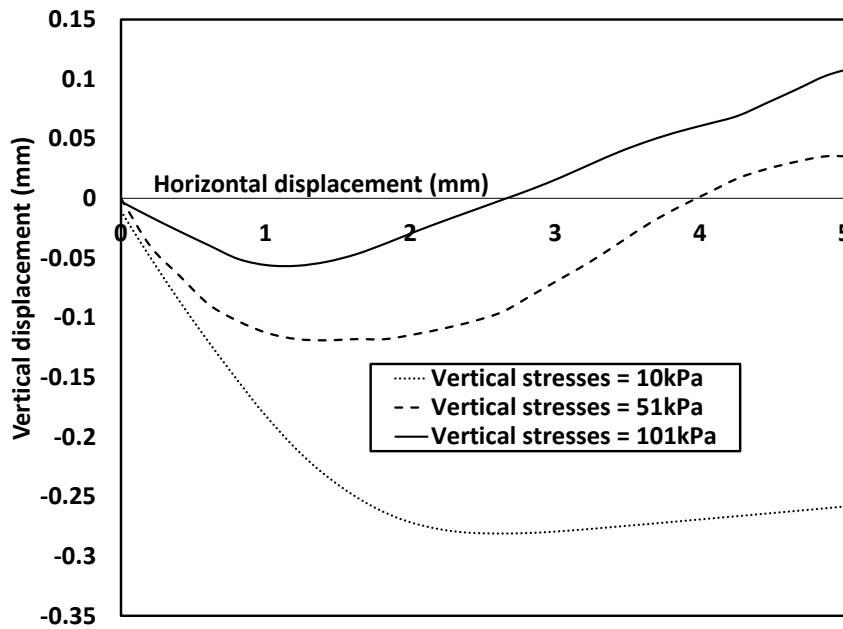
(b)
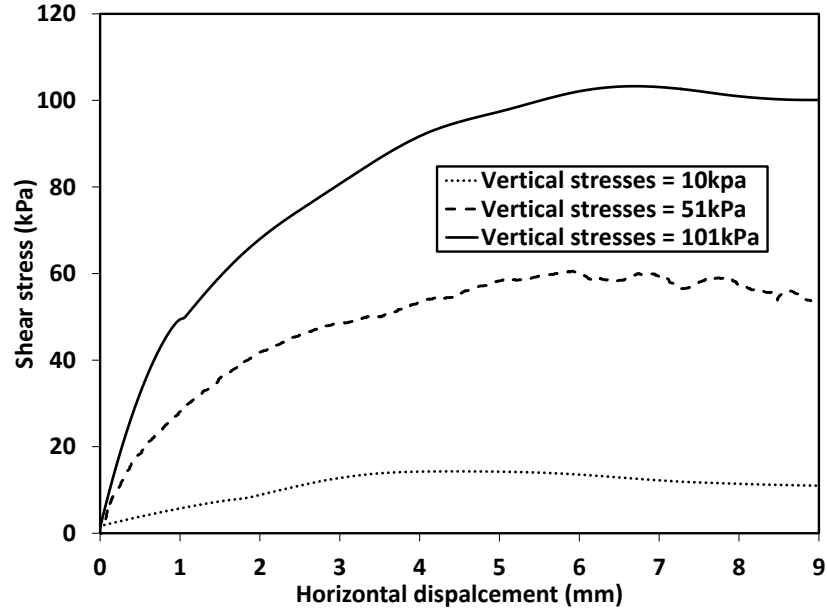
(c)

Figure 4 - 6: Direct shear tests results (a) Shear vs normal stresses; (b) Vertical displacement vs horizontal displacement; (c) Shear stress vs horizontal displacement

The test results showed the effective cohesion, c', residual angle of internal friction $\varphi_{residual}$ and peak angle of internal friction φ_p to be 4 kPa, 32° and 38°, respectively. Considering the range of N values at the location of test specimens, the determined angle of internal friction lies within the upper bound of the relevant range typically found in the literature due to the high angularity of the sand particles.

Relative density and stiffness parameters

The following correlations were found to evaluate the values of soil relative density D_r, Young's modulus E_s, and Poisson's ratio v:

D_r of the soil deposits were correlated N'_{60} values using the following equation (Mayne *et al.*, 2002):

$$D_r = 100 \sqrt{\frac{N'_{60}}{60}} \qquad\qquad (4 - 5)$$

96

The calculated values of D_r w along the top 4m range between 50 to 70%. Given the angle of internal friction and D_r, the soil along the pile length can be classified as medium dense to dense (Bowles, 1996).

Due to the lack of undisturbed retrieved soil samples, the over-consolidation ratio, OCR, was correlated to other parameters or test results. The apparent preconsolidation pressure σ_p' was correlated to N_{60} (Mayne, 1992), i.e.

$$\sigma_p' = 0.47 \ (N_{60})^m \ Pa \tag{4 - 6}$$

where Pa is the atmospheric pressure *and* $m = 0.6$ to 0.8 for silty sands (Mayne, 2006)

Considering the initial in-situ overburden stresses and the evaluated σ_p' using the above equation, the calculated OCR for the top 4 m was approximately 6.

While several equations are available in literature correlating the measured SPT to the soil's E_s, a significant scatter exists between them (Kulhawy and Mayne, 1990). For the present case, and as a first order estimator, E_s for overconsolidated sand can be correlated to the N_{60} using the following equation, i.e.(Kulhawy and Mayne, 1990):

$$E_s/Pa = 15N_{60} \tag{4 - 7}$$

The calculated values of E_s for the top 4 m of the soil profile varied between 30 and 60 MPa.

The representative parameters of the soil along the piles shaft are evaluated based on the field and laboratory tests, and the empirical correlations described above, and the obtained values are summarized in Table 4 – 2.

It should be noted however that the post–installation elastic modulus values are of main interest to this study rather than the values obtained from the empirical correlations. Therefore, as a preliminary estimate, the recommended E_s values by Poulos and Davis (1980) for driven piles in sand were considered. They suggested that, while E_s for sand typically varies with depth, it is also appropriate to consider for analysis purposes an average value along the pile shaft and greater value below the driven pile toe. This

assumption is also acceptable considering the relatively short length of the piles in the present study. The values suggested by Poulos and Davis are 55~70MPa for medium dense sand and 70~100MPa for dense sand. Accordingly, an average E_s of 70MPa was considered for the present case. Additionally, the value of v varies between 0.2 and 0.4 for loose to dense sands (AASHTO, 2002), therefore 0.3 is considered. Finally, considering the average OCR along the top 4m of soil is 6, the average coefficient of earth pressure at rest prior to the pile installation can be given by (Mayne and Kulhawy, 1982):

$$K_{o\text{-}OC} = (1\text{-}Sin\varphi)OCR^{(1\text{-}sin\varphi)} = 0.76 \qquad\qquad (4 - 8)$$

The representative soil parameters after piles installation were calibrated and verified numerically using the results of the piles axial compressive load tests as shown in Chapter 3.

Table 4 - 2: Representative soil parameters

Depth (m)		φ_p (°)	c' (kPa)	Specific gravity G_s	Water content (%)	v	E (MPa)	γ_b (kN/m³)	D_r (%)
From	To								
0	0.5	36	4	2.71	20.5	0.3	70	16.5	55
0.5	4	38							

4.3.2 Test piles

Seven hollow closed ended piles with configurations as shown in Figure 4 - 7 were installed in silty and soil. Three piles were of configuration A, 2 of configuration B and 2 of configuration C. The piles of configurations A and B were made of ductile iron having a rough external surface while those of configuration C were made of steel with conventional (smooth) surface. The wall thickness of all piles was 5.5mm.
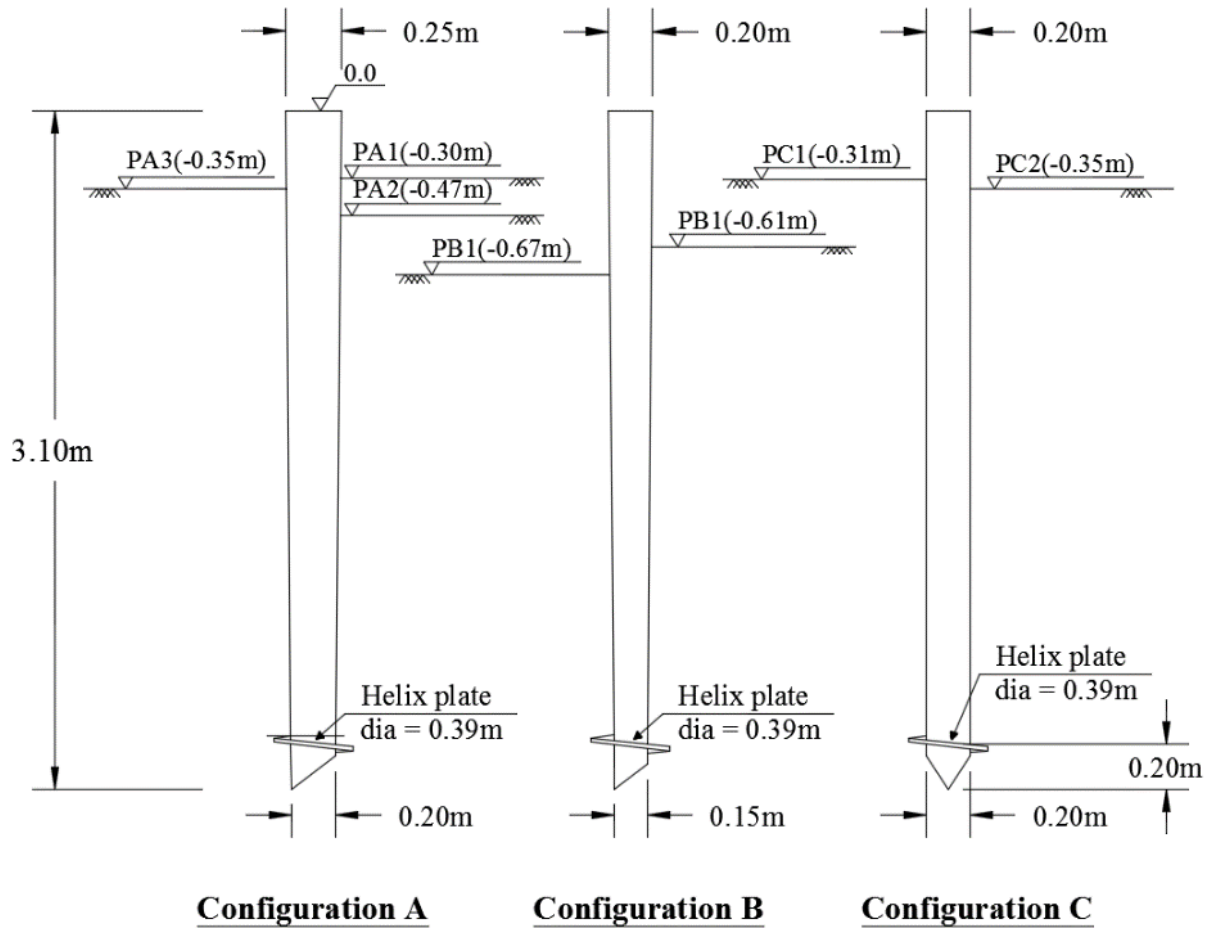
Figure 4 - 7: Tested piles configurations

4.3.3 Instrumentation

In order to evaluate the load transfer mechanism, each pile was instrumented using eight equally spaced electrical resistance strain gauges mounted at locations as shown in Figure 4 - 8 (a). The strain gauges were fixed on specially machined pockets of 1 mm depth as shown in Figure 4 - 8 (b). The lead wires were passed from inside the pile through a small groove to minimize gauges damage during installation.
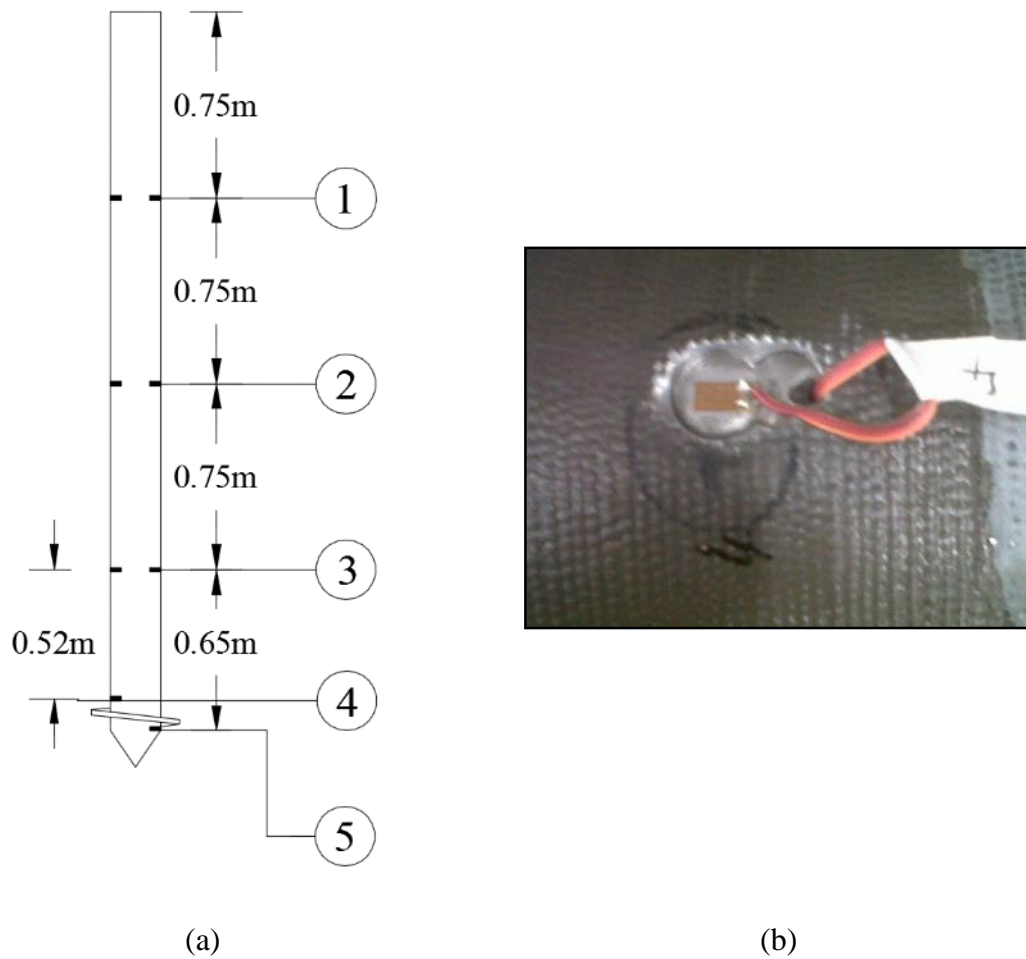
Figure 4 - 8: Strain gauges (a) Locations; (b) Pockets

4.3.3.1 Installation Procedure

Finite element (FE) models were developed for the different piles configurations to determine their torque capacity to ensure the piles integrity during installation, The FE models considered the torque to be applied at the head of each pile while its toe is fully fixed and with no soil along its shaft. This condition represented the upper bound for the shear stresses developed in the pile cross-section during the installation process whereas practically gradual transfer of the stresses will be provided by the soil along the soil-pile interface. The calculated torque capacity values were 58, 32 and 68.5kN.m for piles of configurations A, B and C, respectively.

The mechanical torque head used was a Hitachi UH07 rig, and the torque was applied employing a steel cap bolted to the pile head as shown in Figure 4 - 9. To facilitate the pile vertical alignment, the soil along the top 0.3m to 0.45m was predrilled prior to the piles installation. The applied torque required to overcome the shear resistance at the pile-soil interface was monitored and summarized in Table 4 - 3.

Figure 4 - 9: Field images of loading cap

Table 4 - 3: Pile installation torque readings

Depth (m)	Torque (kN.m)						
	PA1	PA2	PA3	PB1	PB2	PC1	PC2
0.9	4.1	NA	6.8	4.1	NA	NA	NA
1.2	6.8	8.1	10.2	8.1	2.0	4.7	3.4
1.5	11.5	12.2	12.9	11.5	4.7	8.1	8.1
1.8	16.3	16.3	16.3	12.9	8.1	1.4	11.5
2.1	24.4	24.4	23.0	16.3	11.5	23.0	13.6
2.4	29.8	30.5	29.2	20.3	16.3	23.7	18.3
2.7	38.0	38.6	37.3	21.0	19.7	20.3	23.0
3.1	40.7	40.7	40.0	20.3	NA	34.6	27.8

4.3.4 Load test setup, loading sequence and test procedure

The uplift test setup comprised a reaction steel beam and two sets of wood cribbing as shown in Figure 4 - 10. The load was applied to the pile using a hydraulic jack pushing against the reaction beam. The applied load was measured using a load cell placed over the pile head. Additionally, four linear variable displacement transducers (LVDTs) were mounted on the corners of the loading plate attached to the pile head in order to monitor the pile head displacement. The strain gauges, LVDTs and the load cell were connected to a data acquisition system, which recorded the readings every 1 second. It should be noted that a number of the installed strain gauges were damaged due to the high frictional stresses developed during pile installation at the soil-pile, and due to the helix breaking in some cases as described later.
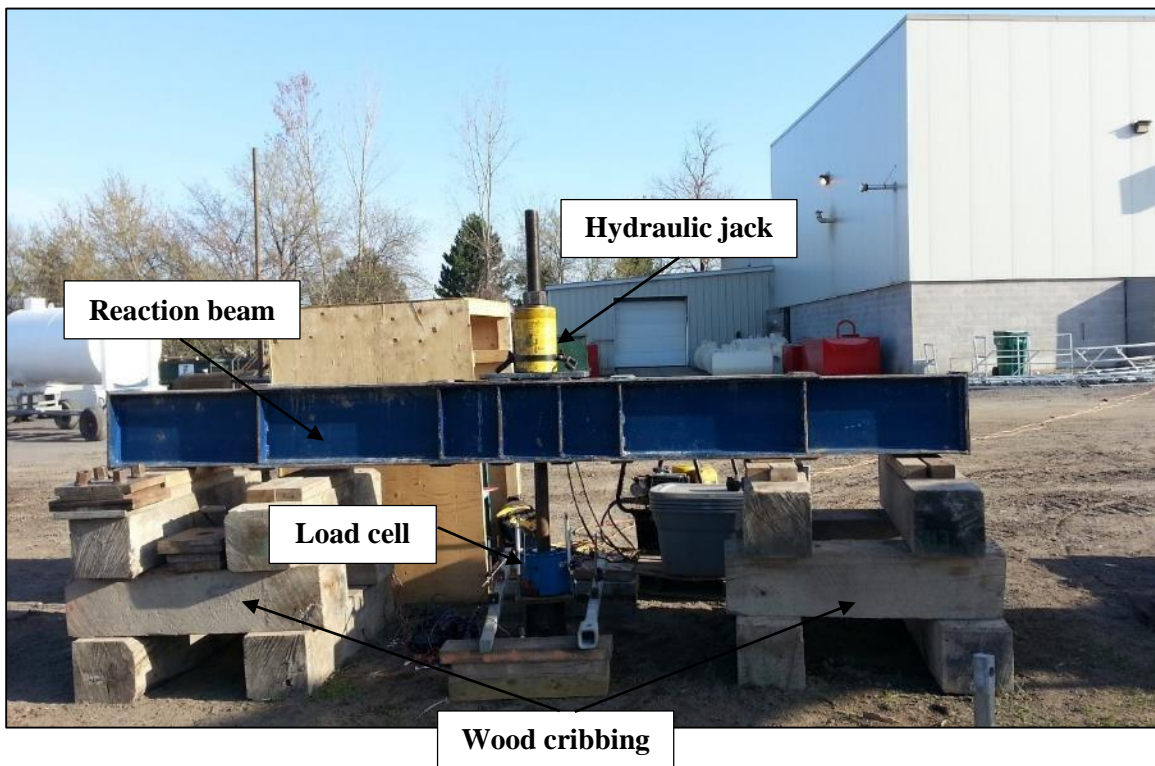
Figure 4 - 10: Test setup - uplift testing

Two load sequences were used to evaluate the effect of cyclic uplift loading and monotonic compression loading on the static uplift performance of the proposed pile system. Four piles were subjected to initial monotonic compression loading followed by monotonic

uplift testing to failure, and three piles were subjected to initial cyclic uplift loading followed by monotonic uplift testing to failure. The loading sequences for the different piles are presented in Table 4 - 4.

Table 4 - 4: Testing sequence

Pile	Configuration	Testing sequence
A1	A	Monotonic compression followed by monotonic uplift
A2	A	Monotonic compression followed by monotonic uplift
A3	A	Cyclic uplift followed by monotonic uplift
B1	B	Monotonic compression followed by monotonic uplift
B2	B	Cyclic uplift followed by monotonic uplift
C1	C	Monotonic compression followed by monotonic uplift
C2	C	Cyclic uplift followed by monotonic uplift

This cyclic loading scheme, illustrated in Figure 4 - 11, simulated wind loading during different storm conditions. In this scheme, the piles were initially loaded in four equal increments up to the expected design load (Q_d). This was followed by two sets of fifteen one-way load cycles (each cycle was completed in 2 min): in the first set, the cyclic load varied from 70% to 130% of Q_d; and in the second set, it varied from 55% to 145% of Q_d.

Figure 4 - 11: Axial cyclic loading pattern

4.3.4.1 Testing Procedure

The monotonic uplift loading followed the quick test procedure specified in ASTM D3689/D3689M (2007), where the piles were loaded in increments of 5% of their expected ultimate capacity with each load increment maintained for 5 min. Load increments were added until failure was reached (i.e. no further loading is required to increase the pile penetration). The final load increment was maintained for 15 min. The piles were then unloaded on 4 equal increments, and each load increment was maintained for 5 min. The pile response was monitored for 15 minutes after it was fully unloaded to ensure its full rebound was captured.

4.4   Results and discussion

4.4.1   Load-deflection curves

The measured load-displacement curves are shown in Figure 4 - 12 and Figure 4 - 13 for piles tested following monotonic compression and cyclic uplift tests, respectively. It can be generally seen that tapered piles PA1 and PA2 developed higher resistance at lower displacements. At greater displacements, the tapered shaft resulted in the release of the lateral confining pressure hence decreasing the mobilized the shaft resistance. This was not the case for the straight shaft piles PC1 and PC2, which mobilized greater resistance at higher displacement.

As shown in Figure 4 - 12, piles PA1, PA2 and PC1 tested following the compression test exhibited an initial linear behavior where the resistance was developed by the shaft resistance (up to 55kN for PA1 and PA2 and to 26kN for PC1). The higher shaft resistance of the tapered piles was attributed to their rough shaft surface as well as the initial higher lateral confinement developed during the preceding compression loading. As the applied load increased exceeding the shaft resistance, PA1 and PC1 experienced significant drop in stiffness (slack zone) because the soil resistance on the helical plate was not mobilized fully due to the loosened soil zone above the helical plate. This slack zone is attributed to gapping between the soil and the helical plate followed by soil caving in during the prior compression testing. As the load continued to increase, the loose soil was re-compacted and the stiffness increased again (at a load of 100kN and 68 kN for PA1 and PC1, respectively), which extended until non-linear behavior was observed just before failure.

The slack zone and non-linear regions, however, were not that obvious for PA2. It appears that no gapping has occurred above the helix, perhaps because the soil was initially loose; hence, PA2 displayed higher stiffness in this slack zone but lower stiffness in the ensuing linear region compared to PA1 and PC1. This is because PA2 experienced significantly higher settlement compared to PA1 and PC1 when tested in compression (87mm compared to 56mm and 52mm).

105

On the other hand, re-compaction of the soil above the helix plate during the initial cyclic uplift tests eliminated the loose soil pockets above the helix. This is manifested in the observed responses presented in Figure 4 - 13; i.e., the piles exhibited stiffer response in the initial stage of monotonic loading with linear behavior extending up to ~ 6mm. In addition, the tapered pile PA3 developed higher resistance than PC2 even at greater displacements owing to the greater soil compaction along the shaft for the tapered profile compared to the straight one, which occurred during cyclic loading.
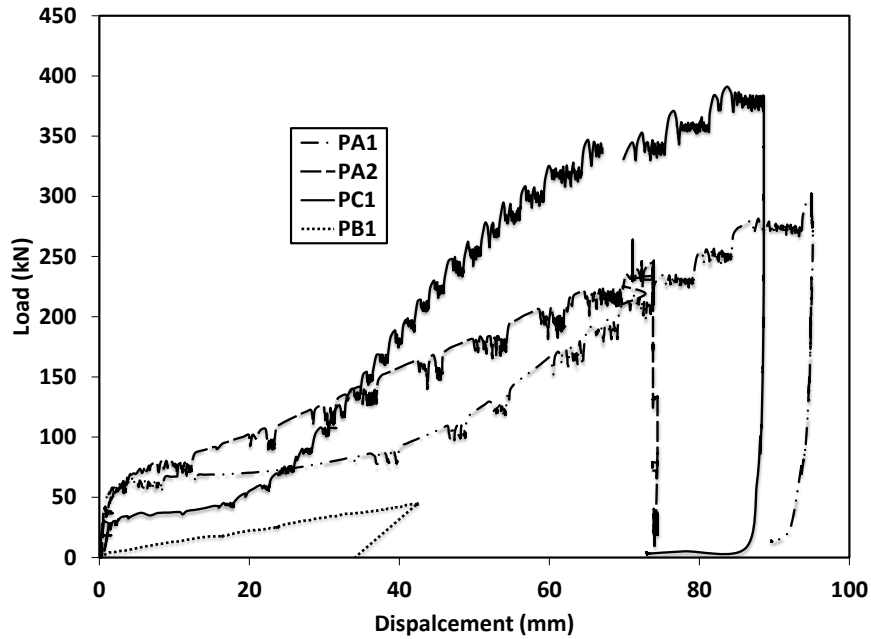
Figure 4 - 12: Load-displacement curves - uplift tests after monotonic compression
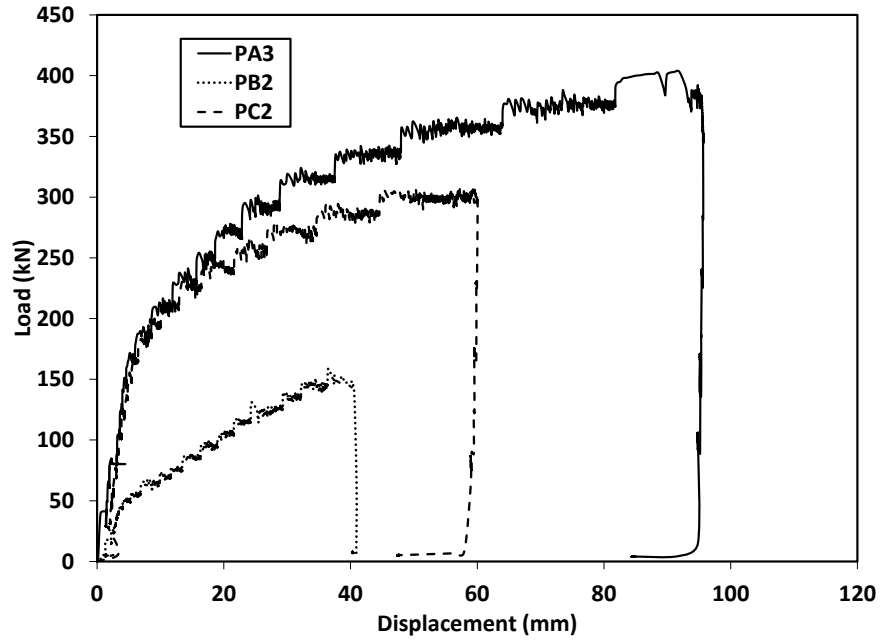
Figure 4 - 13: Load-displacement curves - uplift tests after cyclic uplift

The welding of the helical plates of PB1 and PB2 failed during the uplift loading, which was confirmed following their removal from the ground as shown in Figure 4 - 14. Accordingly, the load-displacement curve represented the shaft resistance only.
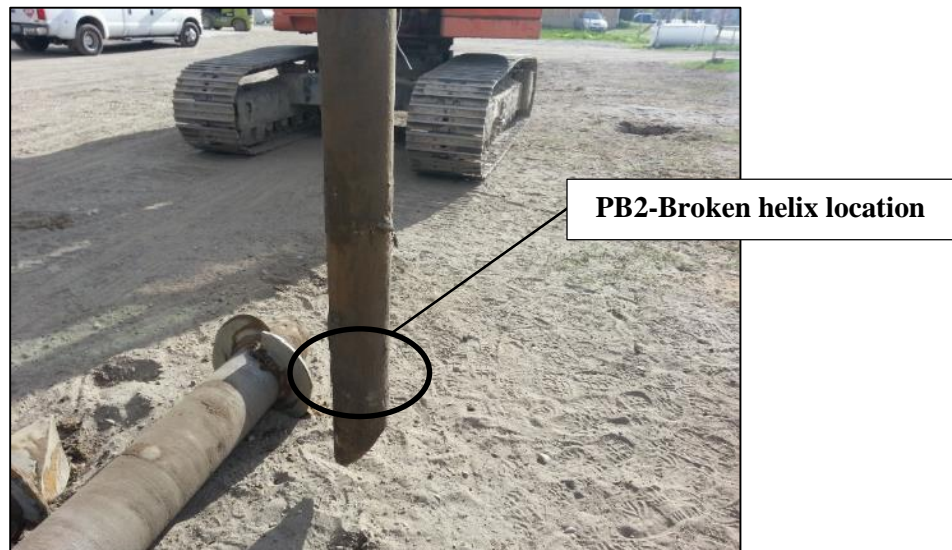
Figure 4 - 14: Field image-PB1 upon removal

4.4.2   Pile ultimate uplift capacity

The ultimate uplift capacity of piles is typically defined using one of three criteria: the load corresponding to the point of the sharpest curvature, the load corresponding to a fixed upward displacement or the load corresponding to the point of intersection of the tangents to the load displacement curve (Sharma *et al.*, 1984). The uplift capacity values of the test piles determined using the latest two criteria are listed in Table 4 - 5. The uplift capacity values are also presented as ratio of the pile corresponding compressive capacity values, which were determined in Chapter 3 using Fuller and Hoy criteria (Fuller and Hoy, 1970). The results are summarized in Table 4 - 5.

Table 4 - 5: Piles ultimate uplift capacity

| Pile | Capacity (kN) | | | |
	Corresponding to 6.25mm displacement (kN)	Uplift-to-compression ratio (considering 6.25 displacement)	Tangents intersection	Uplift-to-compression ratio (considering tangents intersection)
PA1	59.7	0.13	230.0	0.5
PA2	58.0	0.15	NA	NA
PA3	121.0	0.24	295.0	0.5
PB1	10.0	0.04	NA	NA
PB2	50.0	0.15	NA	NA
PC1	2.4	0.01	325.0	0.9
PC2	28.0	0.10	265.0	0.9

It should be noted that interpretation of configuration B piles capacity using the tangent intersection criterion was not possible due to the helix failure during uplift loading. As well PA2 interpretation was not possible since no clear intersection can be determined.

The results show that at smaller displacements, where the capacity mainly results for the shaft resistance, tapered profile piles of configuration A demonstrated higher uplift capacity and uplift-to-compression capacity ratio. At greater displacement, where a further release of soil horizontal confining stress occurred along the profile of tapered piles, the straight shaft piles exhibited higher uplift capacity and higher uplift-to- compression capacity ratio.

Finally, upon unloading the piles recovered a small percentage of their maximum displacement (only 2% to 19%), which means the soil experienced significant plastic strains during the uplift loading phase.

4.4.3 Load transfer mechanism

The readings of the strain gauges were used to evaluate the load transfer mechanism. The axial force at different depths P_{zi} was calculated based on the strains measured, as follows:

$$P_{zi}=\varepsilon A_{pi}E_p \tag{4 - 9}$$

where ε is the measured strain, A_{pi} is the cross-sectional area of the pile at the considered strain gauge location (varies with depth), and E_p is the elastic modulus of the pile material.

The load transfer curves (i.e. distribution of axial force along the shaft) are shown in Figure 4 - 15 and Figure 4 - 16 for piles subjected to an initial monotonic compression loading first, and piles subjected to initial cyclic uplift loading, respectively. Unfortunately, not all strain gauges continued to function properly and some strain gauges were damaged during installation and following the helix breaking.
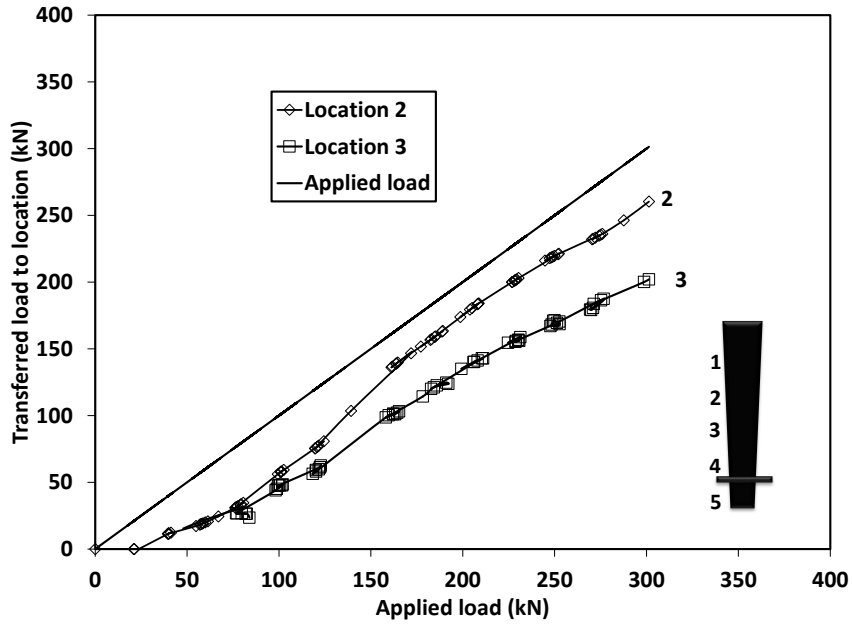
(a)
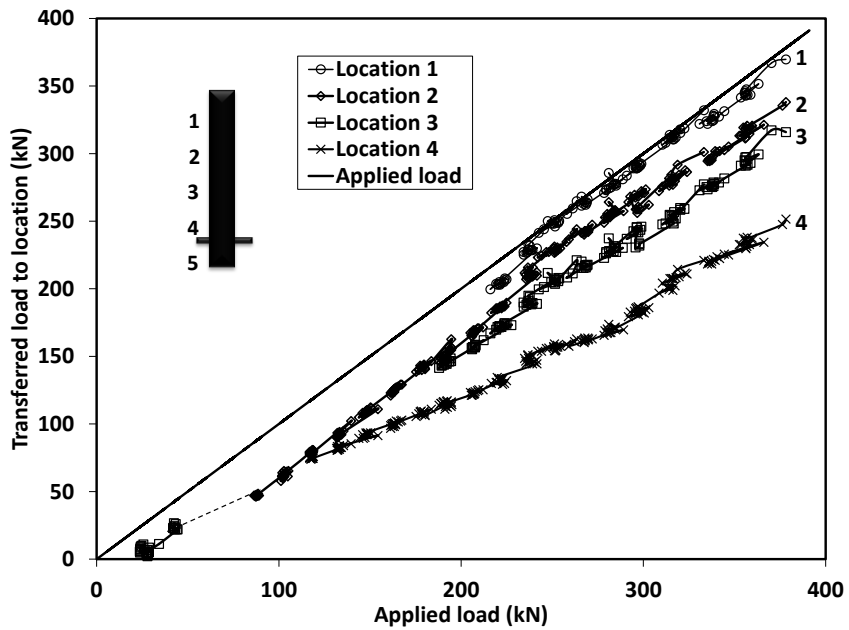
(b)

Figure 4 - 15: Variation of measured load at different levels (a) PA1; and (b) PC1
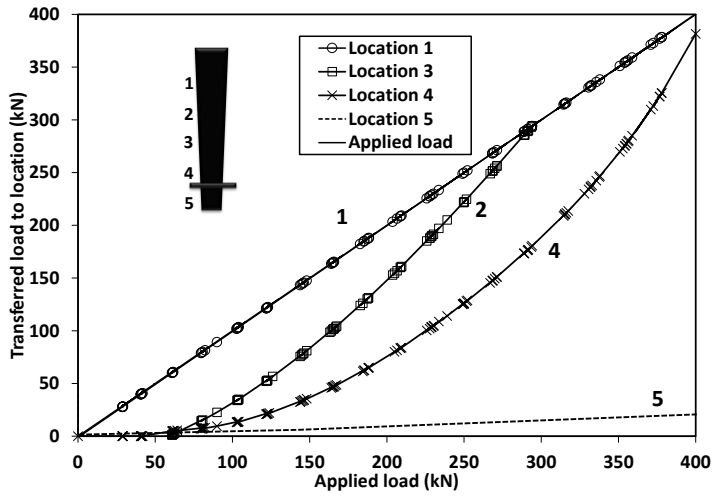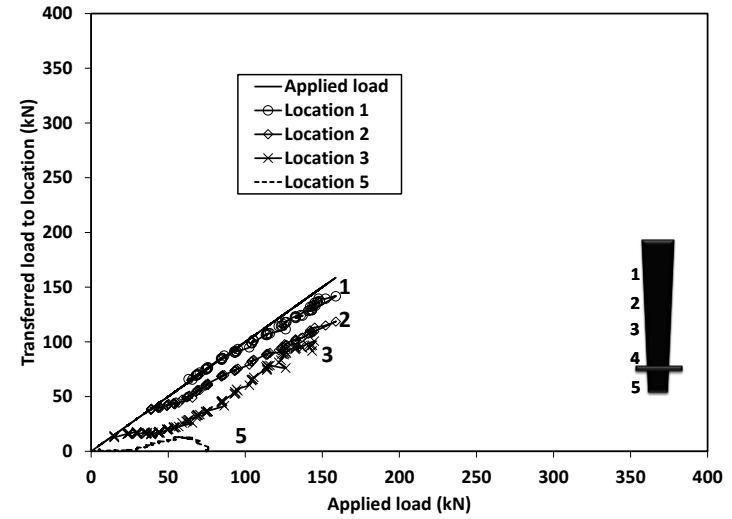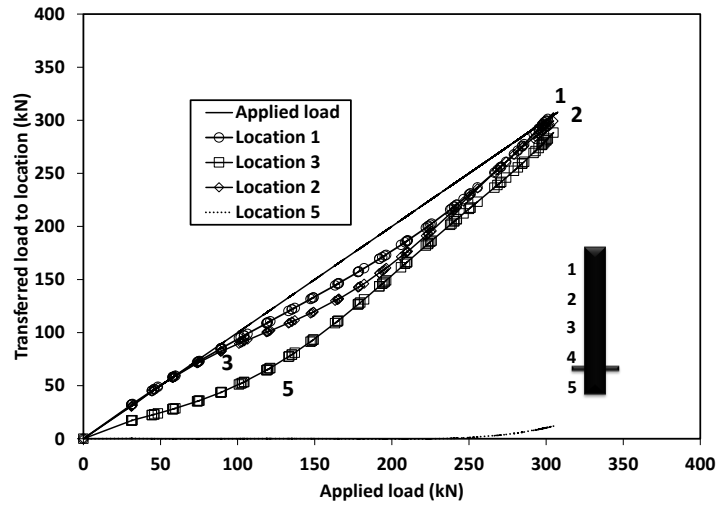
Figure 4 - 16: Variation of measured load at different levels (a) PA3; (b) PB2; and (c) PC2

As expected for dry cohesionless deposits, negligible suction forces at the pile toe were developed where negligible loads were transferred right below the helix plate as shown in Figure 4 - 16.

The readings of the strain gauge mounted on few location of PC1 were not captured at the start of the loading possibly due to the locked in stresses from the prior compression test. The maximum developed shaft stresses were within 64 kPa along the pile shaft except along the top 0.75m ($\approx 2D_{helix}$) above the helix where it reached 48 kPa at the maximum uplift displacement due to the excessive soil flow around the helix. Using the β- method suggested by the Canadian Foundation Engineering Manual considering driven piles in medium dense to dense sand (upper bound $\beta = 1.2$) and adding the adhesive resistance from the cohesion of the soil, the maximum developed stresses along the pile shaft should be 59 kPa. It should be noted however that the former value reflects the value in compression, whereas for piles in uplift, 75% to 80% of it is suggested (El Naggar and Sakr 2000; O'Neil 2001). The resulting stresses distribution shows that, at the maximum applied load, only 34% of it was carried out by the shaft resistance.

The maximum stresses developed along the shaft of PA1 (between locations 2 and 3) was 114 kPa compared to 200 kPa for the compressive loading case as presented in Chapter 3, perhaps due to the fact that the tapered profile releases some of the lateral confining pressure during uplift.

The piles subjected to initial cyclic loading exhibited higher mobilized shaft resistance at lower displacements compared to the case of piles loaded monotonically first. The mobilized resistance, however, decreased at larger displacements due to slippage that took place along the pile-soil interface.

The maximum mobilized stress for PA3 between locations 1 and 3 (0.75 to 2.25m from the pile head) was 60 kPa. This value decreased as the displacement increased, and higher load was resisted through helix bearing. At the maximum applied load, the helix bearing accounted for 90% of the pile resistance (357kN). The helix compressive bearing

component Pu_b can be analytically found using the bearing capacity equation, i.e.(Perko, 2009):

$$Pu_b = A_{helix}[c'N'_C + q(N'_q - 1) + 0.5\gamma'D_{helix}N'_\gamma]$$
(4 - 10)

Where A_{helix} is the helix area, and N_c', N_q' and N_γ' are the combined bearing capacity factors taking into account the shape and depth factors. Using the above equation, the expected helix bearing capacity is 436 kN. The fact that the used factors were not developed for small shaft to helix diameters ratio would be the reason that the measured resistance in 18% lower than the calculated value.

For pile PC2, the maximum mobilized shaft stress was 84kPa, which is very close to the value for the compression loading case (presented in Chapter 3). As displacement increased, slippage occurred at the pile-soil interface and the shaft dropped significantly, and the helix carried more than 94% of the load at the end of the test. For PB2, the maximum developed shaft resistance was 54 kPa, which is comparable to the maximum shaft resistance for PA3.

4.5 Pile capacity-installation torque correlation

Considering the maximum uplift load at which the piles dislodged from the ground, and knowing the installation torque values (shown in Table 4 - 3), K_t values were calculated and compared to the values determined using Equation (4 - 2) as shown in Table 4 - 6.

Table 4 - 6: Calculated torque factors-uplift loading

Pile	K_t (kN/kN.m)	
	Field calculated values	Calculated values using Eq. 4 - 2
PA1	6.8	9.8
PA2	NA	9.8
PA3	10.0	9.8
PB1	NA	12.4
PB2	NA	12.4
PC1	10.9	10.9
PC2	10.8	10.9

While the measured and calculated K_t values for the straight piles were almost identical, the measured value for PA1 was much lower than the calculated value. However, pile PA3 that was subjected to initial cyclic loading, the measured and calculated K_t values were comparable.

4.6   Numerical investigation

To further examine the static uplift behavior of the novel pile system, three-dimensional finite element analysis was conducted for the test pile configurations A and C considering uplift loading following monotonic compression tests. The numerical models were developed using ABAQUS (Hibbitt *et al.*, 2008). The analysis investigated the pile-soil interaction and the effect of the initial compression loading to evaluate the contribution of the helix on the pile uplift performance.

4.6.1   Numerical model

4.6.1.1 Description of finite element model

The pile-soil system is modeled employing a 3D quarter cylindrical mesh. The pile was placed along the axial z-direction of the model. The helical plate was idealized as planar disk for numerical simplification. Figure 4 - 17 presents the model geometry for a single pile of configuration C subjected to axial loading.

The soil medium and the pile were simulated using 8-noded, first order, and reduced integration continuum solid elements (C3D8R) having three active translational degrees of freedom at each node and one integration point located at the centroid. The location of the boundaries was optimized to minimize the boundary effects on the results while reducing the computational effort. The radius of the soil cylinder extended 2.5 m (i.e. 10 times the largest shaft diameter) from the center of the pile shaft. The bottom horizontal boundary was placed at 1.95 m below the pile toe, which is equivalent to 5 helix diameters.
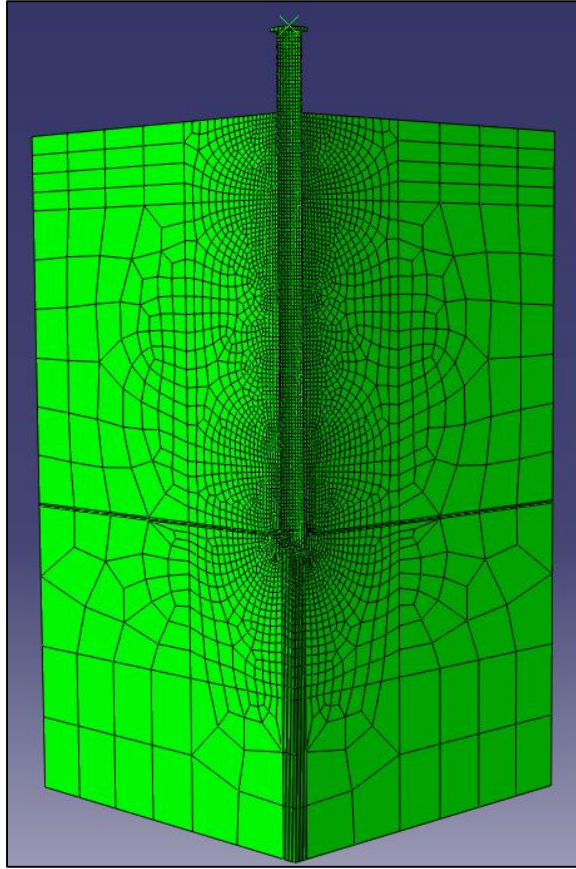
Figure 4 - 17: Finite element model geometry – undeformed mesh-PC1

A stress-free boundary was considered for the soil top surface. The translation of the bottom boundary was restrained in X, Y and Z directions. The vertical boundaries of the soil were restrained from translating in X (Y) direction and rotating around Y and Z (X and Z) where applicable to simulate the case of a full model. The back of the soil quarter cylinder was restrained from moving in X and Y directions (movement along Z direction was allowed).

Mesh refinement at stress/strain concentration zones was necessary to ensure the accuracy of the results. Accordingly, a series of models was developed where the mesh was incrementally refined and the results were compared. When the difference between the results of two consecutive models (i.e. refinements) became less than 2.5%, the most refined model was considered. The elements were most refined along the pile-soil interface and around the helical plate and then their size gradually increased towards the model

boundaries. This process resulted in mesh configurations consisting of 37 309/28 553 elements for pile configurations A/C, with maximum elements side dimension ranging from 250 mm/330 mm at the model boundaries to 20 mm/25 mm at the pile-soil interface. The pile mesh consisted of 1609/1451 for configurations A/C.

4.6.1.2 Soil model

The soil is simulated as an elastic-perfectly plastic isotropic continuum. The soil plasticity and failure were modeled using the Mohr-Coulomb yield criterion where values of the critical state angle of internal friction, φ_{cs}, cohesion yield stress, c' and the dilation angle, ψ. Poisson's ratio, v, and Young's modulus, E_s defined the soil elasticity.

The soil domain was divided into three main sections:
- The top soil (0.5m) layer was modeled with reduced strength and stiffness reflecting the soil disturbance induced during the initial predrilling process;
- Soil along the pile shaft;
- Soil beneath the helix pate was modeled using higher stiffness to account for the soil densification during the installation process.

The soil properties representing the conditions after pile installation were established through the calibration of the numerical model using monotonic compression field test results as presented in Chapter 3. The same soil properties, presented in Table 4 - 7, are used herein. Additionally, the analysis of the uplift testing results confirmed their validity.

Table 4 - 7: Soil parameters considered in FE model (calibrated and verified in Chapter 3)

Depth (m)		φ_{cs} (°)	c' (kPa)	ψ (°)		ν	E_s (MPa)		γ (kN/m³)
From	To			PA2	PC1		PA2	PC1	
0	0.5	32	4	4	4	0.3	35	35	17
0.5	Helix level	32	4	6	4	0.3	70	60	18
Helix level	End of model	32	4	6	6	0.3	91	94	18

In order to account for disturbance of soil above the helix plate during the compression loading, a cylindrical disturbed zone assigned above the helix plate extending to a distance equal to D_{helix} = 0.39m. The properties of soil in this zone were obtained from the calibration process using the uplift results, which yielded friction angle $\varphi = 27°$ and $E_s = 9$ MPa. These values reflect the loose state of the disturbed zone and sheared sands and fall within the typical values for very loose sands (Bowles, 1996).

4.6.1.3 Pile Model

The pile was simulated as linear elastic-perfectly plastic material. The elastic behavior was defined by Poisson's ratio, ν_p, and Young's modulus, E_p. The plastic behavior was represented by the yield strength of the pile material. The mechanical properties of the piles materials are presented in Table 4 – 8. Weaker strength parameters were considered for the helix and base plate welds to accommodate the weld defects observed prior to the piles installation.

Table 4 - 8: Pile mechanical properties considered in FE model

Component	Young's Modulus E_p (kN/m^2)	Poisson's ratio ν_p	Unit weight γ_p (kN/m^3)	Yield strength F_y (MPa)
Shaft- configurations A and B	1.69E08	0.28	77	314
Shaft - configuration C	2.0E08	0.28	77	370
Helix and base plates welded connections	2.0E08	0.28	77	170

4.6.1.4 Pile-Soil Interface Model

The pile-soil interface was simulated using the penalty-type tangential behavior Coulomb's frictional model. No relative tangential motion occurs until the surface traction reaches a critical shear stress value, which is taken as the lesser of the interface shear strength or a fraction of the interface pressure. Pile-soil interface strength is given by $\tan\delta = 0.78$ and 0.5 for tapered and straight piles, respectively. While the first was determined by studying the pile surface roughness in comparison to the soil mean particle size as mentioned in Chapter 3, the latter was considered in accordance to the suggested values by the Canadian Foundation Engineering Manual (2006). These values were calibrated with the axial tests results in Chapter 3. Slippage along the soil-pile interface was allowed.

4.6.1.5 Loading Sequence

An initial loading step of geostatic stresses and equilibrium was applied to consider the initial soil stresses, wishing the pile in. This was followed by a displacement-controlled analysis where the pile was subjected to monotonic compression loading. The compression loading was then reset followed by a displacement-controlled uplift applied to the pile at reference points rigidly connected to the top loading plates.

4.6.2 Results

4.6.2.1 Load-Displacement Curves

The uplift load testing conditions of PA2 and PC1 were simulated and the resulting load-displacement curves are presented in Figure 4 - 18. The agreement between the calculated and observed responses of the tested piles was good as shown in Figure 4 - 18.
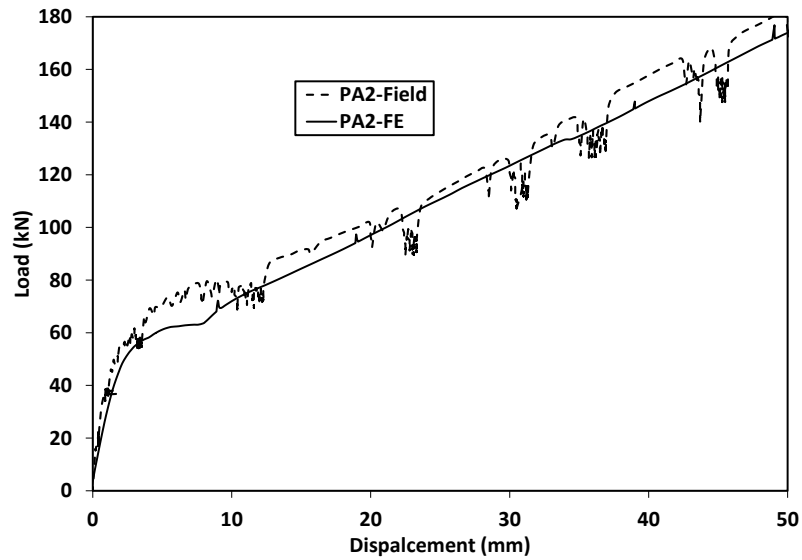
(a)
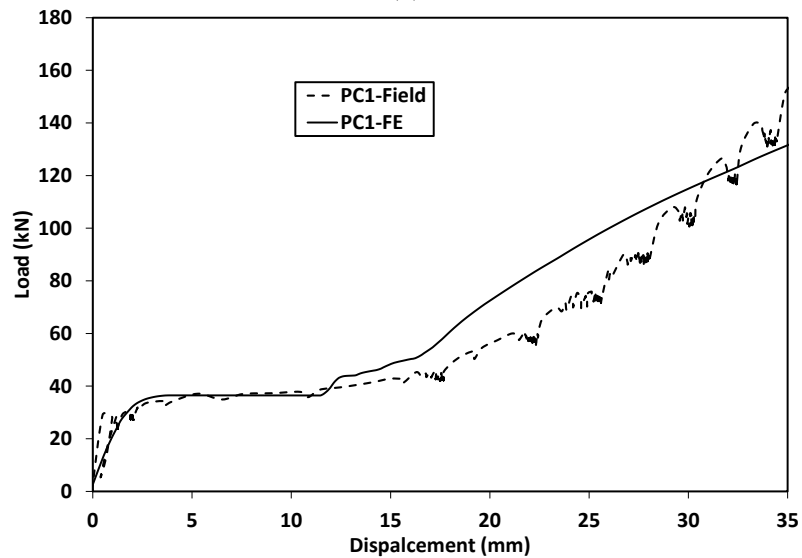
(b)

Figure 4 - 18: Calculated and measured load-displacement curves for a) PA2 and b) PC1

119

The matching process for the numerical model for PA2 under uplift loading yielded coefficient of earth pressure $K_s = 1.1$ (this was 2.0 for the case of compression loading as discussed in Chapter 3). On the other hand, $K_s = 0.85$ was obtained for PC1 (same as in compression).

In order to assess the contribution of the helix plate to the pile uplift resistance, a tapered pile with the same geometrical configuration and boundary conditions as PA2 however with no helix was analyzed. The load-displacement curve of the tapered pile without helix is compared with the response of PA2 in Figure 4 - 19. At low displacements (up to displacement = 0.5% of D_{helix}), where the shaft friction governs the resistance, both configurations exhibit the same behavior.
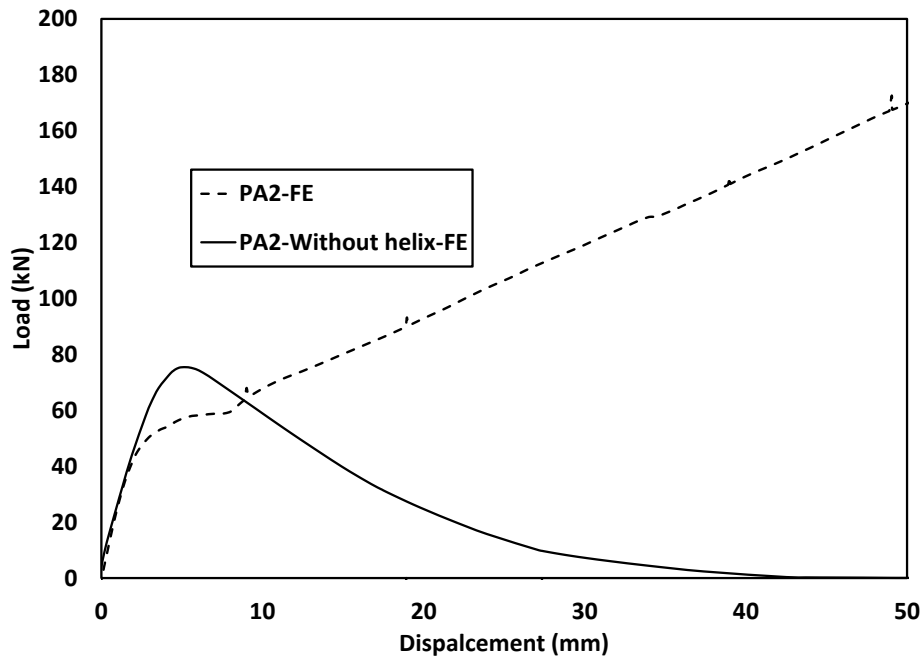
Figure 4 - 19: Load –displacement curves of PA2 with and without helix

As the displacement increased, PA2 with helix developed bearing resistance giving rise to a second segment of the load-displacement curve with different slope. On the other hand, the pile without helix continued with same slope approaching failure, in which case nonlinear behavior was exhibited followed by rapid reduction in the resistance as the

displacement continued to increase. The maximum shaft resistance in this case (74.5 kN) was reached at displacement = 1.2% D_{helix}.

4.6.2.2 Mobilized Shaft Resistance

Figure 4 - 21 demonstrates the mobilized shear stresses along the modeled piles for pile head displacement of 6.25mm for both uplift and compression loadings. The mobilized shaft stresses for the tapered profile under uplift loading are higher than those for the straight pile, but are significantly lower than those developed under compression. The mobilized stresses for the straight pile are essentially the same for uplift and compression loading cases.

Furthermore, during uplift loading for both configurations A and C, the shaft stresses just above the helix (up to 1.5 to 1.8 D_{helix}) were significantly higher than the rest of the shaft due to the flow of soil above the helix associated with the helix bearing pressure.

The soil displacement contours for piles configurations A and C at 5mm and 20mm displacement applied at the pile head are shown in Figure 4 - 20, due to the initial compressive loading followed by the uplift loading. The contours extended radially to a distance = 0.8 and 0.6 D_{helix} for configurations A and C, respectively. This demonstrates that the tapered pile engages more soil in resisting the load. The contours extend above the helix to a distance = 2.0 D_{helix}.

5mm displacement   20mm displacement

(a)

5mm displacement   20mm displacement
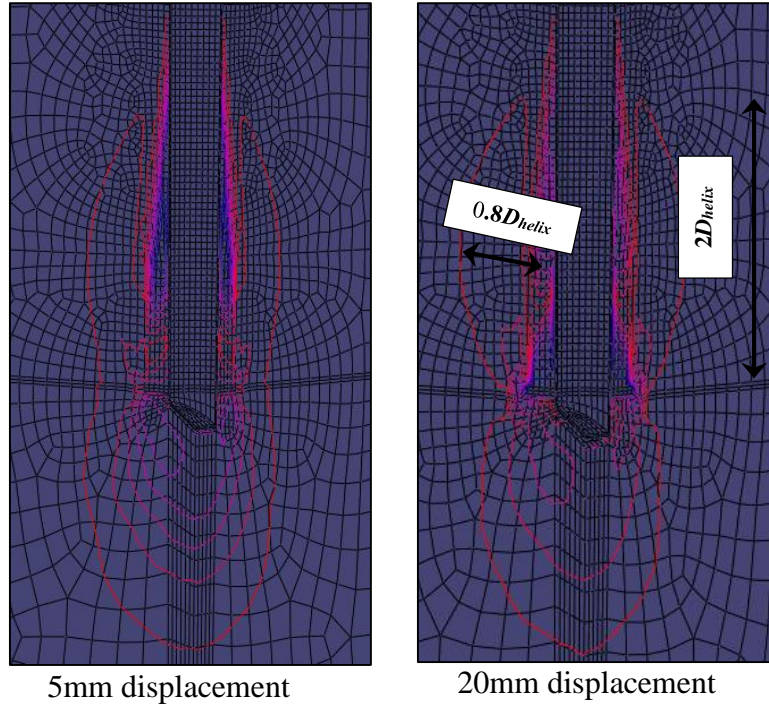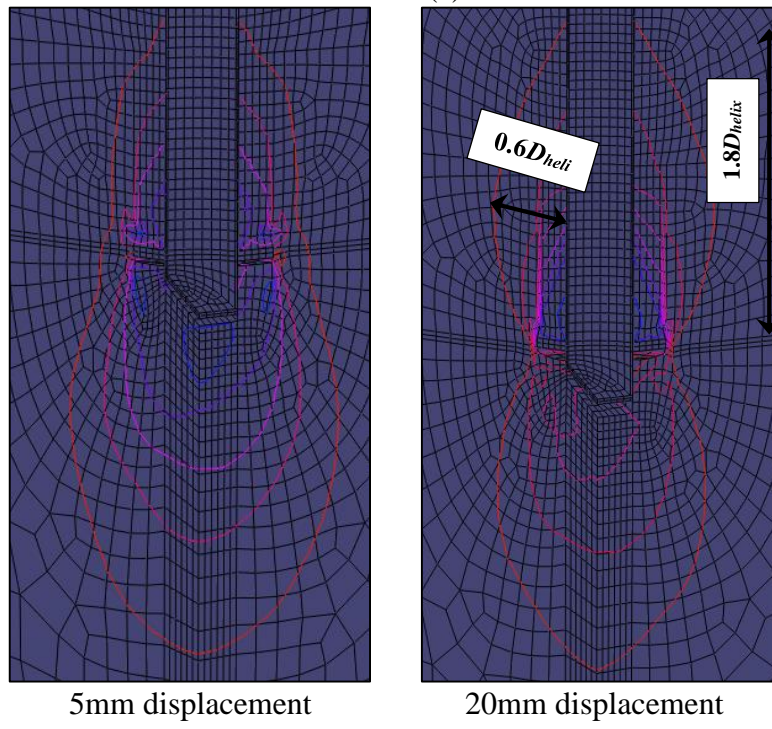
(b)

Figure 4 - 20: Soil displacement contours at pile uplift displacement of 5 and 20mm, a) Configuration A; and b) Configuration C

Finally, the numerical results showed that the shaft resistance contributed 59% and 20% of the pile uplift capacity for configurations A and C, respectively.
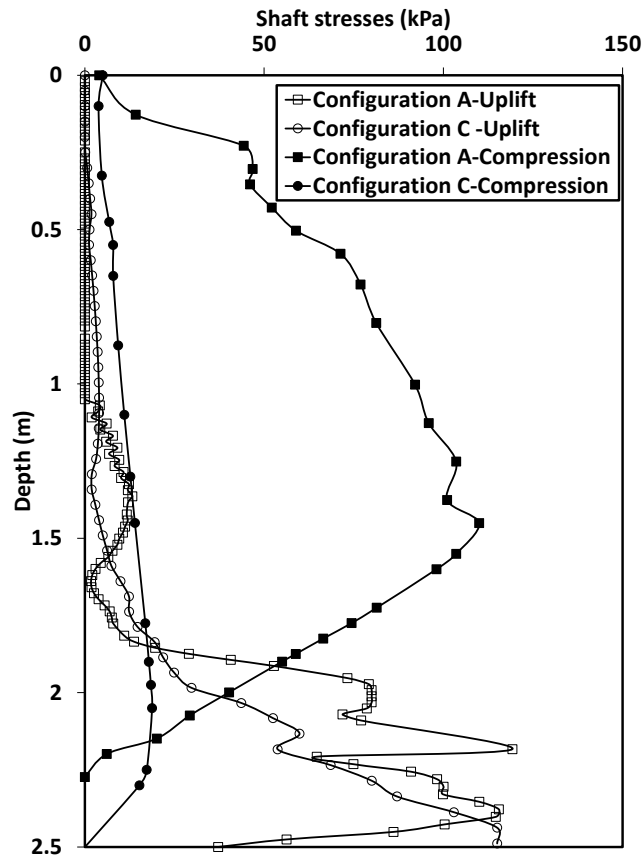
Figure 4 - 21: Developed shaft stresses at 6.25mm displacement for pile configurations A and C

4.6.2.3 Effect of pile length on uplift response

The uplift behavior of longer piles was also investigated. The responses of pile configurations D and E with geometry as presented in Figure 4 - 22 are calculated and compared with those for configurations A and C in Figure 4 - 23.
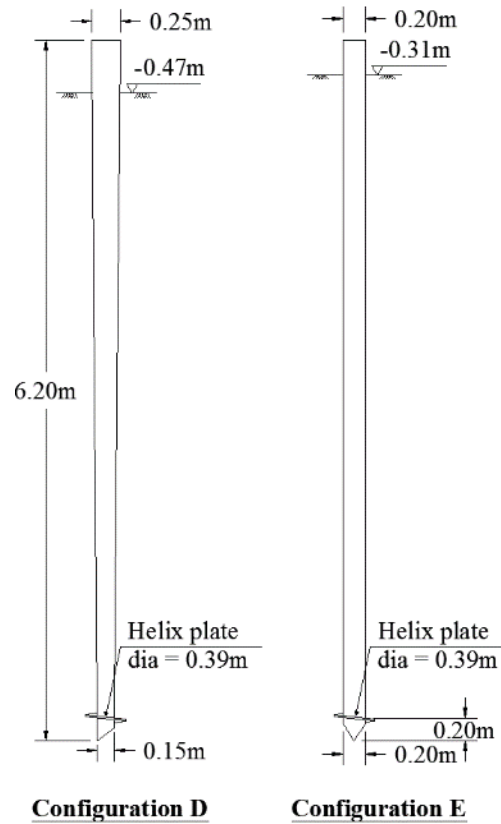
Figure 4 - 22: Piles of configurations D and E geometry

As expected, longer piles yielded higher capacities, especially the tapered pile. The uplift capacity corresponding to 6.25mm displacement of configurations D and E is 414 and 111kN, respectively. The uplift-to-compression capacity ratio reached 35% for configuration D compared to 22% for configuration E. It is also noted from Figure 4 – 25 that the effect of the slack zone is negligible for longer piles where the higher overburden pressure compensated for the disturbance effect.

The developed shaft stresses for configurations D and E at 6.25mm displacement are shown in Figure 4 - 24. The mobilized shear stresses reached 200 kPa for configuration D, i.e. same value as the maximum stress developed in compression (presented in Chapter 3).
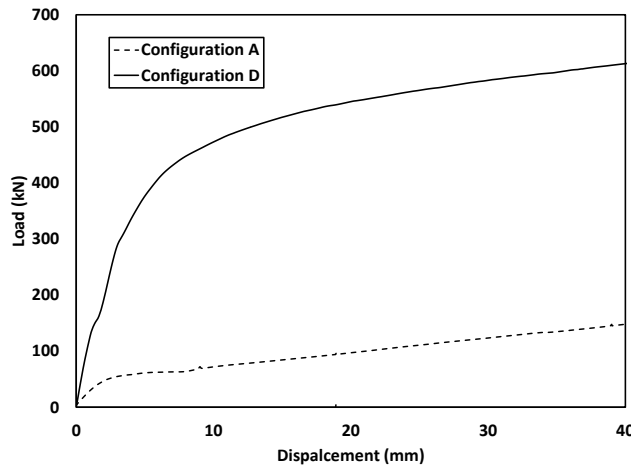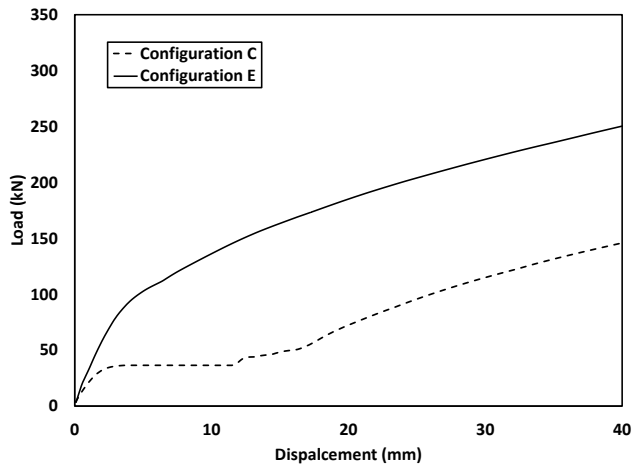
(a)   (b)

Figure 4 - 23: Load-displacement curves: a) Configurations A and D; and b) Configurations C and E
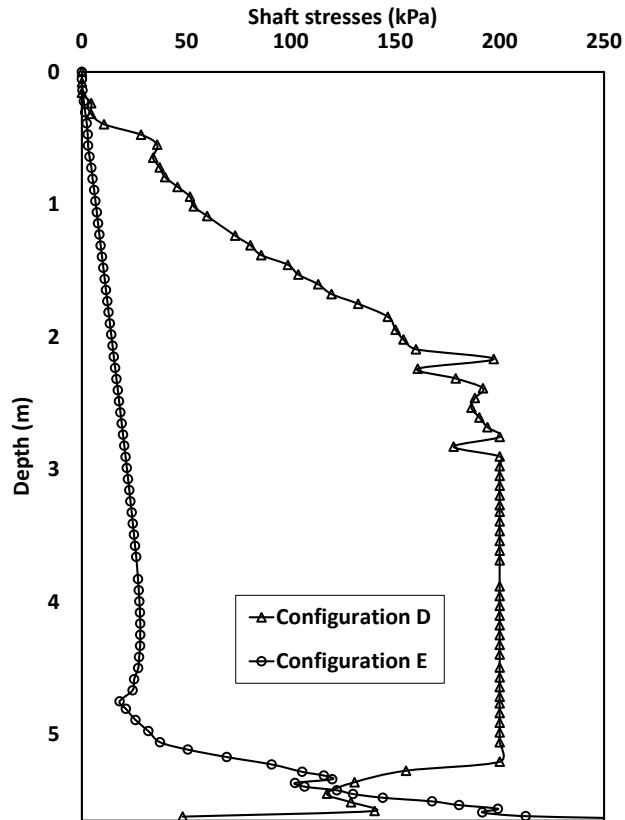
Figure 4 - 24: Developed shaft stresses at 6.25mm uplift displacement- Configurations D and E

It should be noted that several elements along the helix-pile connection yielded upon uplifting of configurations D and E (which is made of cast iron) as shown in Figure 4 - 25, hence thicker pile walls are recommended for this material to ensure its structural integrity when supporting higher uplift loads.

(a)   (b)
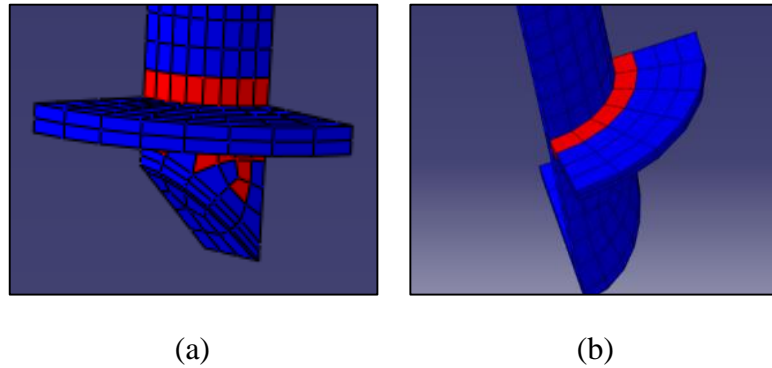
Figure 4 - 25: Yielded pile elements (a) Configuration D; and (b) Configuration E

4.7   Conclusions

The uplift performance of a novel ductile cast iron tapered helical pile system was investigated in this study. Seven piles were installed in silty sand and were subjected to static and cyclic uplift load tests. The test piles included five tapered helical piles with 2 different average diameters but same taper angle and two straight piles. A numerical investigation was also conducted. Two different loading sequences were applied to evaluate the effect of prior monotonic compression and cyclic uplift on the pile static uplift capacity. The results of the field and the numerical analysis are summarized here. The main conclusions drawn from this study are as follow:

1. The proposed helical tapered piles were found to offer higher stiffness at lower displacements. However, at higher displacements the straight piles displayed higher resistance.

2. The initial compression tests may result in a reduction of the stiffness at the start of the uplift loading.

3. For the tapered piles the uplift loading reduced the value of Ks compared to the higher value for the compression loading. This was not the case for the straight shaft piles.

4. The numerical results demonstrated that long tapered helical piles are expected to offer higher uplift resistance compared to the straight shaft helical piles. This however needs to be validated by experimental results.

5. The helical plate increased the uplift capacity of the tapered piles.

6. The cyclic uplift loading prior to the uplift monotonic tests eliminated the effect of gapping-cave in, and hence increased the developed shaft stresses at lower displacement.

4.8 References

AASHTO. 2002. Standard specifications for highway bridges. *HB-17.* American Association of State and Highway Transportation Officials.

ASTM C136. 2006. Standard test method for sieve analysis of fine and coarse aggregates. ASTM international.

ASTM D1556. 2007. Standard test method for density and unit weight of soil in place by the sand-cone method. ASTM international.

ASTM D2487. 2011. Standard practice for classification of soils for engineering purposes (Unified Soil Classification System). ASTM international.

ASTM D3080. 2011. Standard test method for direct shear test of soils under consolidated drained conditions. ASTM international.

ASTM D3689/D3689M. 2007. Standard test methods for deep foundations under static axial tensile load. ASTM international.

ASTM D4318. 2010. Standard test methods for liquid limit, plastic limit, and plasticity index of soils. ASTM international.

Bagheri, F. & El Naggar, M. H. Effects of the installation disturbance on the behavior of the multi-helix screw anchors in sands. GeoMontreal, 2013, Montreal.

Bowles, J. 1996. *Foundation analysis and design*, 5th edition, Mc-Graw hill.

CGS. 2006. *Canadian Foundation Engineering Manual*.4th edition. Canadian Geotechnical Society.

El Naggar, M. H. & Sakr, M. 2000. Evaluation of axial performance of tapered piles from centrifuge tests. *Canadian Geotechnical Journal,* 37(6), 1295-1308.

El Naggar, M. H. & Wei, J. Q. 2000. Uplift behaviour of tapered piles established from model tests. *Canadian Geotechnical Journal*, 37(1), 56-74.

Fuller, F. M. & Hoy, H. E. 1970. Pile load tests including quick load test method, conventional methods and interpretations. HRB 333, 78-86.

Ghaly, A. M. & Hanna, A. 1992. Stress and strains around helical screw anchors in sand. *Soils and Foundations,* 32(4), 27-42.

Hibbitt, H. D., Karlsson, B. I. & Sorensen, E. P. 2008. ABAQUS Standard user's manual. Pawtucket, R. I.: Hibbitt, Karlsson & Sorensen Inc.

Joshi, R. C., Achari, G. & Kaniraj, S. 1992. Effect of loading history on the compression and uplift capacity of driven model piles in sand. *Canadian Geotechnical Journal,* 29(2), 334-341.

Kodikara, J. & Moore, I. 1993. Axial response of tapered piles in cohesive frictional ground. *Journal of Geotechnical Engineering,* 119(4), 675-693.

Kong, G. Q., Yang, Q., Liu, H. L. & Liang, R. Y. 2013. Numerical study of a new belled wedge pile type under different loading modes. *European Journal of Environmental and Civil Engineering,* 17(sup1), s65-s82.

Kulhawy, F. H. & Mayne, P. W. 1990. Manual for estimating soil properties for foundation design. Ithaca, New York: Cornell University.

Mayne, P. W. In-situ characterization of Piedmont residuum in eastern US. Proc. US-Brazil: Application of Classical Soil Mechanics to Structured Soils, 1992, Belo Horizonte. National Science Foundation/USA, 89-93.

Mayne, P. W. 2006. In-situ test calibrations for evaluating soil parameters. Overview Paper on In-Situ Testing- Singapore Workshop.

Mayne, P. W., Christopher, B. & Dejong, J. 2002. Manual on subsurface investigations—Geotechnical site characterization. Washington, DC.: Federal highway administration, U.S. Department of Transportation.

Mayne, P. W. & Kulhawy, F. H. 1982. Ko-OCR Relationships in Soil. *Journal of the Geotechnical Engineering Division,* 108(6), 851-872.

Meyerhof, G. G. 1976. Bearing capacity and settlement of pile foundations. *Journal of the Geotechnical Engineering Division,* 102(3), 195-228.

Mitsch, M. P. & Clemence, S. P. The uplift capacity of helix anchors in sand. In uplift behavior of anchor foundations in soil: Proceedings of a session sponsored by the Geotechnical Engineering Division of the American Society of Civil Engineers in conjunction with the ASCE convention in Detroit, 1985, New York. ASCE, 26-47.

O'Neil, M. W. 2001. Side resistance in piles and drilled shafts. *Journal of Geotechnical and Geoenvironmental Engineering,* 127(1), 3-16.

Perko, H. 2009. *Helical piles: A practical guide to design and installation,* New Jersey, John Willey and Sons Inc.

Poulos, H. G. & Davis, E. H. 1980. *Pile foundation analysis and design*, John Wiley and Sons.

Sakr, M., El Naggar, M. H. & Nehdi, M. 2005. Uplift performance of FRP tapered piles in dense sand. *International Journal of Physical Modelling in Geotechnics,* 5(2), 01-16.

Sharma, H. D., Sengupta, S. D. & Harron, G. 1984. Cast-In-Place bored piles on soft rock under artesian pressure. *Canadian Geotechnical Journal,* 21(4), 684-698.

Skempton, A. W. 1986. Standard penetration test procedures and the effects in sands of overburden pressure, relative density, particle size, aging, and over-consolidation. *Geotechnique,* 36(3), 425-447.

Trofimenkov, J. G. & Maruipolshii, L. G. Screw piles used for mast and tower foundations. Proceedings of the 6th International Conference on Soil Mechanics and Foundation Engineering Conference on Soil Mechanics and Foundation Engineering, 1965, Montreal. 328-332.

Tsuha, C. H. C., Aoki, N., Rault, G., Thorel, L. & Garnier, J. 2012. Evaluation of the efficiencies of helical anchor plates in sand by centrifuge model tests. *Canadian Geotechnical Journal,* 49(9), 1102-1114.

Wei, J. & Naggar, M. H. E. 1998. Experimental study of axial behaviour of tapered piles. *Canadian Geotechnical Journal,* 35(4), 641-654.

Zhan, Y-G., Wang, H. & Liu, F-H. 2012. Numerical study on load capacity behavior of tapered pile foundations. *Electronic Journal of Geotechnical Engineering,* 17, 1969-1980.

Zhang, D. J. Y. 1999. Predicting capacity of helical screw piles in Alberta soils. *MSc thesis.* Edmonton, Alberta: University of Alberta.

Zil'berberg, S. D. & Sherstnev, A. D. 1990. Construction of compaction tapered pile foundation, (from the experience of the Vladspetsstroi Trust). *Soil Mechanics and Foundation Engineering,* 27(3), 96-101.

MONOTONIC LATERAL PERFORMANCE OF SCDI HELICAL TAPERED PILES IN SAND

5.1 Introduction

While almost all pile foundations are prone to some lateral load component (Fleming *et al.*, 2009), that component could be considerably large in cases such as offshore structures, transmission towers and high rise buildings. Tapered piles have been successfully used for many years as an efficient piling system in supporting axial loads capacity (El Naggar and Wei, 1999). In their experimental investigation, El Naggar and Wei (1999) reported that tapered piles installed in cohesionless soils exhibited stiffer response than cylindrical piles at various load levels with more pronounced effects at low confining pressures. They also reported an increase in capacity as high as 77% for a pile taper angle as small as 0.95º.

Owing to their geometry, tapered piles provide an efficient material distribution and have greater flexural rigidity at their top portion, and hence increased lateral stiffness. Sakr *et al.* (2005) investigated the lateral performance of FRP composite tapered piles driven using a novel toe-driving technique. The tested composite tapered piles exhibited a stiffer response and larger lateral resistance compared to conventional driven piles. Considering the ultimate load criteria suggested by (Prakash and Sharma, 1990), the lateral capacity of tapered piles was found to reach up to 200% of the capacity of a cylindrical pile of the same average diameter (Sakr *et al.*, 2005).

Helical piles are gaining wide popularity fuelled by recent advances in construction equipment, which allow further development of these piles, and facilitate their application in projects that subject them to unique and complex loading conditions. Different helical pile systems with large diameter shafts were developed recently offering large lateral capacities (Elkasabgy, 2011; Fleming *et al.*, 2009).

Helical piles are easy to install with low levels of noise and vibration. However, their installation can cause disturbance of the adjacent soil within the zone affected by the penetration of the pile shaft and helices, thus reducing the soil shear strength and consequently, the pile shaft capacity (axial and lateral) is significantly reduced (Bagheri and El Naggar, 2013). The lateral load resistance of long helical piles can be generally estimated using the same techniques adopted for cylindrical piles; however, the installation effects need to be considered in choosing suitable design soil parameters (Puri *et al.*, 1984).

The presence of helical plates at shallow depth can increase the pile's lateral capacity. Prasad and Rao (1996) experimentally studied the lateral response of helical piles in clay. They found that their lateral capacity is generally equal to 1.2 to 1.5 times that of a straight shaft with no helical plates. In addition to the shaft resistance, the developed bearing/uplift resistance on the front/back half of the helical plates once rotated and the friction on the plates' surfaces contribute to the lateral resistance (Prasad and Rao, 1996). For helical piles with helices placed at greater depths, however, the lateral performance is mainly controlled by the pile shaft (Puri *et al.*, 1984). For conservative design purposes, the contribution of the helical plates to the pile lateral capacity is usually neglected (Perko, 2009).

This chapter examines the lateral behavior of an innovative pile that combines the efficiency of the tapered section and the construction advantage of helical piles.

5.2   Objectives and scope of work

The novel piling system investigated in the current study consists of a spun-cast ductile iron tapered pile (Seamless-Pole-Inc., 2010) fitted with a lower helical plate to facilitate its installation. The proposed pile is to be installed using a mechanical torque delivered by a driving motor holding the pile head. The system offers increased lateral capacity and enhanced lateral performance due to the larger section along the upper portion of the pile shaft.

A comprehensive investigation was conducted in order to assess the feasibility and efficiency of the proposed system. It involved field load tests and three-dimensional finite element analyses using the commercial software ABAQUS (Hibbitt *et al.*, 2008). The

lateral performance of the proposed pile under monotonic and cyclic loading was evaluated. In addition, the measurements from the field load tests and the results of the numerical analyses were employed to evaluate the soil reactions to the proposed pile deflections. The results of the monotonic tests are only presented in this chapter.

5.3 Experimental setup

5.3.1 Soil investigation

One borehole was drilled in the vicinity of the test piles at the location shown in Figure 5 - 1. The borehole log shows that the soil profile comprises silty sand/gravelly sand layers that extend from the ground surface to 9.00m below ground surface, followed by a hard silty till that extends to the end of the borehole (i.e. 11m depth). The ground water table was found at 3.5m from the ground surface.
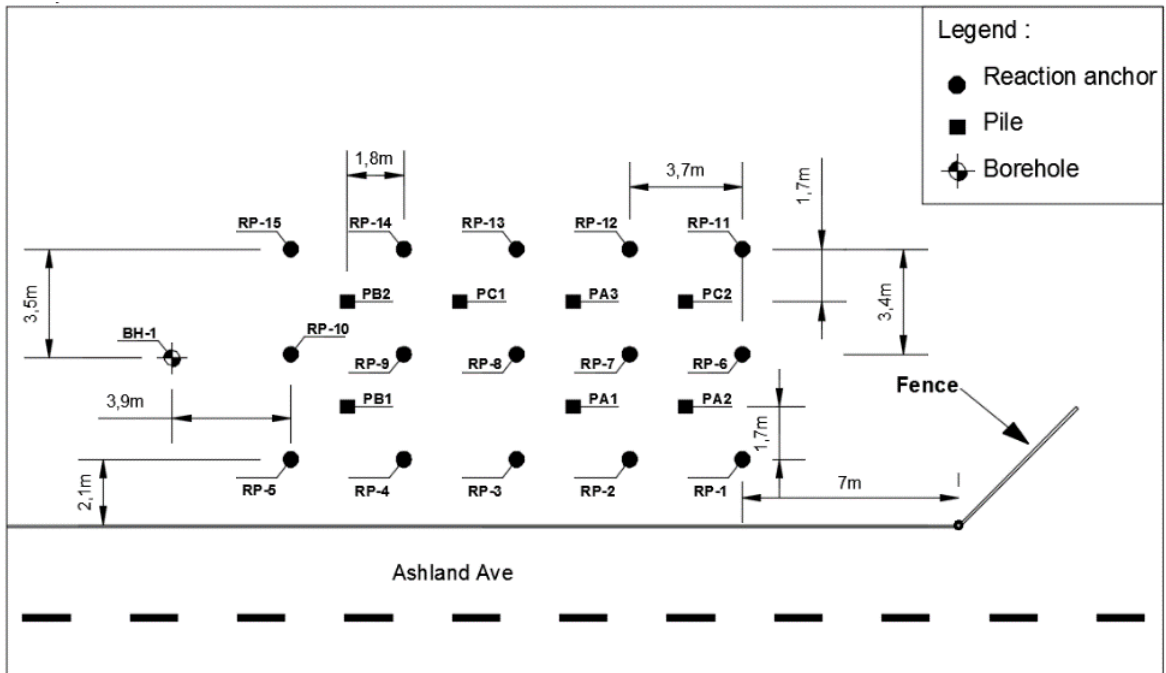
Figure 5 - 1: Site layout showing the drilled borehole location

5.3.1.1 Field tests

A Standard Penetration Test (SPT) was conducted with blow count measurements taken at 0.75m intervals. These values were corrected for hammer energy efficiency and other field procedure conditions to obtain N_{60}, i.e. (Skempton, 1986)

N_{60}=Measured number of blows x $\dfrac{C_R C_S C_B E_m}{0.6}$ $\qquad\qquad$ **(5 - 1)**

where*:*

C_S is sampler correction, equal to 1.2 where sampler without liner was used

C_R is drill rod length correction, equal to 1 at depths greater than 10m and 0.75 for depths less than 4m

C_B is borehole diameter correction, equal 1.15 for diameter D=200mm

E_m is hammer efficiency, equal to 0.8 for hammer used (Bowles, 1996)

These values were then corrected for the overburden pressure producing N_{60}', i.e., (Liao and Whitman, 1986)

$$N'_{60} = N_{60} \sqrt{\frac{100}{\sigma'_v}} \qquad\qquad \textbf{(5 - 2)}$$

where σ'_v is the effective overburden stresses

The resulting variation of N'_{60} with depth along the top 4m of main interest in this study is presented in Figure 5 - 2.
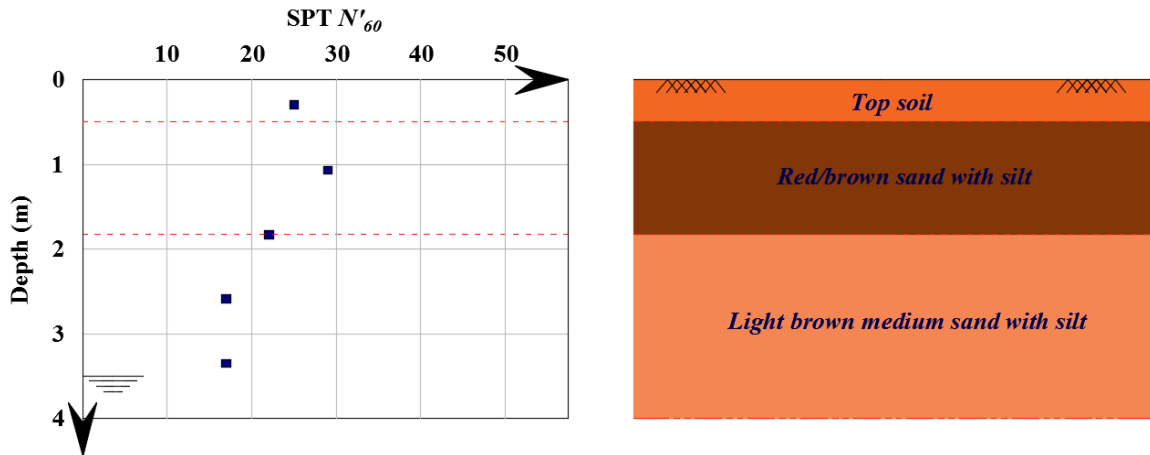
Figure 5 - 2: Variation of SPT N'_{60} with depth

The sand-cone test (ASTM D1556, 2007) was employed to measure the soil in-situ unit weight. The top 0.5m of soil was excavated, and two sand-cone tests were performed on the underlying layer. The average measured bulk density was 16.5kN/m^3.

5.3.1.2 Laboratory testing

Fifteen disturbed samples retrieved from the SPT split-spoon sampler were transported and subjected to various laboratory tests at The University of Western Ontario soils laboratory. The tests included soil classification, determination of the specific gravity, G_S, measurement of water content, W_c, direct shear tests and Atterberg limit determination.

Soil classification and index properties

Sieve analyses of the extracted samples at different depths were performed according to ASTM C136 (2006). The resulting gradation curve is shown in Figure 5 - 3.

The tested piles were only 3.1m long, with an even shorter effective embedment depth due to their free length. Thus, only the top 4m of soil affect the pile response to lateral loads. The classification curve showed that the soil within that depth has only 14.8% fines and almost 0% gravel. Atterberg limits of three samples were measured showing average liquid and plastic limits of 25.3% and 21.5%, respectively (ASTM D4318, 2010). The top layer

is thus classified as silty sand (SM) according to the Unified Soil Classification System USCS (ASTM D2487, 2011). Lower percentages of fines were found at deeper layers and higher percentages at the bottom of the borehole. The average measured G_s of two soil samples extracted at depths of 1.05m and 4.8m was found to be 2.71. The average in-situ W_c was measured to be 20.5%.
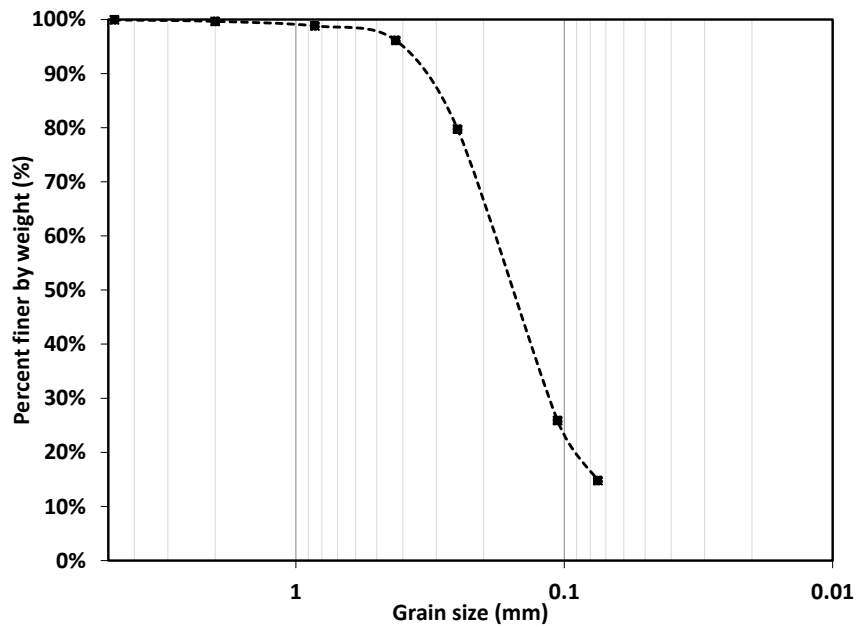
Figure 5 - 3: Grain size distribution for disturbed sample retrieved at 1.05m below the mean ground level

Soil shear strength parameters

Direct shear tests (ASTM D3080, 2011) were conducted on soil specimens retrieved at 0.6m and 1.08m depths in order to determine their shear strength parameters. The horizontal rate of feed was 0.406mm/min. The unit weight of the tested specimens within the direct shear box was set to the field measured unit weight. The variation of shear stresses with normal stresses, vertical displacement and horizontal displacement as well as the residual and peak strength values are presented in Figure 5 - 4. A bilinear shear-normal stress relation was observed with the first section ending at a normal stress of 20 kPa. Based on the direct shear test results, the effective cohesion, c', residual angle of internal friction $\varphi_{residual}$ and peak angle of internal friction φ_p were determined to be 4 kPa, 32° and 38°,

respectively. The determined angle of internal friction lies within the upper bound of the relevant range typically found in the literature for the range of SPT values at the location of test specimen, due to the high angularity of the sand particles (Bowles, 1996).

(a)

(b)

137

(c)
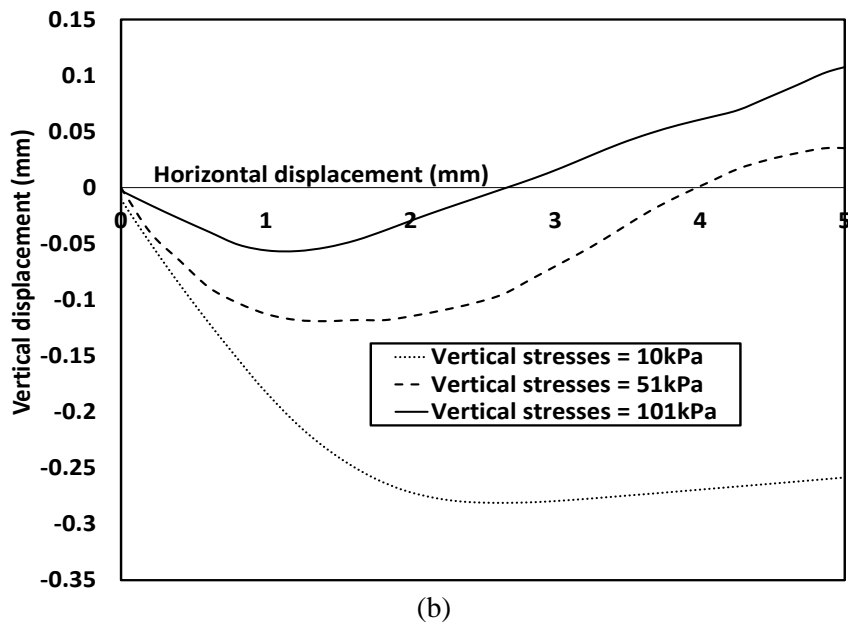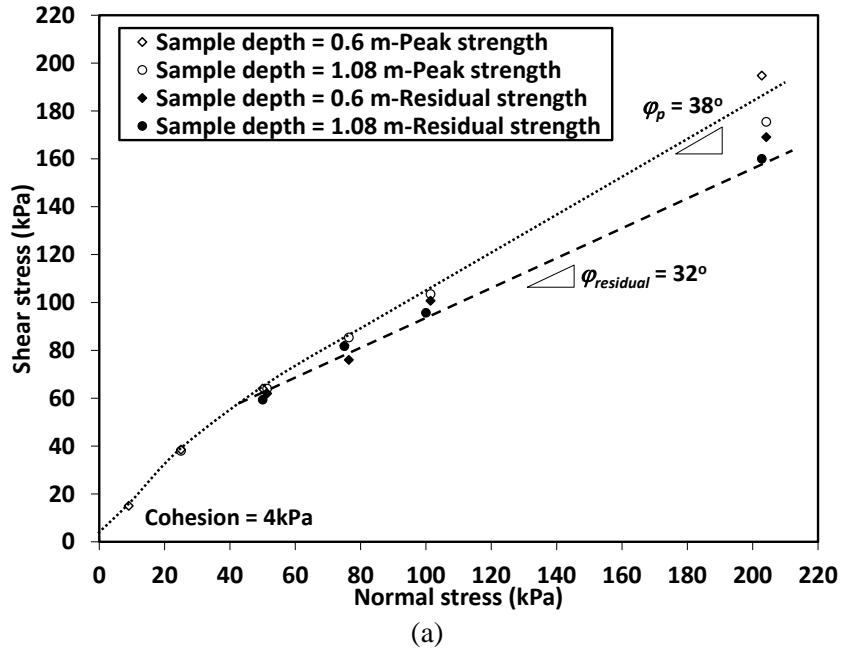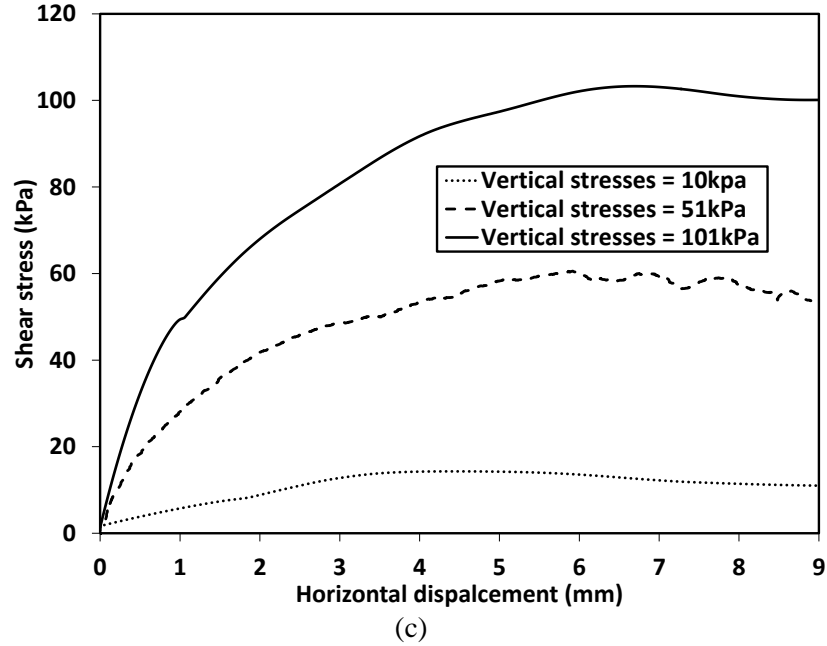
Figure 5 - 4: Direct shear tests results (a) Shear vs normal stresses; (b) Vertical displacement vs horizontal displacement; (c) Shear stress vs horizontal displacement

Relative density and stiffness parameters

The soil relative density D_r, Young's modulus E_s, and Poisson's ratio ν were correlated to the corrected N values. For example, D_r was correlated to the corrected N'_{60}, i.e.(Mayne *et al.*, 2002):

$$D_r = 100 \sqrt{\frac{N'_{60}}{60}} \qquad (5 - 3)$$

The variation of D_r along the top 4m ranges between 50 to 70%, hence, the soil deposits along the pile length can be classified as medium dense to dense sand (Bowles, 1996).

In absence of undisturbed soil samples, the over-consolidation ratio, OCR, is generally correlated to other parameters or test results. The apparent preconsolidation pressure σ_p' for the Sand was correlated to N_{60}, i.e.,(Mayne, 1992.):

$$\sigma_p' = 0.47 \ (N_{60})^m \ Pa \qquad (5 - 4)$$

where P_a is the atmospheric pressure, $m = 0.6$ to 0.8 for silty sands/sandy silts (Mayne, 2006).

138

The variation of σ_p' with depth was obtained employing Eq. 5 – 4 and knowing the initial overburden stresses, the OCR was calculated to be approximately 6 for the top 4 m. This is attributed to the fact that the site is used for storage of heavy steel tanks.

Although several correlations have been developed for soil elastic modulus, E_s, and the measured SPT, a significant scatter exists between the different correlations. For overconsolidated sand, E_s can be correlated to the corrected SPT N_{60}, i.e.(Kulhawy and Mayne, 1990):

$$E_s/Pa = 15N_{60} \tag{5 - 5}$$

It should be noted, however, that the post–installation values are of main interest to this study. For that, and as a preliminary estimation, the recommended values by Poulos and Davis (1980) for driven piles in sand were considered. They suggested that, while E_s for sand typically varies with depth, it is appropriate for analysis purposes to consider an average modulus value along the pile shaft and greater values below the toe of driven piles (Poulos and Davis, 1980). This is also acceptable considering the relatively short length of the piles in the present study. Average values suggested by Poulos and Davis were in the order of 55~70MPa for medium dense sand and 70~100MPa for dense sand layers. Accordingly, an average E_s of 70MPa was considered for the current soil profile.

The value of ν ranges between 0.2 to 0.4 for loose to dense Sands (AASHTO, 2002) hence 0.3 will be considered.

Finally, considering the average OCR of 6 along the first 4m, the average coefficient of earth pressure at rest prior to the pile installation can be given by (Mayne and Kulhawy, 1982):

$$K_{o\text{-}OC} = (1\text{-}Sin\varphi)OCR^{(1\text{-}sin\varphi)} = 0.76 \tag{5 - 6}$$

It should be noted that the soil properties obtained from the laboratory tests represented the soil state prior to the piles installation therefore neglecting the effects of pile installation torque, the top soil predrilling prior to the piles installation as well as the axial load tests performed before the lateral ones. The representative soil parameters are summarized in

Table 5 - 1. These representative soil parameters were numerically calibrated and validated employing the axial field test results as described in Chapters 3 and 4.

Table 5 - 1: Representative soil parameters

Depth (m) From	To	φ_p (°)	c´ (kPa)	Specific gravity G_s	Water content (%)	ν	E_s (MPa)	γ (kN/m³)	D_r (%)
0	0.5	36	4	2.71	20.5	0.3	70	16.5	55
0.5	4	38							

5.3.2 Test piles

Seven hollow closed-end piles with configurations as shown in Figure 5 - 5 were installed using torque. Three piles were of configuration A, two of configuration B and two of configuration C. The piles of configurations A and B were made of ductile iron with rough surface as shown in Figure 5 - 6. Configuration C piles were made of straight shaft steel pipe, which was considered for comparison purposes. The wall thickness of all piles was 5.5mm.
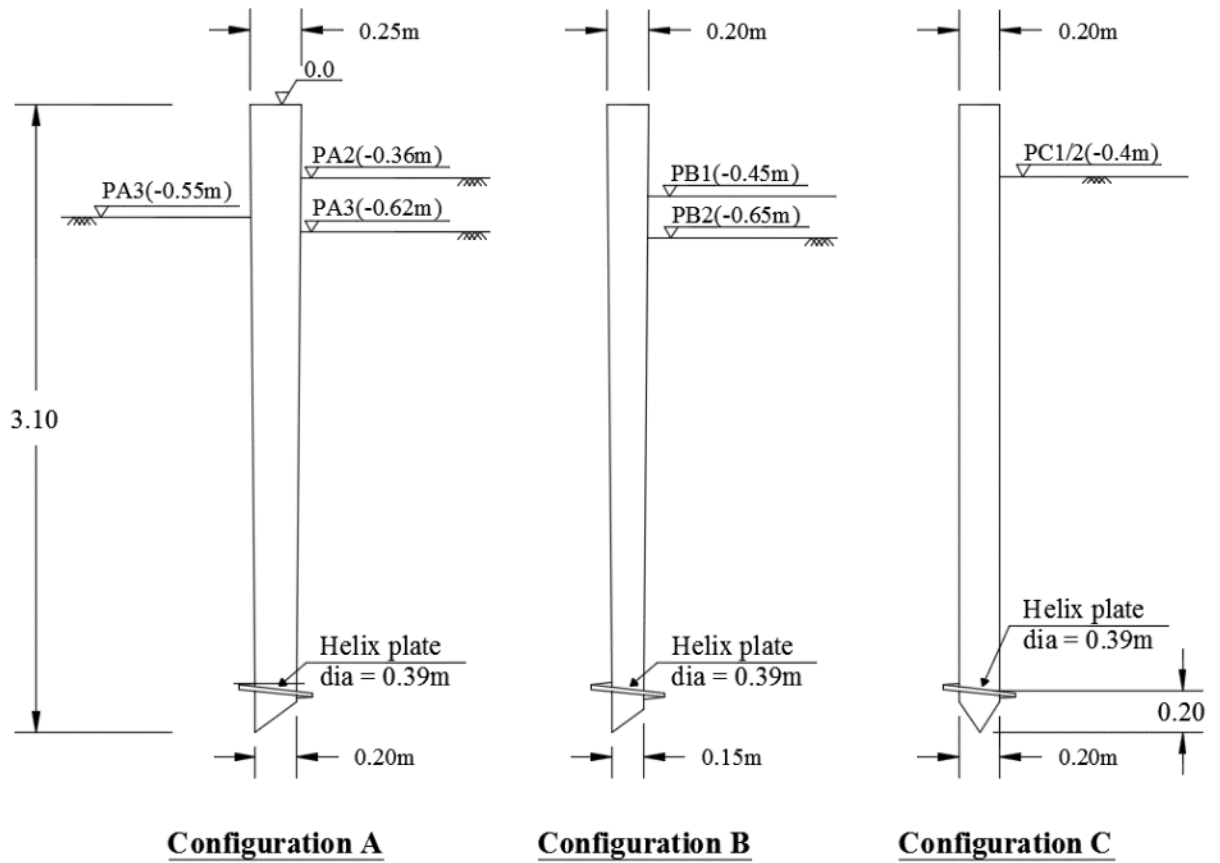
Figure 5 - 5: Tested piles configurations

Figure 5 - 6: Image of the piles external surface –configurations A and B (Seamless-Pole-Inc., 2010)

5.3.3 Instrumentation and test setup

A special setup was designed and fabricated to apply the lateral loading to the piles, which involved loading two piles against each other as shown in Figure 5 - 7. In this setup, the load was transferred to the piles through steel clamps connected to a main loading rod by a hinged connection ensuring a free head condition. Clamps with different diameters were manufactured to fit the different test piles configurations. The applied load was measured using a load cell incorporated into the loading setup as demonstrated in Figure 5 - 7.
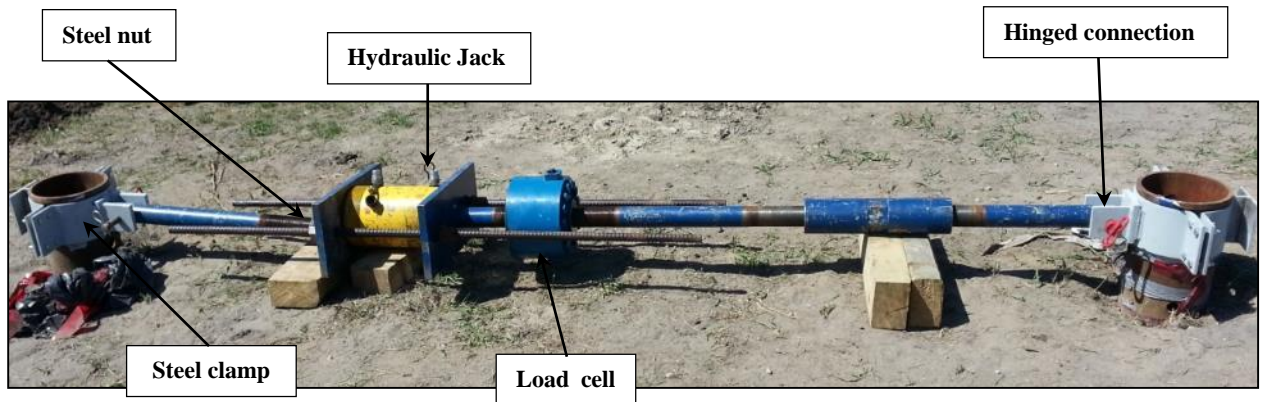
(a)
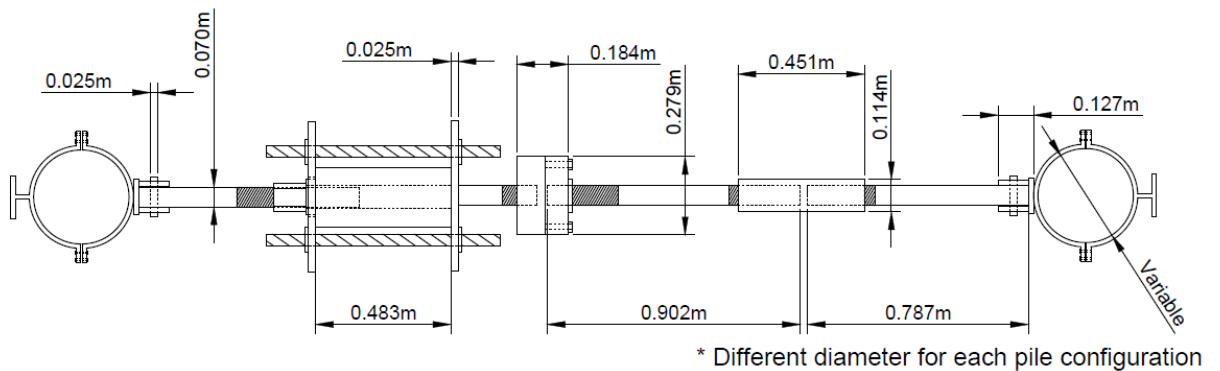
(b)

Figure 5 - 7: Lateral loading setup (a) Image of setup; (b) Dimensions of different components

In order to measure the pile head displacement, two linear variable displacement transducers (LVDTs) were supported on an independent beam and their measuring tips were pushing against a steel plate attached to the pile head as shown in Figure 5 - 8. An additional smaller size LVDT was fixed against each pile inner wall at 0.92m below the pile head to monitor the deflection at that level. The LVDTs and load cell were connected to a data acquisition system, which recorded the readings every 1 second.

(a)   (b)

Figure 5 - 8: Lateral load setup components (a) steel clamp/LVDT plate, (b) clamp-rod connection

5.3.4 Installation procedure

To ensure the piles integrity during installation, finite element (FE) models were developed considering the different piles configurations and material properties to determine the torque capacity of each pile configuration. The FE models considered the pile to be subjected to the torque at its head and full fixation at its toe with no soil along its shaft. This condition represented the upper bound for the shear stresses developed in the pile cross-section due the installation torque. The calculated maximum torque (capacity) of configurations A, B and C are 58, 32 and 68.5kN.m, respectively. The mechanical torque head used was a Hitachi UH07 rig, and the torque was applied through a specially manufactured steel cap bolted to the pile head as shown in Figure 5 - 9. The cap was then removed before the start of the lateral testing.

(a)

(b)
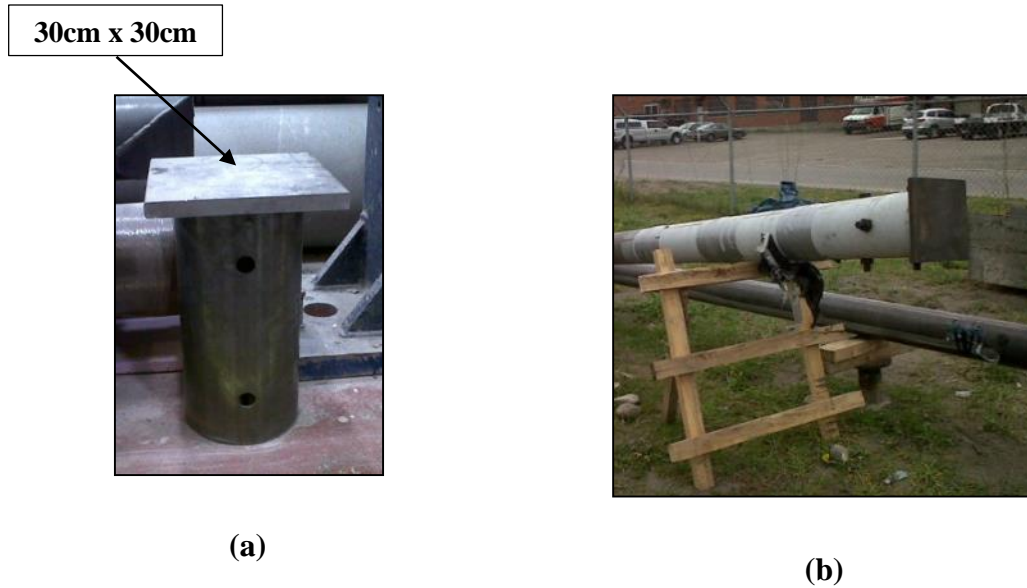
Figure 5 - 9: Field images (a) loading cap, (b) cap-pile connection

Following installation, the inclination angle of the pile head with the vertical axis was measured to examine the piles verticality. The maximum inclination angle measured was less than 2°. The piles free (unsupported) lengths at the start of lateral loading are shown in Table 5 - 2.

Table 5 - 2: Pile head elevation above ground surface

Pile #	Pile head elevation above the ground surface (m)
PA1	0.55
PA2	0.36
PA3	0.62
PB1	0.65
PB2	0.45
PC1	0.40
PC2	0.40

5.3.5   Load test sequence and test procedure

The lateral load tests were conducted on pairs of piles. The sequence of load tests is presented in Table 5 - 3. It should be noted that prior to the lateral load tests, the piles were subjected to static and cyclic axial load tests as reported in Chapters 3 and 4.

Table 5 - 3: Lateral pile test setups

Test setup #	1st pile	2nd pile	Notes
1	PA1	PA2	
2	PA3	PC1	
3	PB1	PB2	
4	PA3	PC2	PA3 was previously tested in setup#2

The piles were loaded monotonically first, followed by two-way cyclic load test. The piles were then loaded monotonically again to evaluate the effect of cyclic loading on their lateral capacity. The monotonic loads were applied in equal increments of 5 kN, each increment maintained for 5 minutes. The cyclic loading encompassed two-way load cycles with increments of 5 kN. At each load increment, 5 full cycles were applied and each load cycle was applied over 30 seconds. The maximum amplitude of cyclic load considered was 35 kN. The pile load testing patterns are illustrated in Figure 5 - 10.
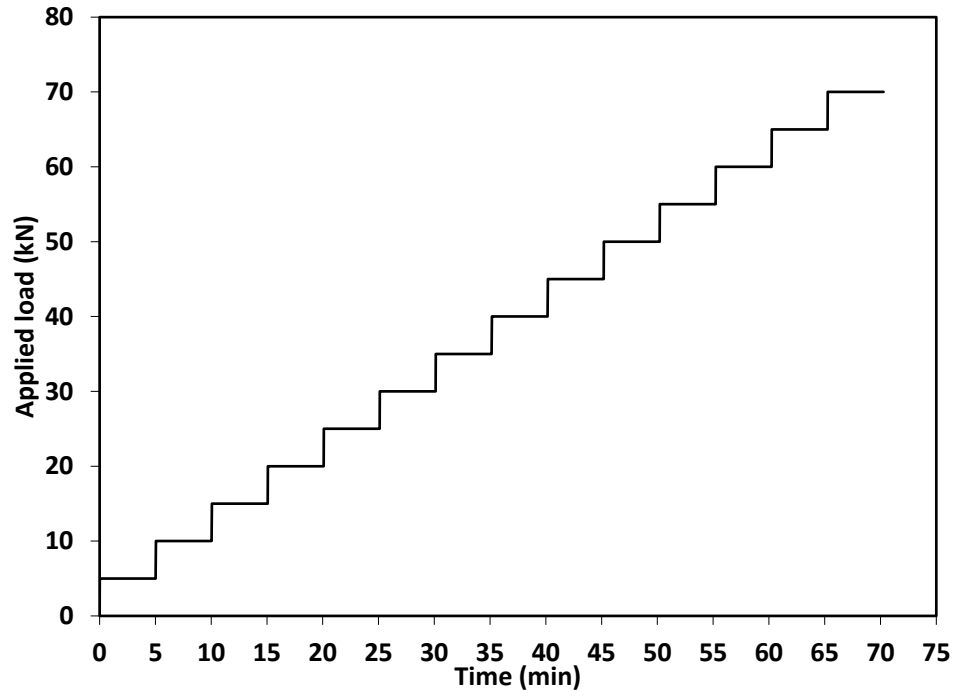
(a)
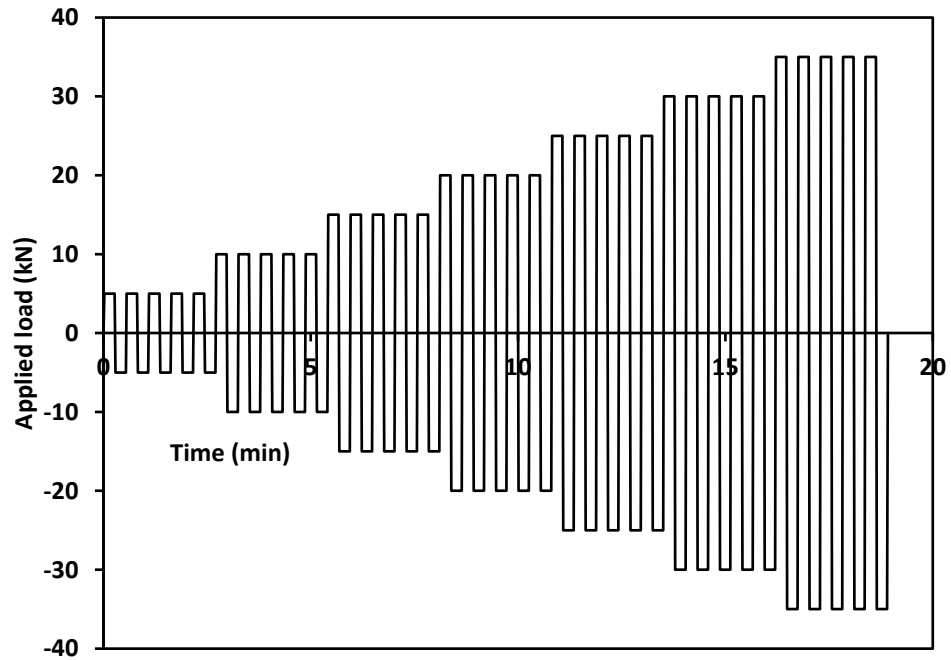
(b)

Figure 5 - 10: Lateral pile loading test patterns (a) Monotonic tests; (b) Cyclic tests

5.4   Results and discussion

5.4.1   Load-deflection curves

The measured load-deflection curves for the piles are presented in Figure 5 - 11 and Figure 5 - 12. Generally, all piles exhibited a stiff behavior with minor non-linear plastic zone and no clear global failure/plastic zone until the termination of the test. This behavior is attributed to the high flexural rigidity of the pile, the rough pile surface and the helix passive resistance.

Figure 5 - 11 presents the results for initial monotonic load tests (before lateral cyclic loading). It is noted that the load-deflection curves are hyperbolic in shape but no sign of failure up to the end of the tests. The performance of the tapered piles of configuration A was better than the piles of configurations B and C in terms of stiffer behavior and higher capacity. The only exception is setup#4 where PA3 showed softer behavior than PC2 because PA3 was tested first in setup#2, which might have resulted in soil failure and hence its strength was characterized by residual strength rather than the peak strength. It can also be noted from Figure 5 - 11 that, in general, tapered piles performed better than straight shafts, especially at higher lateral load levels. At lower load levels, the behavior is believed to be governed by the fixation provided by the helix plate whereas at greater level of loads the pile diameter/stiffness governs the behavior.

Piles of configuration B exhibited softer response than configuration C because they were subjected to uplift loading prior to lateral loading, and the piles were lifted up for more than 20cm hence releasing the initial lateral confinement of the pile surrounding soil and reducing its lateral resistance and increasing the unsupported length of the pile at the start of the lateral test as shown in Table 5 - 2. In addition, the helical plates of piles configuration B were cracked/broken during the uplift loading as observed upon retrieving the piles after test completion.

147
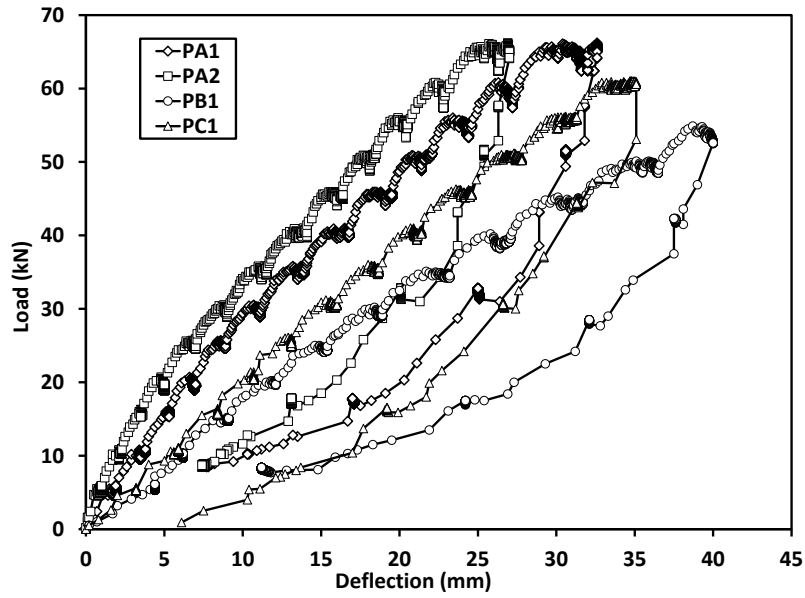
(a)
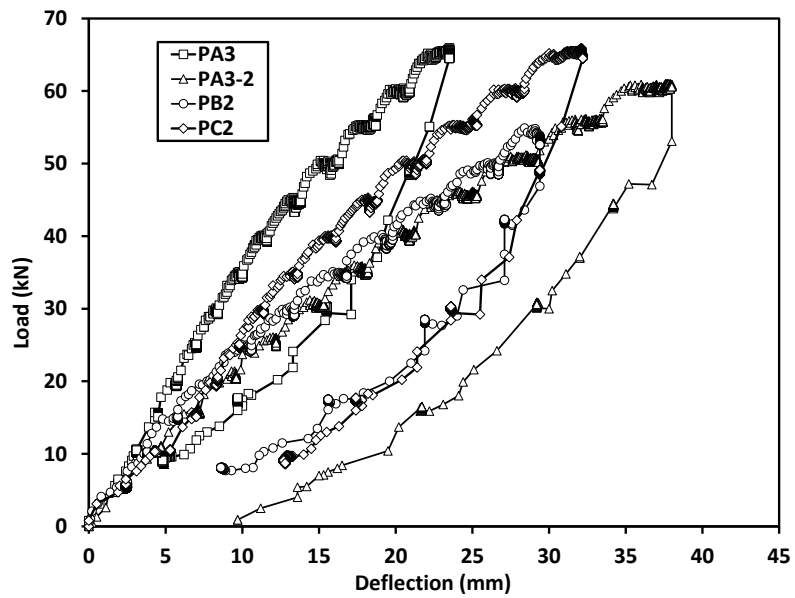
(b)

Figure 5 - 11: Load-deflection curves before cyclic lateral load tests: (a) Piles tested in axial compression before lateral loading; (b) Piles tested in uplift before lateral loading

148

Figure 5 - 12 presents the load-deflection curves for monotonic load tests conducted after the cyclic lateral load tests. The curves exhibit an initial lower stiffness segment due to the loosening of the sand in the vicinity of the pile, and even gap opening, during the cyclic loading. The stiffness reduction (softening) due to gapping was also reported by Pender and Pranjoto (1996) for piles subjected to cyclic lateral loading. An image of the gap formed behind pile PC1 is shown Figure 5 - 13. As the load progressed, the loose caved-in sand was re-compressed/gap closed and the stiffness increased again (i.e. strain hardening) as discussed by Allotey and El Naggar (2008). As the load continued to increase, the soil displayed nonlinear behavior and the pile stiffness started to decrease again.

While initially configuration C piles showed softer behavior than configuration A piles as shown in Figure 5 - 11, the higher degradation effect during the cyclic loading of the latter configuration compared to configuration C piles as further discussed in Chapter 7 resulted in the opposite behavior when tested following the cyclic tests as shown in Figure 5 - 12.
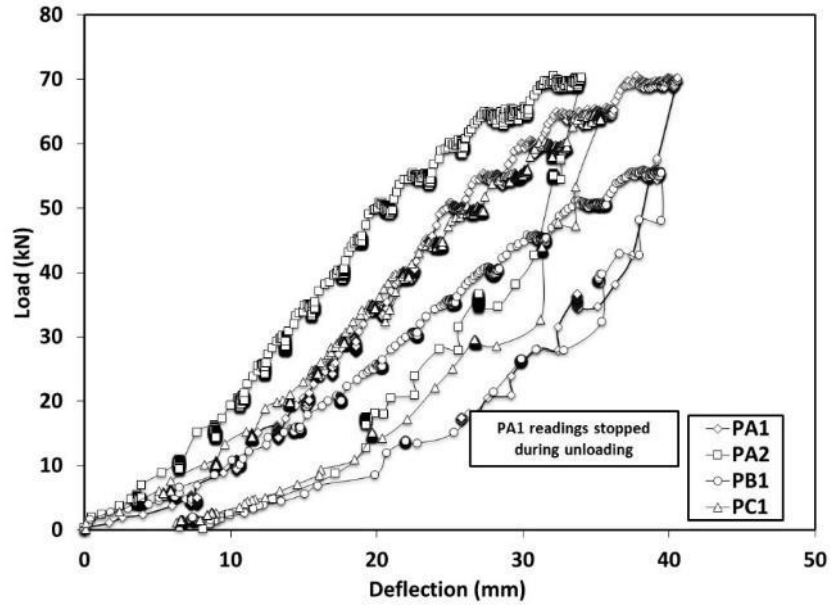
(a)
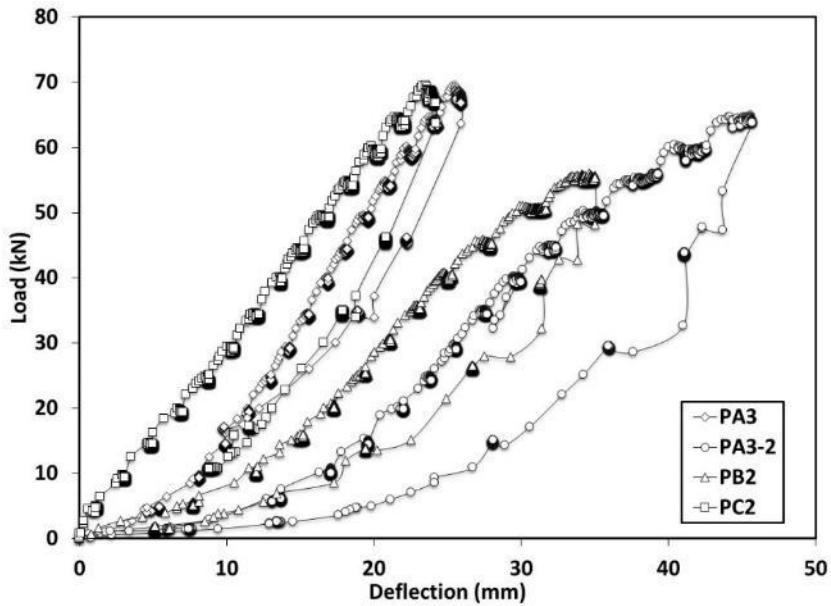
(b)

Figure 5 - 12: Load-deflection curves after cyclic lateral load tests: (a) Piles tested in axial compression before lateral loading; (b) Piles tested in uplift before lateral loading

Figure 5 - 13: An image of the developed gap behind pile PA1 at the end of the cyclic lateral testing

5.4.2 Pile ultimate capacity

While the piles lateral capacity depends on the supported structure deformation tolerance, two criteria are generally adopted to define the ultimate pile lateral capacity; the first defines the ultimate load as the load corresponding to the intersection of the tangents to the load–deflection curve, while the second defines the failure load as the load corresponding to a specific deflection value (typically either 6.25 mm or 12.5 mm) (Prakash and Sharma, 1990). The first criterion was not considered since no clear plastic deformation and failure zones were observed in the load deflection curves (inability to draw the second tangent). Hence, the second criterion was employed herein, and the loads corresponding to 6.25 mm and 12.5 mm are noted. Unfortunately, the loading bar was touching the ground during the lateral load test of PC2 after cyclic loading, which rendered its results unreliable. The resulting values of ultimate pile capacity are summarized in Table 5 - 4.

In general, tapered piles of configuration A provided the highest capacity. However, because of the difference in average pile diameter and embedded pile length, it is more appropriate to present the results in terms of the pile capacity per unit volume. These values are obtained by normalizing the capacity of the piles presented in Table 5 - 4 by their embedded volume, and the results are presented in Table 5 - 5.

Table 5 - 4: Ultimate lateral static capacity

Pile #	Lateral capacity (kN)			
	Before cyclic testing (at 6.25mm)	Before cyclic testing (at 12.5mm)	After cyclic testing (at 6.25mm)	After cyclic testing (at 12.5mm)
PA1	20.2	34.3	4.8	16.3
PA2	24.5	39.4	10.4	27.3
PA3	23.2	43.4	6.6	24.4
PB1	10.3	21.3	5.7	14.4
PB2	18.0	29.4	4.6	12.2
PC1	13.0	25.7	7.9	18.9
PC2	14.0	34.5	N/A	N/A

Table 5 - 5: Ultimate static capacity per unit embedded volume of the tested piles

Pile #	Capacity per unit volume (MN/m^3)			
	Before cyclic testing (at 6.25mm)	Before cyclic testing (at 12.5mm)	After cyclic testing (at 6.25mm)	After cyclic testing (at 12.5mm)
PA1	1.78	3.03	0.42	1.44
PA2	2.02	3.26	0.86	2.26
PA3	2.10	3.93	0.60	2.21
PB1	1.13	2.33	0.62	1.58
PB2	1.85	3.02	0.47	1.25
PC1	1.11	2.19	0.67	1.61
PC2	1.19	2.93	N/A	N/A

Inspecting the results in Table 5 - 5, it is clear that the tapered piles (configurations A and B) provided higher capacity per unit volume in comparison with the straight shaft piles for the case of initial lateral monotonic loading. The increase in capacity per unit volume was up to 82% for configuration A over configuration C piles. The result of the load tests after

cyclic loading showed that all piles exhibited significant decrease in their capacity. However, the reduction in capacity was larger for the case of tapered piles. This was attributed to the larger degradation in soil stiffness and strength near the surface for the case of tapered piles because their free length was larger, which resulted in larger moment in addition to the lateral loading effects.

Upon unloading, the piles recovered 61% to 85% of their maximum displacement which implies significant plastic strains due to the rearrangement of the soil particles as well as the possible crushing of the sand particles.

For piles tested monotonically first, the deflections along the top 0.92m of their shaft are shown in Figure 5 - 14 at the maximum measured head deflections. The results show almost linear variation along this length, with some curvature near the top.

The pile head rotation angle was recorded during the test and the results are shown in Figure 5 - 15. All piles exhibited almost the same behavior, which characterized by three distinct regions. In the first region, the rotation angle increased with loading as the pile rotated as a rigid body and the performance is mainly governed by the soil stiffness. In the second region, the rotation remained almost constant as the applied load increased. This behavior is attributed to the contribution of the passive resistance over the helical plate, which was mobilized due to the relatively large deformations and provided "fixation" at the location of the helix. As the load continued to increase, the pile itself started to deflect and additional rotation occurred in the third region. This is confirmed by the slight curvature observed in Figure 5 - 14. This pile behavior is further verified through the results of the numerical modeling that will be discussed later.
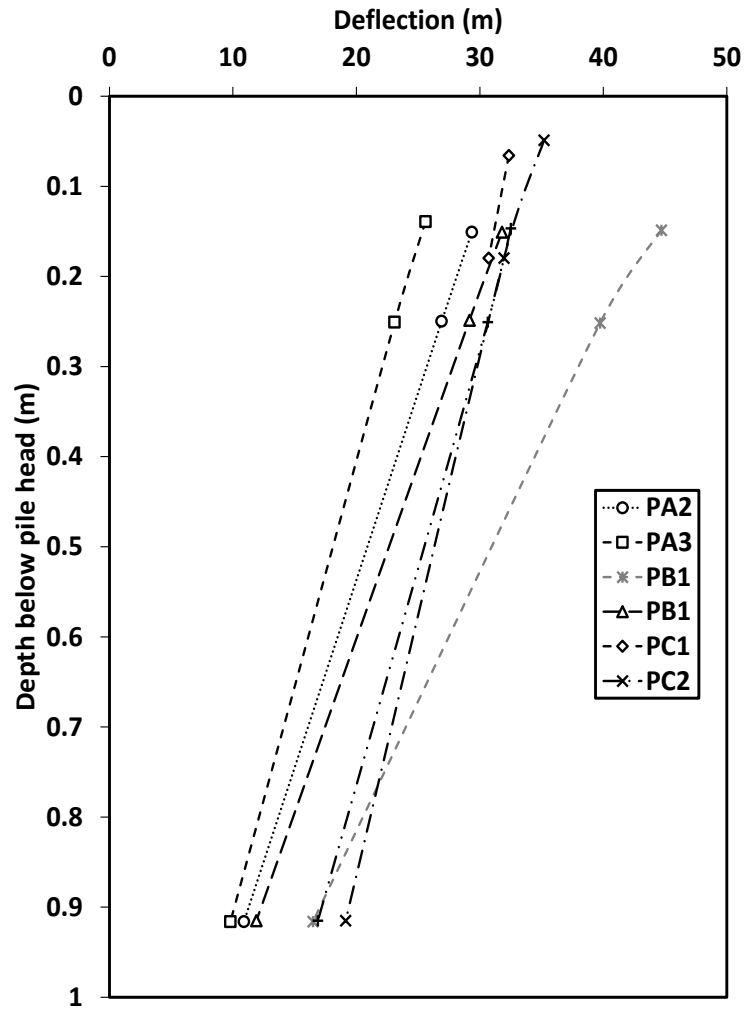
Figure 5 - 14: Variation of the pile deflection along top 0.92m
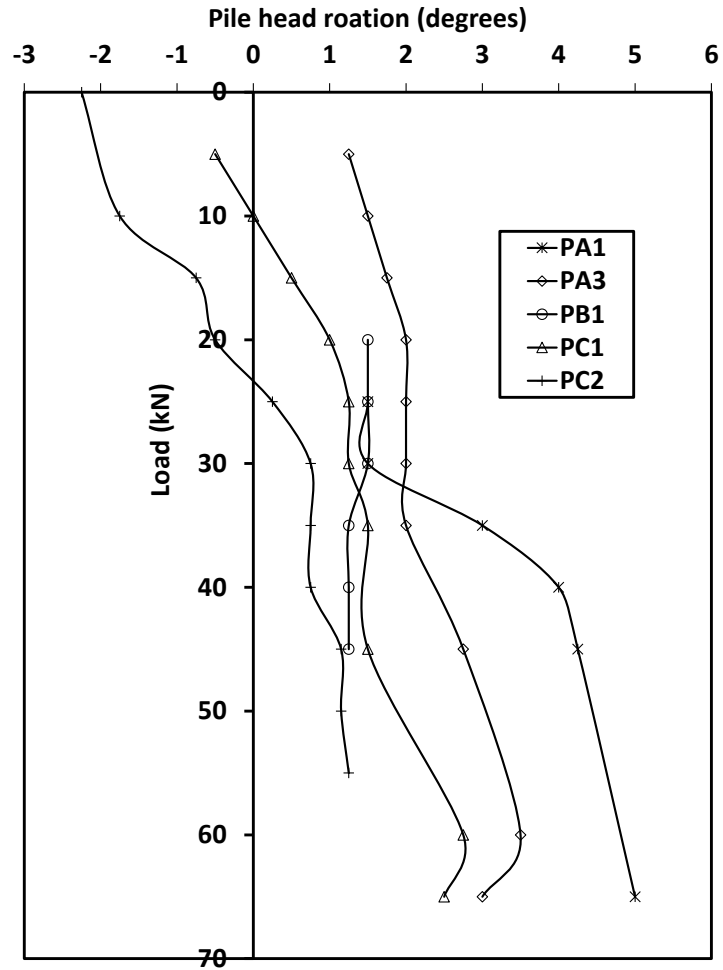
Figure 5 - 15: Variation of the pile head rotation with loading

It should be noted that during the unloading phase of some piles the load dropped suddenly due to the high sensitivity of the used hydraulic jack (displacement controlled hydraulic loading system).

5.5   Numerical analysis

To further examine the lateral static behavior of the tapered helical piles, three-dimensional nonlinear finite element analyses were conducted for the test pile configurations. The numerical models were developed using the ABAQUS software package (Hibbitt *et al.*, 2008). The numerical investigation was focused on the effect of the pile geometry and the helical plate on its performance.

5.5.1 Description of finite element model

The soil-pile system is modeled employing a 3D half-cylindrical mesh. The pile was placed along the axial z-direction of the cylinder and the helix was idealized as a planar cylindrical disk. The piles were assumed intact and wished in place (i.e. no installation effects). Figure 5 - 16 shows the mesh configuration for the pile PC1.
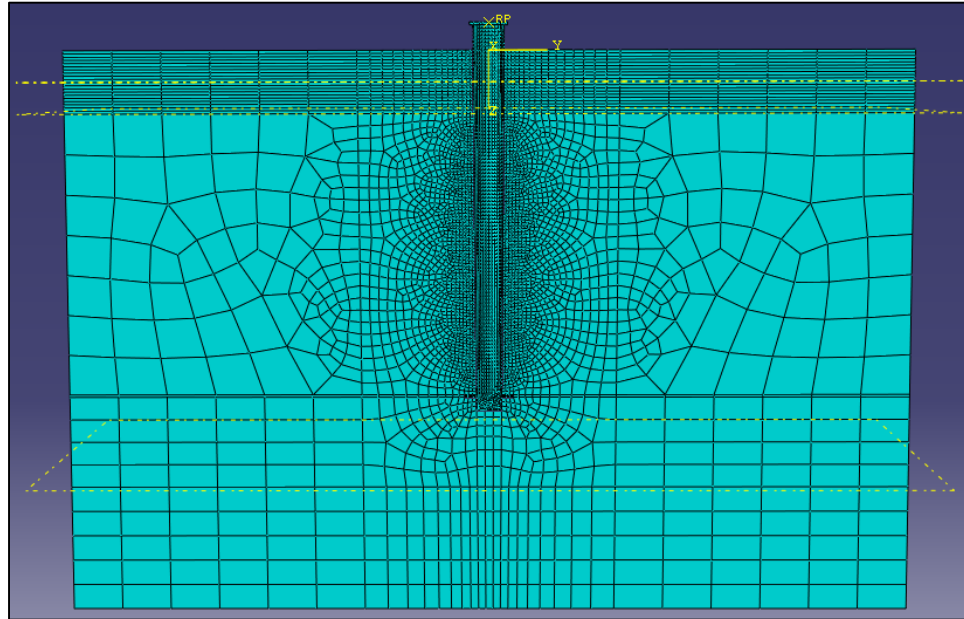
Figure 5 - 16: Numerical model snapshot-un-deformed geometry- PC1

The soil medium and the pile were simulated employing 8-noded, first order, and reduced integration continuum solid elements (C3D8R). Each element has three active translational degrees of freedom at each node, and one integration point located at its centroid.

The locations of the boundaries were optimized to minimize the effects of the boundary conditions on the results maintaining the computational efficiency. The radius of the soil cylinder extended 3.375 m (i.e. approximately 8.5 times the diameter of the helical plate) from the center of the pile shaft. The bottom horizontal boundary was placed at 1.65 m below the pile toe, which is approximately equivalent to 4 helix diameters.

A stress-free boundary was considered for the soil top surface. The translation of the bottom surface of the soil cylinder was restrained in X, Y and Z directions. The vertical

boundaries were restrained from translating in X direction and rotating around Y and Z to simulate the case of a full mode. The back of the soil half-cylinder was constrained in the horizontal directions X and Y and was free to move vertically. To ensure enhanced accuracy, the mesh was refined at the highly stressed/strained zone adjacent to the top section of the pile shaft (approximately 10 times the shaft diameter), which governs the pile lateral behavior. This was achieved by conducting the analysis employing various models in which the mesh was incrementally refined and their results were compared. When the difference between the results of two consecutive models (i.e. refinements) became less than 2.5%, the most refined model was selected for use in the ensuing analyses. The elements were most refined along the pile-soil interface and around the helical plate and then their size gradually increased towards the model boundaries. The final refined mesh configurations consisted of 30170/20681/21336 elements with maximum elements side dimension ranging from 320mm/285mm/335mm at the model boundaries to 25mm/28mm/28mm at the pile-soil interface for pile configurations A, B and C, respectively.

5.5.2 Soil model

The soil was simulated as an elastic-perfectly plastic isotropic continuum. The soil plasticity and failure were modeled using the Mohr-Coulomb yield criterion where values of the critical state angle of internal friction, φ_{cs}, cohesion yield stress, c' and the dilation angle, ψ. Poisson's ratio, v, and Young's modulus, E_s defined the soil elasticity.

The soil domain was divided into three main sections: the upper softer top soil layer (0.5m); the soil along the pile shaft up to the helical plate; and the soil beneath the helical plate. The average strength and stiffness parameters were assigned to these sections as shown in Table 5 - 6. These soil parameters were calibrated and validated employing the axial field tests data. However, the elastic modulus for the top soil layer was selected to reflect the initial soil conditions (rather than the disturbed condition) as the pile was assumed to push against undisturbed soil farther from the pile shaft.

Table 5 - 6: Soil parameters considered in FE model

Depth (m) From	Depth (m) To	$\varphi_{residual}$ (°)	c (kPa)	ψ (°)	ν	E_s (MPa) PA1, PA2, PB1, PC1	γ (kN/m³)
0	0.5	32	4	4	0.3	35	17
0.5	Helix* level	32	4	6	0.3	70	18
Helix level	End of model	32	4	6	0.30	94, 91, 73, 94*	18

*Varies depending on embedded length and pile configuration

5.5.3 Pile model

The pile was simulated as linear elastic-perfectly plastic material. The elastic behavior was defined by Poisson's ratio, v_p, and Young's modulus, E_p. The plastic behavior was represented by the yield strength F_y of the pile material. The piles mechanical properties adopted in the model are summarized in Table 5 - 7. Weaker strength parameters were assumed for the helical and base plates to account for the welding defects observed prior to pile installation.

Table 5 - 7: Pile mechanical properties considered in FE model

Component	Young's Modulus E_p (kN/m²)	Poisson's ratio v_p	Unit weight γ_p (kN/m³)	Yield strength F_y (MPa)
Shaft- configurations A, B and D	1.69E08	0.28	77	314
Shaft - configurations C and E	2E08	0.28	77	370
Helix and base plates welded connections	2E08	0.28	77	170

5.5.4 Pile-soil interface model

The pile-soil interface was simulated using the penalty-type tangential behavior Coulomb's frictional model. No relative tangential motion occurs until the surface traction reaches a critical shear stress value, which is taken as the lesser of the interface shear strength or a

fraction of the interface pressure. Pile-soil interface strength was given by $\tan\delta = 0.78$ and 0.5 for tapered and straight piles configurations, respectively. While the first was determined by studying the pile surface roughness in comparison to the soil mean particle size as mentioned earlier in Chapter 3, the latter was considered in accordance to the suggested values by the Canadian Foundation Engineering Manual (2006). Separation along the pile-soil interface was allowed.

5.5.5 Loading sequence

An initial loading step of geostatic stresses and equilibrium was applied to introduce the initial in-situ soil stresses, wishing the pile in. This was followed by displacement controlled analysis whereby prescribed displacements were applied at reference points rigidly connected to the top loading plates.

5.5.6 Results

The analyses were conducted for lateral load testing conditions of PA1, PA2, PB1 and PC1 and the resulting load-deflection curves are presented in Figure 5 - 17. The results presented in Figure 5 - 17 demonstrate good agreement between the calculated and observed responses of the tested piles.
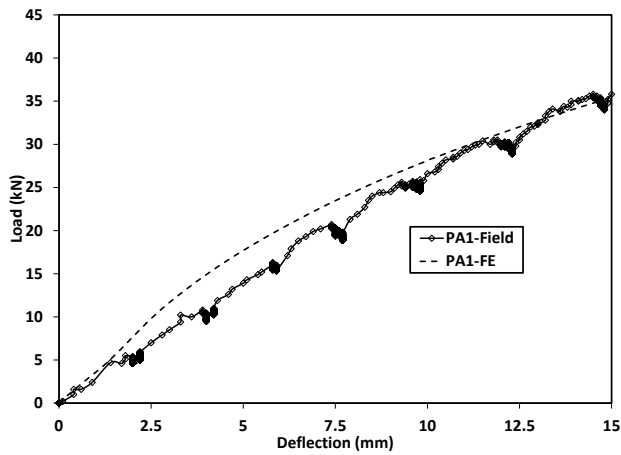
(a)
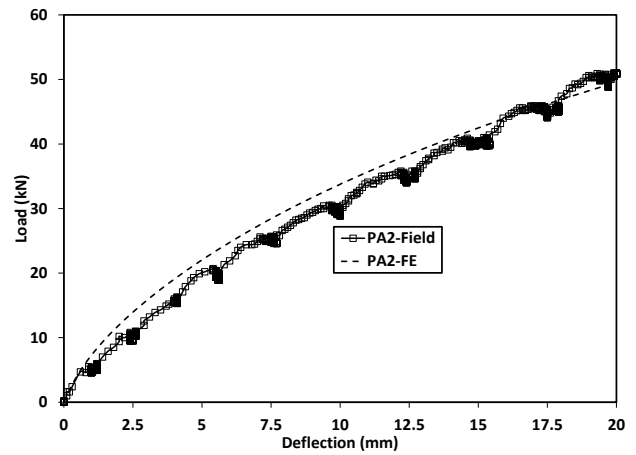
(b)
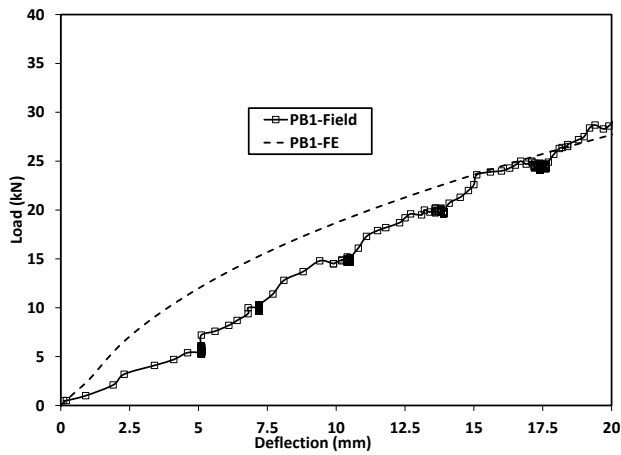
(c)
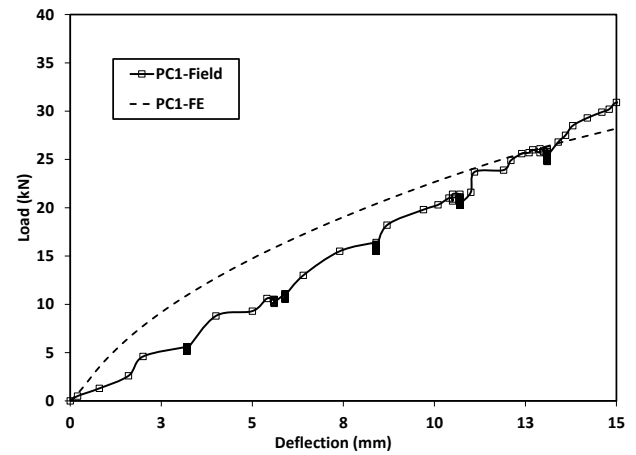
(d)

Figure 5 - 17: Comparison of calculated and measured load-deflection curves for calibration: a) PA1; b) PA2; c) PB1 and c) PC1

The displacement field around PA2 is shown in Figure 5 - 18. While typically the pile lateral response is governed by the properties $3 D_{top}$ along the top $10D_{top}$, Figure 5 - 18 shows that the only the top 1.25m (equivalent to 5 times the top pile diameter D_{top}) experienced appreciable displacement, i.e., soil below that level did not contribute to the pile response. This is attributed to the fixation provided by the helical plate, as the passive bearing pressures on the helix surfaces contributed additional resistance preventing the lower segment of the pile from rotation. This is confirmed in Figure 5 - 19, which presents the normal stresses on the helical plate.

160
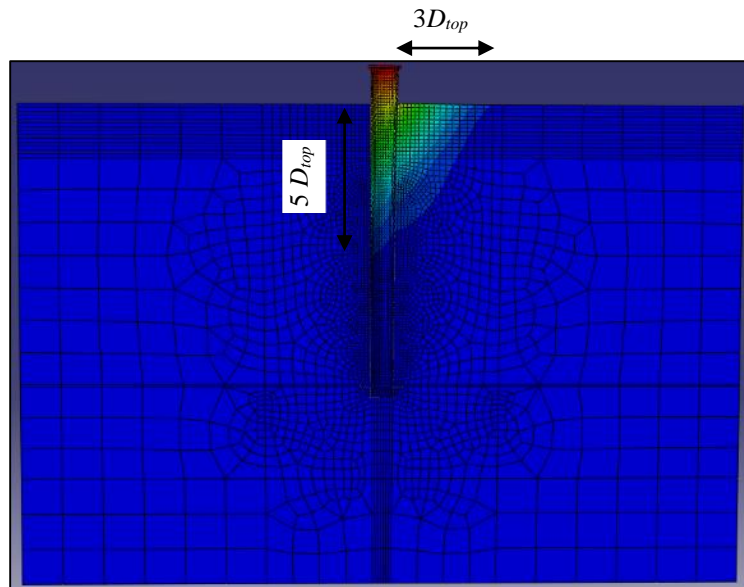
Figure 5 - 18: Displacement field around PA2
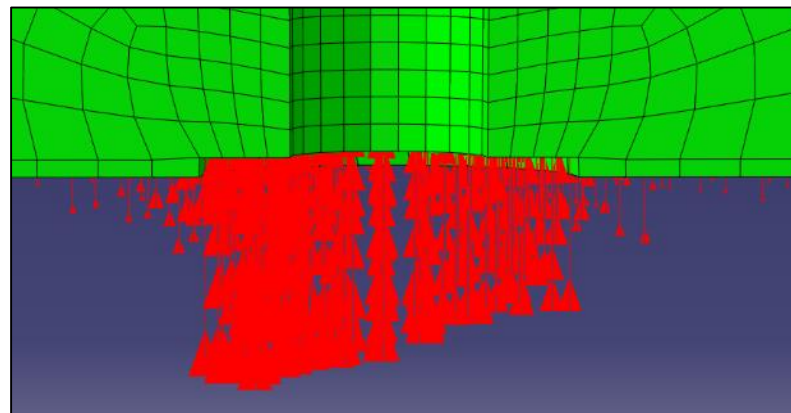
Figure 5 - 19: Normal stress in soil above the helix plate-PA2

Separation along pile-soil back interface was observed at the start of the pile loading with no significant shaft stresses along the pile surface.

To assess the contribution of the helix plate, the lateral response of a pile with the geometrical configuration of PA2, but without helix, was analyzed and the calculated load-deflection curve is presented in Figure 5 - 20. The pile resistance significantly decreased, underscoring the important contribution of the helix to the pile lateral resistance. This explains the transitional rigid pile behavior observed during the load testing. Figure 5 - 20 compares the lateral response of pile PA2 with and without a helix, which clearly demonstrates the benefit of the helix for the case of the short helical pile. Figure 5 – 21

presents the deflected shapes of the pile with and without a helix, which further confirms the contribution of the helical plate to the lateral resistance in terms of preventing the lower segment of the pile from rotation. In such case, the flexural rigidity of the pile cross-section would govern the lateral performance even for weak soil near the ground surface.
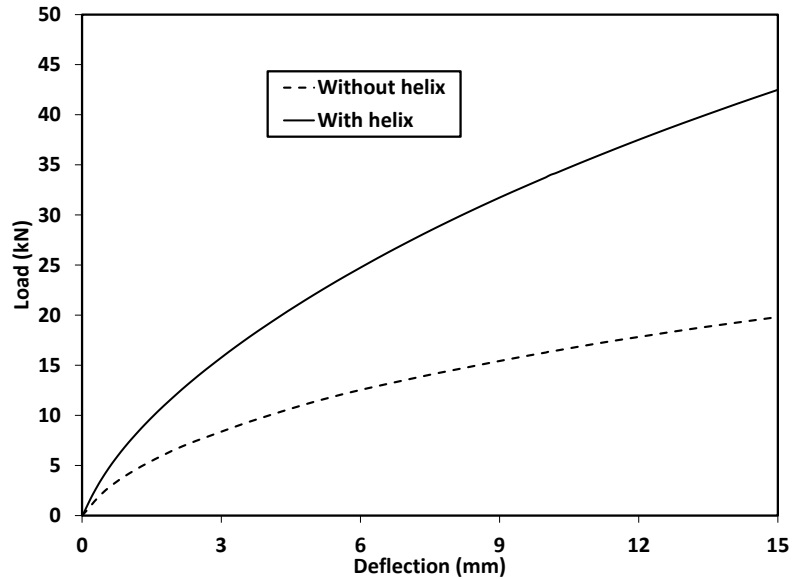
Figure 5 - 20: Load –deflection curves of PA2 with and without helix plate
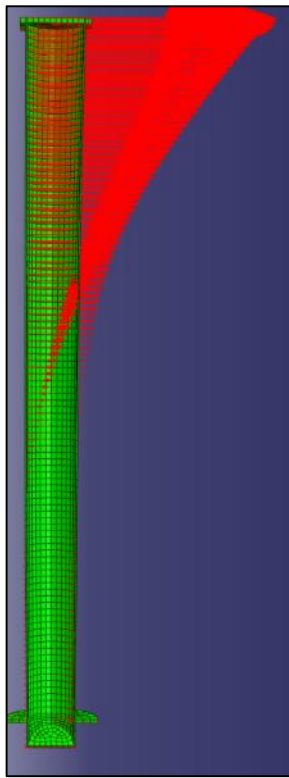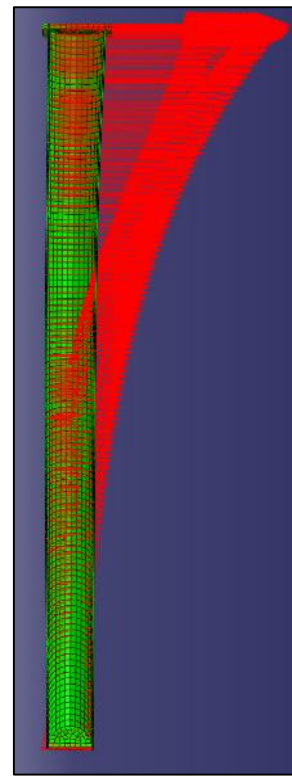
(a)   (b)

Figure 5 - 21: Pile lateral displacement for pile PA2 (a) With helix; (b) Without helix

The lateral response of longer piles (i.e. more practical pile length), denoted configurations D and E, with dimensions as shown in Figure 5 - 22 was also performed.
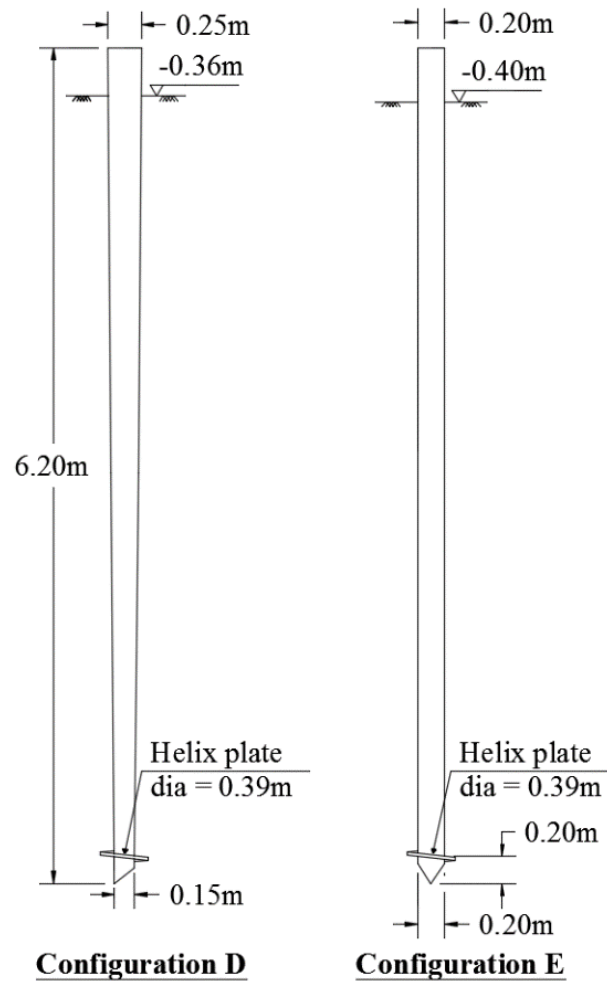
Figure 5 - 22: Configurations D and E piles geometry

These piles have the same material properties and taper angles as configurations A and C, respectively, but double the length. The calculated load-deflection curves are shown in Figure 5 - 23.

It can be noted from Figure 5 - 23 that long pile (i.e. flexible) behavior prevailed. The calculated load-deflection curves of pile configurations D and E are almost identical to those of configurations A and C, respectively. This confirms the benefit of the helical plate to the lateral performance of the shorter piles in terms of providing an equivalent fixation. It gives rise to the idea of using helical plate to enhance the lateral performance of short pile instead of increasing the pile length.
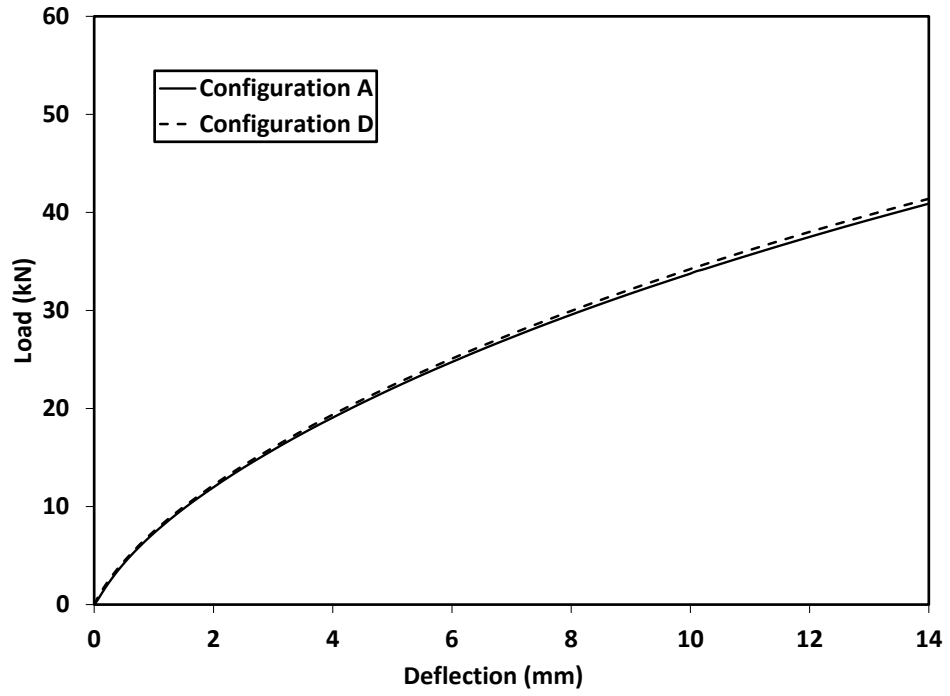
(a)
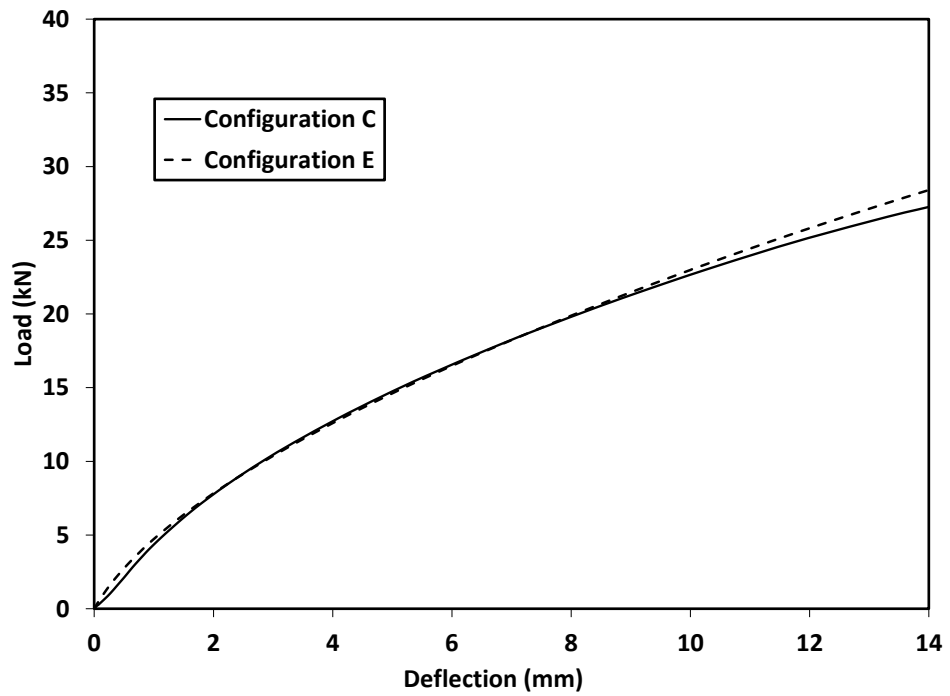
(b)

Figure 5 - 23: Load deflection curve a) Configurations A and D; b) Configuration C and E

One important application for short helical piles is to support solar panels in solar farms renewable energy projects. In this application, the pile loading scheme involves both horizontal load and moments (or high eccentricity horizontal loads). To investigate the performance of helical tapered piles in this case, a number of numerical simulations were conducted considering piles of configurations A, C, D and E subjected to a combination of horizontal load and moment and the calculated interaction diagram is shown in Figure 5 - 24. The graph presents the variation of dimensionless applied moment $\bar{M}$ and horizontal forces $\bar{H}$ normalized by the values of the pure moment and horizontal forces resulting in 12.5mm head deflection respectively. This graph can be used for the design of helical tapered piles subjected to a combination of significant moment and lateral loads. This normalization technique reflects the serviceability limits as previously adopted for determining the piles capacity as shown in Table 5 - 4. The curves further confirm the superiority of the tapered sections where the latter can sustain higher $\bar{M}$ at the same $\bar{H}$ value compared to the straight shaft piles. Equations of the best fit trendiness for both tapered piles (configurations A and D) and straight piles (configurations C and E) are shown in Figure 5 - 25.
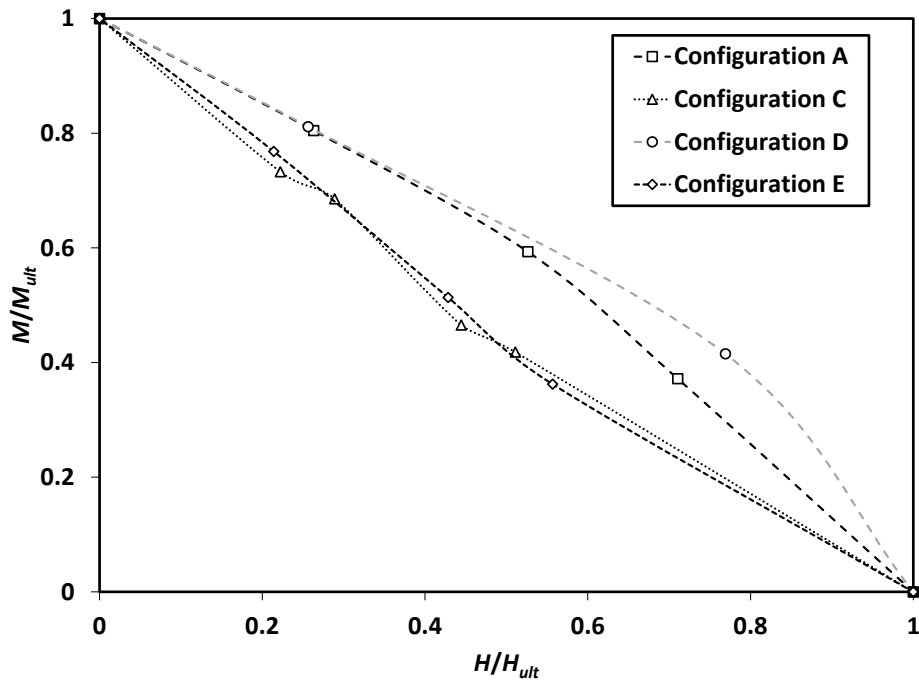
Figure 5 - 24: Moment – horizontal force interaction diagrams
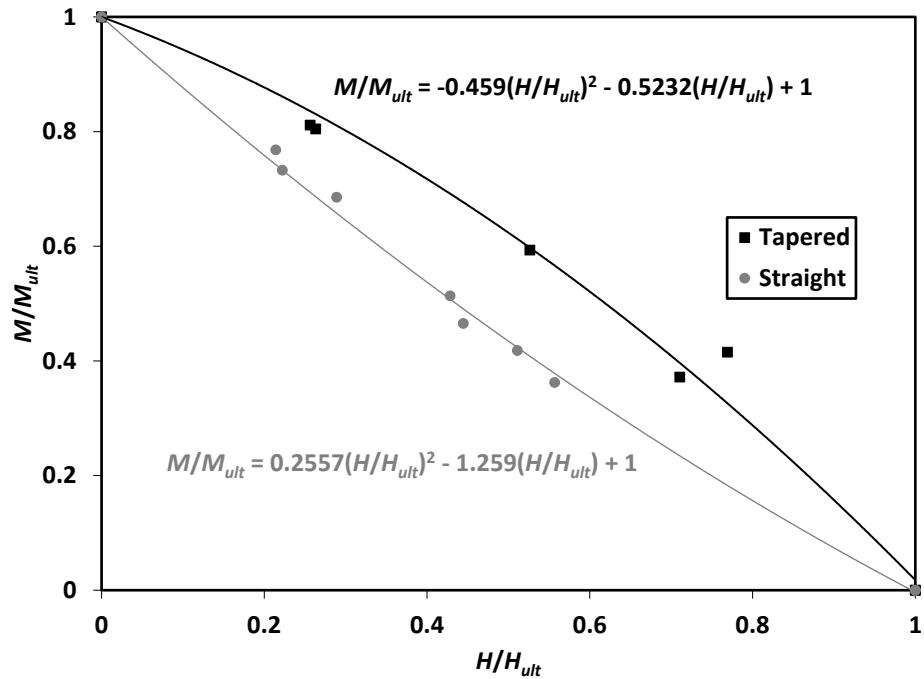
Figure 5 - 25: Moment – horizontal force interaction diagram-best fit equations

It should be noted that, while the actual tension tests performed on specimens of configuration C piles showed the strength parameters presented in Table 5 - 7, the standard mechanical parameters for steel A53 grade B steel (ASTM A53/A53M, 2012) were considered for configurations C and E in calculating the interaction diagrams for a more generic design aid.

5.6 Conclusions

The lateral performance of a novel ductile cast iron tapered helical pile was investigated in this study. Seven piles were installed in a silty sand soil profile and were subjected to static and cyclic lateral load tests. The test piles included five tapered helical piles with 2 different average diameters and same taper angle and two straight-shaft helical piles. The effect of cyclic lateral loading on the pile lateral capacity was also studied. In addition, a numerical investigation was conducted to better understand the performance characteristics of the tapered helical piles. The effects of pile length and helical plate on the pile lateral response were assessed. The main conclusions drawn from this study are as follows:

1. The tapered piles generally exhibited stiffer response and higher ultimate capacity compared to the straight-shaft piles owing to the greater diameter and flexural rigidity at the top portion of the pile, which governs its lateral response;

2. The results demonstrated that the spun cast iron with rough surface is a viable material for piling products.

3. The helical plate was found to significantly increase the lateral pile capacity for short piles. On the other hand, the helical plate did not influence the lateral performance of the long piles;

4. The cyclic loading was found to significantly reduce the lateral stiffness and capacity of all tested piles. This was mainly attributed to the development of a gap along the upper portion of the pile and a zone of loose soil of the caved-in sand.

5. Moment–horizontal force interaction diagrams are provided to aid in design of helical piles subjected to a combination of significant moment and horizontal load such as the case for helical piles supporting solar panels in solar farm applications.

5.7 References

AASHTO. 2002. Standard specifications for highway bridges. *HB-17.* American Association of State and Highway Transportation Officials.

Allotey, N. & El Naggar, M. H. 2008. A numerical study into lateral cyclic nonlinear soil-pile response. *Canadian Geotechnical Journal,* 45(9), 1268-1281.

ASTM A53/A53M. 2012. Standard specification for pipe, steel, black and hot-dipped, zinc coated, welded and seamless. ASTM international.

ASTM C136. 2006. Standard test method for sieve analysis of fine and coarse aggregates. ASTM international.

ASTM D1556. 2007. Standard test method for density and unit weight of soil in place by the sand-cone method. ASTM international.

ASTM D2487. 2011. Standard practice for classification of soils for engineering purposes (Unified Soil Classification System). ASTM international.

ASTM D3080. 2011. Standard test method for direct shear test of soils under consolidated drained conditions. ASTM international.

ASTM D4318. 2010. Standard test methods for liquid limit, plastic limit, and plasticity index of soils. ASTM international.

CGS. 2006. *Canadian Foundation Engineering Manual.*4th edition. Canadian Geotechnical Society.

Bagheri, F. & El Naggar, M. H. Effects of the installation disturbance on the behavior of the multi-helix screw anchors in sands. GeoMontreal, 2013, Montreal.

Bowles, J. 1996. *Foundation analysis and design*, 5th edition, Mc-Graw hill.

El Naggar, M. H. & Wei, J. Q. 1999. Response of tapered piles subjected to lateral loading. *Canadian Geotechnical Journal,* 36(1), 52-71.

Elkasabgy, M. 2011. Dynamic and static performance of large-capacity helical piles in cohesive soils. *PhD thesis.* London, Ontario, Canada: The University of Western Ontario.

Fleming, K., Weltman, A., Randolph, M. & Elson, K. 2009. *Piling engineering*, Taylor and Francis Group.

Hibbitt, H. D., Karlsson, B. I. & Sorensen, E. P. 2008. ABAQUS Standard user's manual. Pawtucket, R. I.: Hibbitt, Karlsson & Sorensen Inc.

Kulhawy, F. H. & Mayne, P. W. 1990. Manual for estimating soil properties for foundation design. Ithaca, New York: Cornell University.

Liao, S. S. C. & Whitman, R. V. 1986. Overburden correction factors for SPT in sand. *Journal of Geotechnical Engineering,* 112(3), 373-377.

Mayne, P. W. In-situ characterization of Piedmont residuum in eastern US. Proc. US-Brazil: Application of Classical Soil Mechanics to Structured Soils, 1992, Belo Horizonte. National Science Foundation/USA, 89-93.

Mayne, P. W. 2006. In-situ test calibrations for evaluating soil parameters. Overview Paper on In-Situ Testing- Singapore Workshop.

Mayne, P. W., Christopher, B. & Dejong, J. 2002. Manual on subsurface investigations—Geotechnical site characterization. Washington, DC.: Federal highway administration, U.S. Department of Transportation.

Mayne, P. W. & Kulhawy, F. H. 1982. Ko-OCR Relationships in Soil. *Journal of the Geotechnical Engineering Division,* 108(6), 851-872.

Pender, M. J. & Pranjoto, S. Gapping effects during cyclic lateral loading of piles in clay. Proceedings of the 11th World Conference on Earthquake Engineering, 1996, Acapulco, Mexico, 23-28

Perko, H. 2009. *Helical piles: A practical guide to design and installation,* New Jersey, John Willey and Sons Inc.

Poulos, H. G. & Davis, E. H. 1980. *Pile foundation analysis and design*, John Wiley and Sons.

Prakash, S. & Sharma, H. D. 1990. *Pile foundation in engineering practice,* New York, John Wiley and Sons.

Prasad, Y. V. S. N. & Rao, S. N. 1996. Lateral capacity of helical piles in clay. *Journal of Geotechnical Engineering,* 122(11), 938-941.

Puri, V. K., Stephenson, R. W., Dziedzic, E. & Goen, L. 1984. Helical anchor piles under lateral loading. Laterally loaded deep foundations: Analysis and Performance. ASTM STP 835. Edited by J. A. Langer, E. T. Mosley, and C. D. Thompson. American Society for Testing and Materials, 194–213.

Sakr, M., El Naggar, M. H. & Nehdi, M. Lateral behaviour of composite tapered piles in dense sand. *Proceedings of the Institution of Civil Engineers-Geotechnical Engineering,* 2005, 158(3). 145-157.

Seamless Pole Inc 2010. Ductile iron poles. Birmingham, AL. (*http://www.seamlesspole.com/*)

Skempton, A. W. 1986. Standard penetration test procedures and the effects in sands of overburden pressure, relative density, particle size, aging, and over-consolidation. *Geotechnique,* 36(3), 425-447.

CYCLIC AXIAL PERFORMANCE OF SCDI HELICAL

TAPERED PILES IN SAND

6.1 Introduction and motivation of research

Different pile alternatives featuring different configurations, materials and installation techniques are currently available and used in practice. Nevertheless, the construction industry is always pursuing new foundation systems featuring more efficient use of construction materials and available ground support. In this study, a spun-cast ductile iron (SCDI) tapered pile (Seamless-Pole-Inc., 2010) fitted with a lower helical plate is investigated.

The investigated pile configuration combines the construction advantage of helical piles and the efficiency of the tapered section to support axial loads. It is installed by applying mechanical torque to the pile head. This installation technique minimizes vibration, noise and soil spoils, making it suitable for foundations in urban areas.

In this chapter, the pile cyclic axial performance is studied. This includes experimental testing and numerical analysis to evaluate the cyclic axial performance of the pile installed in silty sand.

6.2 Literature survey

While extensive studies exist in literature on the axial cyclic performance of piles in general, less attention was given to the cyclic performance of tapered piles or helical piles.

The rhythmic loads imposed by sources such as machines, waves or wind loads can significantly reduce the capacity of piles in sands where failure might occur at loading amplitude as low as 30% of their static capacities for one-way loading, with even less amplitude for two-way loadings (Chan and Hanna, 1980). Poulos (1989) suggested that for two-way cyclic loading, degradation of skin and base resistance would govern, while the

accumulation of plastic strains prevails in case of one-way loading, especially in case of softening behavior along the pile-soil interface. He observed greater shaft degradation with increasing cyclic displacement amplitude, with significant shaft degradation when the cyclic displacement amplitude exceeds the required displacement to develop the limit shaft stresses under static loading conditions. He also noticed that most of the degradation occurs within the first 10 cycles, with greater shaft friction degradation for piles in calcareous sand compared silica sand due to the former greater compressibility. The skin friction degradation was not affected by the effective overburden stresses nor the overconsolidation ratio of the sand. The possible strength and stiffness degradation may be attributed to the developed of excess pore pressure, the accumulation of plastic deformations and the rearrangement of soil particles around the piles (Poulos, 1981). On the other hand, he suggested that only minor soil modulus degradation can be expected in sands and, in absence of other data, end bearing degradation can be neglected.

The capacity and stiffness losses associated with the two-way loading case was also reported by Jardine and Standing (2012) for open steel pipe piles in marine sand. They concluded that the capacity and stiffness reduction depends on many factors including the cyclic loading amplitude. Similarly, Abdel-Rahman and Achmus (2011) concluded that cyclic load amplitudes below a threshold cyclic load amplitude would not cause reduction in the pile capacity. Such threshold cyclic amplitudes are suggested by Schwarz (2002) in terms of the ratio between the cyclic load amplitude and the static pile capacity for different soil types as summarized in Table 6 - 1. An example of piles' shaft degradation pattern in sand is shown in Figure 6 - 1 with increasing number of cycles (Abdel-Rahman and Achmus, 2011).

Table 6 - 1: Threshold amplitude values for cyclic loading-for different soil types (Schwarz, 2002)

Soil type	Critical cyclic amplitude to static pile capacity
Sand	0.10~0.40
Silt	0.40~0.60
Normally consolidated Clay	0.30~0.55
Overconsolidated Clay	0.85~1.00

In their study, El Naggar and Wei (2000) suggested keeping the cyclic amplitude for tapered piles within 25% and 75% of their static axial compressive and uplift capacity respectively. Within these limits, tapered piles are expected to show an enhanced performance compared to the cylindrical one (El Naggar and Wei, 2000). They suggested that keeping the cyclic loading amplitude within the uplift capacity of the pile would lead to the increase of the system stiffness with the applied loading cycles due to the densification of the sand surrounding the pile, however not necessarily in case of dense sand.

For helical piles, it is recommended to keep the cyclic loads within 25% of the static capacity (Perko, 2009). This is based on the findings of Ghaly and Clemence (1998) who reported that the upward creep is fully recoverable when the cyclic loads are kept within these limits.
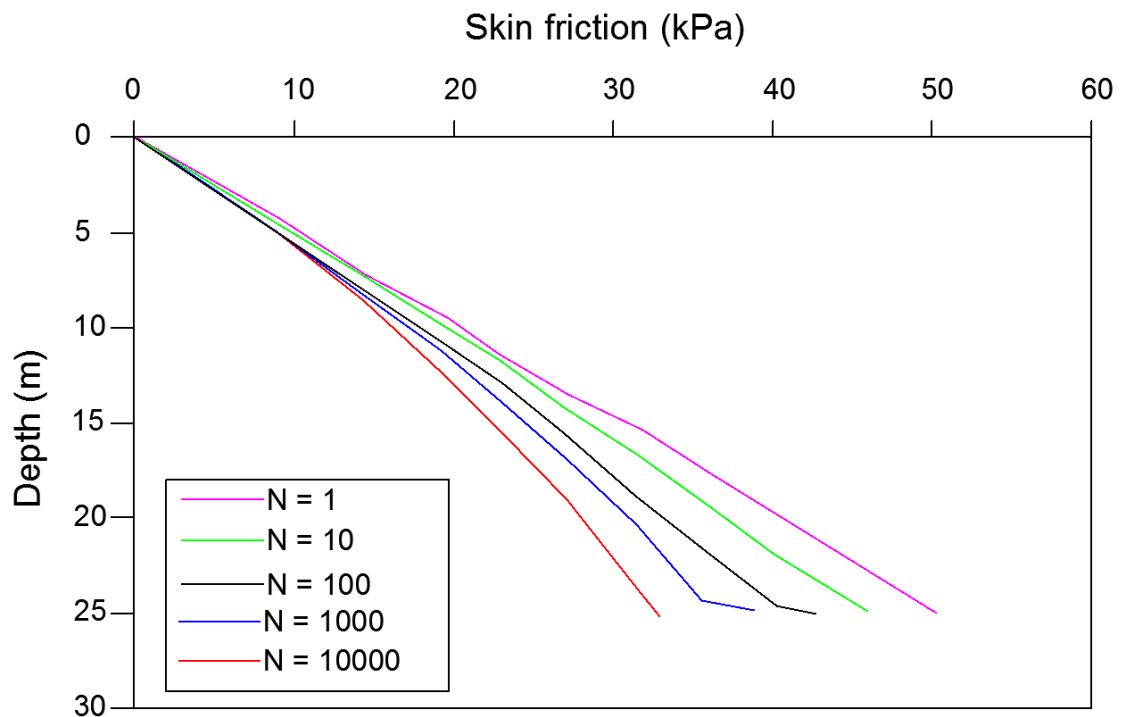
Figure 6 - 1: Degradation effect on pile shaft resistance in sand with number of cycles (Reproduced after Abdel-Rahman and Achmus, 2011)

Studying the performance of steel pipe piles in marine sand, Rimoy *et al.* (2013) showed that the piles cyclic stiffness remained within 20% of the static values until approaching

the cyclic failure, with rate of plastic strain accumulation sensitive to the mean and cyclic loading levels.

El Sharnouby and El Naggar (2012) evaluated the effect of cyclic/static loading on the performance of FRP-steel fibre-reinforced helical pulldown micropiles. Small cyclic displacements were observed during the few first loading cycles, with negligible permanent displacements when the piles were previously statically tested up to higher loading levels (El Sharnouby and El Naggar, 2012). Whereas when subjected to higher cyclic loads compared to the initial static one, the observed shaft degradation was counteracted by the resulting soil stiffening from the lead section (El Sharnouby and El Naggar, 2012). They showed that the application of cyclic load may increase the axial capacity by up to 15% (El Sharnouby and El Naggar, 2012). The application of low-level cyclic loads can also increase the tension capacity of piles by up to 20% (Jardine and Standing, 2012).

El-Gharabawy and Olson (1999) investigated the uplift capacity of suction caissons in sand. They suggested that the long term static capacity can be taken as the threshold of cyclic loading, beyond which excessice dispalecmenets and degradation of the soil strength would occur. They also reported that the increasing loading frequency and load inclination would increase the resulting pile displacement (El-Gharbawy and Olson, 1999).

Clemence and Smithling (1984) attributed stiffening or degrading effects of cyclic uplift loading of helical anchors to the rate of soil disturbance during installation: for greater installation disturbance, the cyclic loading would densify the soil hence increases its stiffness; whereas for installations that increase the soil stiffness, the application of cyclic load will loosen the soil and reduce the pile static resistance (Clemence and Smithling, 1984). They also found that the static post-cyclic capacity of helical anchors is reduced due to the loose soil zone surrounding the anchors developed during the cyclic loading (Clemence and Smithling, 1984).

With repetitive loading, the developed plastic strains decrease with increasing cycles (di-Prisco and Zambelli, 2003), reaching a resilient state after a certain number of loading cycles, where no further plastic strains accumulate. This trend, referred to as the shakedown

phenomena, was observed to occur after 300~1000 loading cycles for sands with contact pressure ranging from 100 to 119 kPa (Brown *et al.*, 2008).

Begemann (1973) investigated cyclic performance of steel H-piles under a sequence of compressive and uplift loads in sand. He observed significant deterioration of the pile frictional resistance and found that overstressing the piles could reduce the frictional resistance by 33%, with no signs of long term strength recovery during the following two months.

It can be concluded that several studies are available in literature, providing design guidelines for conventional piling systems when subjected to cyclic axial loads. This includes the expected cyclic behavior, the possible change in soil stiffness and/or strength during load cycling and suggested limitations on the cyclic loading amplitudes. However, much less attention was given to the cyclic performance of helical and tapered piles with more scarce data for the latter system. Accordingly, analysis of the novel system provides a better understanding, not only of the cyclic axial performance of the combined system, but also of the performance of each system (helical and tapered) individually.

6.3   Experimental setup

6.3.1   Test site soil

Prior to the pile testing, a single 11m depth borehole was drilled in the vicinity of the piles as shown in Figure 6 - 2.
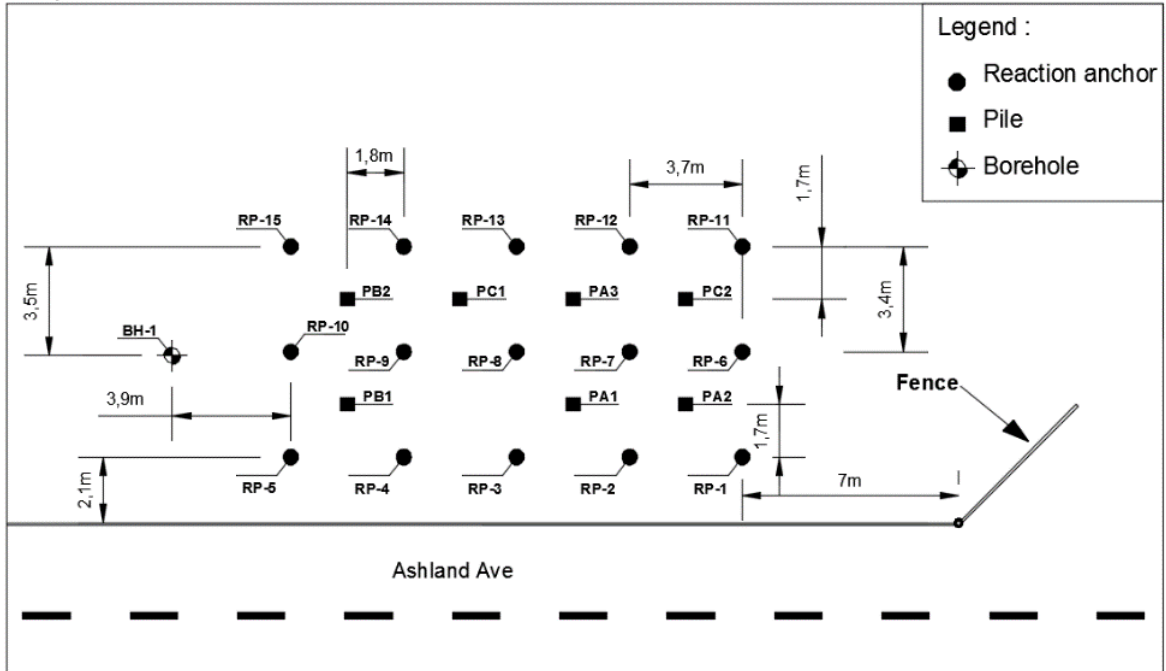
Figure 6 - 2: Site layout showing the drilled borehole location

The soil profile as shown from the borehole log can be described as follow:

A top 0.5m thick layer of silty sand underlain by a 4.5 thick silty sand layer, followed by a 1m thick gravelly sand layer then a 3m thick coarse sand layer with lower percentage of silt. Finally, a hard silty till layer was encountered to the end of the borehole. The ground water table was found at 3.5m below the ground surface.

6.3.2 Field tests

During the borehole drilling, Standard Penetration Test (SPT) was carried out at 0.75m intervals with blow count measurements. The corrected values N_{60} for hammer efficiency and other field procedure conditions were obtained, i.e.,(Skempton, 1986):

N_{60}= **Measured number of blows x** $\dfrac{C_R C_S C_B E_m}{0.6}$ (6 - 1)

where

σ'_v is the effective overburden stresses;

C_S is sampler correction factor, equal to 1.2 considering sampler without liner;

C_R is drill rod length correction factor, equal to 0.75 for depths less than 4m;

C_B is borehole diameter correction factor, equal 1.15 for borehole diameter D=200mm;

E_m is hammer efficiency factor, equal to 0.8 (Bowles, 1996).

The corrected blow count values for overburden pressure effect N'_{60} was calculated as follows (Liao and Whitmann, 1986):

$$N'_{60} = N_{60} \sqrt{\frac{100}{\sigma'_v}} \qquad (6 - 2)$$

The resulting variation of N'_{60} with depth is presented in Figure 6 - 3 along the top 4m, of main interest in this study.
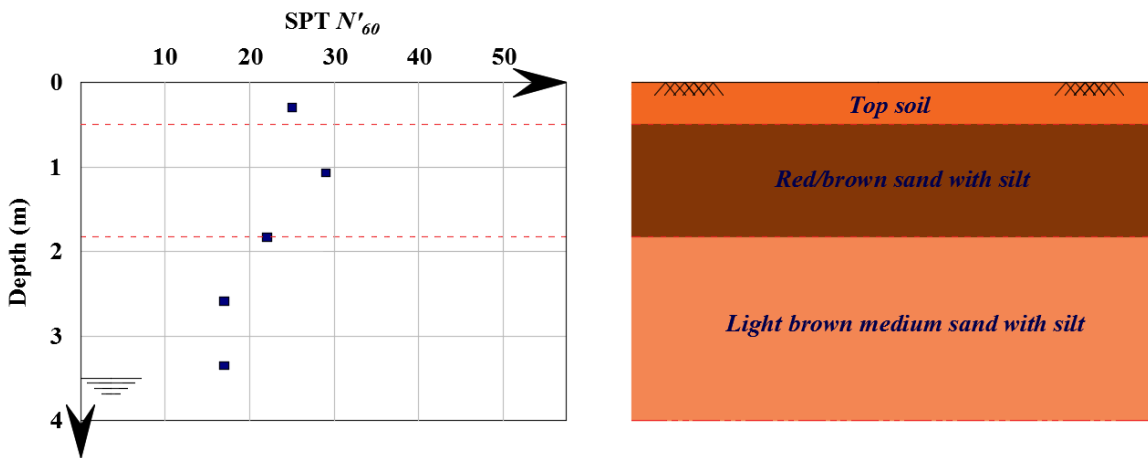
Figure 6 - 3: Variation of SPT N'_{60} with depth

The in-situ soil unit weight was measured using the sand-cone device (ASTM D1556, 2007). The top 0.5m of soil was first excavated and then two sand-cone tests were done over the underlying layer. An average measured bulk density of 16.5kN/m^3 was found.

6.3.3 Laboratory testing

Fifteen disturbed samples were retrieved from the SPT split-spoon sampler, and were transported and tested at The University of Western Ontario soil laboratory. The performed tests included sieve analysis, determination of the specific gravity G_S, measurement of water content W_c; determination of Atterberg limits; and direct shear tests.

Soil classification and index properties

The resulting gradation curve from the sieve analyses, performed according to ASTM C136 (2006) is shown in Figure 6 - 4.
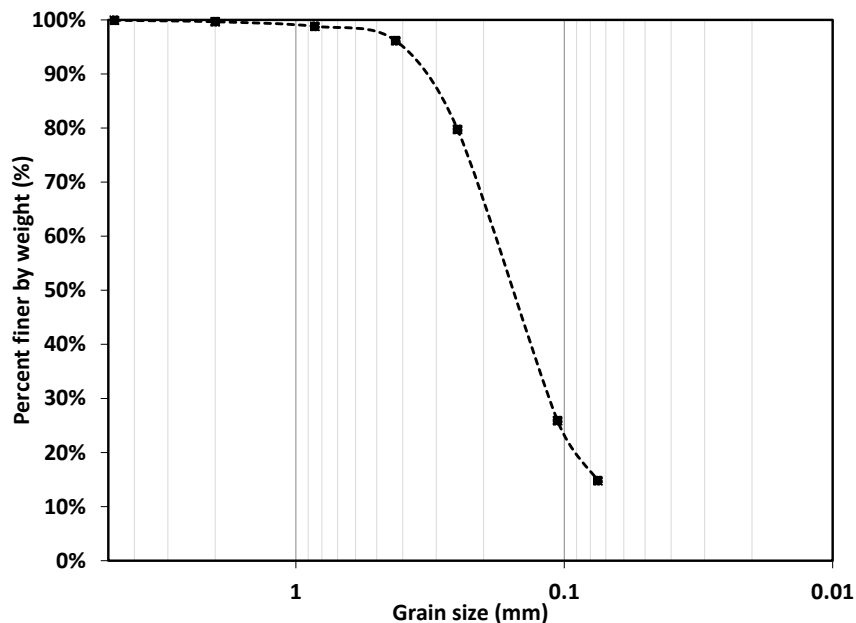
Figure 6 - 4: Grain size distribution for a disturbed sample retrieved 1.05m below the ground surface

Considering the short piles' length (3.1m) and their even shorter embedded depth, the soil sample at 1.05m depth was deemed representative of soil properties along the pile shaft. The representative sample had 14.8% fines with almost no gravel. Atterberg limits of 3 tested samples showed average measured liquid and plastic limits of 29% and 6%, respectively (ASTM D4318, 2010). According to the Unified Soil Classification System USCS (ASTM D2487, 2011), the soil layer is hence classified as silty sand (SM). The

average in-situ W_c was 20.5%. The average determined G_s of two extracted samples at depths of 1.05m and 4.8m was 2.71.

Soil shear strength parameters

Direct shear tests (ASTM D3080, 2011) were conducted to measure the soil shear strength parameters of soil samples retrieved at 0.6m and 1.08m below the ground surface. The tests were carried out with horizontal rate of feed of 0.406mm/min. Same unit weight as the field measured value was set for the tested samples.

The test measurement, i.e., the shear stress, normal stress, vertical displacement and horizontal displacement are shown in Figure 6 - 5 with the measured residual and peak strength values shown.
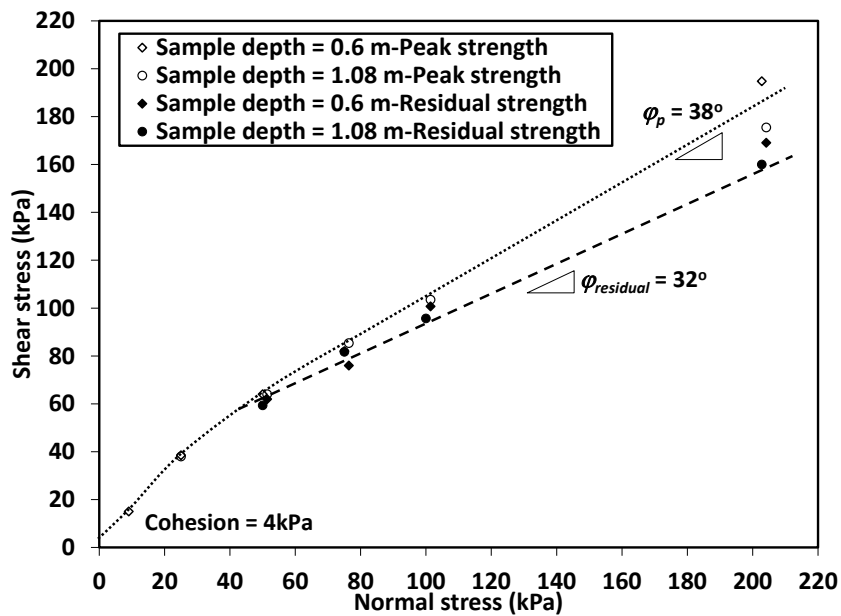
(a)
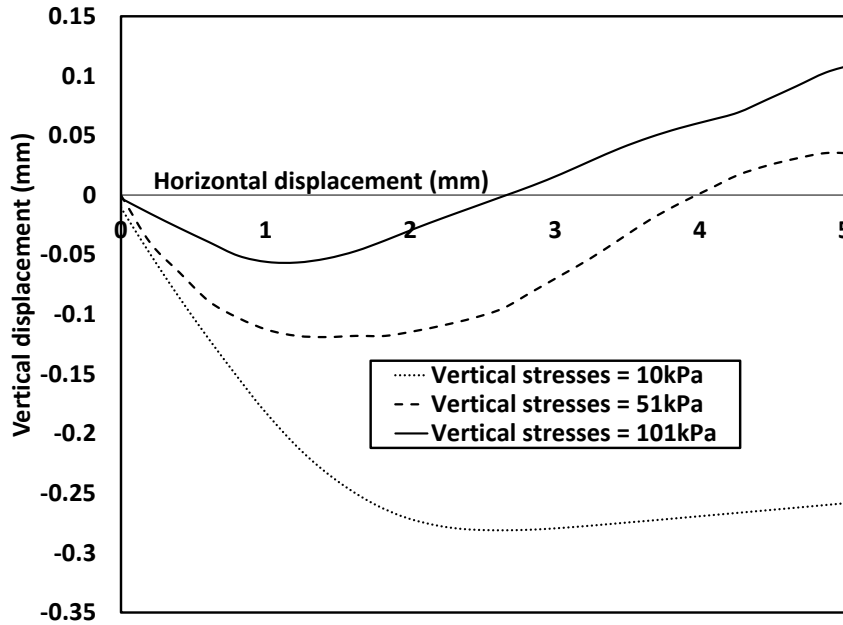
(b)
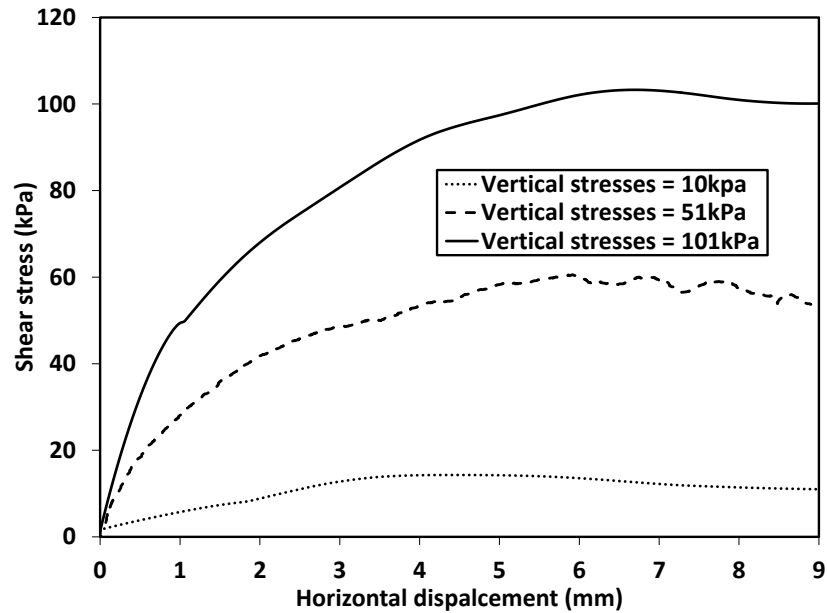
(c)

Figure 6 - 5: Direct shear tests results (a) Shear vs normal stresses; (b) Vertical displacement vs horizontal displacement; (c) Shear stress vs horizontal displacement

A bilinear shear-normal stress relation was shown with the chart slope changing at a normal stress of 20 kPa.

The following parameters were determined from the tests results:

Effective cohesion, $c' = 4$ kPa;

Residual angle of internal friction $\varphi_{residual} = 32^{\circ}$;

Peak angle of internal friction $\varphi_p = 38^{\circ}$.

The determined angle of internal friction lies within the upper bound of the relevant range for the measured SPT values at the same specimens location as typically found in the literature due to the high sand particles angularity.

Relative density and stiffness parameters

The relative density, D_r of the soil deposits was correlated to N'_{60}, i.e.,(Mayne *et al.*, 2002):

$$D_r = 100 \sqrt{\frac{N'_{60}}{60}} \qquad \qquad \textbf{(6 - 3)}$$

The calculated D_r values range between 50 to 70% along the top 4m. Hence the soil can be classified as medium dense to dense along the pile length (Bowles, 1996).

Measurement of the over-consolidation ratio, OCR, of the soil was not possible in absence of retrieved undisturbed soil samples. Instead, the apparent preconsolidation pressure σ_p' was correlated to N_{60}, i.e.,(Mayne, 1992):

$$\sigma_p' = 0.47 \; (N_{60})^m \; Pa \qquad \qquad \textbf{(6 - 4)}$$

where Pa is the atmospheric pressure and $m = 0.6$ to 0.8 for silty sands (Mayne, 2006).

Using the determined σ_p' values and the calculated initial in-situ overburden stresses, the approximate calculated OCR value along the top 4 m is 6.0. This value is attributed to the fact that the test site is used for storage of steel tanks (i.e. heavy loads at the surface).

Considering the significant scatter between the available correlations in literature between the measured SPT and the soil's E (Kulhawy and Mayne, 1990), a first order estimator of E_s for overconsolidated sand can be correlated to the N_{60}, i.e.,(Kulhawy and Mayne, 1990):

$E_s/Pa = 15N_{60}$ (6 - 5)

Eq. 6 - 5 gives E_s values between 30 and 60 MPa for the top 4m of soil. It should be noted, however, that the above values reflect the soil state prior to the piles installation, whereas the post–installation values are of main interest to this study. Accordingly, the recommended E_s values by Poulos and Davis (1980) for driven piles in sand were considered as a preliminary estimate. They suggested E_s values of 55~70MPa for medium dense sand and 70~100MPa for dense sand. Therefore, an average value of 70MPa was considered in this study. For analysis purposes, they also suggested that it is appropriate to consider a single average E_s value along the pile shaft and a greater value below the driven piles' toe. This assumption is also accepted for the present case, especially considering the relatively short embedment depth.

For loose to dense sands, Poisson's ratio ν ranges between 0.2 and 0.4 (AASHTO, 2002), thus 0.3 is considered for this study. Finally, considering the calculated average OCR value, the average coefficient of earth pressure at rest prior to the pile installation can be given by (Mayne and Kulhawy, 1982):

$K_{o\text{-}OC} = (1\text{-}Sin\varphi)OCR^{(1\text{-}sin\varphi)} = 0.76$ (6 - 6)

Table 6 - 2 summarizes the main representative parameters of the soil along the piles shaft.

Table 6 - 2: Representative soil parameters

Depth (m)		φ_p (°)	C' (kPa)	Specific gravity G_s	Water content W_c (%)	ν	E_s (MPa)	γ_b (kN/m³)	D_r (%)
From	To								
0	0.5	36	4	2.71	20.5	0.3	70	16.5	55
0.5	4	38							

The post-installation parameters, accounting for the effects of the installation torque and the top soil pre-drilling, were calibrated and verified numerically using the monotonic axial and lateral field tests results as shown in Chapters 3, 4 and 5.

6.3.4 Test piles

Seven hollow closed ended piles with configurations as shown in Figure 6 - 6 were installed in silty sand (SM) profile. Three piles were of configuration A, two of configuration B and two of configuration C. Piles of configurations A and B were made of ductile iron with grainy rough surface as shown in Figure 6 - 7. The straight shaft piles of configuration C were made of smooth steel and were considered for comparison purposes. The wall thickness of all configurations is 5.5mm.
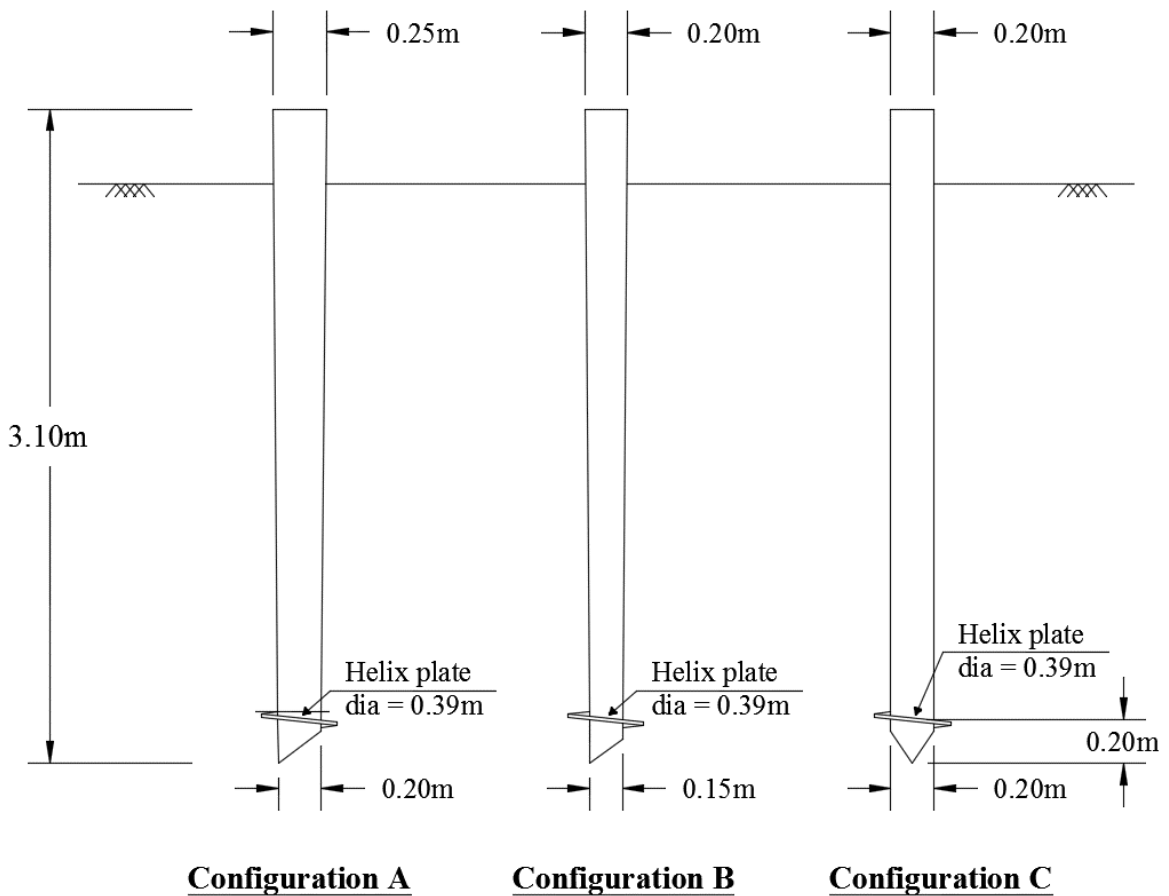
Figure 6 - 6: Tested piles configurations
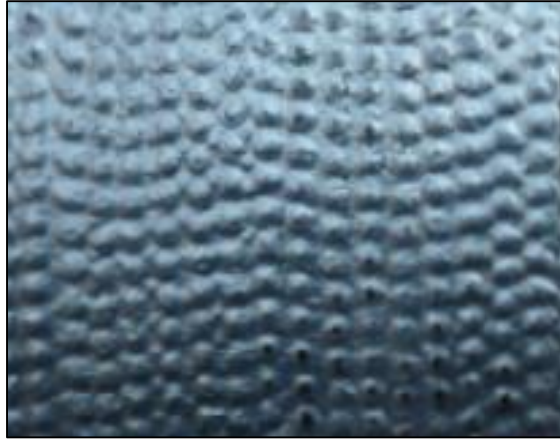
Figure 6 - 7: Image of the tapered piles external surface-configurations A and B (Seamless-Pole-Inc., 2010)

6.3.5   Instrumentation and test setup

Two load test setups comprising a set of reaction beams were used as shown in Figure 6 - 8 (a) and (b) for compressive and uplift tests, respectively. The load was applied to the test pile using a hydraulic jack pushing against the reaction beam. To measure the pile head displacement, four LVDTs were mounted on the loading plate corners as shown in Figure 6 - 9.
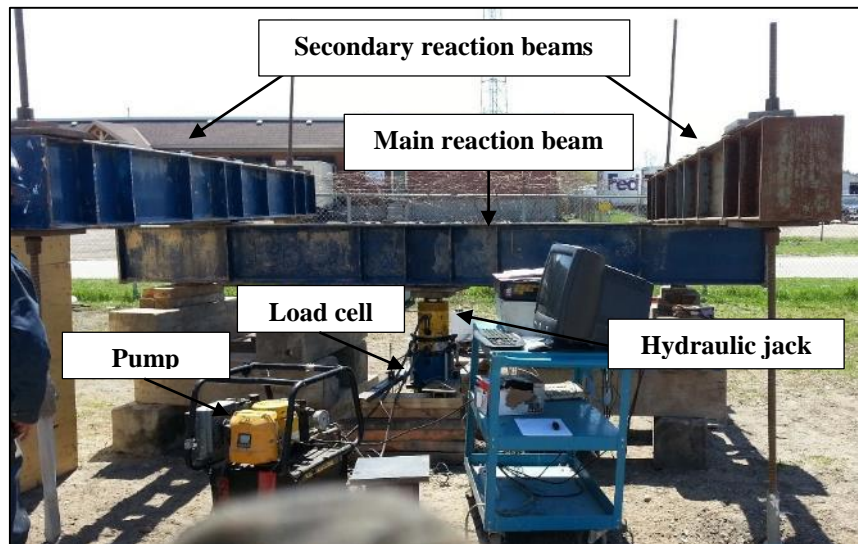
(a)
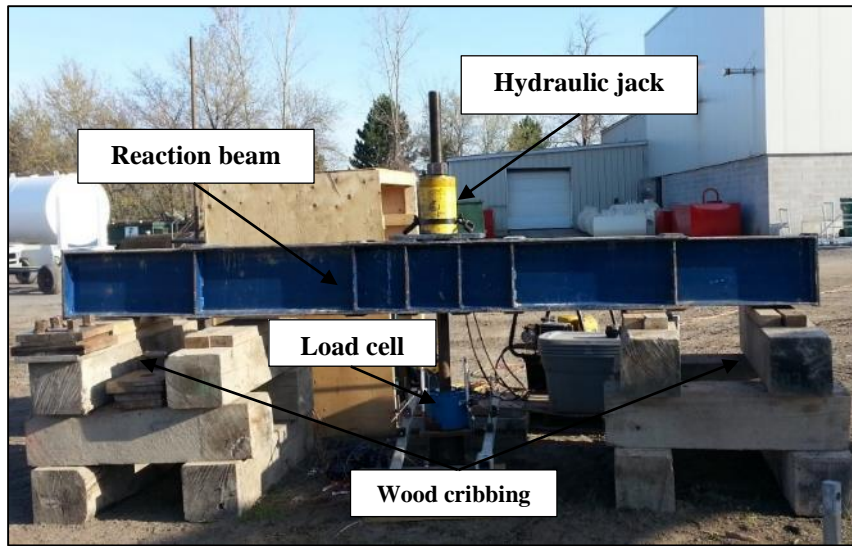
(b)

Figure 6 - 8: The used setup for (a) compressive testing; and (b) uplift testing

Figure 6 - 9: Mounted LVDTs measuring pile displacement for axial tests

Each test pile was instrumented with eight equally spaced electrical resistance strain gauges to evaluate the load transfer mechanism. The strain gauges were mounted at locations as shown in Figure 6 - 10 (a). They were fixed on specially machined pockets of 1 mm depth as shown in Figure 6 - 10 (b). In order to minimize the lead wires tearing and gauges damage during installation, the wires were passed from inside the pile through a small

groove as shown in Figure 6 - 10 (b). The load cell, strain gauges and the LVDTs were connected to a data acquisition system recording the readings every 1 second.

(a)   (b)
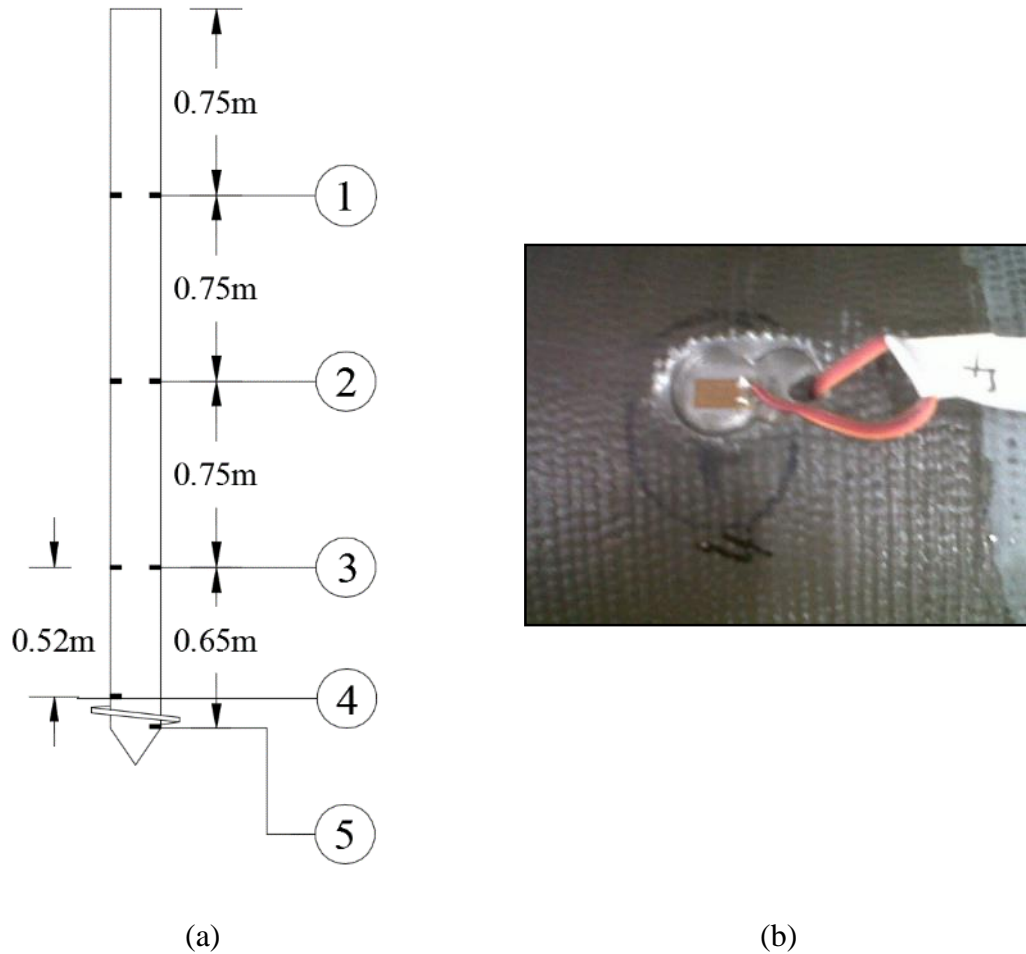
Figure 6 - 10: Strain gauges (a) Locations; (b) Pockets

6.3.6 Installation procedure

A mechanical torque head (Hitachi UH07 rig) was used to install the piles. The torque was applied employing steel cap bolted to the pile head. Images for the loading caps used for compressive and uplift tests are shown in Figure 6 - 11 (a) and (b), respectively. To facilitate the pile vertical alignment, the soil along the top 0.3m to 0.45m was predrilled prior to the piles installation.
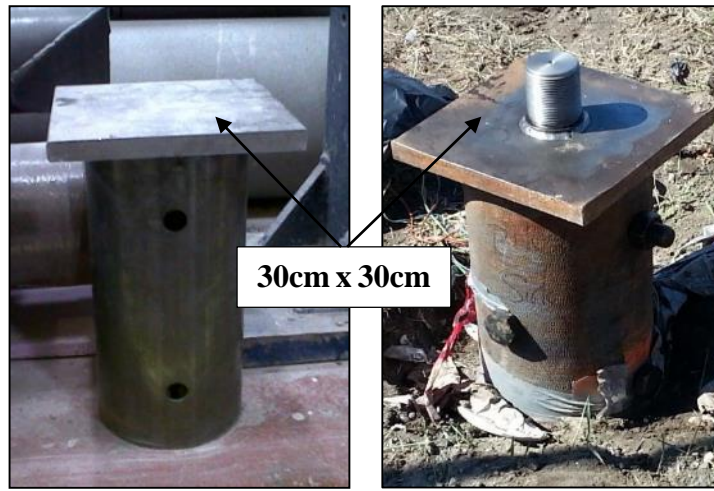
(a)	(b)

Figure 6 - 11: Field images of loading caps (a) used for compressive loading; (b) used for uplift loading

Following the installation process, the inclination angle of each pile head with the vertical axis was measured to check the piles verticality. The maximum inclination angle for all piles (in any direction) was found to be less than 2 degrees. The piles free (unsupported) lengths are summarized in Table 6 - 3.

Table 6 - 3: Pile head elevation above ground at the start of the pile testing

Pile #	Cyclic compression	Cyclic uplift
PA1	0.48	0.39
PA2	061	0.54
PA3	0.35	0.39
PB1	NA	NA
PB2	0.71	0.72
PC1	0.45	0.38
PC2	0.36	0.40

6.3.7 Load test sequence and test procedure

Two different loading sequences were adopted for the axial tests as presented in Table 6 - 4.

Table 6 - 4: Axial testing sequence

Pile	Testing sequence	Sequence
A1	Monotonic uplift followed by cyclic uplift followed by cyclic compression	A
A2	Monotonic uplift followed by cyclic uplift followed by cyclic compression	A
A3	Cyclic compression followed by monotonic compression followed by cyclic uplift	B
B1	Monotonic uplift followed by cyclic uplift followed by cyclic compression	A
B2	Cyclic compression followed by monotonic compression followed by cyclic uplift	B
C1	Monotonic uplift followed by cyclic uplift followed by cyclic compression	A
C2	Cyclic compression followed by monotonic compression followed by cyclic uplift	B

For all the performed tests, piles were initially loaded in four equal increments up to the expected static design load Q_d. This was followed by a set of fifteen one-way load cycles, each completed in 2 min where the load varied from 70% to 130% of Q_d. A number of piles (5 in compression and 2 in uplift) were also subjected to a second set of loading cycles with loads ranging from 55% to 145% of Q_d as illustrated in Figure 6 - 12.
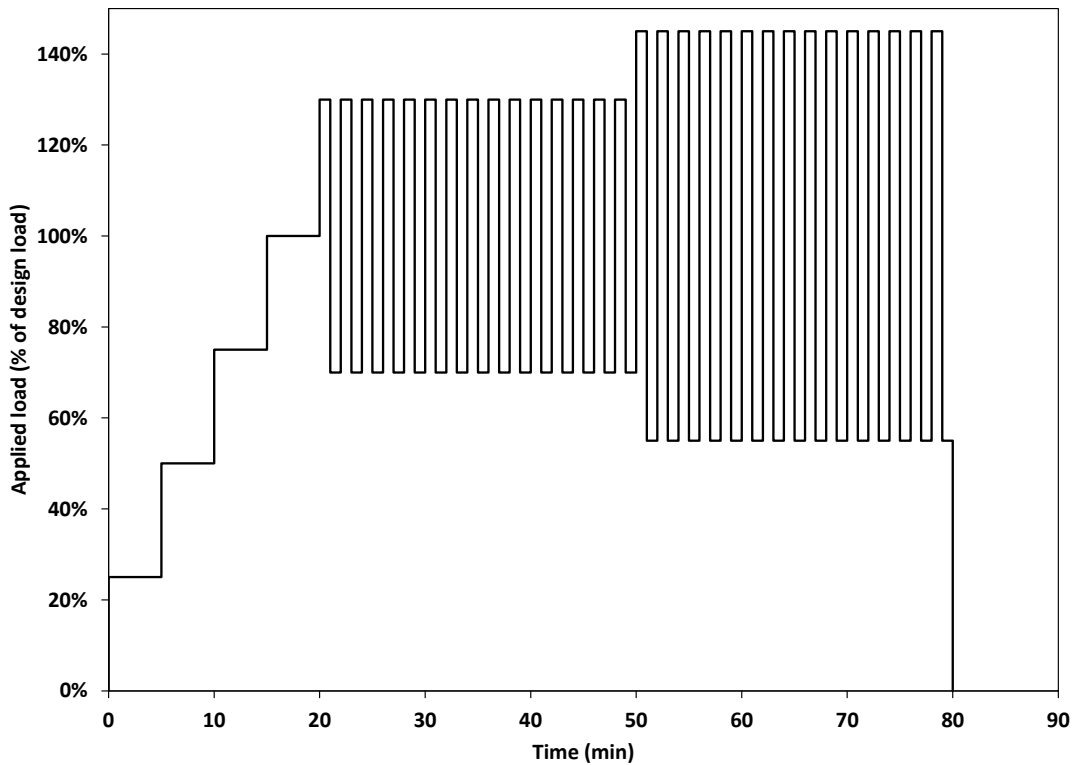
Figure 6 - 12: Axial cyclic loading pattern

6.4 Results and discussion

6.4.1 Pile surface roughness

A profilometer was used to scan the pile external surface and to plot longitudinal and radial surface profiles along the pile surface in order to quantitatively evaluate the effect of the surface roughness on the interface behavior and therefore on the piles' shaft resistance. The resulting profiles are as shown in Figure 6 – 13.
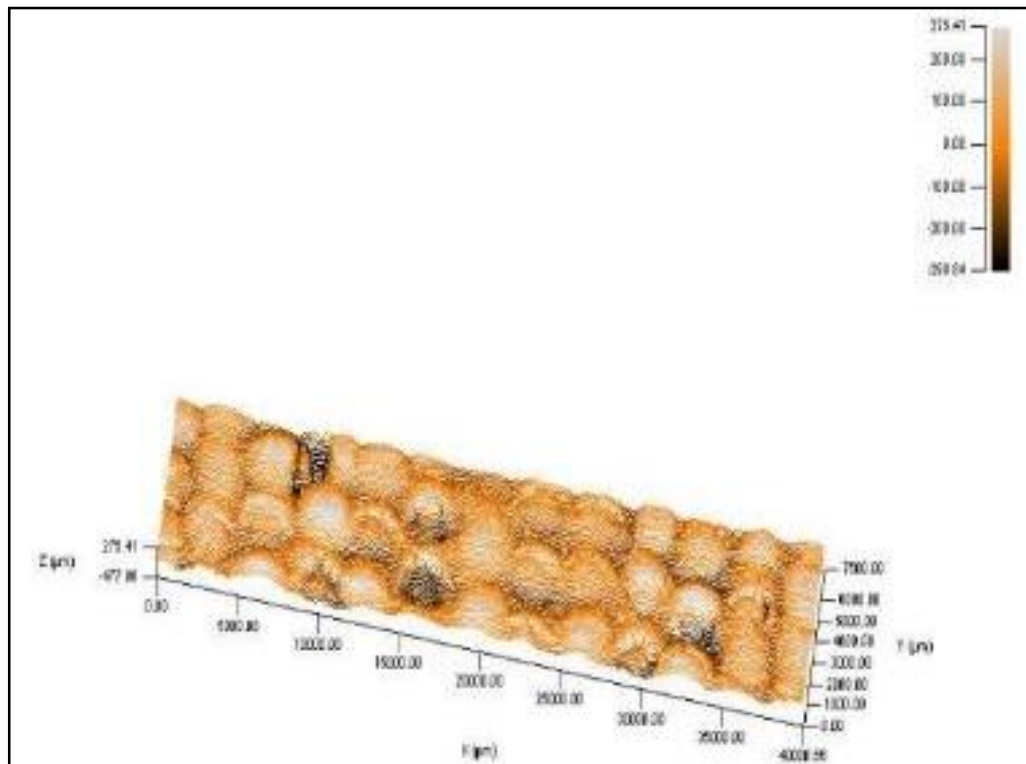
(a)
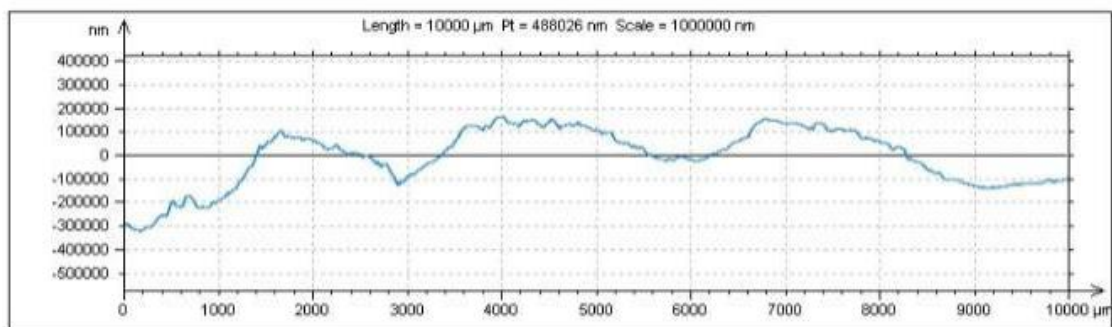
(b)
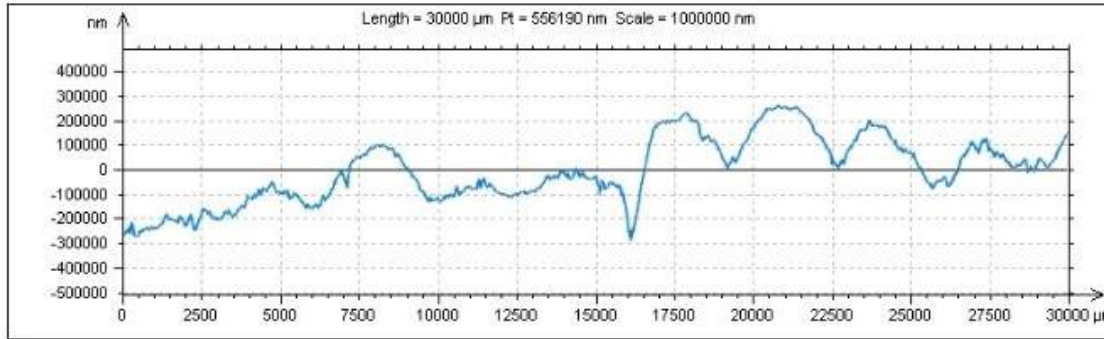
(c)

Figure 6 - 13: Piles external surface –configurations A and B: (a) Three-dimensional surface scan; (b) Surface profile along 100 mm length - longitudinal direction; (c) Surface profile along 30 mm length - radial direction

The measured surface roughness R_a was 8783nm. Two distinct interface conditions were identified by Lings and Dietz (2005) who studied the sand-steel interface strength considering their relative roughness, defined as (R_a/D_{50}) where D_{50} is the soil median particle size. Dilatant behavior associated with particles rolling would govern for relative roughness values greater than 0.003, whereas at lower values, non-dilatant behavior associated with particles sliding would be expected. Considering the measured D_{50} of the soil along the pile-soil interface determined from Figure 6 - 4 and the measured R_a value, the resulting relative roughness is equal to 0.052 thus depicting a dilatant behavior along the tapered pile interface. Furthermore, Dove and Jarrett (2002) showed that, for granular soils in contact with rough surfaces, some passive resistance may be mobilized in case of large asperity spacing and height compared to the soil grain size.

6.4.2 Field tests

6.4.2.1 Cyclic compression results

6.4.2.2 Load displacement curves

The load-displacement curves for piles subjected to initial cyclic compression and those subjected to initial cyclic uplift are shown in Figure 6 - 14 (a) and (b), respectively. The

helical plate of PB1 was cracked/damaged during the initial uplift test, so the results of its cyclic compression shown in Figure 6 - 15 represent the behavior after the helical plate was damaged. Thus, the load-displacement curve displayed in Figure 6 - 15 does not present the expected performance of the tapered helical pile. This can be further illustrated by comparing its results with the response of intact piles.
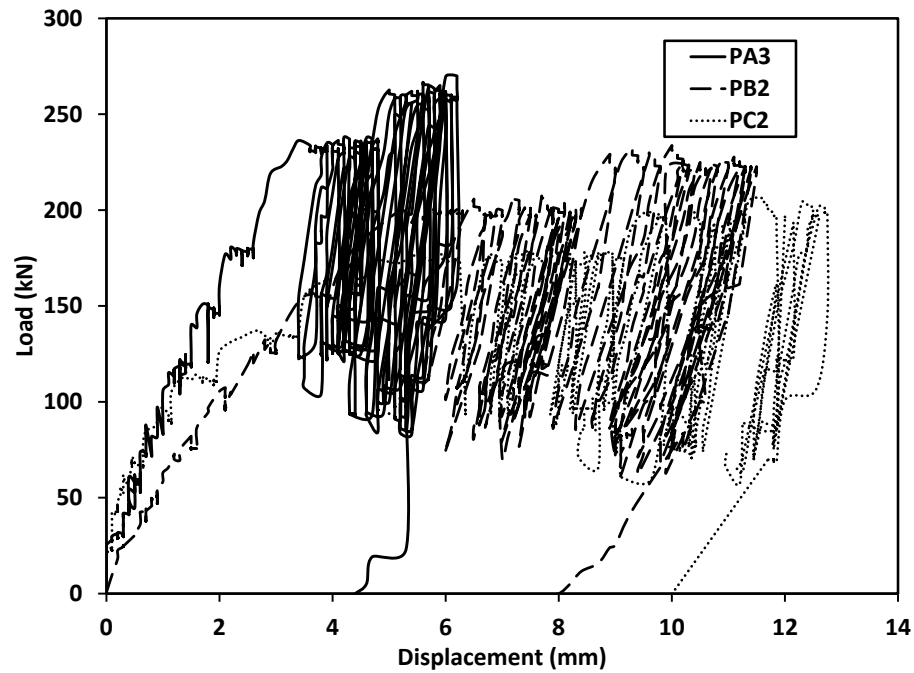
(a)
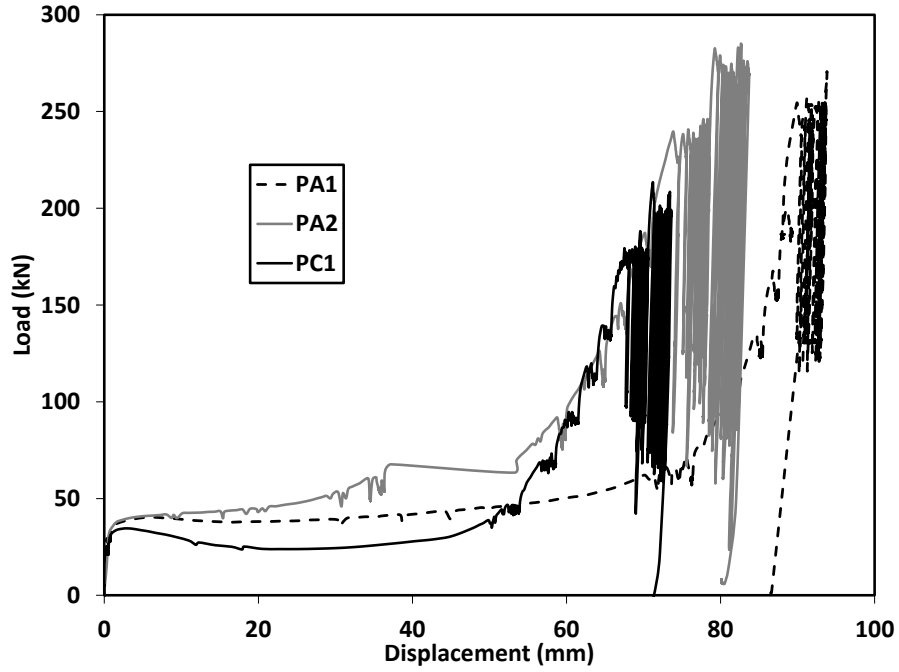
(b)

Figure 6 - 14: Load-displacement curve-cyclic compression- (a) Firstly tested in cyclic compression; (b) Prior tested in cyclic uplift
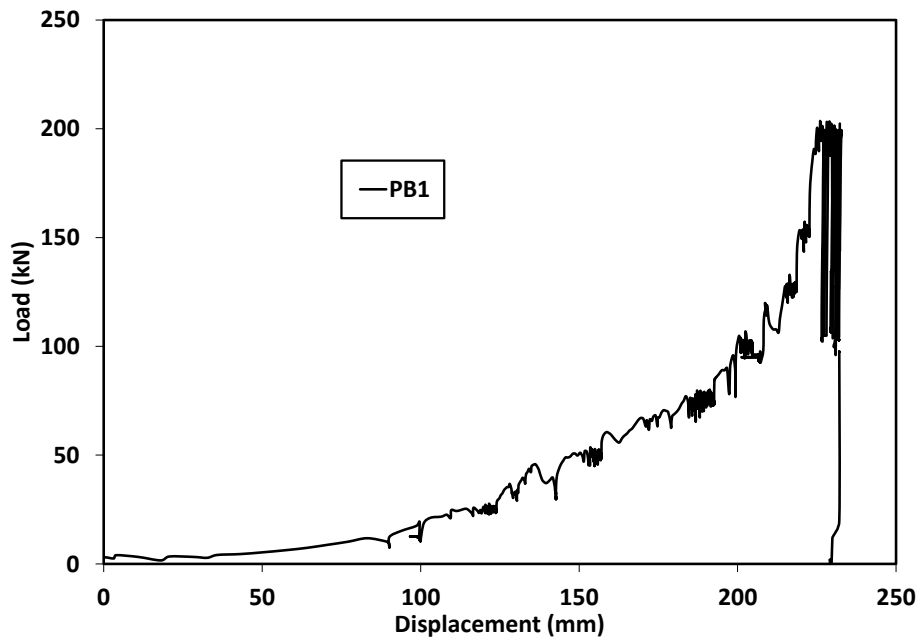
Figure 6 - 15: Load-displacement curve-cyclic compression test of PB1

The segment of monotonic load-displacement, prior to the cyclic loading, for piles PA3, PB2 and PC2 exhibited the same behavior characterized by an initial linear part followed by a non-linear zone extending up to the start of load cycling as shown in Figure 6 - 14 (a). PA3 showed the stiffest behavior thanks to the greater developed resistance along the tapered shaft profile as discussed in Chapter 3. PC2 showed an initial stiffer behavior than PB2. This can be attributed to the greater embedded length and the larger average diameter compared to PB2.

On the other hand, the monotonic loading portions of PA1, PA2 and PC1 following cyclic uplift tests exhibited different behavior. The load-displacement curves were characterized by an initial linear zone extending to applied load of 30~32kN, where the resistance is mainly developed by the shaft friction. As the applied load increased, a slack zone characterized by low stiffness developed where the helical plate/toe bearing resistance was not fully mobilized due to the loosened soil zone below the helical plate and pile toe. This loosened soil zone resulted from the gapping/cave in process during the prior uplift tests. This low stiffness zone extended to 75mm, 52mm and 51mm for PA1, PA2 and PC1, respectively. The larger low-stiffness movement for PA1 resulted from the greater uplift displacement during the prior monotonic uplift testing compared to PA2 and PC1 as previously shown in Chapter 4. As the load increased, the loose soil was re-compacted and the stiffness significantly increased up-to the start of the cyclic loading.

For PB1 that had a detached/cracked helix, unsuccessful trials were made to test the pile in cyclic uplift following the monotonic uplift tests. During these trials, the pile dislodged from the ground, which further released the confining pressure, hence reducing the shaft resistance. This effect was clearly demonstrated in the load-displacement curve shown in Figure 6 - 15, where a negligible initial linear zone was observed along with a significantly extended low-stiffness zone compared to PA1, PA2 and PC1.

To better illustrate the cyclic performance of the piles, the development of the accumulated displacements with number of loading cycles is presented in Figure 6 - 16.
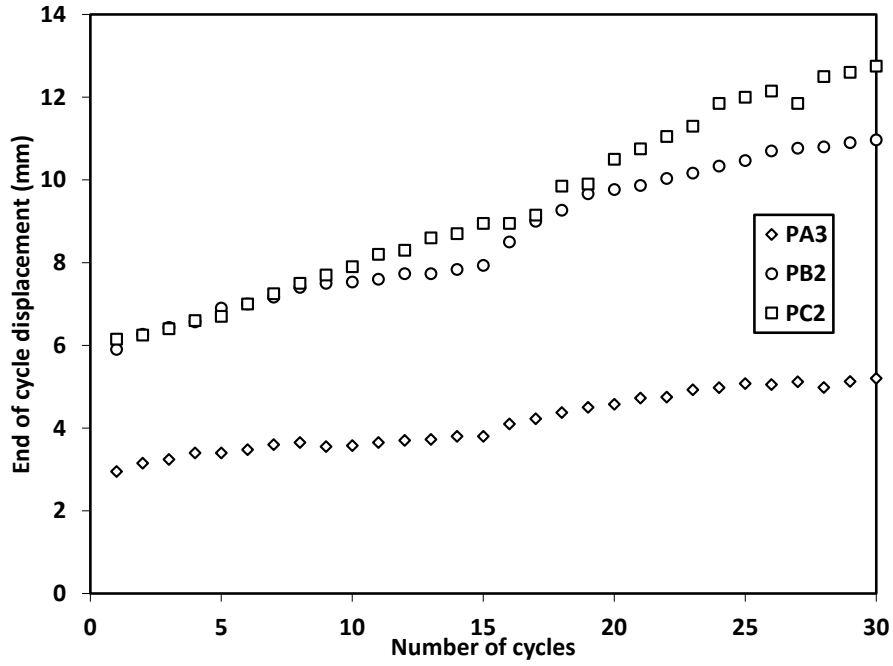
(a)
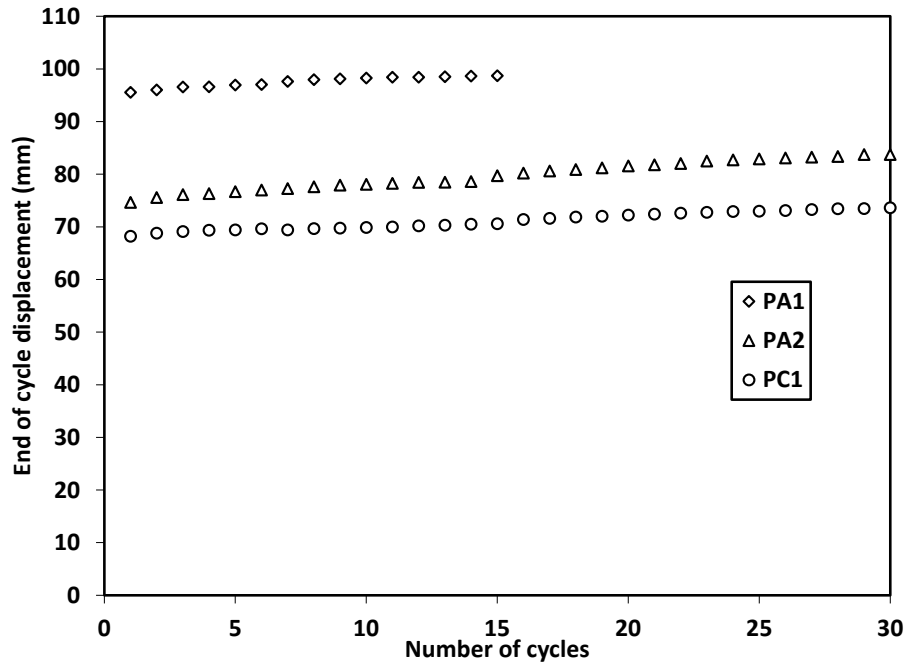
(b)

Figure 6 - 16: End of cycle's settlement-cyclic compression tests (a) Firstly tested in cyclic compression; (b) Previously tested in cyclic uplift
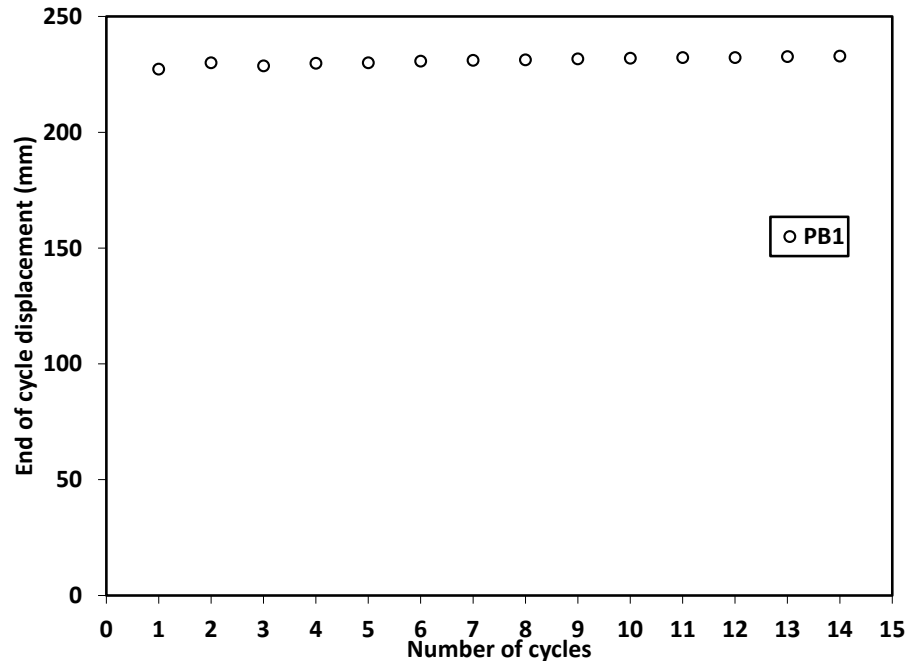
Figure 6 - 17: End of cycle's settlement-cyclic compression test-PB1

For the piles subjected initially to cyclic compression, PA3, PB2 and PC2, the cyclic displacements after the first 15 loading cycles (70% to 130% of Q_d) were 0.9mm, 2.0mm and 2.8mm, while the displacements for the following 15 cycles (55% to 145% of Q_d) were 1.1mm, 2.5 and 3.8mm, respectively. The lower cumulative displacements of the tapered piles indicate the superiority of the tapered piles (configurations A and B) over the straight shaft ones (configuration C). It was also observed that the rate of cyclic displacement for PA3 and PB2 decreased with the number of loading cycles; i.e. most of the displacement occurred within the first few loading cycles due to the compaction of the surrounding/bearing soils with the repetitive loading. This behavior occurred to a much smaller extent for PC2. This behavior is further underscored by comparing the responses of PC2 and PB2. They displayed comparable performance during the first few loading cycles, however, PC2 experienced greater displacement as the cyclic loading continued.

For the piles tested following cyclic uplift loading, the first 15 cycles of PA1, PA2, PB1 and PC1 resulted in 3.2mm, 5.1mm, 5.63mm and 2.4mm cyclic displacements, respectively. The piles PA2 and PC1, which were subjected to further 15 load cycles resulted in 3.5mm and 2.23mm, respectively. Unlike the piles subjected to virgin cyclic

196

compression loads, the straight shaft piles performed better than the tapered piles, notwithstanding that the tapered ones were subjected to higher loading amplitudes. This is attributed to the release of confining pressure due to uplift loading on the tapered shafts and hence reducing the shaft resistance.

To evaluate the effect of cyclic loading on the pile stiffness, the pile axial stiffness K during each load cycle was calculated as:

$$K = \frac{Q_{max} - Q_{min}}{\delta_{max} - \delta_{min}}$$

(6 - 7)

where Q_{max} and Q_{min} are the maximum and minimum applied loads during each load cycle, δ_{max} and δ_{min} are the corresponding maximum and minimum displacements, respectively. The variation of K with the number of load cycles is plotted in Figure 6 - 18.
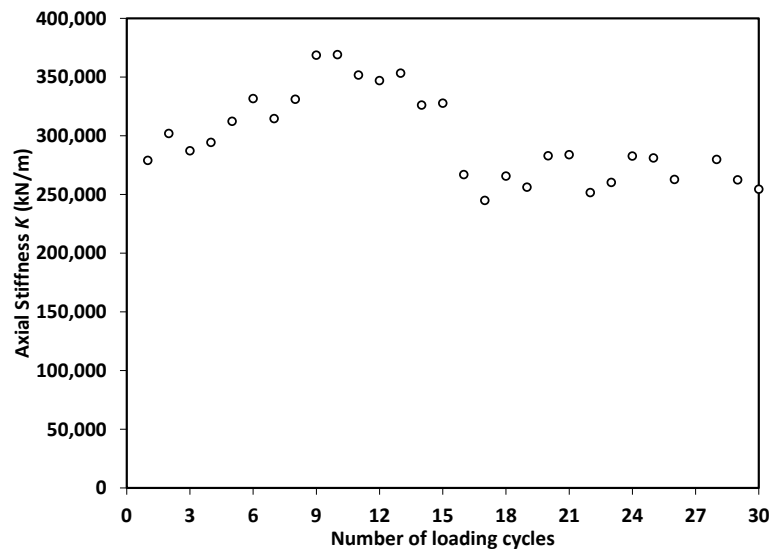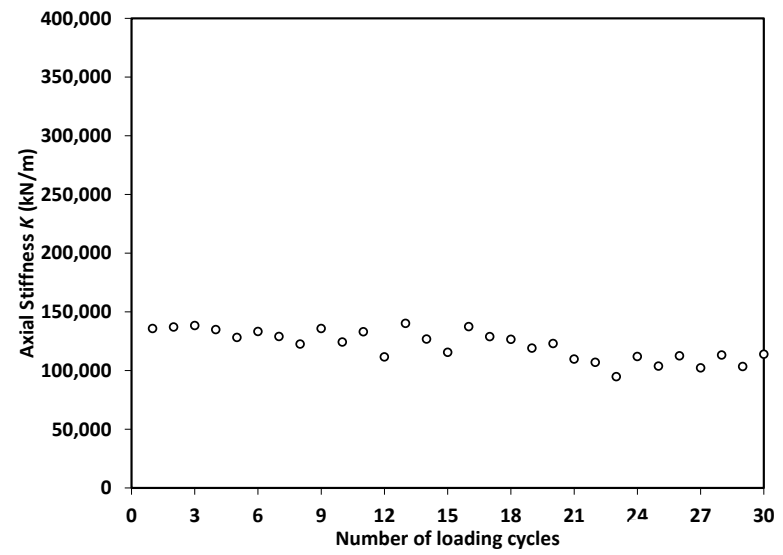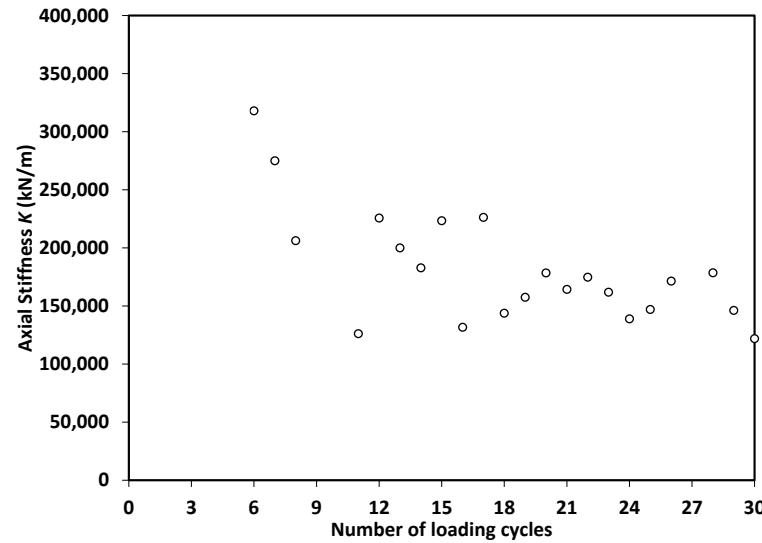
Figure 6 - 18: Variation of the axial stiffness with loading cycles-cyclic compression tests (a) PA3; (b) PB2; (c) PC2
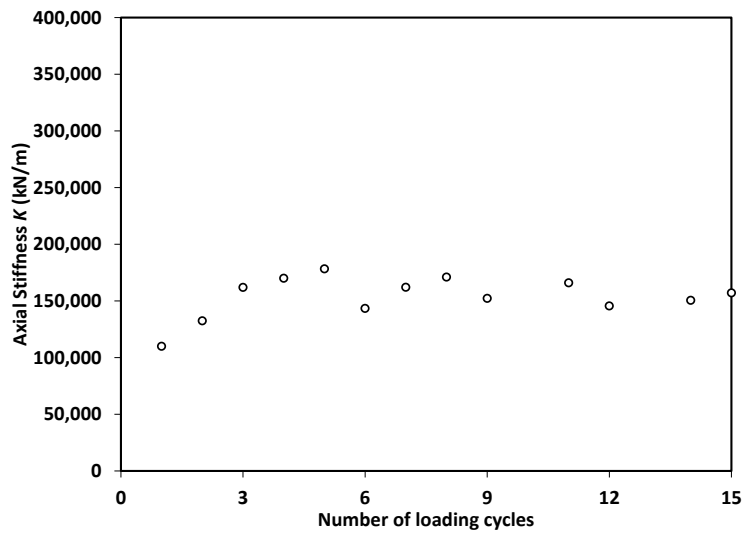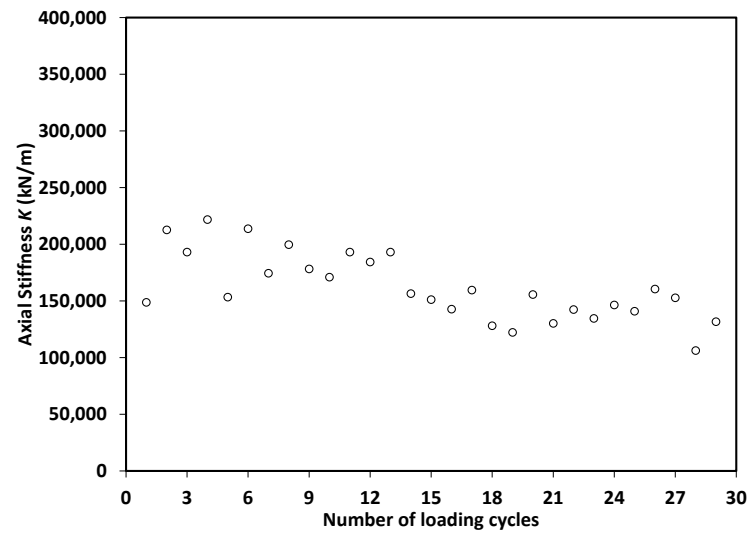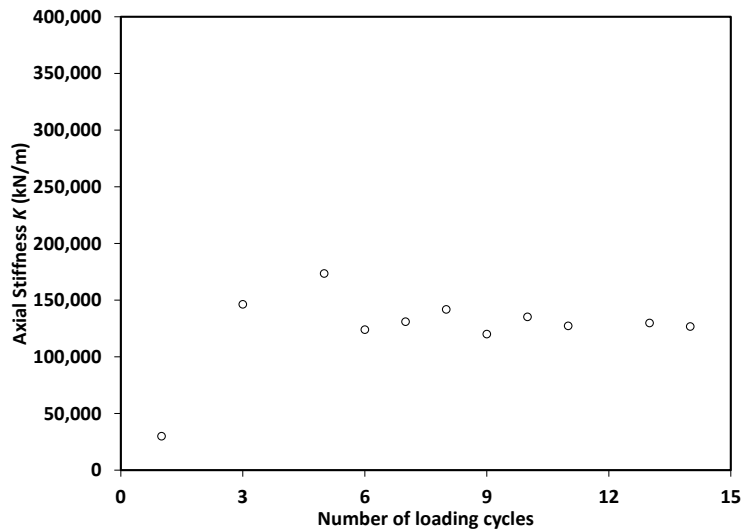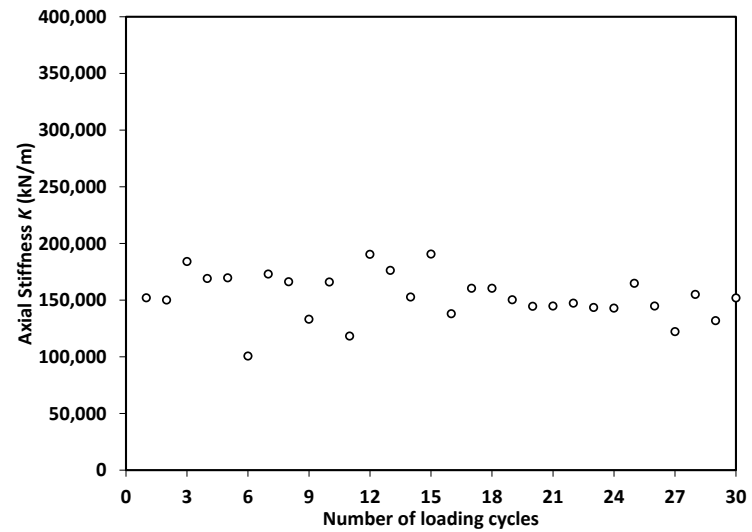
Figure 6 - 19: Variation of the piles axial stiffness with loading cycles-cyclic compression tests (a) PA1; (b) PA2; (c) PB1; (d) PC1

199

Piles PA3 and PB2 (loaded in cyclic compression first) exhibited same behavior, their stiffness increased with number of load cycles but at a decreasing rate during the first 9 to 10 loading cycles, owing to the positive effect of the tapered profile, which compacted the soil during loading. At higher loading amplitudes, (load cycles 15 to 30) the rearrangement of the soil particles decreased the soil stiffness initially then reached an almost constant value. Due to some technical problems in the data acquisition system during the testing of PC2, some data points were masked during the first five loading cycles and therefore calculation of the stiffness was not possible. Similar to PA3 and PB2, it is possible that PC2 would follow the same trend and that its stiffness would increase during these first loading cycles. Starting from the 6th loading cycles, the available reading showed a stiffness degradation with more prominent effect than the tapered piles.

While the initial cyclic stiffness of PC2 was higher than that of PB2 due to larger embedded length, the stiffness of the tapered pile increased to become almost equal to that of PC2, even though PB2 was subjected to higher load amplitude.

A similar trend was observed for PA1, PA2 and PB1, which were initially tested in cyclic uplift. The results showed the negative effect of the uplift loading on tapered piles, which reduce the soil confinement and consequently lower shaft resistance and stiffness were observed for PA1 and PA2 compared to PA3.

It can be generally noted that piles tested in compression first displayed higher average stiffness, whereas piles subjected to uplift loading first exhibited less stiffness degradation (e.g. PC1 had less stiffness degradation compared to PC2). This may be attributed to the fact that the soil along the shaft has already degraded during the previous cyclic uplift tests.

Following the pile unloading, significant permanent settlements were observed, which reflected considerable plastic strains in the soil. For example, only 27%, 27% and 21% of the maximum displacement were recovered for PA3, PB2 and PC2, respectively. Even higher plastic deformations were shown for piles previously tested in cyclic uplift as only 7%, 4%, 1% and 2% of the maximum displacement were recovered for PA1, PA2, PB1 and PC1, respectively.

6.4.2.3 Load transfer mechanism

The load transferred at the different strain gauges locations P_{zi} was calculated as follows:

$$P_{zi} = \varepsilon A_{pi} E_p \qquad\qquad\qquad\qquad\qquad (6 - 8)$$

where ε is the measured strain, A_{pi} is the cross-sectional area of the pile at the strain gauge location (varies with depth), and E_p is the elastic modulus of the pile material.

The stress reversal for some of the tested piles damaged the strain gauges bonding agent and the harsh installation conditions resulted in losing the readings of some strain gauges. The measured distribution of the axial force along the pile shaft for different applied load levels are presented in Figure 6 - 20.
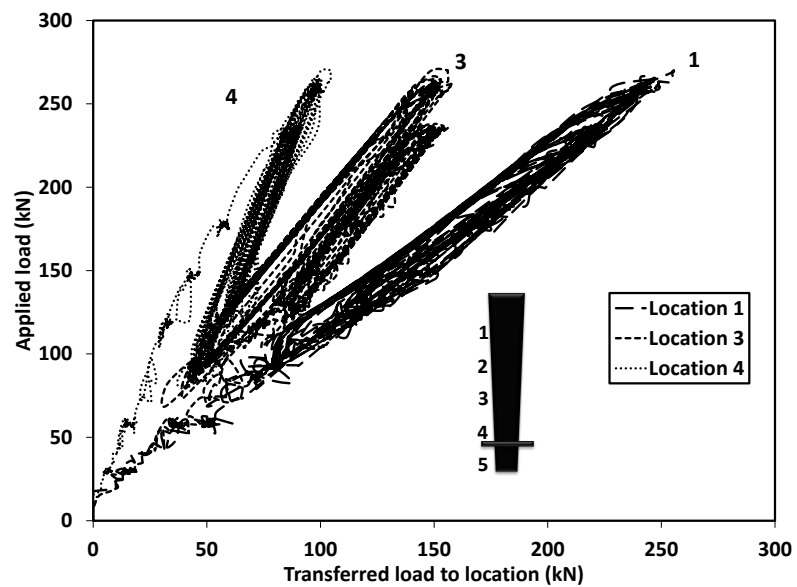
(a)
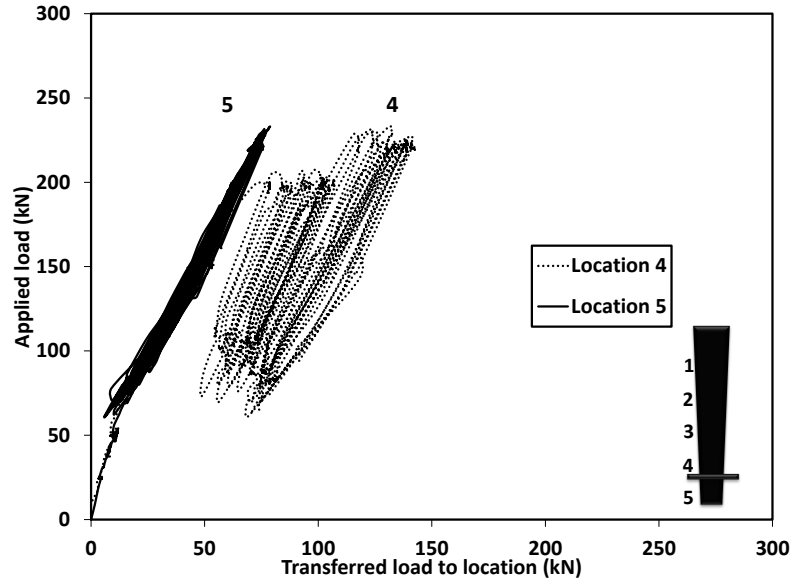
(b)
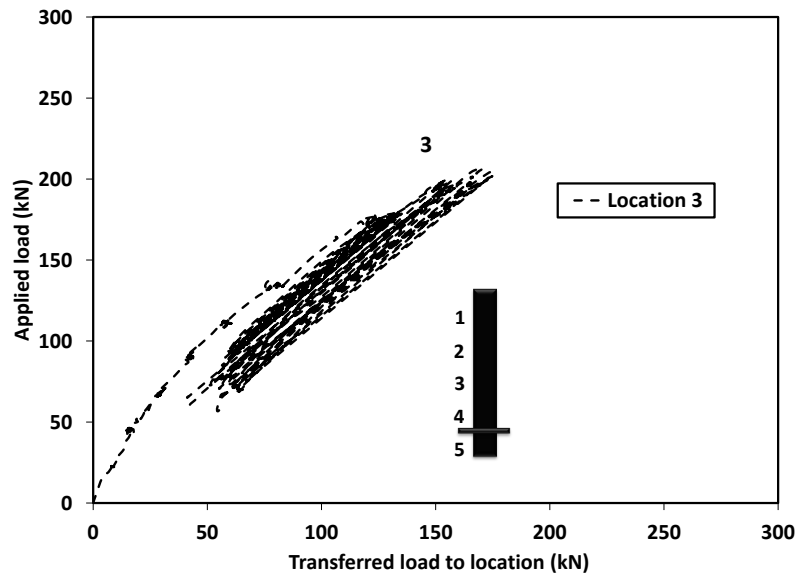
(c)

Figure 6 - 20: Variation of the measured load at different pile sections (a) PA3; (b) PB2; (c) PC2

Figure 6 - 20 (a) shows that the shaft resistance of PA3 at the maximum applied cyclic load decreased slightly from 64% at the start of the load cycling to 61% by the end of loading, suggesting small degradation of soil resistance along the shaft. This was compensated by the increase in bearing resistance on the helical plate due to the compaction of the soil

underneath. The available strain gauges' readings of PA3 showed a maximum developed shaft stresses of 145 kPa (between gauges locations 3 and 4).

The shaft resistance of PB2 exhibited greater degradation, as it decreased from 60% of the applied load during the first load cycle to only 37% during the last load cycle. Similar observation of greater degradation for smaller diameter pile (PB2 compared to PA3) was made by Tabucanon *et al.*(1995) who suggested that, for a given normalized displacement amplitude, smaller diameter piles would experience greater degradation due to cyclic loading. On the other hand, greater bearing resistance of soil below the helical plate was observed for PB2, due to the larger area of the helical plate compared to PA3. In addition, 32% of the load was carried by the toe bearing at the maximum applied load. Finally, from the available strain gauges readings of PB2, and assuming as an approximation a constant distribution of stresses from top to location 4 strain gauge, the developed shaft stress was 105 kPa.

The only available strain readings for PC2 were at of the strain gauge at location 3 (2.25m below pile head). While the exact distribution of shaft stresses cannot be determined from only one strain gauge, assuming a uniform distribution of shaft stresses along the top 2.25m of the pile shaft yields maximum developed shaft stresses of 44 kPa during the first load cycle and 23 kPa during the last cycle.

6.4.2.4 Cyclic Uplift Results

6.4.2.4.1 Load Displacement Curves

The measured load-displacement curves of the piles tested following monotonic uplift load tests (PA1, PA2 and PC1) and those tested following monotonic compression tests (PA3 and PC2) are shown in Figure 6 - 21 (a) and (b), respectively. PC1 was further re-tested at an higher cyclic loading amplitude and its load-displacement curve is shown in Figure 6 - 22.
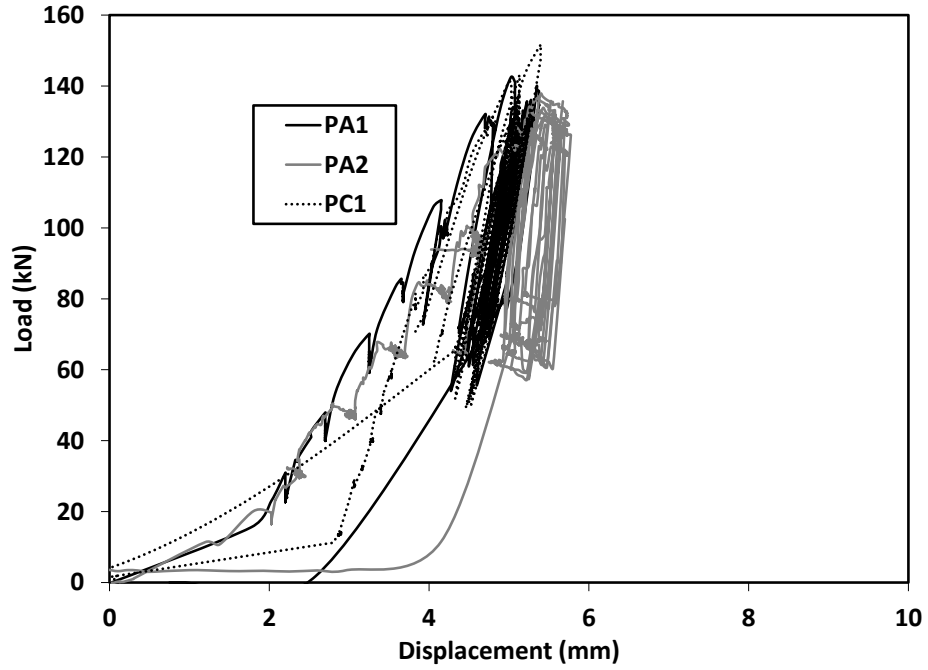
(a)
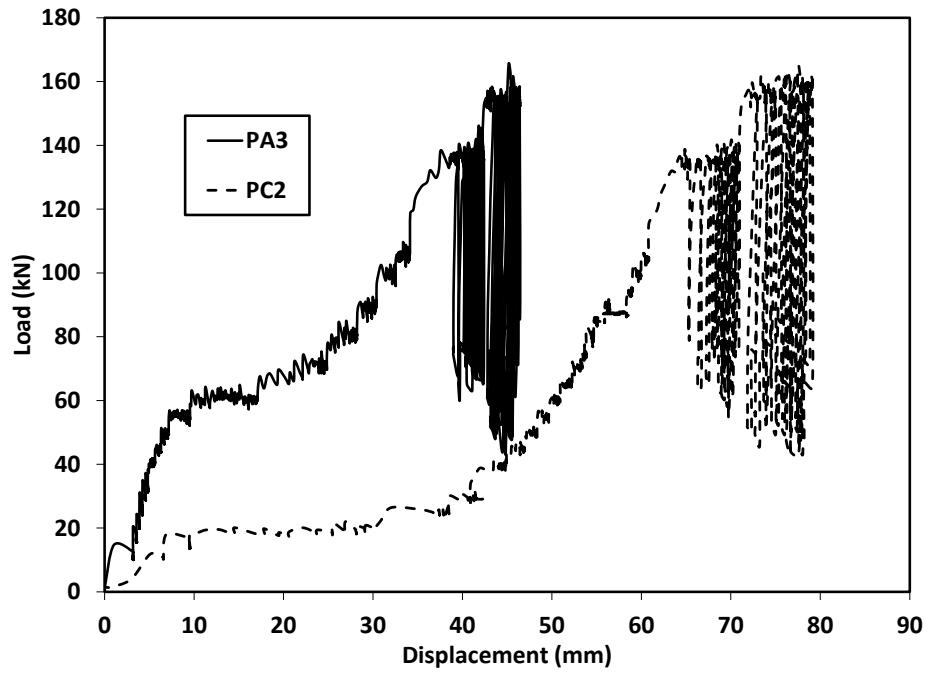
(b)

Figure 6 - 21: Load-displacement curve-cyclic uplift tests (a) Prior tested in monotonic uplift; (b) Prior tested in monotonic compression
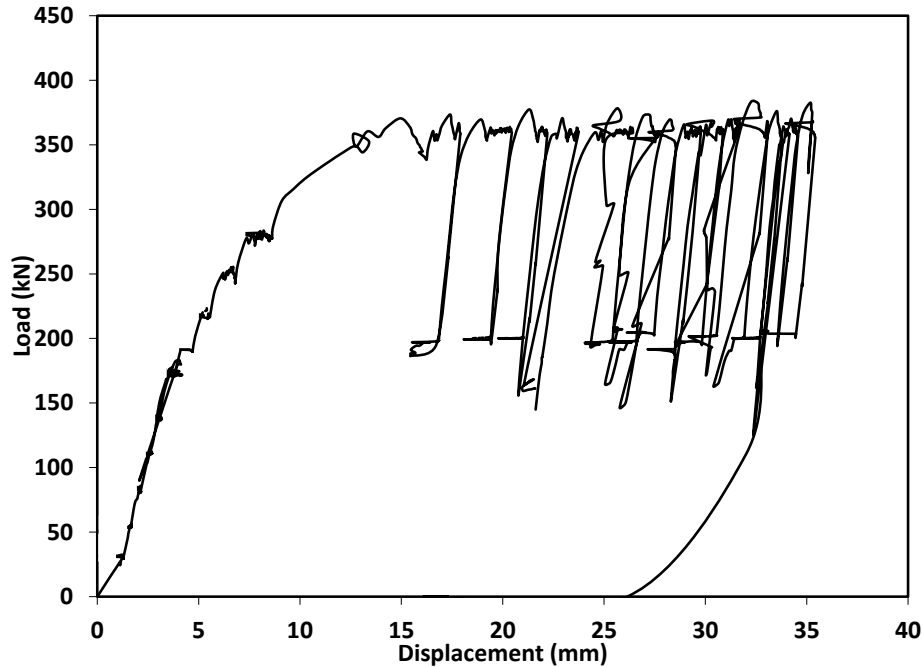
Figure 6 - 22: Load-displacement curve-cyclic uplift test-PC1-higher cyclic loading amplitude

Figure 6 - 21 (a) demonstrates that the static portion of the curves are characterized by an initial low stiffness zone that extended up to 2~3mm. Several factors can causes this: the negative residual shaft stresses build up during unloading the previous static uplift tests; the disturbed zone above the helical plate following the unloading; and for tapered piles, the loose state of the caved-in soil surrounding the pile shaft during the previous monotonic uplift tests. This was followed by a linear portion with higher stiffness extending up to the start of the load cycling.

PC1 displayed cyclic displacements comparable to those of PA1 and PA2. However it exhibited significantly higher accumulated cyclic displacement when re-tested at an higher loading amplitude as shown in Figure 6 - 22.

For piles prior tested in monotonic compression first (PA3 and PC2), the initial linear segment with high stiffness was followed by another segment with low stiffness and finally a linear segment extending up to the start of cyclic loading. The low stiffness segment is due to the loading reversal where loose caved-in soil region was developed above the

helical plate during the compression test. It should be noted that during initial trial of testing of PB2 in cyclic uplift, the helix weld to the shaft failed, therefore, the test was halted.

The development of the measured displacement with loading cycles of the different piles are presented in Figure 6 - 23.

The results clearly demonstrate the negative effect of the prior uplift loading on the tapered piles performance. The decrease in the confining pressure acting on the shaft and the possible gap opening and soil cave-in below the helical plate during the uplift loading were manifested in the larger cyclic displacement for tapered piles as shown in Figure 6 - 23 (a). The cyclic displacements of PA1, PA2 and PC1 were 0.57mm, 0.57mm, and 0.43mm, respectively.

For PA3 and PC2 on the other hand, the additional confining pressure of the soil surrounding the shaft due to the prior compressive loading resulted in higher shaft resistance during the cyclic uplift tests, and consequently, lower cyclic displacement of PA3 (6. 2 mm) compared to PC2 (12.6mm) as shown in Figure 6 - 23 (b).

The piles loaded in monotonic uplift first, most of the cyclic displacement occurred within the first 2 to 4 loading cycles. The rate of displacement accumulation then decreased significantly. Same behavior was observed for piles loaded in monotonic compression first; however the rate of displacement accumulation was higher compared to the piles loaded in uplift first. On the other hand, upon testing at an higher cyclic load amplitude (between 360kN and 200kN), PC1 exhibited much larger cyclic displacement (17.53mm), and the displacement accumulation continued to the last load cycle as shown in Figure 6 - 24.
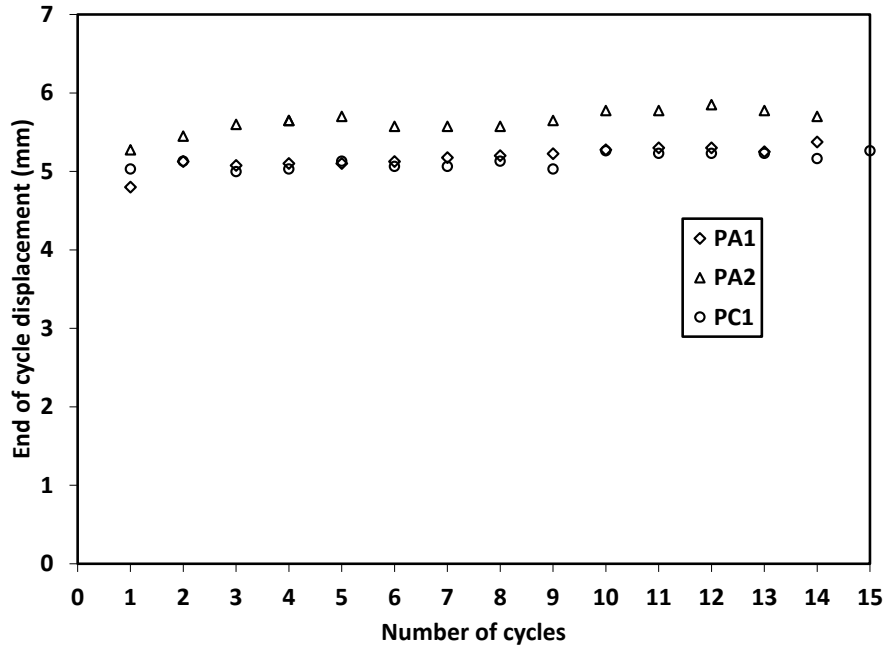
(a)
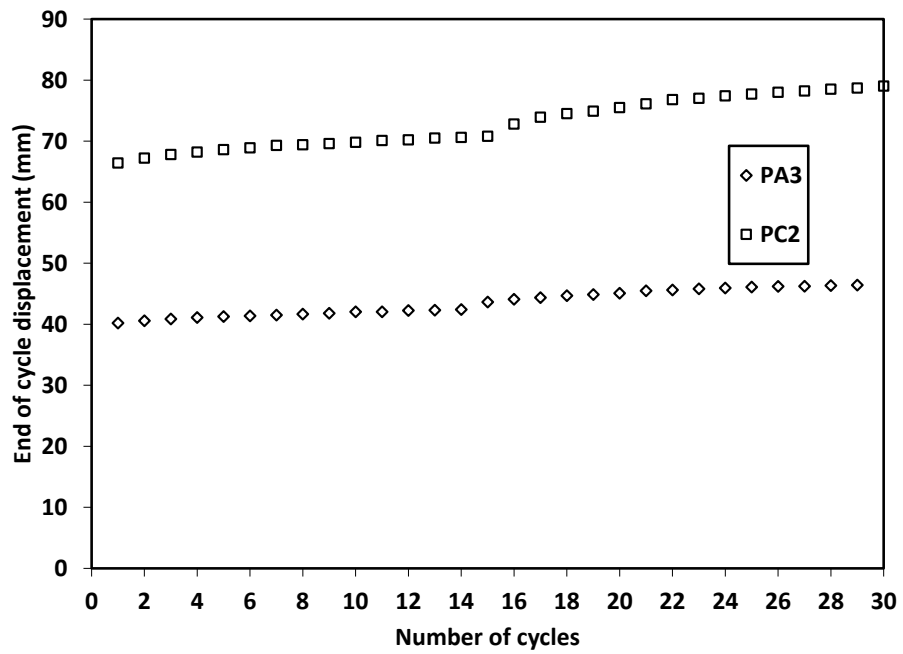
(b)

Figure 6 - 23: End of cycle's settlement-cyclic uplift tests (a) Prior tested in monotonic uplift; (b) Priory tested in monotonic compression
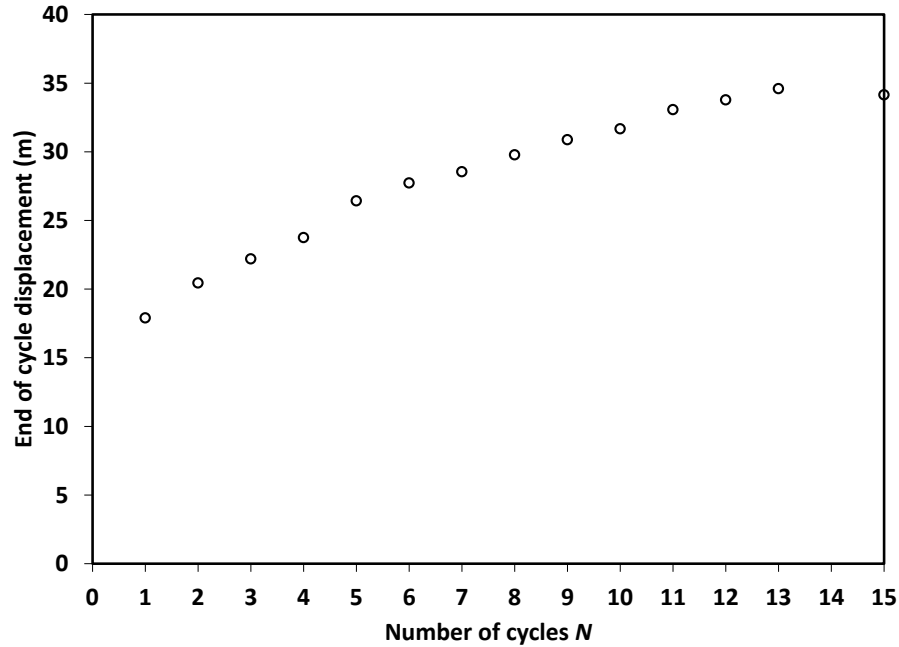
Figure 6 - 24: End of cycle's settlement-cyclic uplift tests-PC1 at higher loading amplitude

The variation of the pile axial stiffness K with number of load cycles are plotted as shown in Figure 6 - 25 and Figure 6 - 26 for piles loaded first in monotonic uplift and monotonic compression, respectively.

Piles PA1, PA2 and PC1 displayed similar behavior, i.e., a constant or slight increase in stiffness through the cyclic loading. On the other hand, the stiffness of PC1 degraded when was loaded at higher load amplitude as shown in Figure 6 - 25 (d). PC2, which was loaded in monotonic compression first, experienced stiffness degradation due to soil stress reversal. However, PA3 did not experience stiffness degradation (Figure 6 - 26 (a)) owing to the positive effect of the shaft taper, which compacted the adjacent soil during the initial compression loading.
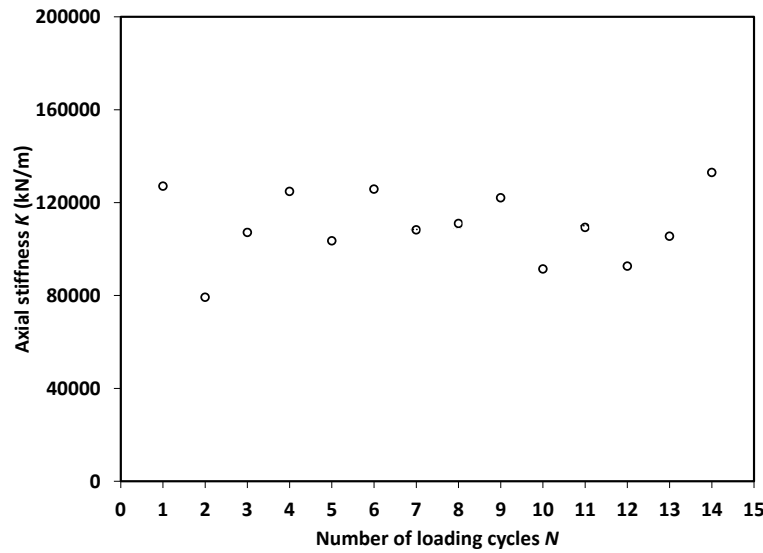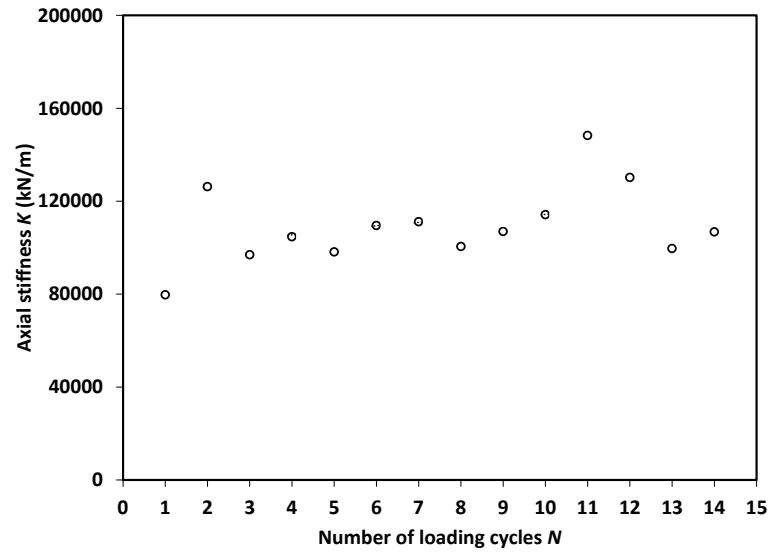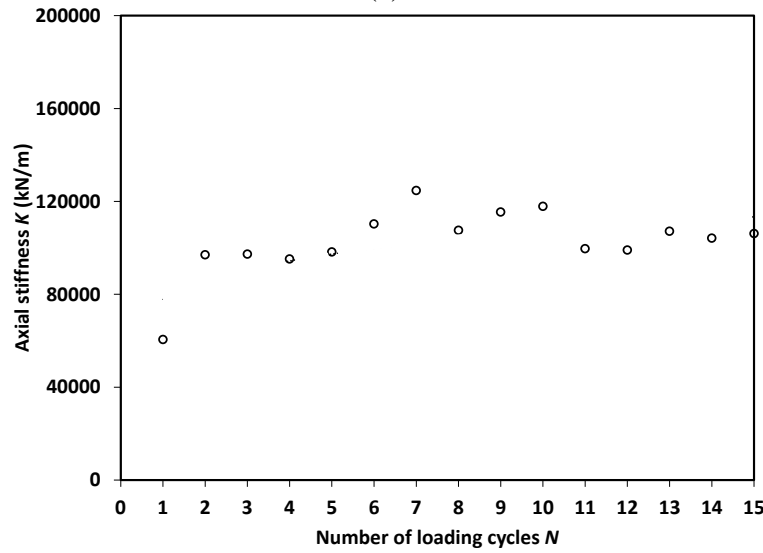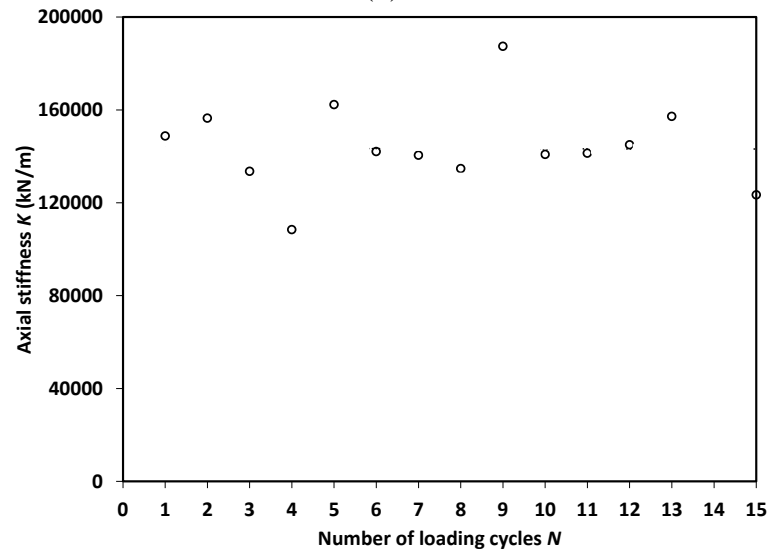
Figure 6 - 25: Variation of the piles axial uplift stiffness with loading cycles (a) PA1; (b) PA2; (c) PC1 (lower loading amplitude); (d) PC1 (higher loading amplitude)

209
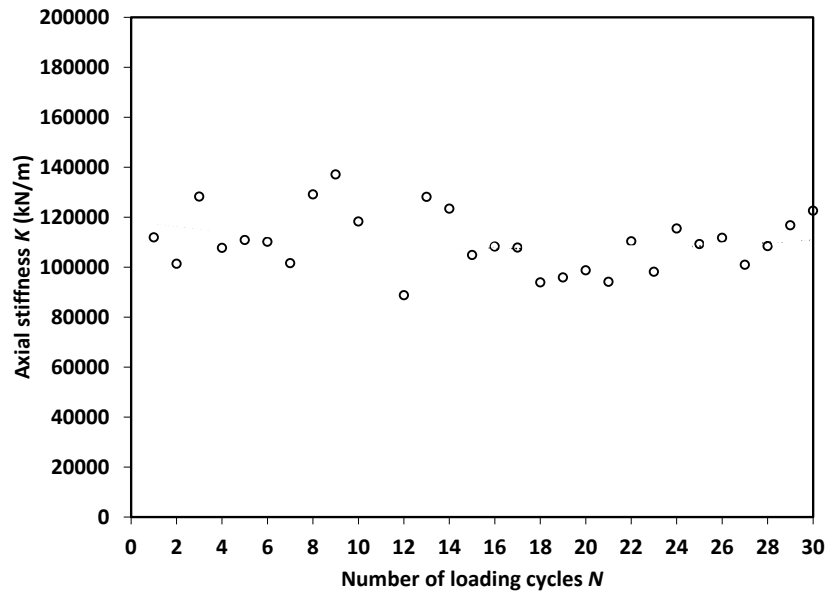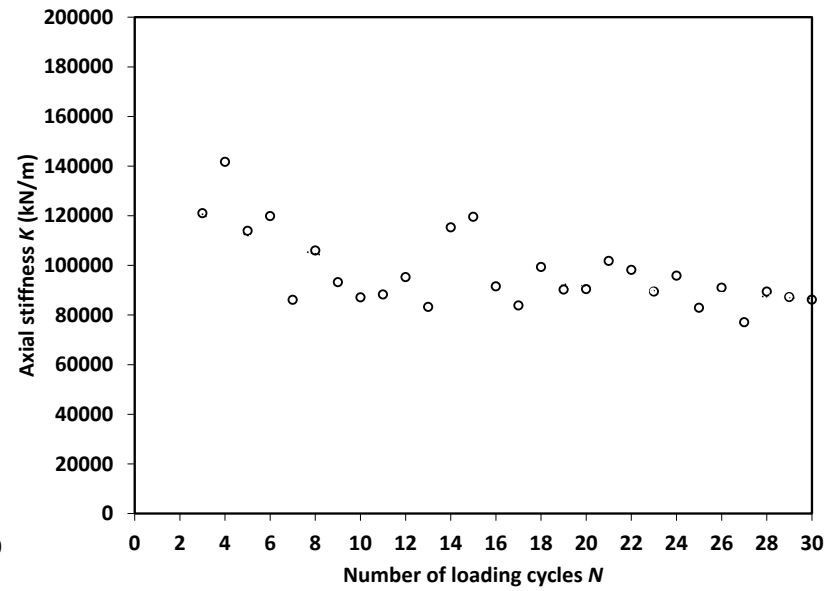
Figure 6 - 26: Variation of the piles axial uplift stiffness with loading cycles (a) PA3; (b) PC2

6.5 Numerical analysis

To further understand the cyclic axial performance of the tested piles, three-dimensional finite element models were developed using the computer program ABAQUS (Hibbitt *et al.*, 2008). The developed models were used to simulate the cyclic uplift and cyclic compression load testing of piles of configurations A, B and C.

6.5.1 Description of finite element model

A 3D quarter cylindrical mesh represented the pile-soil system. The pile was placed along the axial z-direction of the model. For numerical simplification, a planar disk was used to model the helical plate. Figure 6 - 27 presents the developed model geometry for a single pile of configuration A.
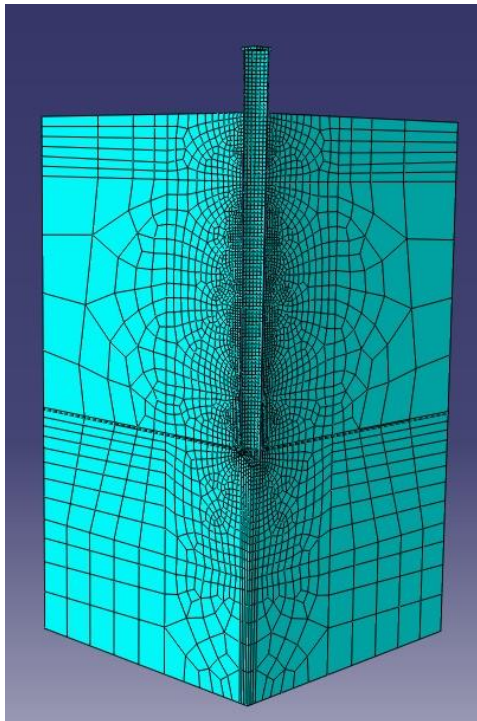
Figure 6 - 27: Finite element model geometry–undeformed mesh-PA3

The pile and the soil medium were discretized using 8-noded, reduced integration first order solid elements (C3D8R) with three translational degrees of freedom at each node and

one integration point located at the centroid. The locations of the vertical and horizontal boundaries were optimized to minimize boundary conditions effect as well as the computational effort. The optimization process resulted in a soil cylinder radius extending 2.5 m from the center of the pile shaft. The bottom (horizontal) boundary of the model was placed at 1.95 m below the pile toe, which is equivalent to 5 helix diameters. The applied model boundary conditions are illustrated in Figure 6 - 28.

Mesh refinement at stress/strain concentration zones was necessary to ensure the accuracy of the results. Accordingly, a series of models was developed where the mesh was incrementally refined and the results were compared. When the difference between the results of two consecutive models (i.e. refinements) became less than 2.5%, the most refined model was considered. The elements were most refined along the pile-soil interface and around the helical plate and then their size gradually increased towards the model boundaries. This process resulted in mesh configurations consisting of 37 309/33 267/28 553 elements for pile configurations A/B/C, with maximum elements side dimension ranging from 250 mm/500 mm/330 mm at the model boundaries to 20 mm/17 mm/25 mm at the pile-soil interface. The pile mesh consisted of 1609/869/1451 for configurations A/B/C.

Figure 6 - 28: FE model-applied boundary conditions

6.5.2 Soil model

The soil is simulated as an elastic-perfectly plastic isotropic continuum. The soil plasticity and failure were modeled using the Mohr-Coulomb yield criterion employing the critical state angle of internal friction, φ_{cs}, cohesion yield stress, c' and the dilation angle, ψ. The soil elasticity was defined by Poisson's ratio, v, and Young's modulus, E_s.

The soil domain was divided into three main sections:

- The top soil (0.5m) layer was modeled with reduced strength and stiffness reflecting the soil disturbance induced during the initial predrilling process;

- Soil along the pile shaft;

- Soil beneath the helix plate was modeled using higher stiffness to account for the soil densification during the installation process.

The soil properties considered in the model, as summarized in Table 6 - 5, were established through the calibration process of the numerical model using monotonic compression field test results and were then validated with further compressive, uplift and lateral field testing data as shown in Chapters 3, 4 and 5.

Table 6 - 5: Soil parameters considered in FE model

Depth (m)		φ_{cs} (degrees)	ψ (degrees)		C' (kPa)	ν	E_s (MN/m^2)			Effective unit weight γ' (kN/m^3)
From	To		Config A and B	Config C			Config A	Config B	Config C	
0	0.5	32	4	4	4	0.3	35	35	35	17
0.5	Helix* level	32	6	4	4	0.3	70	70	60	18
Helix level	End of model	32	6	6	4	0.35	94	73	94	18

The validated values of earth pressure coefficient K_s are 2, 1.2 and 0.85 for configurations A, B and C respectively in compression. For uplift loading, K_s values of 1.1 and 0.85 were used for configurations A and C respectively.

6.5.3 Pile model

The pile was modeled as elastic-perfectly plastic material. The adopted mechanical properties of the pile material are summarized in Table 6 - 6. It should be noted that weakened sections along the weld sections (helix-shaft and base plate-shaft) were considered to accommodate the visually inspected defects prior to the piles installation. These lower strength parameters, presented in Table 6 - 6, were also calibrated and

---

*Varies depending on embedded length and pile configuration

validated with static compressive, uplift and lateral tests results as presented in Chapters 3, 4 and 5.

Table 6 - 6: Pile parameters considered in FE model

Component	Young's Modulus E_p (kN/m^2)	Poisson's ratio v_p	Unit weight γ_p (kN/m^3)	Yield strength F_y (MPa)
Shaft- configurations A and B	1.69E08	0.28	77	314
Shaft - configuration C	2.0E08	0.28	77	370
Helix and base plates welded connections	2.0E08	0.28	77	170

6.5.4 Pile-soil interface model

Penalty-type tangential behavior Coulomb's frictional model was used to simulate the pile-soil interface conditions. The surface traction has to reach a maximum shear stress value before any relative tangential motion occurs. This critical shear stress value is the lesser of the interface shear strength or a fraction of the interface pressure. The validated soil-pile interface strength $\tan\delta$ values of 0.78 and 0.5 were considered for tapered iron (configurations A and B) and straight steel (configuration C) piles, respectively. While the first was determined by studying the pile surface roughness in comparison to the soil mean particle size as mentioned earlier in Chapter 3, the latter was considered in accordance to the suggested values by the Canadian Foundation Engineering Manual (2006). Separation along the pile-soil interface was permitted.

6.5.5 Loading sequence

The piles were wished in place. An initial loading step of geostatic stresses and equilibrium was applied to reflect the initial in-situ soil stresses. This was followed by load controlled analysis whereby prescribed loading patterns, as shown in Figure 6 - 12, were applied at a reference point rigidly connected to the pile top loading plates.

6.5.6 Soil degradation

The aforementioned calibrated soil parameters have been considered during the initial monotonic part of the loading pattern. With the start of the load cycling, the soil along the shaft-soil interface is expected to experience stiffness degradation due to the repetitive loading as observed from the field tests results. To account for stiffness deterioration, a calibration process was performed by reducing the soil stiffness during each loading cycle to match the performance of the field load displacement curve. The soil stiffness was degraded using a temperature-based stiffness reduction model incorporated in ABAQUS, thus the model temperature was set to increase with load cycles.

6.5.7 Cyclic compression

The load-displacement curves for PA3, PB2 and PC2 loaded in cyclic compression are shown in Figure 6 - 29. The calculated response is in good agreement with the field measurements as shown in Figure 6 - 29.

(a)

216
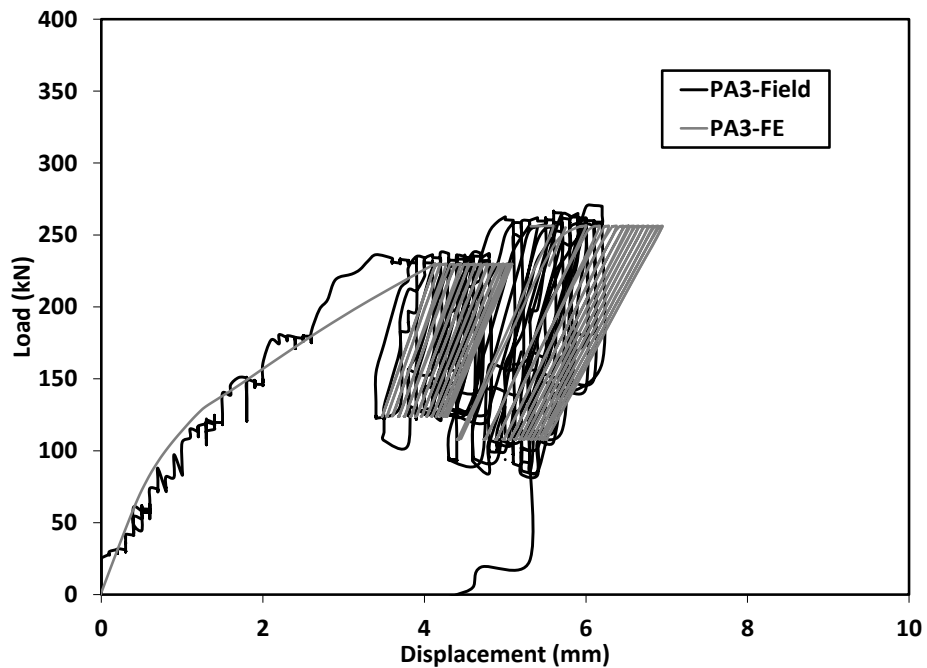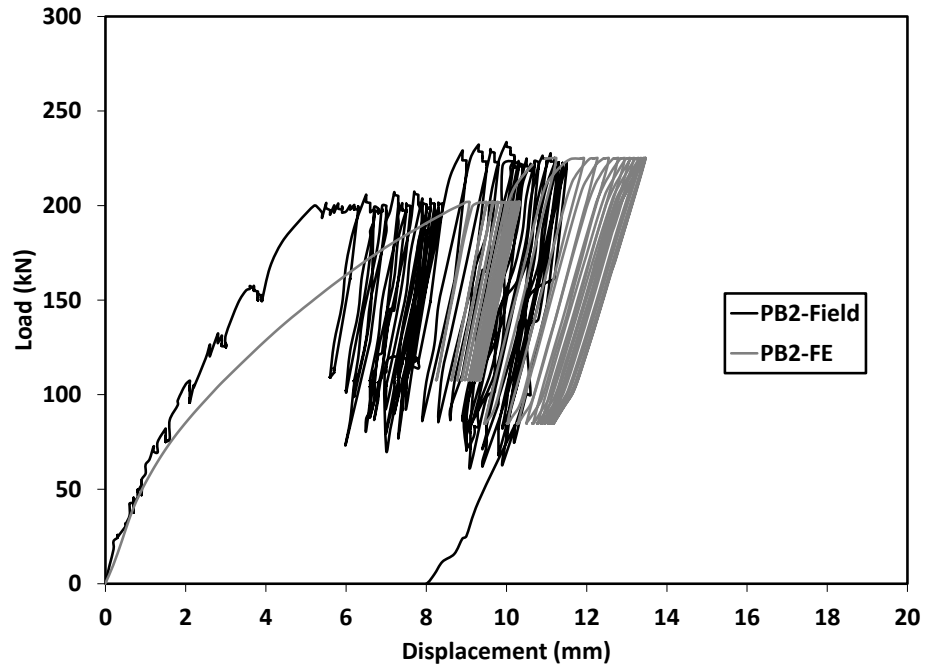
(b)
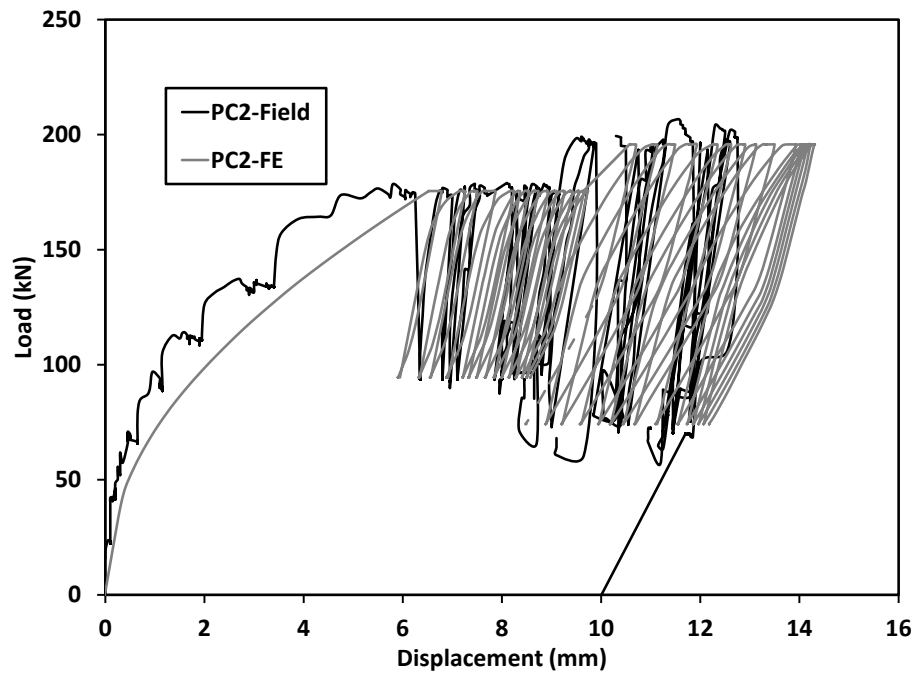
(c)

Figure 6 - 29: Comparison of calculated and measured load-displacement curves for calibration-cyclic compression (a) PA3; (b) PB2; (c) PC2

The calibration process indicated degradation of the shear modulus G of soil along the pile shaft but no degradation for the soil beneath the helical plate nor the pile toe. The variation of the shear modulus reduction curve, G/G_{max} (where G_{max} is the small strain (maximum) shear modulus), with the average calculated shear strain in the soil elements along the pile shaft for PA3, PB2 and PC2 are shown in Figure 6 - 30. The values of G/G_{max} ranged from 33% to 7%. This shear modulus reduction may be attributed to the decrease in the radial stresses along the pile shaft, hence reducing the soil octahedral stresses. from the first to last load cycle, the average radial stresses acting on the pile shaft decreased by 15%, 34% and 19% for PA3, PB2 and PC2, respectively. Similar behavior was observed by Jardine and Standing (2012) where a fractured shear zone would develop along the pile interface and local slip would occur with the reduction of the soil radial stresses (Jardine and Standing, 2012). The greater reduction in the radial stresses with cyclic loading of configuration B piles explains its greater stiffness degradation observed during the field testing.

The shear modulus reduction curves for the three analyzed piles fit within the shear modulus reduction curves available in the literature for sands as shown in Figure 6 - 30. It is also noted from Figure 6 - 30 that soil adjacent to tapered piles PA3 and PB2 experienced higher shear strains compared to PC2. This is attributed to the shaft taper, which exert additional pressure on the surrounding soil during compressive loading and hence increase the elements shear stresses and strains.
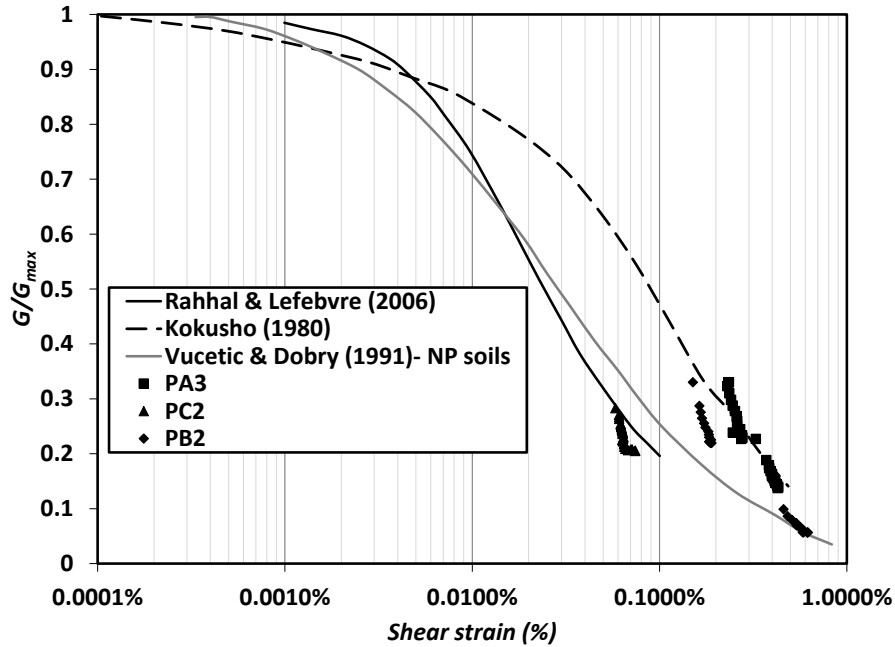
Figure 6 - 30: Variation of the shear modulus degradation factor with shear strain-FE cyclic compression results

6.5.8 Cyclic uplift

The calculated load-displacement curves for PA1 and PC1 loaded in cyclic uplift are presented in Figure 6 - 31. Unlike the compression case, negligible stiffness degradation is observed for both pile configurations. This is due to the decrease in shaft stresses because of the Poisson's ratio effect for PC1 and due the release of confining pressure for PA1, which resulted in reduced shear strains along the pile-soil interface. Negligible difference was found between the calculated radial stresses applied on the pile surface during the first and last loading cycles (less than 1% difference for both analyzed piles) for PA1 and PC1.
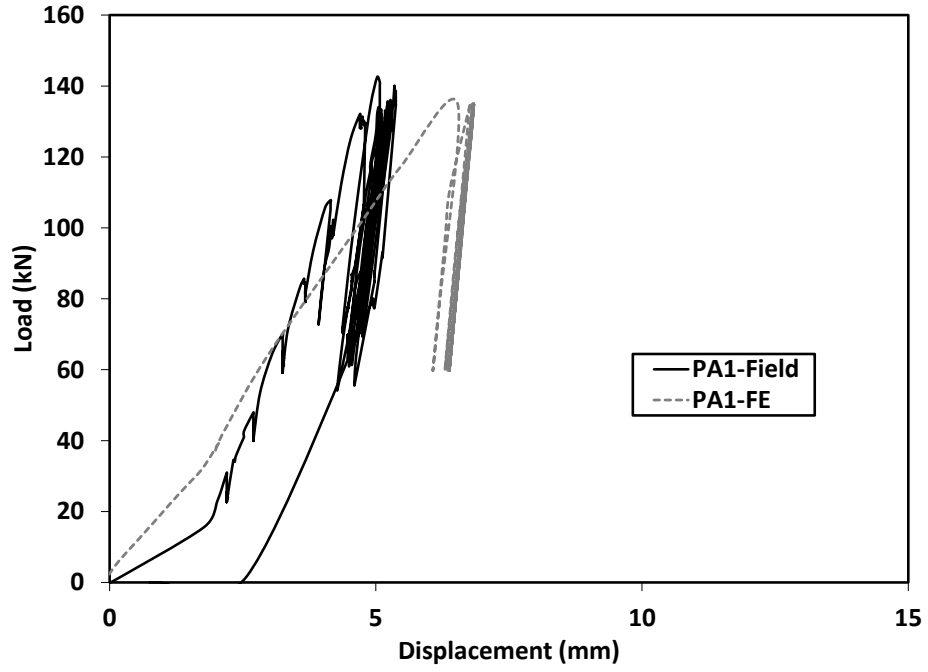
(a)
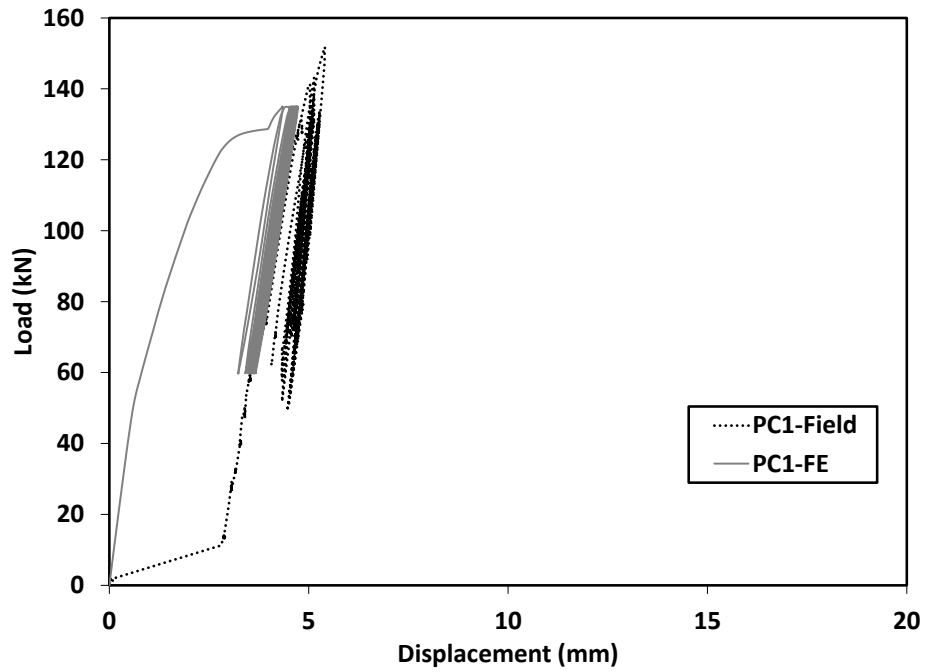
(b)

Figure 6 - 31: Comparison of calculated and measured load-displacement curves for calibration-cyclic uplift (a) PA1; (b) PC1

The variation of the shear modulus degradation ratio with the average shear strain in the soil elements surrounding the pile shaft for PA1 and PC1 are shown Figure 6 - 32.
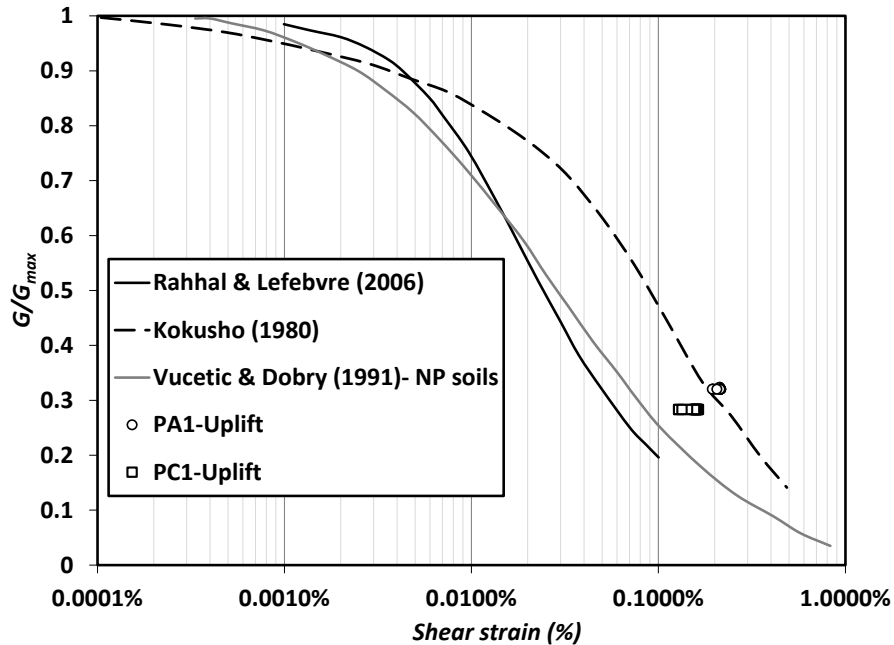
Figure 6 - 32: Variation of the shear modulus degradation factor with shear strain- FE cyclic uplift results

6.6   Conclusions

The cyclic axial performance of a ductile cast iron tapered helical pile was investigated in this study. A total of seven piles were installed by torque in a silty sand profile and were subjected to cyclic compression and uplift load tests. The test piles included five tapered helical piles with 2 different average diameters, same length and shaft taper angle in addition to two straight helical piles. The piles were tested in 2 different loading sequences and the effect of prior monotonic and cyclic tests on the piles' cyclic performance was evaluated. Finally, three-dimensional finite element analysis was conducted to delineate the cyclic performance characteristics of the proposed novel piles. The following main conclusions were drawn:

1. The proposed piling system showed a better cyclic compressive performance compared to the straight large diameter helical piles.

2. The application of a prior cyclic uplift tests had a negative effect on the performance of the proposed piling system. The release of the additional confining pressure surrounding the pile shaft reduced the developed shaft resistance. For that loading sequence, large diameter helical straight shafted piles performed better when subjected to cyclic compressive performance.

3. When tested following monotonic uplift tests, the cyclic uplift performance of the helical tapered piles were satisfactory with even performance for the large diameter straight shaft piles.

4. The application of prior monotonic compression tests reduced the cyclic uplift displacement of the tapered helical piles compared to the straight shafted ones.

6.7 References

AASHTO. 2002. Standard specifications for highway bridges. *HB-17.* American Association of State and Highway Transportation Officials.

Abdel-Rahman, K. & Achmus, M. Behavior of foundation piles for offshore wind energy plants under axial cyclic loading. Simulia customer conference, 2011, Barcelona/Spain. 1-13.

ASTM C136. 2006. Standard test method for sieve analysis of fine and coarse aggregates. ASTM international.

ASTM D1556. 2007. Standard test method for density and unit weight of soil in place by the sand-cone method. ASTM international.

ASTM D2487. 2011. Standard practice for classification of soils for engineering purposes (Unified Soil Classification System). ASTM international.

ASTM D3080. 2011. Standard test method for direct shear test of soils under consolidated drained conditions. ASTM international.

ASTM D4318. 2010. Standard test methods for liquid limit, plastic limit, and plasticity index of soils. ASTM international.

Begemann, H. K. S. P. Alternating loading and pulling tests on steel I-Beam piles. Proceedings of the 8th international conference on soil mechanics and foundation engineering, 1973, Moscow, 13-17.

Bowles, J. 1996. *Foundation analysis and design*, 5th edition, Mc-Graw hill.

Brown, S. F., Juspi, S. & Yu, H. S. 2008. Experimental observations and theoretical predictions of shakedown in soils under wheel loading. *Advances in Transportation Geotechnics*. Proceedings of the 1st International Conference on Transportation Geotechnics, 2008, Nottingham, UK.

CGS. 2006. *Canadian Foundation Engineering Manual*.4th edition. Canadian Geotechnical Society.

Chan, S. F. & Hanna, T. H. 1980. Repeated loading on single piles in sand. *Journal of Geotechnical Engineering Division,* 106(GT2), 171-188.

Clemence, S. P. & Smithling, A. P. Dynamic uplift capacity of helical anchors in sand. Proceedings of the 4th Australia-New Zealand conference on geomechanics, 1984. 88-93.

Di-Prisco, C. & Zambelli, C. 2003. Cyclic and dynamic mechanical behaviour of granular soils: experimental evidence and constitutive modelling. *Revue francaise de génie civil,* 7(7-8), 881-910.

Dove, J. E. & Jarrett, J. B. 2002. Behavior of dilative sand interfaces in a geotribology framework. *Journal of Geotechnical and Geoenvironmental Engineering,* 128(1), 25-37.

El Naggar, M. H. & Wei, J. Q. 2000. Cyclic response of axially loaded tapered piles. *Geotechnical Testing Journal,* 23(1), 100-115.

El Sharnouby, M. M. & El Naggar, M. H. 2012. Axial monotonic and cyclic performance of fibre-reinforced polymer (FRP)-steel fibre-reinforced helical pulldown micropiles (FRP-RHPM). *Canadian Geotechnical Journal,* 49(12), 1378-1392.

El-Gharbawy, S. & Olson, R. The cyclic pullout capacity of suction caisson foundations. Proceedings of the ninth international offshore and polar engineering conference, 1999, Brest, France. 660-667.

Ghaly, A. M. & Clemence, S. P. 1998. Pullout performance of inclined helical screw anchors in sand. *Journal of Geotechnical and Geoenvironmental Engineering,* 124(7), 617-627.

Hibbitt, H. D., Karlsson, B. I. & SORENSEN, E. P. 2008. ABAQUS Standard user's manual. Pawtucket, R. I.: Hibbitt, Karlsson & Sorensen Inc.

Jardine, R. J. & Standing, J. R. 2012. Field axial cyclic loading experiments on piles driven in sand. *Soils and Foundations,* 52(4), 723-736.

Kokusho, T. 1980. Cyclic triaxial test of dynamic soil properties for wide strain range. *Soils and Foundations*, 20(2), 45-60.

Kulhawy, F. H. & Mayne, P. W. 1990. Manual for estimating soil properties for foundation design. Ithaca, New York: Cornell University.

Liao, S. S. C. & Whitman, R. V. 1986. Overburden correction factors for SPT in sand. *Journal of Geotechnical Engineering,* 112(3), 373-377.

Lings, M. L. & Dietz, M. S. 2005. The peak strength of sand-steel interfaces and the role of dilation. *Soils and Foundations,* 45(6), 1-14.

Mayne, P. W. In-situ characterization of Piedmont residuum in eastern US. Proc. US-Brazil: Application of Classical Soil Mechanics to Structured Soils, 1992, Belo Horizonte. National Science Foundation/USA, 89-93.

Mayne, P. W. 2006. In-situ test calibrations for evaluating soil parameters. Overview Paper on In-Situ Testing- Singapore Workshop.

Mayne, P. W., Christopher, B. & Dejong, J. 2002. Manual on subsurface investigations—Geotechnical site characterization. Washington, DC.: Federal highway administration, U.S. Department of Transportation.

Mayne, P. W. & Kulhawy, F. H. 1982. Ko-OCR Relationships in Soil. *Journal of the Geotechnical Engineering Division,* 108(6), 851-872.

Perko, H. 2009. *Helical piles: A practical guide to design and installation,* New Jersey, John Willey and Sons Inc.

Poulos, H. G. 1981. Cyclic axial response of single pile. *Journal of Geotechnical Engineering Division,* 107(1), 41-58.

Poulos, H. G. 1989. Cyclic axial loading analysis of piles in sand. *Journal of Geotechnical Engineering,* 115(6), 836-852.

Poulos, H. G. & Davis, E. H. 1980. *Pile foundation analysis and design*, John Wiley and Sons.

Rahhal, M. E. & Lefebvre, G. Characterizing shear moduli reduction in soils cyclic behavior. Geotechnical Engineering in the Information Technology Age, 2006. GeoCongress, 1-5.

Rimoy, S. P., Jardine, R. J. & Standing, J. R. Displacement response to axial cycling of piles driven in sand. Proceedings of the ICE-Geotechnical Engineering, 2013, 166(2). 131-146.

Schwarz, P. 2002. Beitrag zum Tragverhalten von Verpresspfählen mit kleinem Durchmesser unter axialer zyklischer Belastung. *Lehrstuhl und Prüfamt für Bodenmechanik und Felsmechanik der Technischen Universität München,* 33.

Seamless Pole Inc 2010. Ductile iron poles. Birmingham, AL. (*http://www.seamlesspole.com/*)

Skempton, A. W. 1986. Standard penetration test procedures and the effects in sands of overburden pressure, relative density, particle size, aging, and over-consolidation. *Geotechnique,* 36(3), 425-447.

Tabucanon, J. T., Airey, D. W. & Poulos, H. G. 1995. Pile skin friction in sands from constant normal stiffness tests. *Geotechnical Testing Journal,* 18(3), 350-364.

Vucetic, M. & Dobry, R. 1991. Effect of soil plasticity on cyclic response. *Journal of Geotechnical Engineering,* 117(1), 89-107.

CYCLIC LATERAL PERFORMANCE OF SCDI HELICAL

TAPERED PILES IN SAND

7.1   Introduction

In effort to sustainably meet the ever-increasing electricity demands and to reduce carbon emissions associated with fossil-based energy production, the recent years have witnessed a surge in the solar farms construction. In addition to their own weight, solar panels might also be subjected to a number of external environmentally induced forces such as seismic, wind and snow loads.

Currently, various pile types of different shapes and materials can be used to support solar panels. Yet, the construction industry is pursuing foundation systems featuring more efficient installation techniques and novel configurations in order to meet the variable construction challenges while satisfying the demands for sustainable practices and cost saving solutions. In this study, a novel piling system is investigated under cyclic lateral loading conditions experienced by solar panel foundations. The system comprises a short spun-cast ductile iron (SCDI) tapered pile (Seamless-Pole-Inc., 2010) fitted with a lower helical plate. It combines the construction advantages of helical piles, the load carrying efficiency of the tapered section and the practical size and weight of short hollow iron section, hence it represents a sustainable and efficient foundation system for solar panels. The proposed pile is installed using a mechanical torque conveyed by a driving motor holding the pile head. The proposed system's configuration and installation technique offer many advantages compared to the conventional pile types, including enhanced compressive and lateral capacity that have been proven numerically and experimentally in Chapters 3 and 5.

In this chapter, the pile cyclic lateral behavior is studied including experimental and numerical testing. The effect of the previous monotonic lateral load on the pile cyclic performance is also investigated.

7.2 Literature survey

When subjected to lateral cyclic loads, the pile-soil system may experience performance degradation with the repetitive loading. Typically, two degradation forms can take place: mechanical degradation and material degradation (Mosikeeran, 1990). While the first reflects the developed plastic deformations in the soil, the latter results in the change of the soil parameters. Together, these actions would result in greater pile deflections, rotations, developed bending stresses and ultimately lower system resistance. It is generally observed that cyclic loading levels exceeding 70 to 80% of the static system capacity would result in the degradation of the lateral piles resistance, mostly developed within the first few loading cycles (Mosikeeran, 1990). More significant degradation effects and higher developed plastic strains were observed for piles subjected to one-way cyclic load tests than in case of two-way cyclic load tests (Long and Vanneste, 1994).

The soil gapping and the possible soil cave-in processes represent other important phenomena affecting the piles lateral cyclic behavior, which are manifested by the pinched hysteretic loops (Allotey and El Naggar, 2008). Considering the two-way cyclic loading, of relevance to the case studied herein, when the pile is pulled from one side to another, a soil gap develops and the effective overburden stresses (hence lateral stresses) at shallow depths might not be sufficient to close that gap (Mosikeeran, 1990). Following the gap development, the sand falls down behind the pile filling that gap, which creates a looser soil zone behind the pile. As a result of this gapping and cave-in process, a non-symmetric performance would result where stiffer system response governs one side (firstly loaded) of the pile than the other (El Sharnouby and El Naggar, 2013).

The cave-in and recompression process was also found to decrease the maximum pile bending moment, to move its location to a shallower depth and to increase the dissipation of hysteretic energy (Allotey and El Naggar, 2008). The beneficial effects of the cave-in and recompression are more obvious in case of impaired piles as it further confines the developed hinges along the pile (Allotey and El Naggar, 2008). However, different findings were observed by Guo *et al.* (2014) studying the lateral performance of H-Piles in sand. They suggested that the deeper developed gap in case of cyclic lateral loads would move

the location of the maximum bending moment to a deeper location compared to the monotonic case (Guo *et al.*, 2014).

On the other hand, Reese and Van Impe (2001) suggested that during cyclic loading of piles in sand, the void ratio of the soil mass near the ground surface reaches a critical value, implying that cycling of denser soils would degrade it while looser soils would densify during cyclic loading (Reese and Van Impe, 2001). The stiffening effect was also observed by Verdure *et al.* (2003), who reported that the secant stiffness of piles tested in one-way cyclic load tests is 1.5 to 3 times larger than that of the initial monotonic loading (until reaching the cyclic amplitude level) with the stiffness slightly increasing with loading cycles (Verdure *et al.*, 2003). With 1000 applied lateral loading cycles, Li *et al.* (2010) found no significant axial settlements for centrifuge modelled mono-piles supporting offshore wind turbines. They also suggested that the rate of deflection increases with loading amplitude where more densification of the surrounding soil takes place (Li *et al.*, 2010).

While several models have been developed to predict the accumulated displacement during cyclic lateral loading of piles in sand (e.g. Little and Briaud, 1988; Lin and Liao, 1999; LeBlanc *et al.*, 2010; Bienen *et al.*, 2012), many of them were found to yield underestimated displacement values (Li *et al.*, 2014).

7.3   Experimental setup

7.3.1   Soil investigation

In order to evaluate the test soil properties, one borehole of 11m depth was drilled in the vicinity of the piles as shown in Figure 7 - 1.
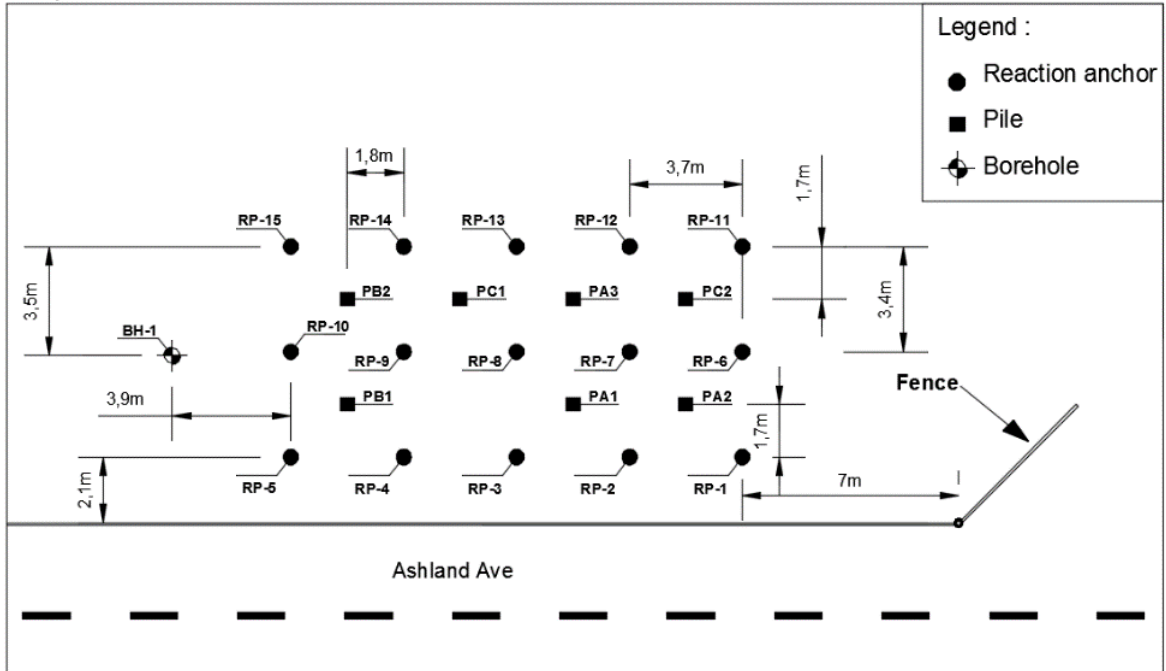
Figure 7 - 1: Site layout showing the drilled borehole location

As measured from the ground surface, the deduced stratigraphy can be described as follows:

- 0m to 0.5m: A top silty sand layer mixed with metallic residues. The presence of the residues was attributed to using the test site as a storage yard for steel tanks;

- 0.5m to 4.5m: silty sand layer;

- 4.5m to 5.5m: gravelly sand layer;

- 5.5m to 8.5m: coarse sand layer with lower silt percentage than the first layer;

- 8.5m to 11m: hard silty till.

The ground water table was found at 3.5m below the mean ground level.

The top 4m were of particular interest in this study considering the pile embedded depth. Accordingly, thorough examination of the soil properties along that depth was carried out and the results are summarized in the following sections.

7.3.1.1 Field tests

Standard penetration test (SPT) was carried at 0.75m intervals during the borehole drilling. The corrected blow counts N_{60} values were determined using the following equation (Skempton, 1986):

$$N_{60} = \textbf{Measured number of blows x } \frac{C_R C_S C_B E_m}{0.6} \tag{7 - 1}$$

where:

C_S is the sampler correction factor, equals to 1.2 for a sampler without liner;

C_R is the drill rod length correction factor, equals to 0.75 for shallower depths than 4m;

C_B is the borehole diameter correction factor, equals to 1.15 for borehole diameter $D = 200$mm;

E_m is the hammer efficiency factor, equals to 0.8 for the used hammer (Bowles, 1996).

The determined values were then corrected for the overburden pressure effect producing N_{60}', i.e.(Liao and Whitman, 1986):

$$N'_{60} = N_{60} \sqrt{\frac{100}{\sigma'_v}} \tag{7 - 2}$$

Where σ'_v is the effective overburden stresses.

The resulting variation of N'_{60} with depth is shown in Figure 7 - 2.

Figure 7 - 2: Variation of SPT *N'₆₀* with depth

The in-situ unit weight of the soil layers was determined using the sand-cone test (ASTM D1556, 2007). The top 0.5m of soil was excavated, followed by two performed sand-cone tests on the underlying layer. The average measured bulk soil density was 16.5kN/m^3.

7.3.1.2 Laboratory testing

Fifteen disturbed samples were retrieved from the split-spoon sampler and were transported to The University of Western Ontario soils laboratory. The collected samples were then subjected to several laboratory tests including sieve analysis, determination of the specific gravity G_S, determination of Atterberg limits, water content W_c measurement, and direct shear tests.

Soil classification and index properties

The resulting particle distribution curves from the sieve analyses (ASTM C136, 2006) are presented in Figure 7 - 3.
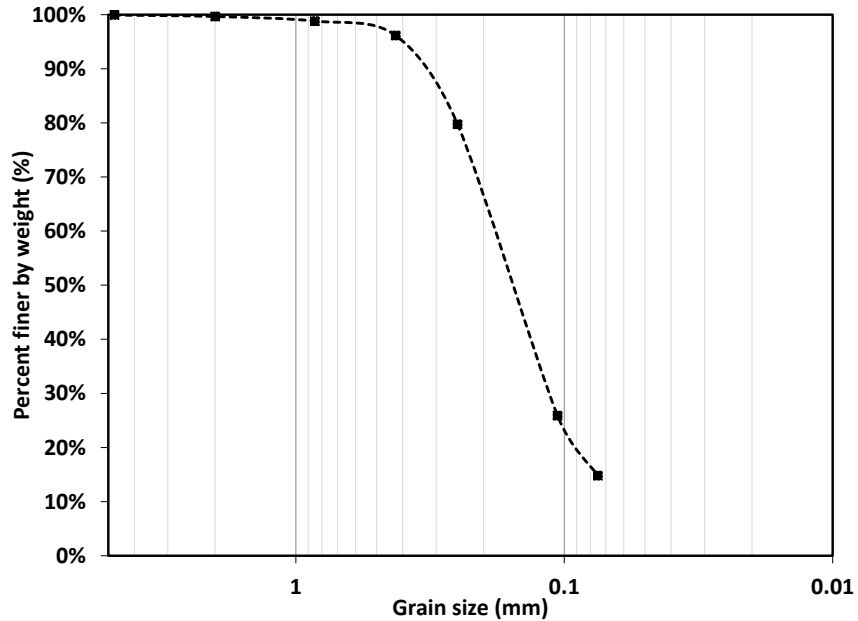
Figure 7 - 3: Grain size distribution for disturbed sample retrieved at 1.05m below ground surface

The average G_s of two samples extracted at depths of 1.05m and 4.8m was found to be 2.71. Considering the short embedded pile depth ranging from 2.45m to 2.75m below the ground surface, the soil sample retrieved at 1.05m depth was deemed representative of soil properties along the pile shaft. The latter had almost no gravel and 14.8% fines. Atterberg limits of three samples were measured and showed average liquid and plastic limit values of 25.3% and 21.5%, respectively (ASTM D4318, 2010). Accordingly, the soil layer is classified as silty sand (SM) according to the Unified Soil Classification System USCS (ASTM D2487, 2011). The average measured in-situ water content was 20.5%.

Soil shear strength parameters

The soil shear strength parameters were determined using a series of direct shear tests (ASTM D3080, 2011). The tests were conducted on soil specimens retrieved at 0.6m and 1.08m depths. The tested specimens unit weight was set to the onsite measured value. The horizontal rate of feed was 0.406mm/min.

The tests results are shown in Figure 7 - 4, which demonstrates the variation of the shear stress with normal stress, vertical displacement and horizontal displacement as well as the residual and peak strength values.

(a)

(b)

(c)
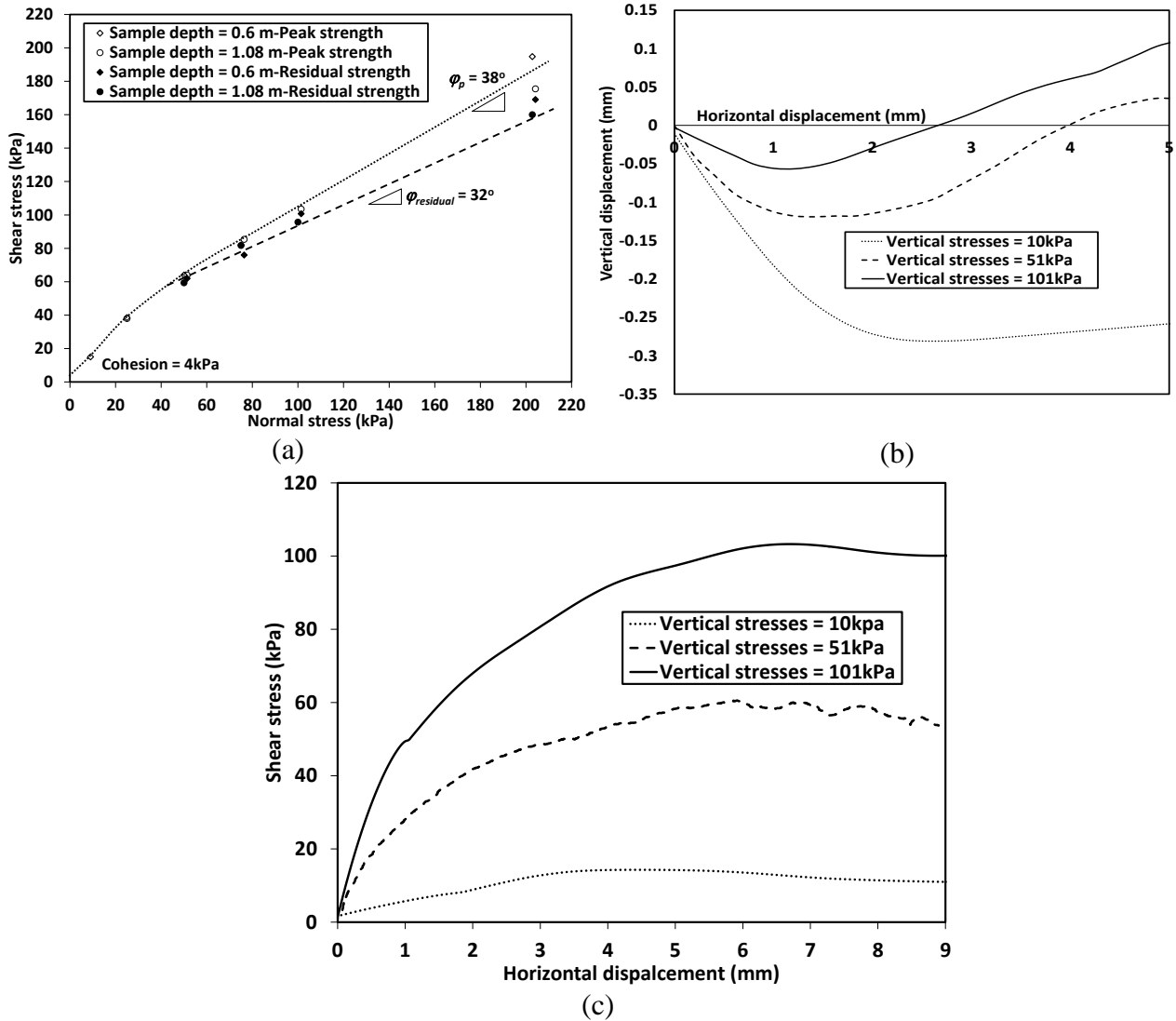
Figure 7 - 4: Direct shear tests results (a) Shear vs normal stresses; (b) Vertical displacement vs horizontal displacement; (c) Shear stress vs horizontal displacement

The shear-normal stresses curve showed a bilinear behavior with the chart slope changing at a normal stress of 20 kPa. Based on the direct shear tests results, the following parameters were found:

Effective soil cohesion, $c' = 4$ kPa;

The residual angle of internal friction $\varphi_{residual} = 32°$;

The dilation angle $\psi = 6°$.

Considering the measured SPT values at the same depth, the determined angle of internal friction lies within the upper bound of the relevant range as typically found in the literature due to the high particles angularity (Bowles, 1996).

Relative density and stiffness parameters

The following equation was used to correlate the soil relative density D_r to N'_{60} values (Mayne *et al.*, 2002):

$$D_r = 100 \sqrt{\frac{N'_{60}}{60}} \qquad (7\text{-}3)$$

The equation yielded D_r values ranging between 50 to 70% along the top 4m depicting medium dense to dense sand along the pile length (Bowles, 1996).

Since only disturbed soil samples were retrieved, direct measurement of the soil over-consolidation ratio, OCR, was not possible. Instead, the apparent preconsolidation pressure σ_p' was calculated using the following equation (Mayne, 1992) and then the OCR values were determined:

$$\sigma_p' = 0.47 \, (N_{60})^m \, Pa \qquad (7\text{-}4)$$

where Pa is the atmospheric pressure and $m = 0.6$ to 0.8 for silty sands (Mayne, 2006).

Using the calculated σ_p' values and the in-situ overburden stresses, the calculated OCR value for the top 4 m of soil is 6.

For overconsolidated sands, the in-situ Young's modulus E_s can be given by (Kulhawy and Mayne, 1990):

$$E_s/Pa = 15N_{60} \qquad (7\text{-}5)$$

However, it should be noted that the post-installation values are of main interest to this study. Therefore, the proposed post-installation E_s values for driven piles in sand proposed by Poulos and Davis (1980) were considered as a preliminary approximation. While typically E_s varies with depth, they also suggested using an average E_s value along the pile shaft and greater values below the pile toe. This assumption was considered satisfactory for the studied case in view of the relatively short piles. Poulos and Davis (1980) proposed average E_s values in the order of 55~70MPa for medium dense sand and 70~100MPa for dense sand, hence an average value of 70MPa was used in this study.

Values of Poisson's ratio ν ranging between 0.2 and 0.4 are suggested for loose to dense sands (AASHTO, 2002), hence 0.3 is considered for this study. Finally, the average value of the coefficient of earth pressure at rest K_o prior to the pile installation can be given by (Mayne and Kulhawy, 1982):

$$K_o\text{-}_{OC} = (1\text{-}Sin\varphi)OCR^{(1\text{-}sin\varphi)} = 0.76 \qquad (7 - 6)$$

The value of the small strain shear modulus G_{max} was correlated to N_{60}, i.e.(Schnaid *et al.*, 2004):

$$G_{max} = 450 \, (N_{60}\sigma_v'P_a^2)^{1/3} \qquad (7 - 7)$$

The above equation is intended to determine lower bound G_{max} value for cemented (residual) soil and also the upper bound value for uncemented soils. The equation yielded an average G_{max} value along the piles' embedded length is 78.52 MPa.

It should be noted that the properties obtained from the laboratory tests reflected the soil state prior to the piles installation hence neglecting the effects of the top soil predrilling prior to the piles installation, the piles installation torque as well as the axial pile testing performed before the lateral tests as explained in the following section. In summary, the representative parameters of the soil along the piles shaft are summarized in Table 7 - 1.

Table 7 - 1: Representative soil parameters

Depth (m)		φ_p (°)	c' (kPa)	Specific gravity G_s	Water content W_c(%)	ν	E_s (MPa)	γ_b (kN/m³)	D_r (%)
From	To								
0	0.5	36	4	2.71	20.5	0.3	70	16.5	55
0.5	4	38							

7.3.2 Test piles

A total of seven piles with configurations as shown in Figure 7 - 5 were installed and tested in the silty sand profile. The test piles included three of configuration A, two of configuration B and two of configuration C. Configurations A and B piles were made of ductile iron with grainy rough surface as shown in Figure 7 - 6 while configuration C piles were made of smooth surface steel. The piles were all hollow and closed ended with wall thickness of 5.5mm. It should be noted that the helical plates of the two configuration B piles were cracked/damaged during prior axial tests hence their results were omitted as they do not represent the intact proposed system behavior.
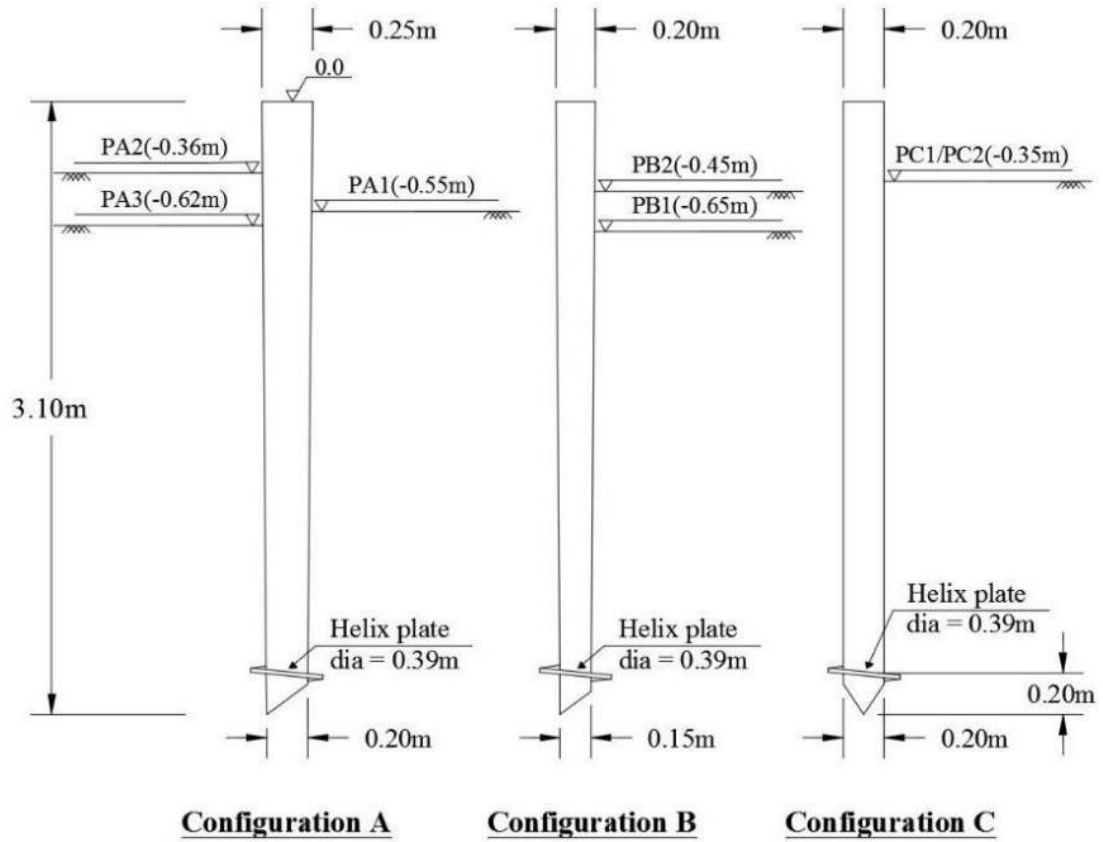
Figure 7 - 5: Tested piles configurations

Figure 7 - 6: Image of the tapered piles external surface-configurations A and B (Seamless-Pole-Inc., 2010)

7.3.3 Instrumentation and test setup

Using the designed loading setup shown in Figure 7 - 7 (a), each two piles were tested simultaneously against each other. The load was transferred to the piles through steel clamps attached to the main loading rod via hinged connections, as shown in Figure 7 - 8 (b), to satisfy free head condition. Different clamps diameters were manufactured to fit the different test piles configurations. The applied load was measured using a load cell connected along the main loading bar as shown in Figure 7 - 7.

The head deflection of each pile was monitored using two linear variable displacement transducers LVDTs as shown in Figure 7 - 8 (a). The LVDTs were supported on an independent beam and their measuring toes were pushing against a steel plate fixed to the pile head. The load cell and the LVDTs were hooked-up to a data acquisition system recording the readings every 1 second.
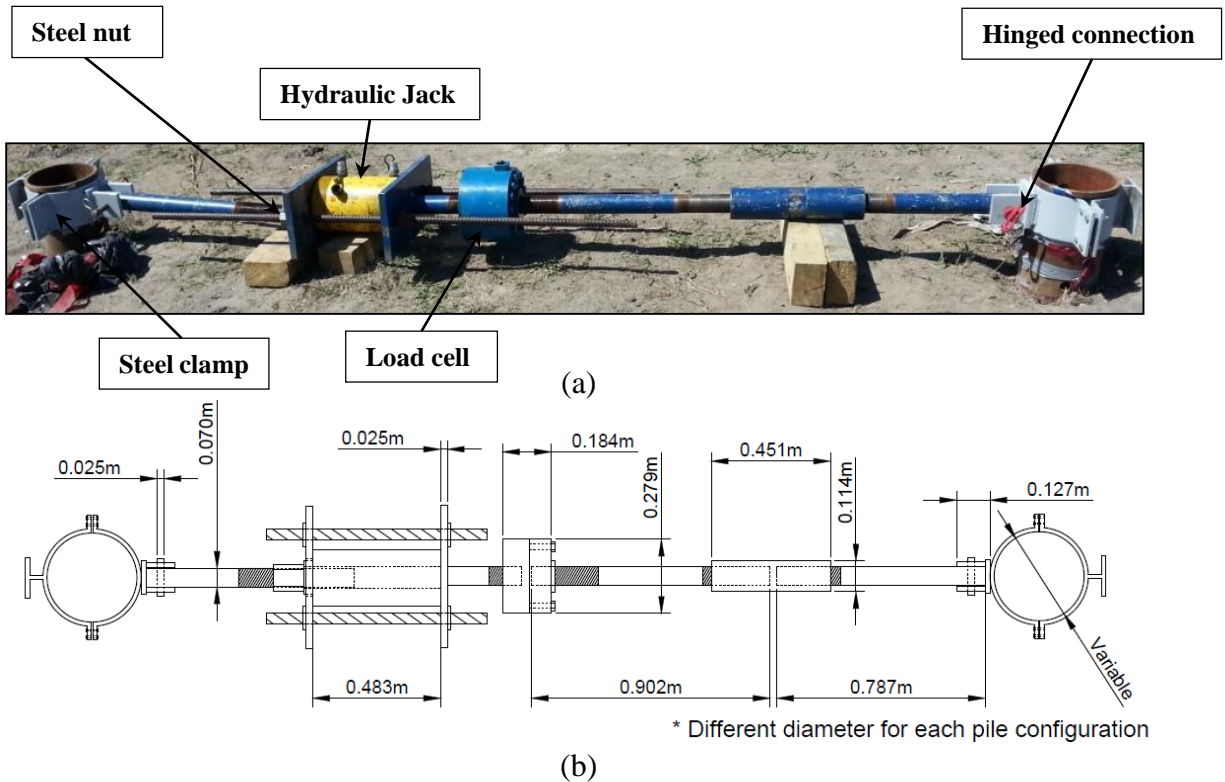
Figure 7 - 7: Lateral loading setup (a) Image of setup; (b) Dimensions of different components

<center>(a)   (b)</center>

Figure 7 - 8: Lateral load setup components (a) Steel clamp/LVDT plate; (b) Clamp-rod connection

7.3.4 Installation procedure

Prior to the piles installation, soil along the top 0.3m to 0.45m was predrilled to facilitate the pile vertical alignment. To install the piles, a mechanical torque was applied to each pile head using a Hitachi UH07 rig. The torque was applied to a steel cap bolted to the pile head as shown in Figure 7 - 9. The cap was removed prior to the lateral testing.

30cm x 30cm
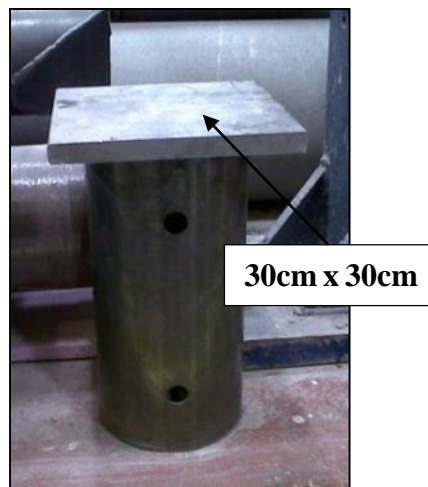
Figure 7 - 9: Field image of steel cap

The verticality of the piles was examined following the installation process using a magnetic angle locator. The maximum measured inclination angle was found to be less than 2 degrees. The piles free (unsupported) lengths at the start of the piles lateral testing are shown in Figure 7 - 5.

7.3.5   Load test sequence and test procedure

The lateral load tests were performed on pairs of piles as presented in Table 7 - 2.

Table 7 - 2: Lateral pile test setups

Test setup #	1st pile	2nd pile	Notes
1	PA1	PA2	
2	PA3	PC1	
3	PB1	PB2	
4	PA3	PC2	PA3 was previously tested in setup#2

Prior to lateral load testing, the piles were subjected to axial loading. The piles were then subjected to the loading sequence presented in Table 7 - 3.

Table 7 - 3: Load testing sequence

Pile	Testing sequence
PA1, PA2, PB1 and PC1	Cyclic compression followed by lateral monotonic test followed by cyclic lateral test
PA3, PB2 and PC2	Monotonic uplift followed by lateral monotonic test followed by cyclic lateral test

As shown above, all piles were first tested in monotonic lateral loading with the loading pattern shown in Figure 7 - 10 (a) followed by two-way cyclic lateral tests with the loading pattern shown in Figure 7 - 10 (b).The cyclic tests encompassed two-way loading cycles applied in increments of 5kN; 5 load cycles were applied at each load increment with each load cycle lasting 30 seconds. The maximum applied cyclic amplitude was 35 kN. This chapter presents the result of the cyclic lateral tests only.
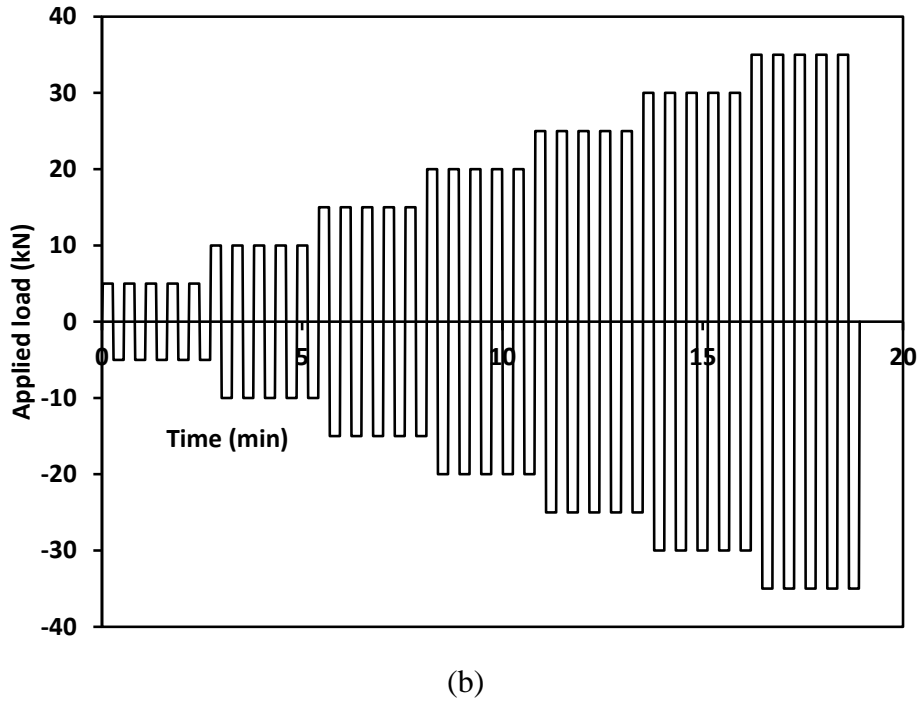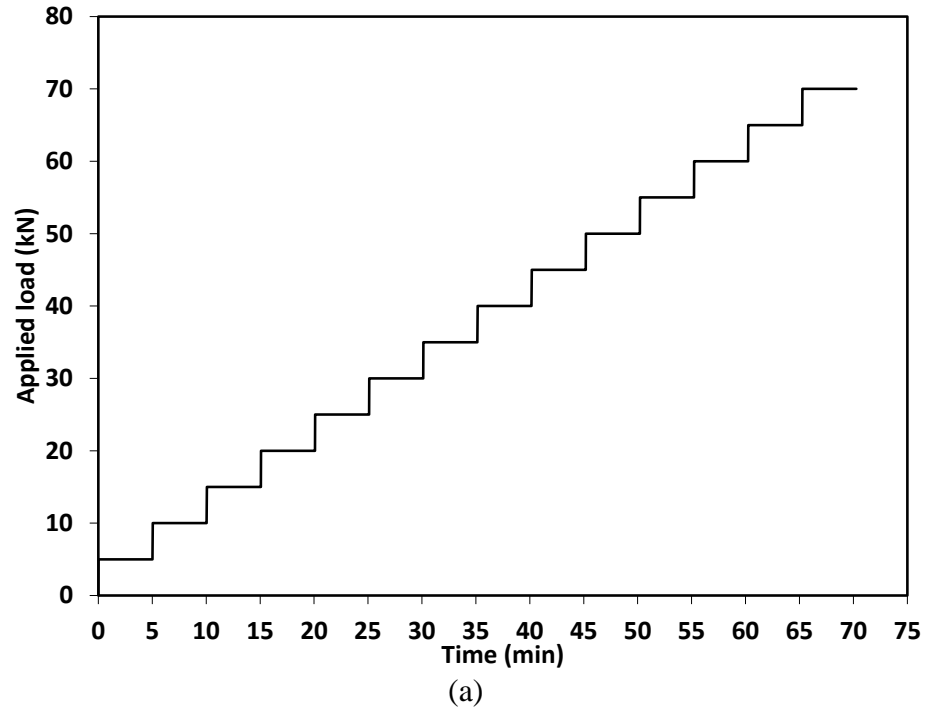
Figure 7 - 10: Lateral pile loading test patterns (a) Monotonic tests; (b) Cyclic tests

7.4 Results and discussion

7.4.1 Field tests

7.4.1.1 Load deflection curves

The load deflection curves for the tested piles of configurations A and C are presented in Figure 7 - 11 and Figure 7 - 12, respectively.

The application of the prior monotonic lateral tests resulted in the curves being shifted towards the side of the initial monotonic loading. For tapered piles, the developed gap and the soil cave-in process behind the pile, which resulted in a lower density soil zone, was reflected by the pinched shape of the curve. The development of the load deflection curves during the load reversal was characterized by a zone of very low resistance (almost vertical line) where the reduced soil modulus behind the pile governed the behavior. This was then followed by non-linear loading zone until the full applied load was reached. The gapping/cave-in process was more obvious at higher loading levels as shown in Figure 7 - 13 and Figure 7 - 14, where the first and last cycles' loops are plotted for piles of configuration A and C, respectively. The results also showed that this effect was less obvious for straight piles (PC1 and PC2), as they exhibit fatter hysteretic loops. This is attributed to the greater compacted soil zone for the tapered piles of larger average diameter at the pile head where the gap develops. The gap width and depth increased with the number of load cycles as visually observed during the tests. Also, the load deflection curves demonstrate greater energy dissipation through the deformation along the direction of initial monotonic loading (i.e. larger hysteretic loop area). This is a consequence of the greater strains and therefore the higher frictional losses. Figure 7 - 15 presents the developed gap at the end of testing on the side of initial monotonic loading.
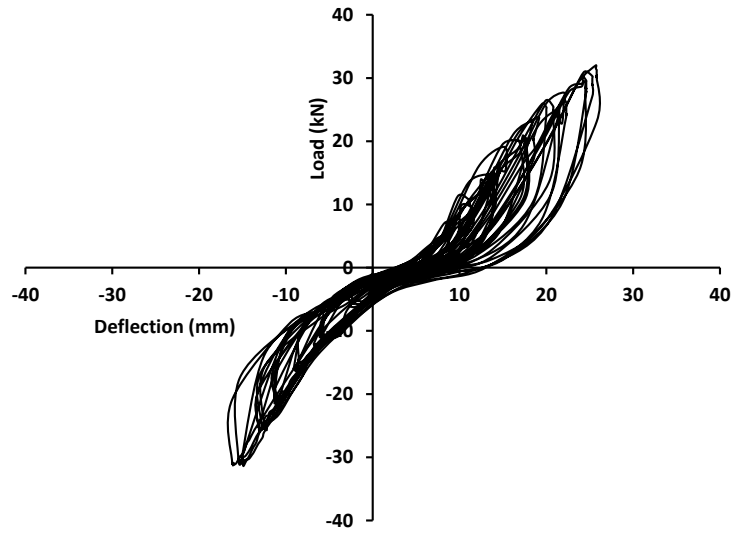
(a)
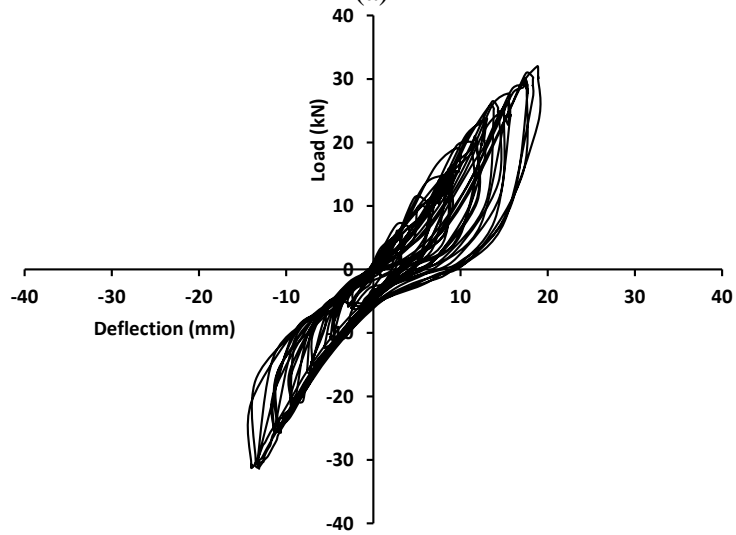
(b)
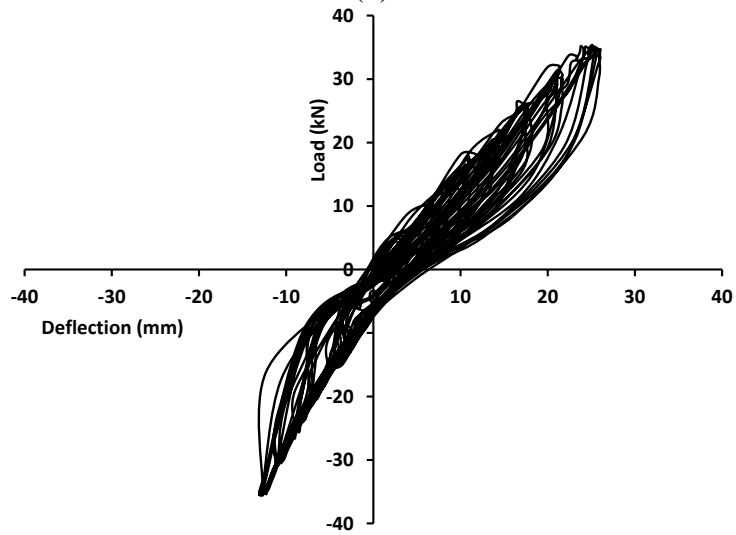
(c)

Figure 7 - 11: Load deflection curves-cyclic lateral tests (a) PA1; (b) PA2; (c) PA3
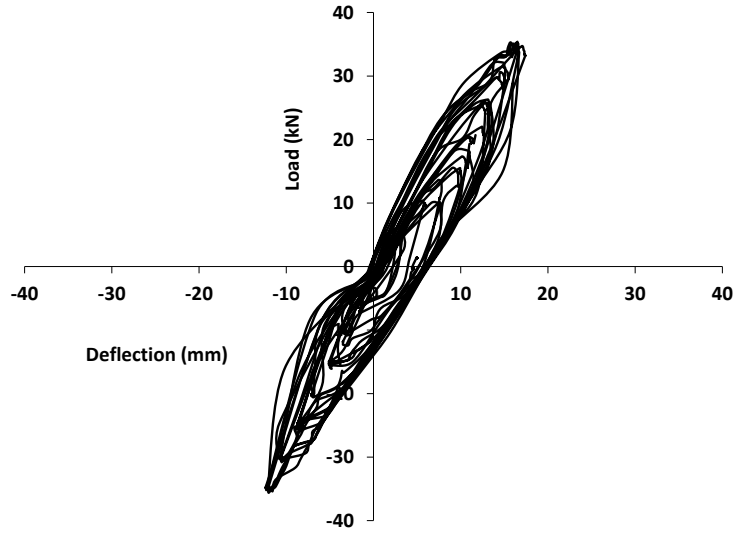
(a)
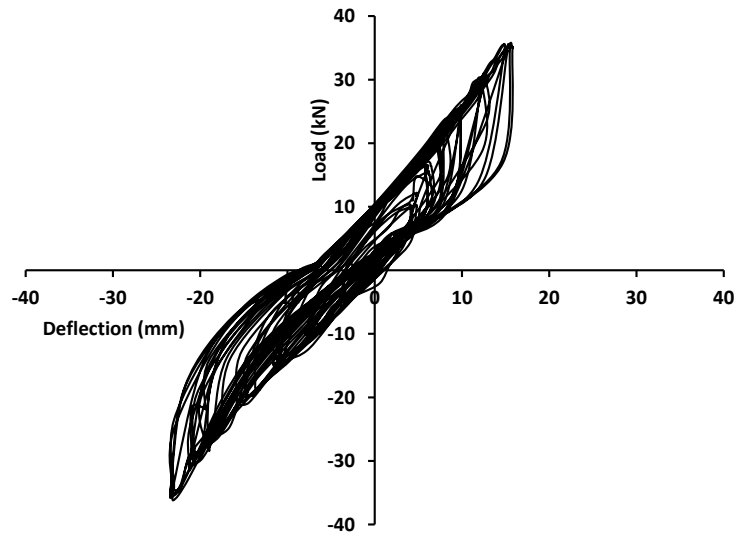
(b)

Figure 7 - 12: Load deflection curves (a) PC1; (b) PC2

244
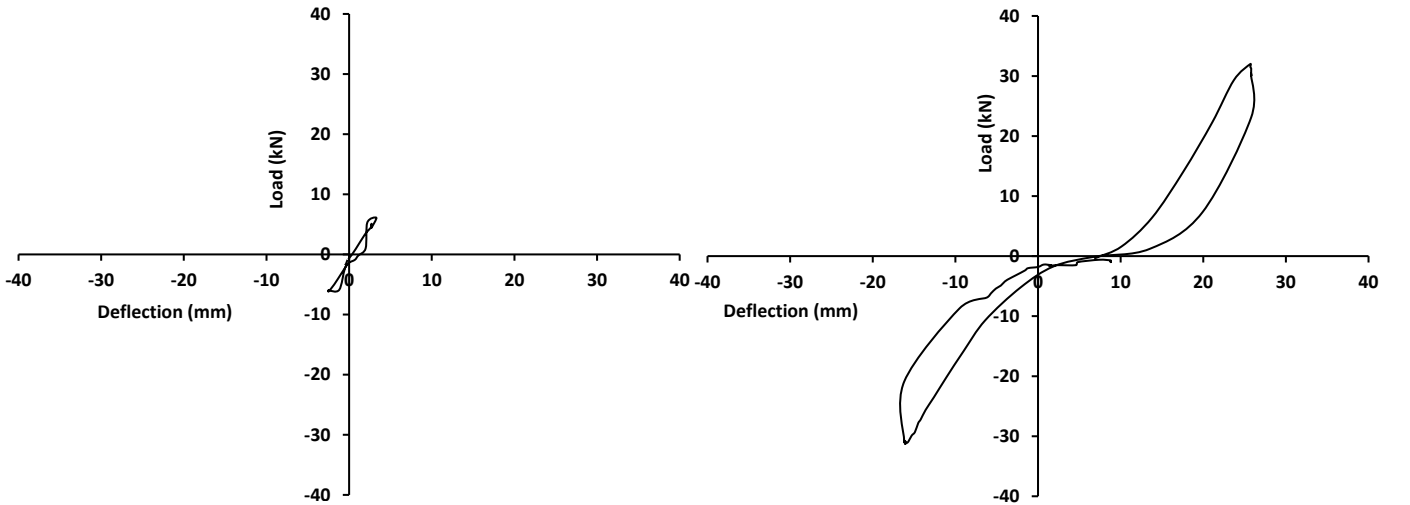
(a)
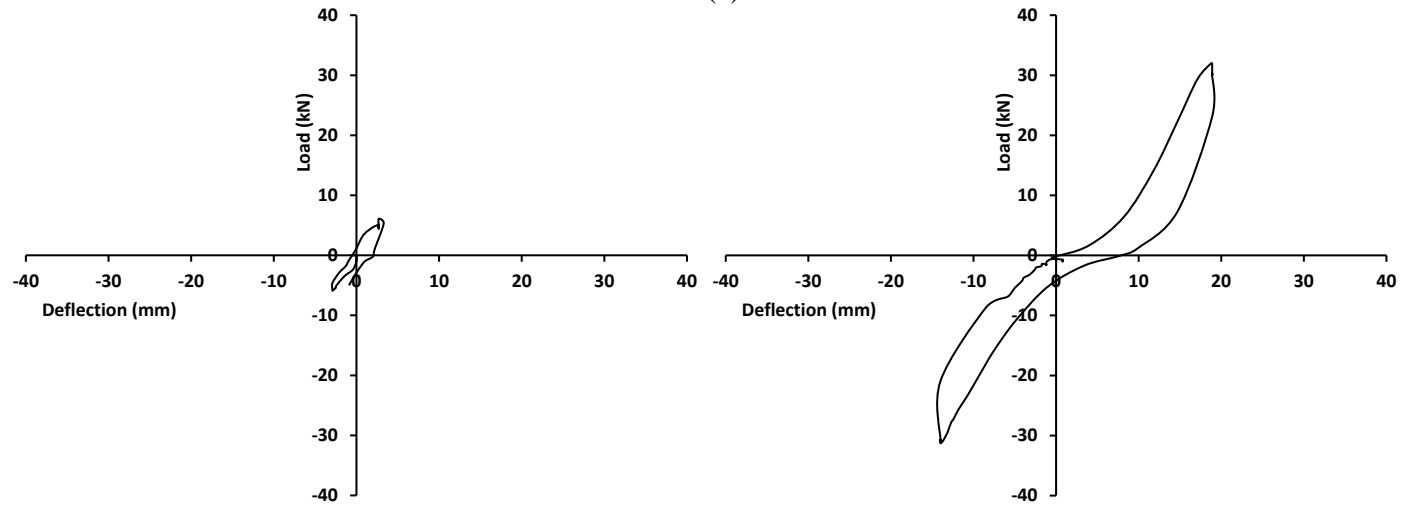
(b)
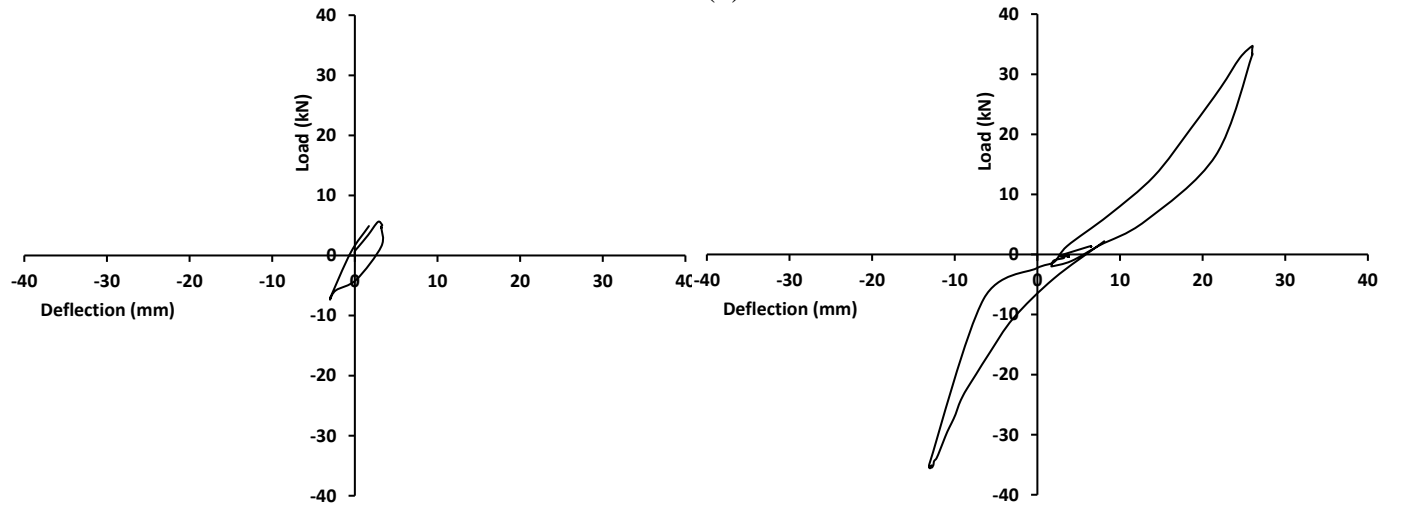
(c)

Figure 7 - 13: Hysteretic loop for first and last loading cycles for (a) PA1; (b) PA2; (c) PA3
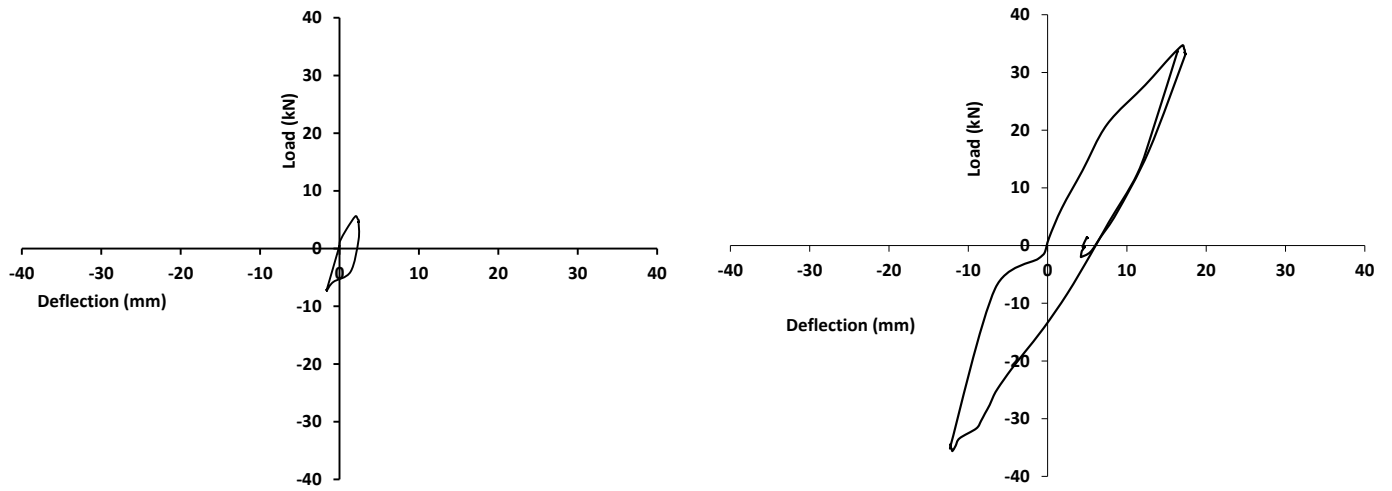
(a)
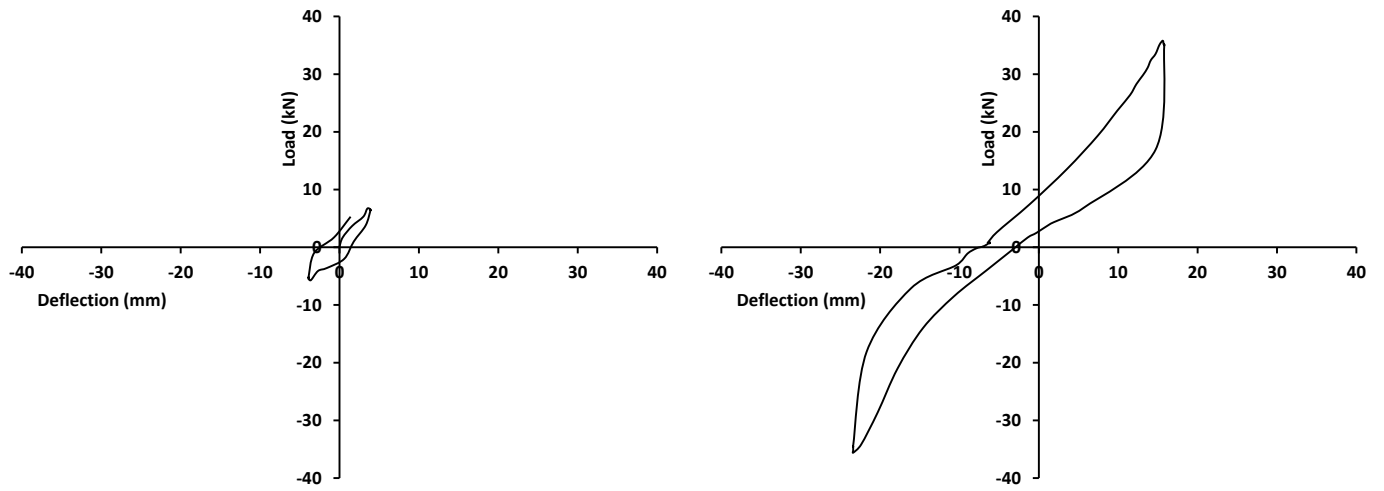
(b)

Figure 7 - 14: Hysteretic loop for first and last loading cycles for (a) PC1; (b) PC2

Figure 7 - 15: A field image of the developed gap behind pile PA1 at the end of the cyclic lateral testing

The development of the piles deflection with loading cycles is shown in Figure 7 - 16 (a) and (b) for piles of configuration A and C, respectively. The figures show that the performance of the tapered and straight helical piles was similar. This is attributed to the effects of gapping and soil cave-in, which resulted in stiffness degradation and comparable performance of both configurations. In addition, piles of configuration A; specially PA1 and PA3; had greater free (unsupported) lengths and hence were subjected to higher bending moments compared to configuration C piles.
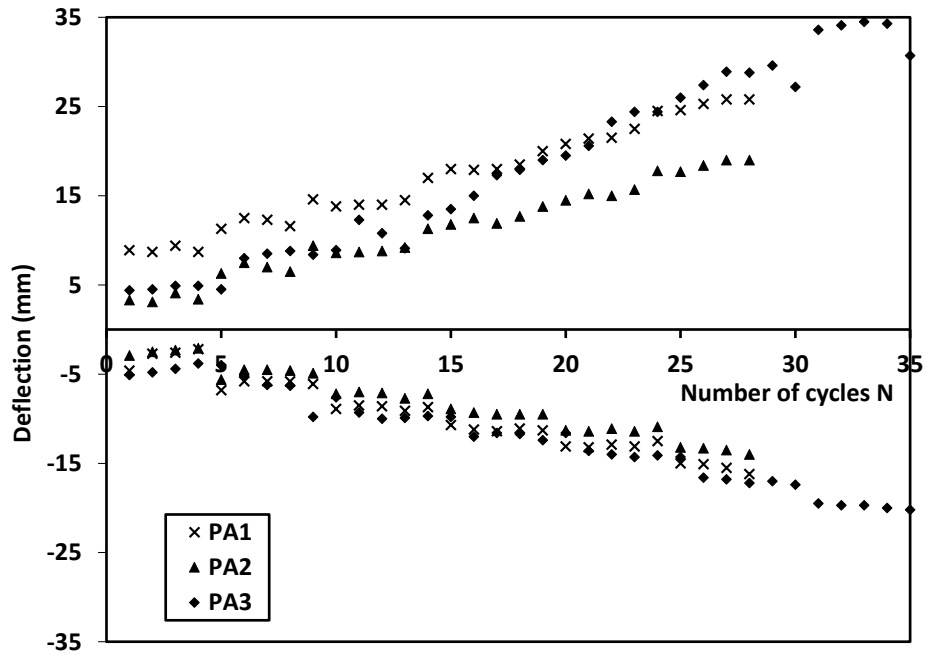
(a)
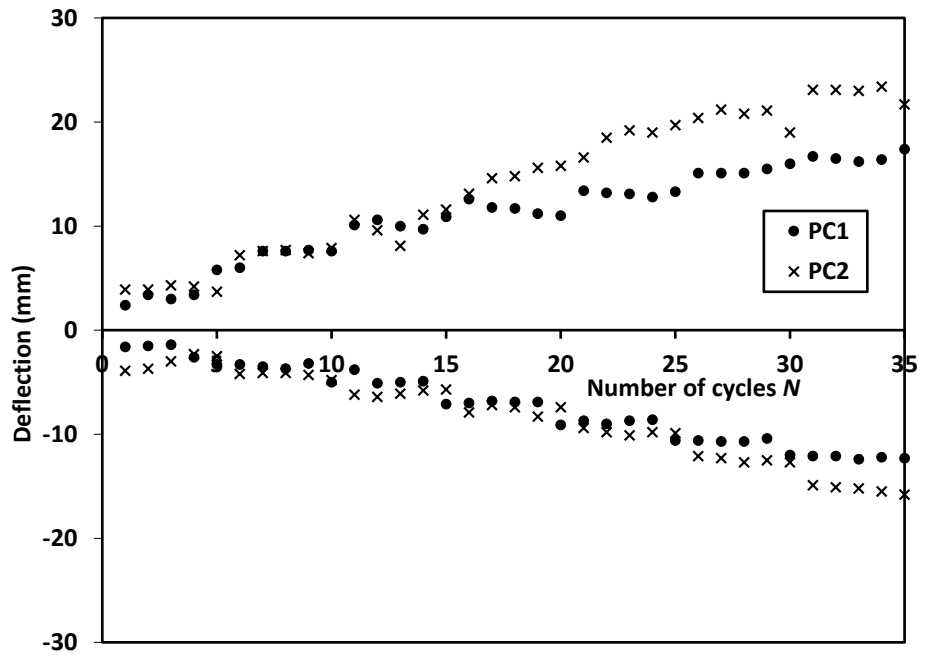
(b)

Figure 7 - 16: Measured pile head deflection with loading cycles (a) Configuration A piles; (b) Configuration C piles

7.4.1.2 System stiffness

The envelop of the measured cyclic load-deflection curves (loading branches) are plotted along with the monotonic curves (from Chapter 5) in Figure 7 - 17 and Figure 7 - 18 for piles of configurations A and C, respectively. The measured responses can be approximated by linear curves with no change in slope to the end of the tests, i.e., no plastic deformations of the piles. This behavior is attributed to the high flexural rigidity of the tested piles. It is also noted that the stiffness of the piles during the cyclic loading tests (i.e. slope of the linear curves) is less than the observed stiffness during the monotonic load tests due to the cyclic degradation of stiffness.

The higher degradation effect for tapered piles is attributed to their larger unsupported lengths (stick out), especially PA1 and PA3, which resulted in larger applied moment to the pile in addition to the lateral load. The effect was more obvious in PA1 compared to PA3 where the former was further pushed during the prior monotonic lateral test as presented in Chapter 5.

(a)

249

(b)

(c)
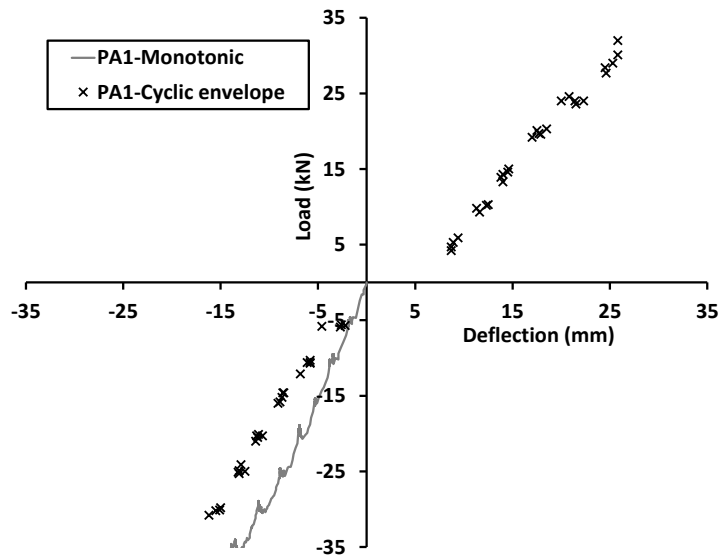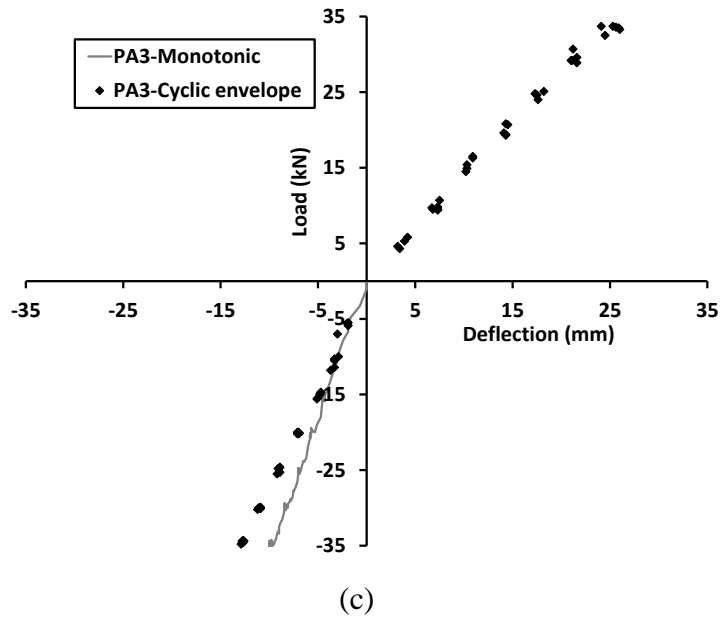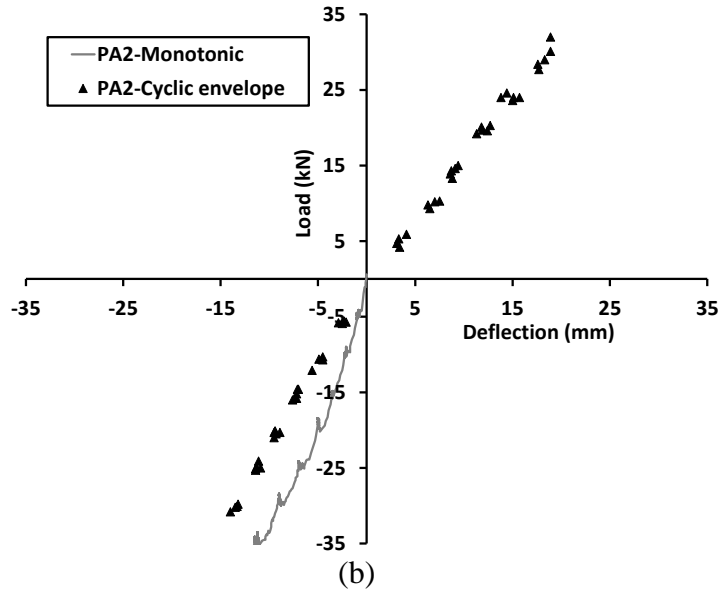
Figure 7 - 17: Monotonic and cyclic load deflection envelope (a) PA1; (b) PA2; (c) PA3
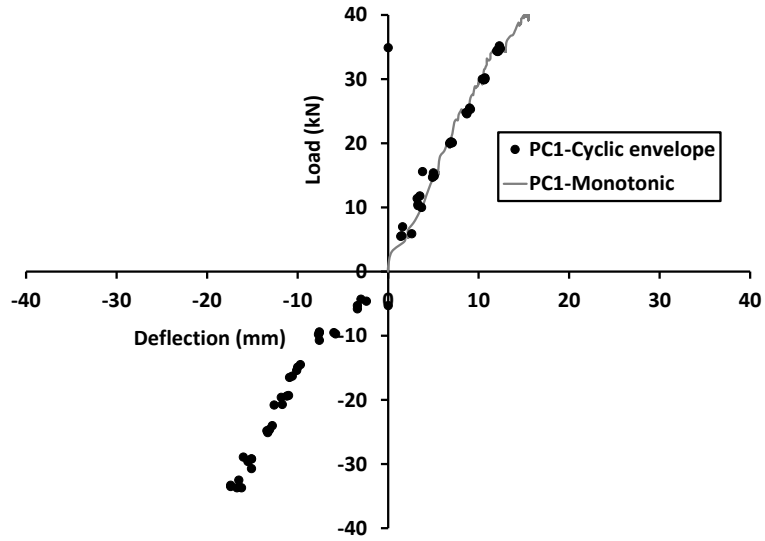
(a)
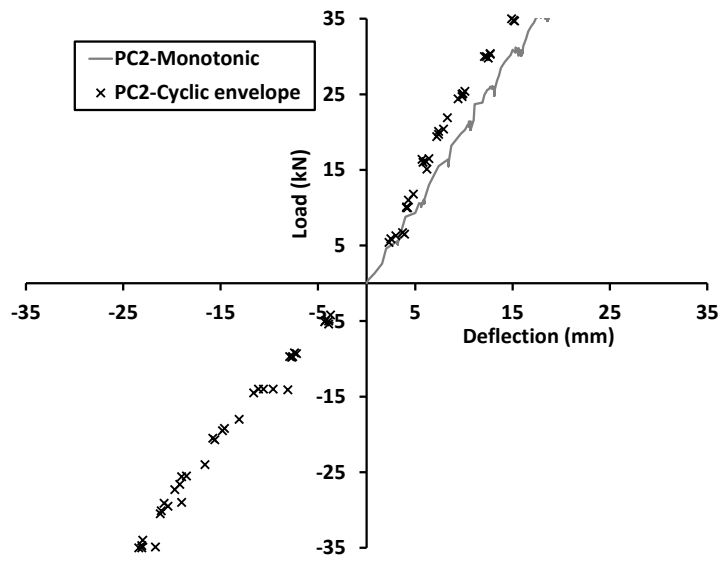
(b)

Figure 7 - 18: Monotonic and cyclic load deflection envelope (a) PC1; (b) PC2

The change in the pile lateral stiffness with the number of load cycles is represented in terms of the variation of the slope of the load deflection curve loops, K_L, given by:

$$K_L = \frac{Q_{max} - Q_{min}}{\delta_{max} - \delta_{min}}$$

(7 - 8)

Where Q_{max} and Q_{min} are the maximum and minimum applied loads during each loading cycle, δ_{max} and δ_{min} are the corresponding maximum and minimum resulting deflections respectively.

Figure 7 - 19 demonstrates the variation of K_L with the number of load cycles. The determined stiffness of both tested pile configurations are comparable. The results show a minor decrease in the stiffness of PA2 and PA3, while PA1 exhibited a small increase in stiffness as the number of cycles increased. It is also noted that PA1 exhibited generally lower stiffness since it was pushed farther than PA2 and PA3 during the prior monotonic lateral test as presented in Chapter 5, resulting in greater gap opening and soil cave-in and hence the presence of greater volume of looser soil in front of the pile. It appears that cyclic loading helped re-compact the soil in the vicinity of PA1 and K_s increased as well as the pile stiffness. On the other hand, Figure 7 - 19 (b) shows that the straight shafted piles (PC1 and PC2) exhibited constant or slightly increasing stiffness as the number of load cycles increased.
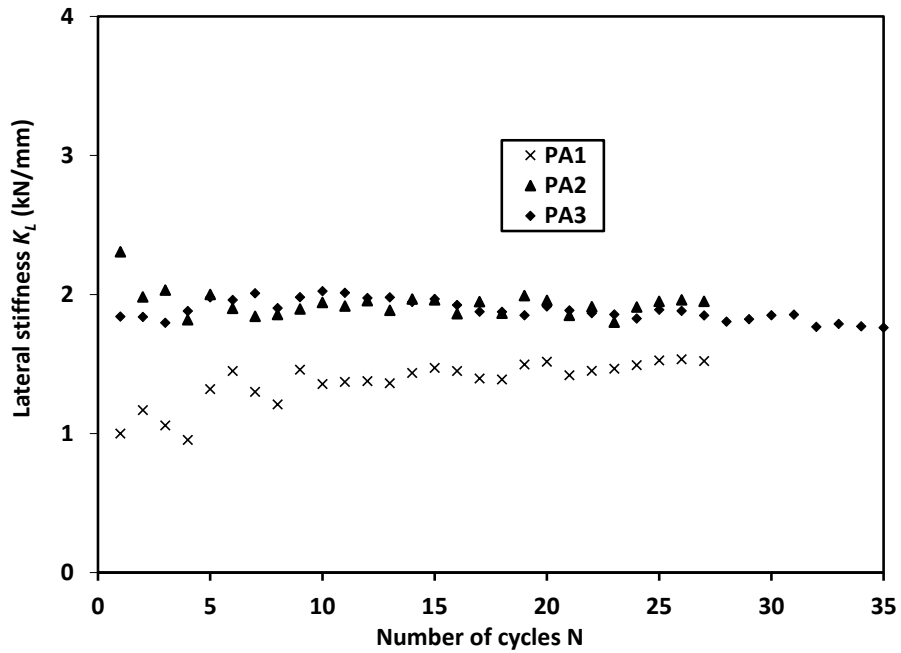
(a)
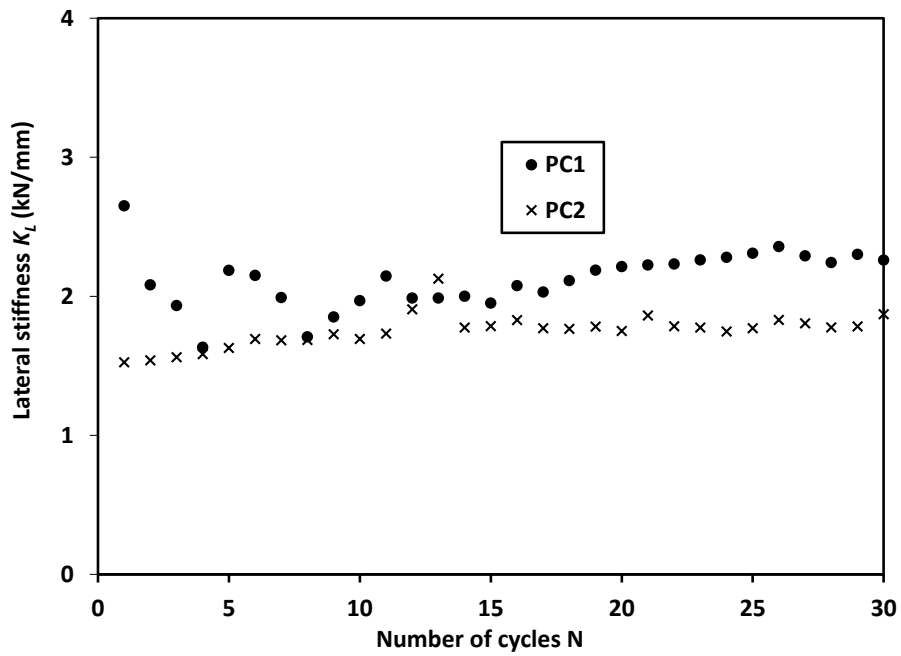
(b)

Figure 7 - 19: Variation of the piles lateral stiffness with loading cycles (a) Configuration A piles; (b) Configuration C piles

The variation of the degradation ratio K_L/K_1 (where K_1 is the system stiffness at the first cycle of each load increment) with number of loading cycles for configuration A piles was also calculated and is plotted in Figure 7 - 20. The loading amplitude values are presented as ratios of the average static ultimate lateral load P_{uL} =22.6kN (defined as the load corresponding to lateral deflection of 6.25mm).

The results of PA1, PA2 and PA3 can be fitted with a power function given by:

$$K_L/K_1 = aN^t \qquad\qquad\qquad (7 - 9)$$

The deduced equations are shown in Figure 7 - 20. For the lowest cyclic load (0.2 P_{uL}), the positive power of N (i.e. t) reflects the increasing in stiffness with number of load cycles. Whereas for higher loading ranges, associated with stiffness degradation due to the gapping and soil cave-in exhibited negative (but negligible) t values.
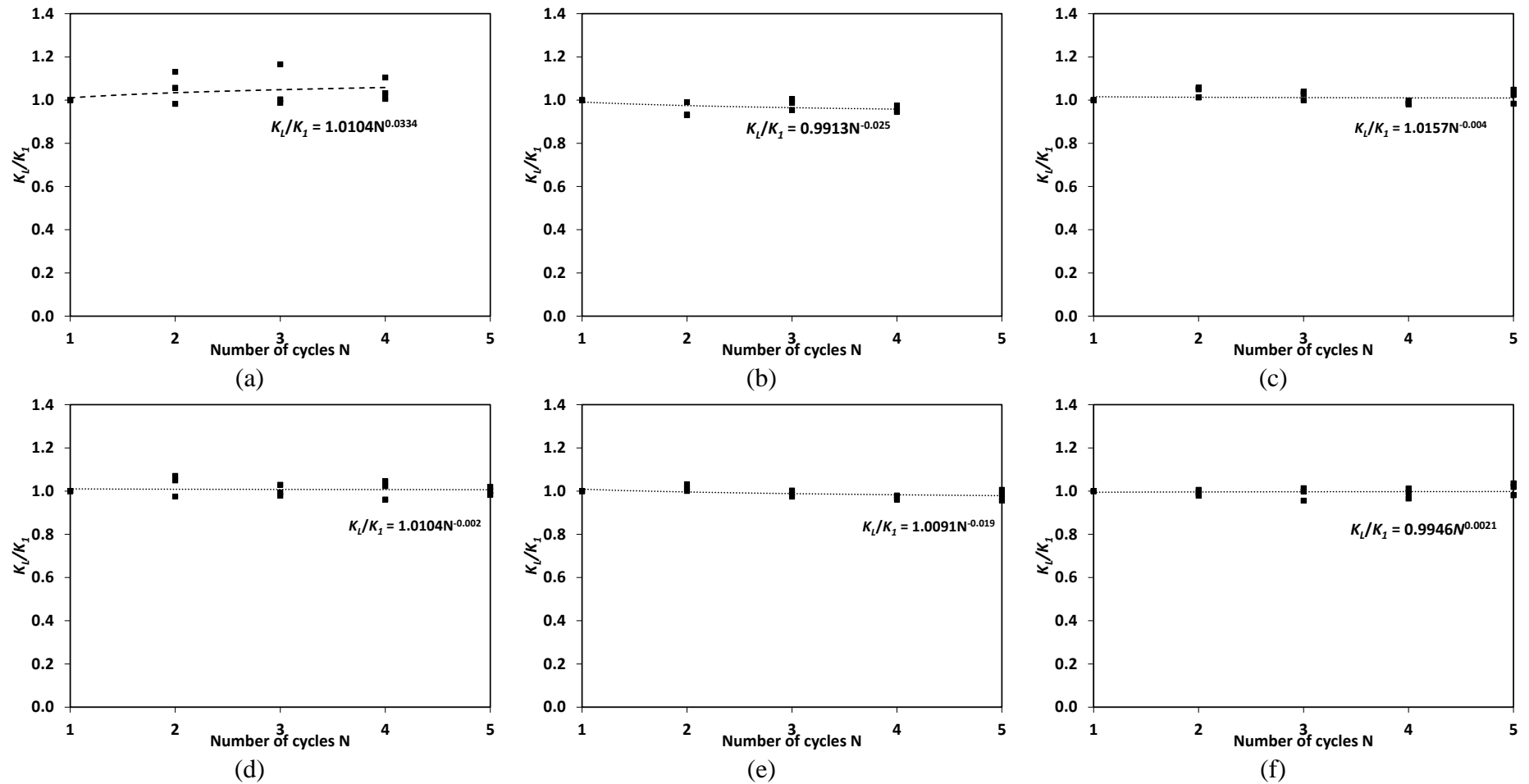
Figure 7 - 20: Variation of the degradation ratio with number of loading cycles for configuration A piles (a) Loading amplitude = 0.2 P_{uL}, (b) Loading amplitude = 0.4 P_{uL}; (c) Loading amplitude = 0.7 P_{uL}; (d) Loading amplitude = 0.9 P_{uL}; (e) Loading amplitude = 1.1 P_{uL}; (f) Loading amplitude = 1.3 P_{uL}

Residual deformations were observed at the end of cyclic loading. At the end of the tests and following the piles' unloading, the average measured residual deflection for configuration A piles was 21% of the maximum measured deflection during the cyclic lateral tests compared to 30% for configuration C piles. Both cases were in the previously loaded sides

7.4.2   Numerical analysis

To further understand the cyclic lateral performance of the tested piles, three-dimensional nonlinear finite element analyses were conducted simulating the behavior of PA2 and PC2 using the ABAQUS software package (Hibbitt *et al.*, 2008).

7.4.2.1   Description of finite element model

A 3D half-cylindrical mesh was used to simulate the soil-pile system. Wished in place pile was assumed along the axial z-direction of the half cylinder and the helix was idealized as a planar cylindrical disk.

The pile and soil medium were idealized employing 8-noded, first order, and reduced integration continuum solid elements (C3D8R). The considered elements have one integration point located at their centroid and three active translational degrees of freedom at each node.

The locations of the boundaries were selected through a sensitivity study such that the results are not affected by the boundaries conditions while minimizing the number of elements and hence the computational effort. The sensitivity study resulted in an optimum soil model with radius equal to 3.375 m (i.e. approximately 8.5 times the diameter of the helical plate) from the center of the pile shaft. The bottom horizontal boundary was positioned at 1.65 m beneath the pile toe, approximately equivalent to 4 helix diameters. The applied boundary conditions are shown in Figure 7 - 21.
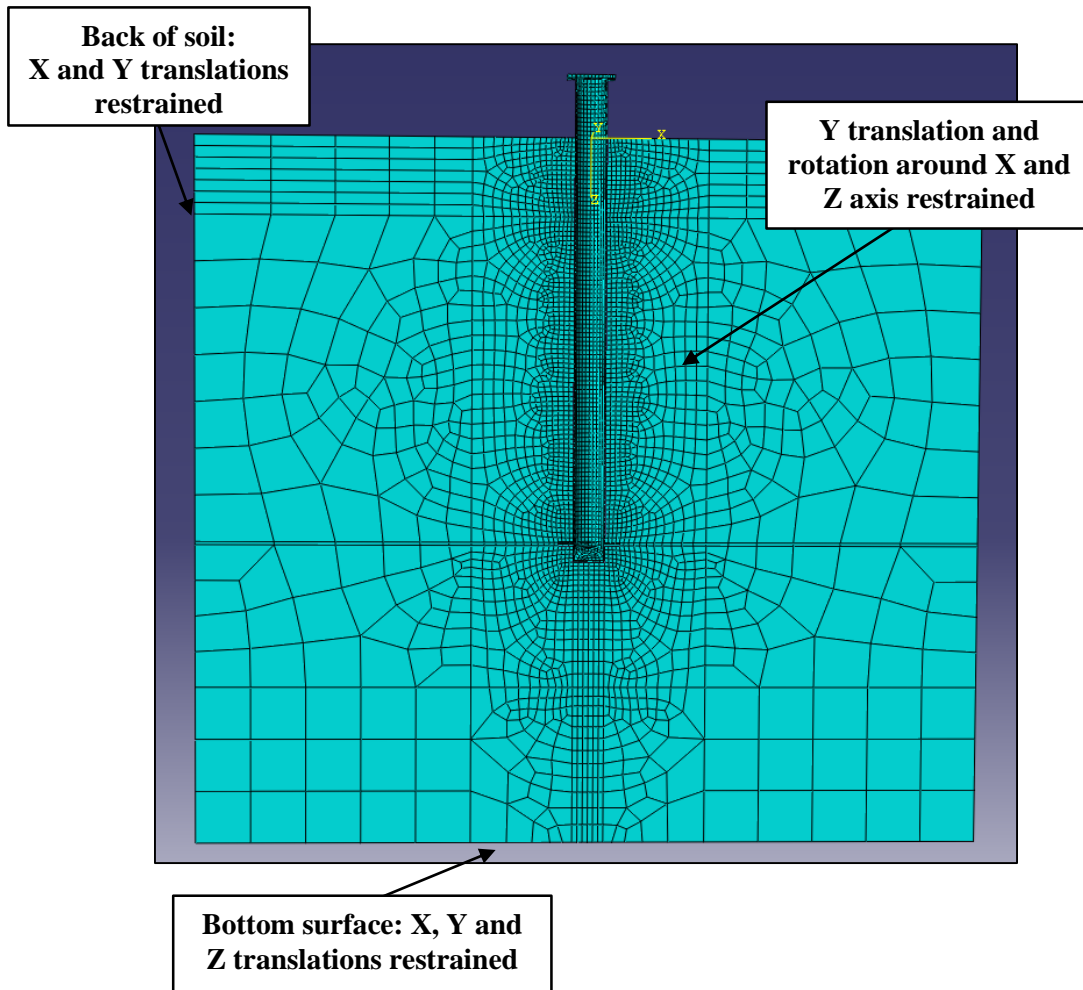
Figure 7 - 21: FE model-applied boundary conditions-un-deformed geometry-PC2

The mesh was further refined at zones with stress concentration and high strains as shown to ensure enhanced accuracy. The final mesh configuration was reached by conducting sensitivity analysis in which the mesh was incrementally refined and the results were compared. When the difference between the results of two consecutive models (i.e. refinements) became less than 2.5%, the most refined of them was used in the ensuing analyses. The elements were most refined along the pile-soil interface and around the helical plate and then their size gradually increased towards the model boundaries. This process resulted in mesh configurations consisting of 30170/21336 elements with maximum elements side size ranging from 320mm/335mm at the model boundaries to 25mm/28mm at the pile-soil interface for piles of PA2 and PC2, respectively.

7.4.2.2 Soil model

Elastic-perfectly plastic isotropic continuum was used to simulate soil properties. The Mohr-Coulomb yield criterion was used to model the soil plasticity and failure. Values of the critical state angle of internal friction φ_{cs}; cohesion, c'; dilation ψ; Poisson's ratio v; and elastic modulus, E_s were prescribed.

The soil domain was divided into three main sections:

-   The upper softer top soil layer 0.5m thick with weaker parameters to account for the predrilling process prior to the pile installation;

-   The soil along the pile shaft up to the helical plate;

-   The soil beneath the helical plate.

The assigned strength and stiffness parameters to these three sections are summarized in Table 7 - 4. These parameters were previously calibrated and validated employing the monotonic compressive and uplift field tests data as described in Chapters 3 and 4, respectively. It should be noted, however, that the intact elastic modulus for the top soil layer was selected to reflect the initial soil conditions (rather than the disturbed condition) because the piles were to push against undisturbed soil farther from the pile shaft. This assumption was validated with monotonic lateral field tests as presented in Chapter 5.

Table 7 - 4: Soil parameters considered in FE model

depth (m)		φ_{cs} (°)	C' (kPa)	ψ (°)	v	E_s (MPa)	γ' (kN/m³)
From	To						
0	0.5	32	4	4	0.3	35	17
0.5	Helix* level	32	4	6	0.3	70	18
Helix level	End of model	32	4	6	0.30	94	18

*Varies depending on embedded length and pile configuration

7.4.2.3 Pile model

The pile was modeled as linear elastic-perfectly plastic material where the elastic behavior was defined by Poisson's ratio, v_p, and Young's modulus, E_p, and the plastic behavior was represented by the material yield strength, F_y. The adopted piles mechanical properties are summarized in Table 7 - 5. Weaker strength parameters were assigned for the helical and base plates connections to the piles shaft to reflect the welding defects observed prior to pile installation.

Table 7 - 5: Pile mechanical properties considered in FE model

Component	Young's Modulus E_p (kN/m²)	Poisson's ratio v_p	Unit weight γ_p (kN/m³)	Yield strength F_y (MPa)
PA2 shaft	1.69E08	0.28	77	314
PC2 shaft	2E08	0.28	77	370
Helix and base plates connection to shaft	2E08	0.28	77	170

In order to model the possible degradation in the soil parameters due to the cyclic loading, the numerical model was calibrated by adjusting the soil parameters until the calculated results matched the field tests results. The soil elastic modulus along the pile shaft was further reduced each cycle to match the performance of the field load displacement results. Because the material model (Mohr-Coulomb) does not allow simulating the material degradation with cyclic loading directly, the soil stiffness was set to decrease as the model temperature increased, and the temperature was increased with each loading cycle.

7.4.2.4 Pile-soil interface model

The pile-soil interface behavior was simulated using a penalty-type tangential behavior Coulomb's frictional model. No relative tangential motion is allowed until a critical surface shear stress (traction) value is reached, which is given by the lesser of the interface shear strength or a fraction of the interface pressure. The interface strength was given by $\tan\delta = 0.78$ and 0.5 for tapered and straight piles configurations, respectively, where δ is the

interface angle of friction. The first was determined by studying the pile surface roughness in comparison to the soil mean particle size as mentioned earlier in Chapter 3, and the latter was considered in accordance to the suggested values by the Canadian Foundation Engineering Manual (2006). The interface model allowed the separation along the pile-soil interface.

7.4.2.5   Loading sequence

The following loading sequence was considered for the simulated piles:

- An initial loading step of geostatic stresses and equilibrium was applied to introduce the initial in-situ soil stresses;

- A load controlled analysis step was then conducted, whereby prescribed lateral load was applied at a reference point rigidly connected to the pile head. This step simulates the prior monotonic lateral test where the loading pattern presented in Figure 7 - 10 (a) was applied;

- This was followed by a static step where the pile was unloaded;

- Finally, a load controlled analysis step was performed whereby prescribed lateral load was applied at the reference point, simulating the cyclic lateral test. The loading pattern presented in Figure 7 - 10 (b) was considered.

7.4.2.6   Results of numerical simulations

The resulting load deflection curves of PA2 and PC2 obtained from the numerical simulations are displayed in Figure 7 - 22. The numerical results are in good agreement with the field test data as shown in Figure 7 - 22.
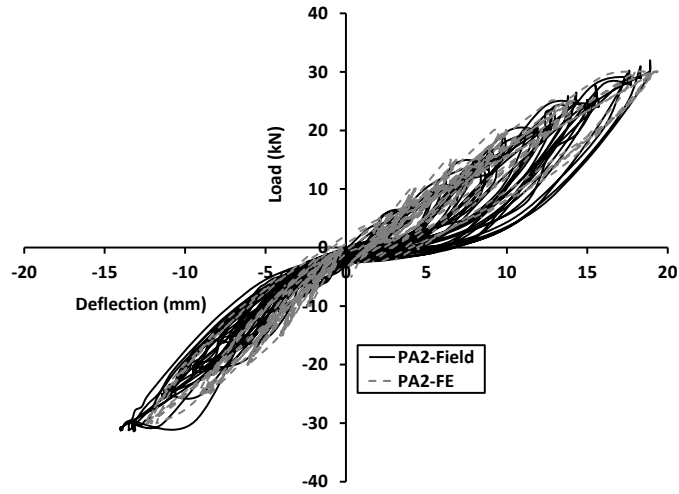
(a)
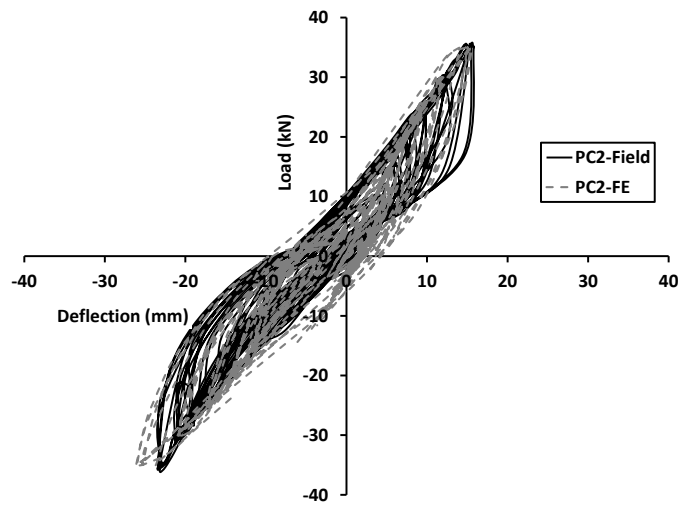
(b)

Figure 7 - 22: Comparison of calculated and measured load-deflection curves for calibration: (a) PA2; (b) PC2

The calibration process revealed that the shear modulus of the soil adjacent to the pile shaft has degraded through each load cycle. The variation of the calculated shear modulus reduction factor, G/G_{max} (G is the soil shear modulus), with number of load cycles for PA2 and PC2 is shown in Figure 7 - 23igure 7 - 23. Values of G/G_{max} ranged from 11% to 33%. While comparable degradation in the soil stiffness was shown for PA2 and PC2, noticeable degradation was observed for the latter at the start of the loading and then decreased until reaching an almost constant G/G_{max} values at the end of the test. On the other hand, G/G_{max}

for PA2 continued to decrease at an almost constant rate to the end of the test. This can be attributed to the greater gapping/soil cave-in effect in case of PA2 as discussed earlier.
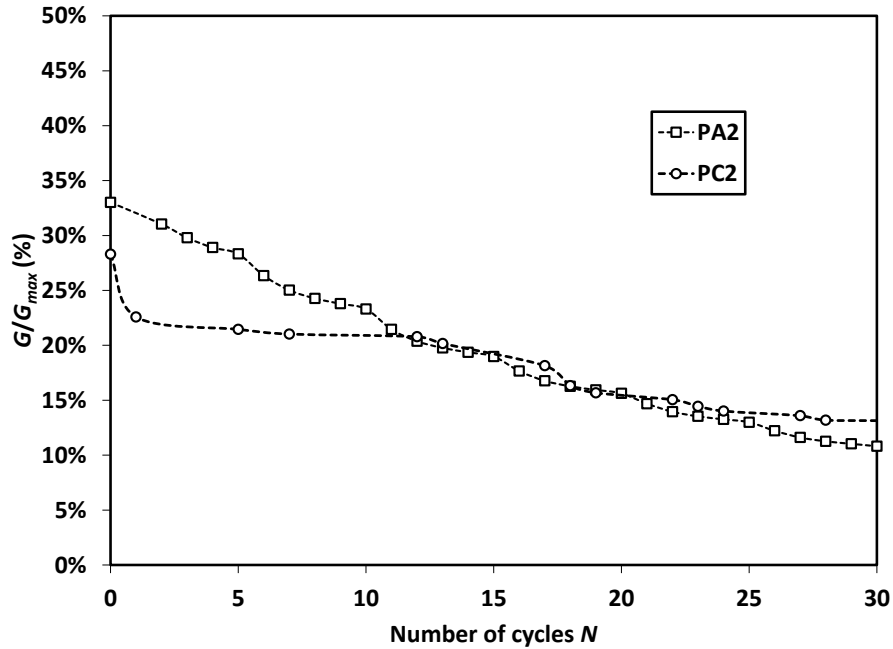
Figure 7 - 23: Variation of the shear modulus degradation factor with loading cycles-FE results

The variation of G/G_{max} with shear strain measured at the soil elements adjacent to the pile shaft for PA2 and PC2 are plotted in Figure 7 - 24. The degradation curve matched well with the literature reported data concerning the cyclic behavior of sands as plotted on the figure within the relevant shear strain levels. However, at higher loading amplitudes, significant shear strains developed in the soil elements depicting a highly non-linear behavior.
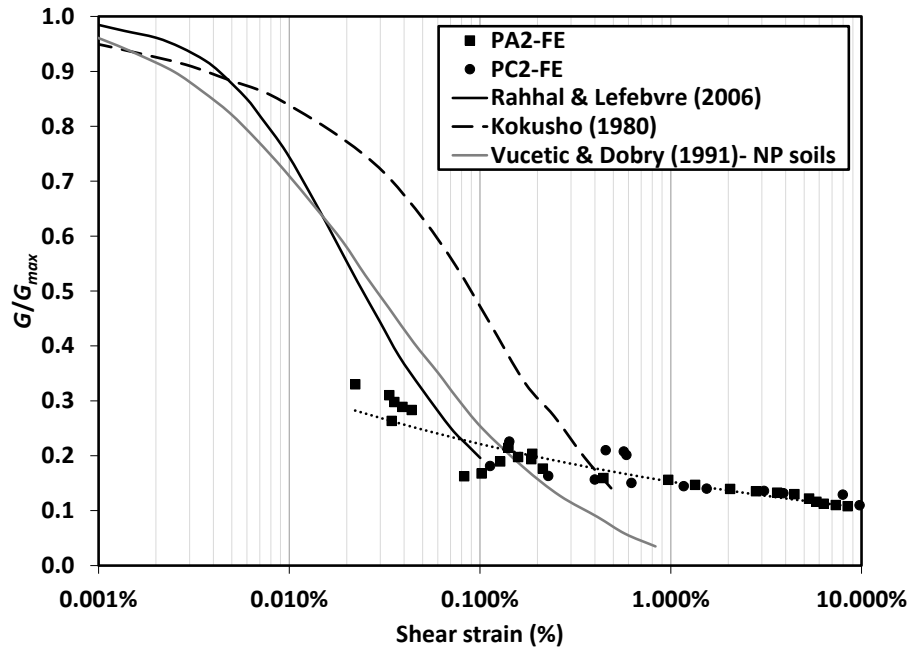
Figure 7 - 24: Variation of the shear modulus degradation factor with shear strain- FE results

The above degradation curves described the stiffness of the soil along the pile side that was not subjected to initial monotonic loading to failure. Considering the soil stiffness situated along the other, prior loaded, side, it is noted that the initial monotonic test reduced the initial shear modulus (during the first loading cycle) by 35% and 69% for PA2 and PC2, respectively. The more severe degrading effect for PC2 resulted from the greater head deflection during the prior monotonic lateral test as presented in Chapter 5. This was then followed by trend of shear modulus reduction with loading cycles similar to that observed for the soil on the other side.

Typically, the lateral behavior of piles is governed by the soil resistance along the top distance equal to 10 times the pile diameter. However, as can be noted from Figure 7 - 25 (a), the displacement field of the soil adjacent to PA2 demonstrates significant soil deformation only along the top $6.4D_{avg}$, where D_{avg} is the average pile diameter. This is due to the fixation provided by the passive soil resistance developed on the helical plate, which prevents the lower portion of the pile from rotation. This offers an advantage for helical piles in applications where the foundation is subjected to relatively high lateral loading.

The active displacement field behind the pile (away from loading direction) reflects the gapping effect right after the load reversal where the soil was unable to fully rebound. The radial extent of the displacement field is shown in Figure 7 - 25 (b) where the affected zones extended to a maximum radial distance of 2.4 D_{avg}. No significant shaft stresses were observed at the pile surface.
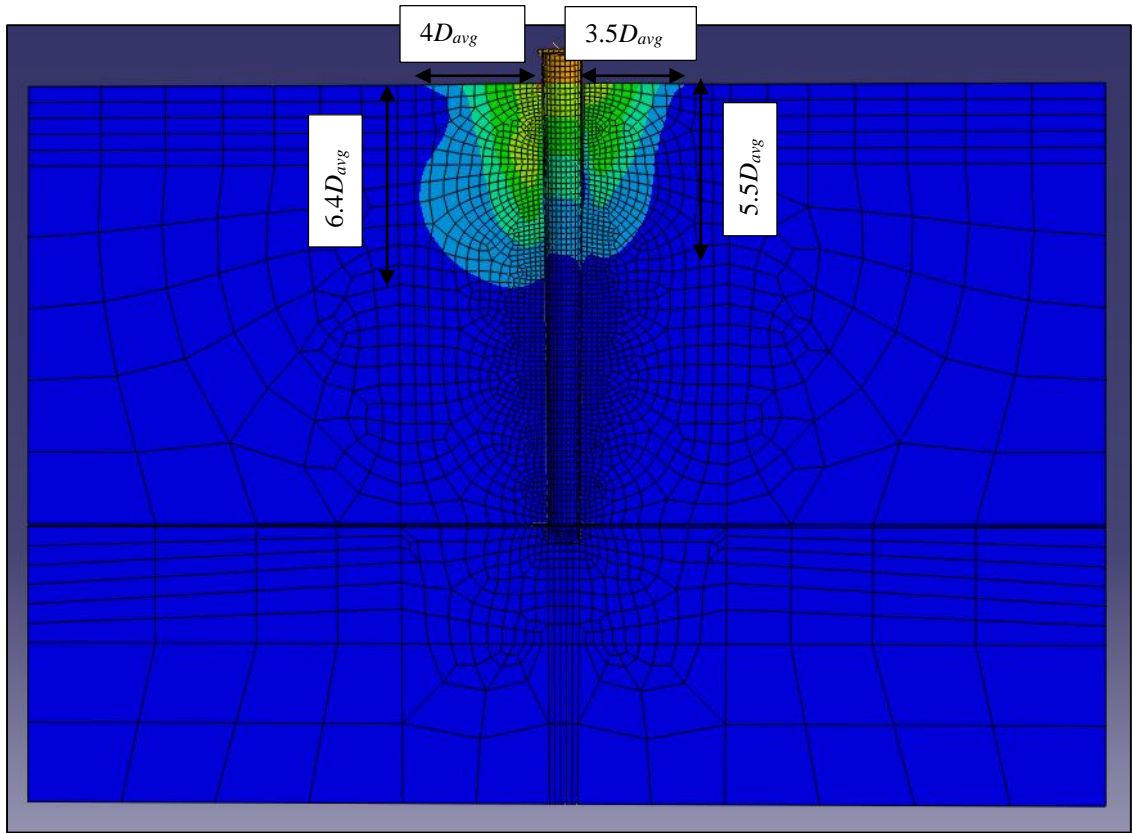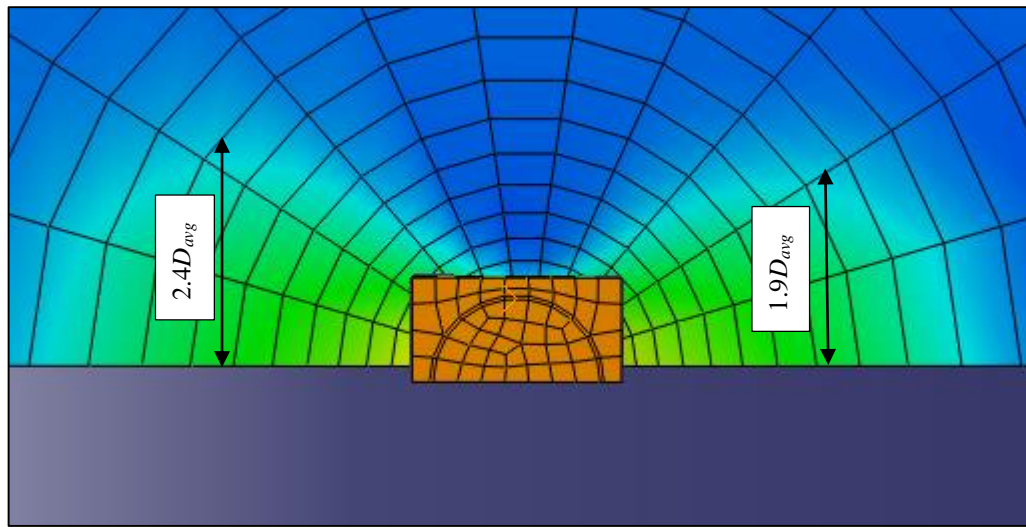
Figure 7 - 25: Displacement field around PA2 (a) Elevation; (b) Top view

7.5   Conclusions

In this study, the cyclic lateral performance of a ductile cast iron tapered helical pile was investigated. Three piles of the proposed pile configuration were installed and tested in a silty sand soil profile. In addition, two large diameter straight shafted steel helical piles were tested in the same soil profile for comparison purposes. The piles were subjected to monotonic lateral tests followed by cyclic lateral load tests. The results of the cyclic tests were summarized. The cyclic performance of the proposed piles was evaluated. Moreover, the effect of the previous monotonic lateral test on the piles cyclic performance was studied. In addition, numerical simulation of the field tests was conducted to better understand the performance characteristics of the tested piles and to evaluate any possible change in the soil stiffness. The main conclusions drawn from this study are summarized as follows:

1. Both helical tapered and helical straight piles performed similarly satisfactorily under the lateral loading schemes applied in the current study.

2. The lateral stiffness of the proposed helical piles remained practically unchanged through the cyclic loading applied in the current study.

3. The application of initial monotonic lateral test degraded the pile cyclic performance. The resulting load deflection curves were shifted towards the direction of initial monotonic loading.

7.6 References

AASHTO. 2002. Standard specifications for highway bridges. *HB-17.* American Association of State and Highway Transportation Officials.

Allotey, N. & El Naggar, M. H. 2008. A numerical study into lateral cyclic nonlinear soil-pile response. *Canadian Geotechnical Journal,* 45(9), 1268-1281.

ASTM C136. 2006. Standard test method for sieve analysis of fine and coarse aggregates. ASTM international.

ASTM D1556. 2007. Standard test method for density and unit weight of soil in place by the sand-cone method. ASTM international.

ASTM D2487. 2011. Standard practice for classification of soils for engineering purposes (Unified Soil Classification System). ASTM international.

ASTM D3080. 2011. Standard test method for direct shear test of soils under consolidated drained conditions. ASTM international.

ASTM D4318. 2010. Standard test methods for liquid limit, plastic limit, and plasticity index of soils. ASTM international.

Bienen, B., Dührkop, J., Grabe, J., Randolph, M. F. & White, D. J. 2012. Response of piles with wings to monotonic and cyclic lateral loading in sand. *Journal of Geotechnical and Geoenvironmental Engineering,* 138(3), 364-375.

Bowles, J. 1996. *Foundation analysis and design*, 5th edition, Mc-Graw hill.

CGS. 2006. *Canadian Foundation Engineering Manual*.4th edition. Canadian Geotechnical Society.

El Sharnouby, M. M. & El Naggar, M. H. Lateral static and cyclic behaviour of the composite steel-fibre reinforced helical pulldown micropiles-innovative foundation solutions for seismic applications. 21st Vancouver Geotechnical Society Symposium: Foundation and Lifeline Engineering, 2013, Vancouver.

Guo, P. X., Xiao, Y. & Kunnath, S. K. 2014. Performance of laterally loaded H-Piles in sand. *Soil Dynamics and Earthquake Engineering,* 67, 316-325.

Hibbitt, H. D., Karlsson, B. I. & Sorensen, E. P. 2008. ABAQUS Standard user's manual. Pawtucket, R. I.: Hibbitt, Karlsson & Sorensen Inc.

Kokusho, T. 1980. Cyclic triaxial test of dynamic soil properties for wide strain range. *Soils and Foundations,* 20(2), 45-60.

Kulhawy, F. H. & Mayne, P. W. 1990. Manual for estimating soil properties for foundation design. Ithaca, New York: Cornell University.

Leblanc, C., Houlsby, G. T. & Byrne, B. W. 2010. Response of stiff piles in sand to long-term cyclic lateral loading. *Geotechnique,* 60(2), 79-90.

Li, W., Gavin, D. & Doherty, P. Review of design models for lateral cyclic loading of monopoles in sand. Proceedings of the 8th International Conference on Physical Modelling in Geotechnics, 2014. 819-825.

Li, Z., Haigh, S. K. & Bolton, M. D. Centrifuge modelling of mono-pile under cyclic lateral loads. Physical Modelling in Geotechnics, 2010, Zurich. 965-970.

Liao, S. S. C. & Whitman, R. V. 1986. Overburden correction factors for SPT in sand. *Journal of Geotechnical Engineering,* 112(3), 374-377.

Lin, S-S. & Liao, J-C. 1999. Permanent strains of piles in sand due to cyclic lateral loads. *Journal of Geotechnical and Geoenvironmental Engineering,* 125(9), 798-802.

Little, R. L. & Briaud, J-L. 1988. Full scale cyclic lateral load tests on six single piles in sand. Texas A&M University College Station Department of Civil Engineering.

Long, J. H. & Vanneste, G. 1994. Effects of cyclic lateral loads on piles in sand. *ASCE Journal of Geotechnical Engineering,* 120(1), 225-244.

Mayne, P. W. In-situ characterization of Piedmont residuum in eastern US. Proc. US-Brazil: Application of Classical Soil Mechanics to Structured Soils, 1992, Belo Horizonte. National Science Foundation/USA, 89-93.

Mayne, P. W. 2006. In-situ test calibrations for evaluating soil parameters. Overview Paper on In-Situ Testing- Singapore Workshop.

Mayne, P. W., Christopher, B. & Dejong, J. 2002. Manual on subsurface investigations—Geotechnical site characterization. Washington, DC.: Federal highway administration, U.S. Department of Transportation.

Mayne, P. W. & Kulhawy, F. H. 1982. Ko-OCR Relationships in Soil. *Journal of the Geotechnical Engineering Division,* 108(6), 851-872.

Mosikeeran, T. 1990. Cyclic lateral load behaviour of piles. Report No.500. Auckland, New Zealand.

Poulos, H. G. & Davis, E. H. 1980. *Pile foundation analysis and design*, John Wiley and Sons.

Rahhal, M. E. & Lefebvre, G. Characterizing shear moduli reduction in soils cyclic behavior. Geotechnical Engineering in the Information Technology Age, GeoCongress, 2006. 1-5.

Reese, L. C. & Van Impe, W. F. 2001. *Single piles and pile groups under lateral loading,* London, UK, Taylor and Francis group plc.

Schnaid, F., Oliveira, L. A. K. & GEHLING, W. Y. Y. 2004. Unsaturated constitutive surfaces from pressuremeter tests. *Journal of Geotechnical and Geoenvironmental Engineering,* 130(2), 1-12.

Seamless Pole Inc 2010. Ductile iron poles. Birmingham, AL. (*http://www.seamlesspole.com/)*

Skempton, A. W. 1986. Standard penetration test procedures and the effects in sands of overburden pressure, relative density, particle size, aging, and over-consolidation. *Geotechnique,* 36(3), 425-447.

Verdure, L., Garnier, J. & Levacher, D. 2003. Lateral cyclic loading of single piles in sand. *International Journal of Physical Modelling in Geotechnics,* 3(3), 17-28.

Vucetic, M. & Dobry, R. 1991. Effect of soil plasticity on cyclic response. *Journal of Geotechnical Engineering,* 117(1), 89-107.

MONOTONIC AXIAL AND LATERAL PERFORMANCE OF

SCDI HELICAL TAPERED PILES IN CLAY

8.1 Introduction

The construction of solar farms to harness solar energy has witnessed unparalleled growth in recent years in order to meet the ever-increasing electricity demands. The foundations of solar panels are subjected to complex loading scheme due to the environmental loads in addition to the panels own weight. In order to withstand these loads, an innovative piling system is proposed herein, which combines the efficiency of the tapered cross-section and the construction advantages of helical piles as well as the competitive cost, effectiveness and durability of spun cast ductile iron with rough surface. The proposed system comprises spun cast ductile iron helical piles with tapered shaft.

The efficiency of the proposed system installed in sand was extensively investigated as presented in Chapter 3 to 7. This includes evaluating its axial and lateral performance under monotonic and cyclic conditions using numerical analysis and field tests.

The performance of the spun cast ductile iron helical piles with tapered shaft in clay is examined numerically in this chapter. Nonlinear finite element analysis of the proposed pile configuration installed in a clay profile was carried out and the results are summarized. This includes the performance of a single pile subjected to static lateral, compression and uplift loads.

8.1 Literature survey

Owing to their numerous construction advantages, helical piles are gaining wide popularity, especially in projects requiring fast installation and quick loading of the foundation. They are used in a wide range of applications such as power transmission

towers, bridges and residential and commercial buildings, which involve both static and cyclic compressive, uplift and lateral loading (Elsherbiny and Naggar, 2013).

The helical piles are installed by applying torque to their head with minimal vibration, noise and soil spoils. However, their installation may cause soil disturbance, which leads to the reduction of the soil shear strength and consequently the pile capacity (Lutenegger *et al.*, 2014).

The axial capacity of helical piles can be estimated through monitored the installation torque and employing capacity to torque correlations, thus providing a mean for quality assurance/control. The axial capacity can be predicted, given the installation torque, using the following equation (Hoyt and Clemence, 1989):

$P_u=K_tT$ (8 - 1)

where P_u is the ultimate axial capacity, K_t is the capacity-to-torque ratio and T is the installation torque. Perko (2009) conducted regression analysis of the results of more than 300 pile load tests and proposed the following expression for K_t:

$$K_t=\frac{\lambda_k}{d_{eff}^{0.92}}$$ (8 - 2)

Where: d_{eff} is effective shaft diameter and λ_k is a curve fitting factor $=1433\text{mm}^{0.92}/\text{m}$ (22 $\text{in}^{0.92}/\text{ft}$).

For helical piles with a single helix, of relevance to the suggested system herein, the capacity is given by the bearing resistance on the helix and the shear resistance along the pile shaft. Helical piles with slender shafts would only sustain limited lateral loads compared to other greater diameter piles. However attempts were made to develop helical piles with large diameter shafts thus offering large axial and lateral capacity (Fleming *et al.*, 2009; Abdeghany and El Naggar, 2010; El Sharnouby and El Naggar, 2012; Elkasabgy and El Naggar, 2013).

The lateral capacity long helical piles can be evaluated using the same techniques used for drilled and driven cylindrical piles; however, the installation effects should be considered

in choosing suitable design soil parameters (Puri *et al.*, 1984). For shorter helical piles, the presence of helical plates at shallow depth would increase the pile's lateral capacity. Prasad and Rao (1996) experimentally studied the lateral response of helical piles in clay and concluded that their capacity is generally equal to 1.2 to 1.5 times that of a straight shaft with no helical plates. The developed bearing/uplift resistance on the front/back half of the helical plates once rotated as well as the frictional resistance on the plates' surfaces contribute to the piles' lateral resistance (Prasad and Rao, 1996). The increase in the lateral resistance of short helical piles was observed from the lateral load test results of the examined piles installed in silty sand as discussed in Chapter 5.

On the other hand, tapered piles of decreasing circumference with depth have been successfully used as an efficient alternative to conventional cylindrical piles in sand for many years. While many researchers studied the axial and lateral performance of tapered piles in sand (e.g. Norlund 1963; Zil'berberg and Sherstnev 1990; Wei and El Naggar 1998; Sakr *et al.* 2005), much scarce data exists concerning their performance in fine grained soils.

8.2   Objectives and scope of work

The pile investigated in the current chapter consists of a spun-cast ductile iron tapered shaft (Seamless Pole Inc., 2010) fitted with a lower helical plate. The pile is to be installed using a mechanical torque conveyed by a driving motor holding the pile head.

In order to assess the feasibility and efficiency of the proposed pile in clay, three-dimensional finite element analyses were performed using the commercial software ABAQUS (Hibbitt *et al.*, 2008) to evaluate its performance when subjected to monotonic compressive, uplift and lateral loads.

8.3   Piles configurations

Four hollow closed ended piles with configurations as shown in Figure 8 - 1 were considered in this chapter. The pile shafts have 5.5mm thick walls.
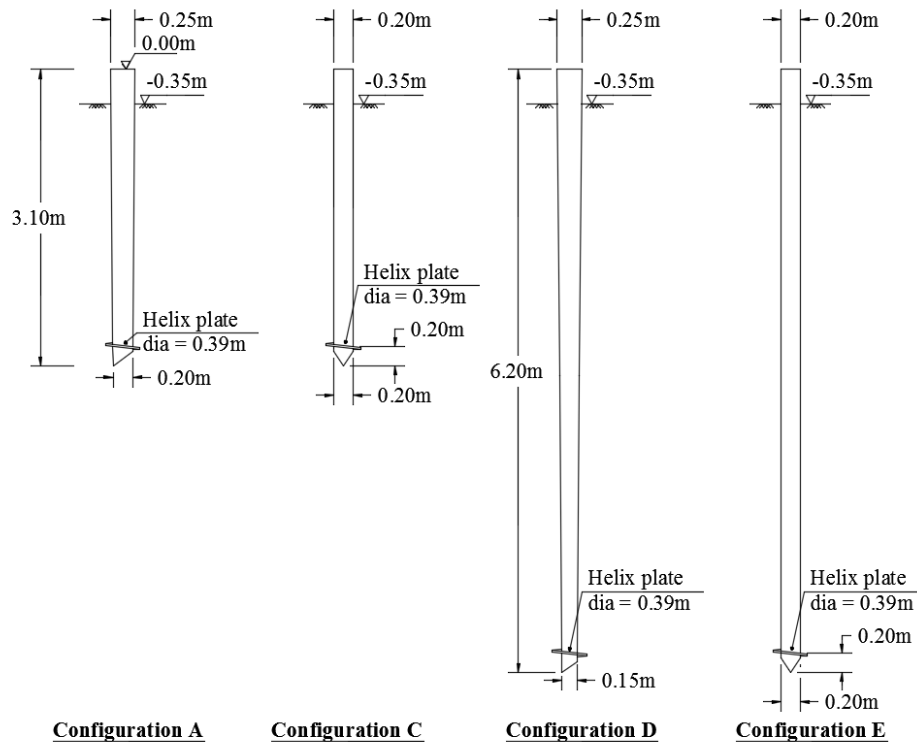
Figure 8 - 1: Simulated piles configurations

Piles A and D are made of ductile iron with rough surface as shown in Figure 8 - 2. Pile A simulates the pile tested in the field when installed in silty sand as discussed in Chapters 3 to 7, while Pile D reflects a longer version of the pile, which can currently be produced by the same manufacturer using the same manufacturing technique. Piles C and E on the other hand are conventional smooth steel pipe piles of the same average diameter as Pile D and were simulated for comparison purposes where the former was also field tested in silty sand.

Figure 8 - 2: Image of pile external surface –configurations A and D (Seamless Pole Inc., 2010)

8.2 Finite element model

Three-dimensional finite element models of the 4 analyzed configurations were developed using the ABAQUS software package (Hibbitt *et al.*, 2008). The details of the models are provided in the following sections.

8.2.1 Description of finite element models

8.2.1.1 Axial loading

The soil-pile system is modeled using a 3D quarter-cylindrical mesh. The pile was placed along the axial z-direction of the quarter-cylinder and the helix was idealized as a planar cylindrical disk instead of a true helix. This approximation is believed to have insignificant effect on the model accuracy while reducing the computational efforts.

Both the soil and pile were simulated by 8-noded, first order, and reduced integration continuum solid elements (C3D8R) having three active translational degrees of freedom at each node with one integration point located at the centroid. Locations of the model boundaries were optimized through a sensitivity study in order to minimize the effects of the boundary conditions on the results while reducing the computational effort. The

274

optimized model comprised a soil cylinder with radius of 2.5 m (i.e. 10 times the greatest shaft diameter) from the center of the pile shaft. The bottom horizontal boundary was placed at 1.95 m below the pile toe, which is equivalent to 5 helix diameters.

Mesh refinement at highly stressed/strained zones was necessary to ensure the accuracy of the results. Accordingly, a series of models were developed where the mesh was incrementally refined and the results were compared. When the difference between the results of two consecutive models (i.e. refinements) became less than 2.5%, the most refined model was considered. This process resulted in mesh configurations consisting of 25838/15821/24052/27894 elements for Piles A/C/D/E, with maximum side dimension of the elements ranging from 25cm/33cm/50cm/33cm at the model boundaries to 2cm/3cm/1.7cm/2.5cm at the pile-soil interface respectively. The applied boundary conditions are shown in Figure 8 - 3 (a).

8.2.1.2 Lateral loading

The soil-pile system is modeled using a 3D half-cylindrical mesh. Same type of elements used for the axial loading simulations was employed. The location of the boundaries was optimized to avoid the effects of the boundary conditions on the results and to minimize the computational effort. The radius of the soil cylinder extended 3.375 m (i.e. approximately 8.5 times the helix plate diameter) from the center of the pile shaft. The bottom horizontal boundary was placed at 1.65 m below the pile tip, which is approximately equivalent to 4 helix diameters. The applied boundary conditions are illustrated in Figure 8 - 3 (b).
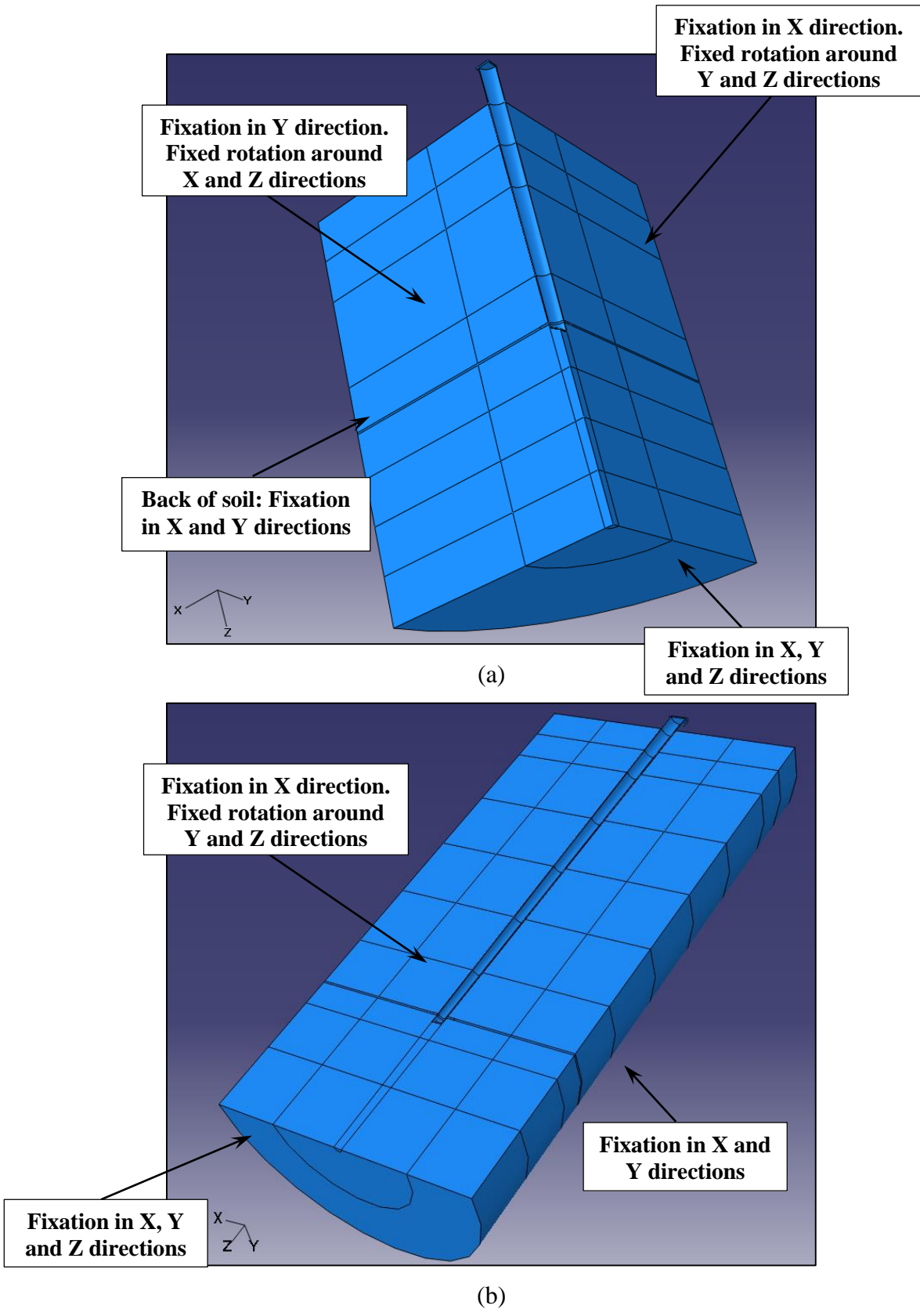
Figure 8 - 3: FE model-applied boundary conditions (a) Axial loading; (b) Lateral loading

8.2.2 Model properties

8.2.2.1 Soil properties

A clay profile was assumed where the different mechanical parameters were determined using the following empirical correlations:

$$S_u/\sigma_v'=0.11+00.37PI \text{ (Skempton, 1957)} \qquad (8 - 3)$$

Where σ_v' is the effective overburden stress.

$$K_o=0.44+0.42PI \text{ (Massarsch, 1979)} \qquad (8 - 4)$$

A plasticity index *PI* of 37% was assumed. Accordingly an earth pressure coefficient at rest K_o of 0.6 was considered. E_s/S_u ratio of 550 was used where E_s is the soil Young's modulus and S_u is its undrained shear strength (Duncan and Buchignani, 1976). Undrained clay Poisson's ratio v of 0.45 was used (Briaud, 2013).

The above correlations and assumptions resulted in a soil profile with a variation of Young's modulus and undrained shear strength with depth as shown in Figure 8 - 4 (a) and (b). Due to the limitations of the used software however, the linearly changing parameters were replaced by a layered soil profile as shown in Figure 8 - 4 (c). The profile was divided into 9 sub-layers, each was 1m thick except the top 2 layers that were 0.5m thick each to ensure the accuracy of the results especially for lateral loading cases.
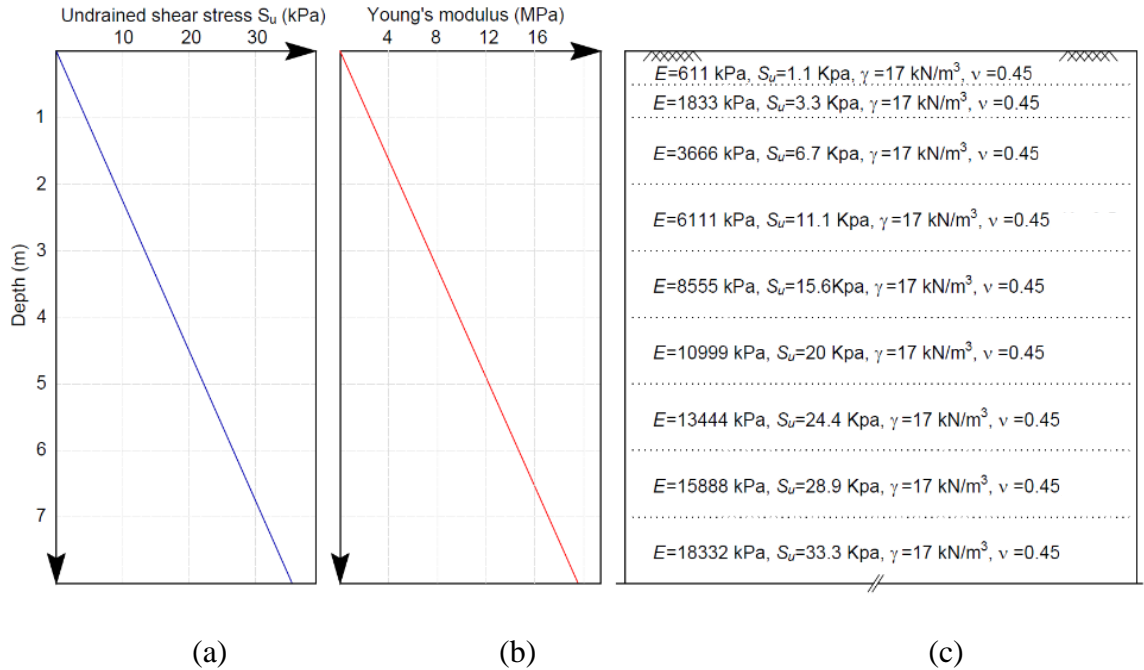
Figure 8 - 4: Assumed clay profile (a) Undrained shear strength Vs depth; (b) Young's modulus Vs depth; (c) Average considered parameter in the FE model

It should be noted that accurate simulation of the installation effects was not possible in absence of any experimental data at the time of writing this chapter.

8.2.2.2 Pile model

Piles were modeled as linear elasto-pastic material. The elastic behavior was defined by Poisson's ratio, v_p, and Young's modulus, E_p. The plastic behavior was represented by the yield strength of the pile material. The considered mechanical properties adopted in the model are summarized in Table 8 - 1. Weaker strength parameters were considered for the helix and the base plates (closing the modeled piles toe). These reduced properties were considered to accommodate the welding defects visually observed prior to the piles installation during the field testing in silty sand and were validated with field tests results in sand as presented in Chapters 3 to 7.

Table 8 - 1: Pile mechanical properties considered in FE model

Component	Young's Modulus E_p (kN/m^2)	Poisson's ratio ν_p	Unit weight γ_p (kN/m^3)	Yield strength F_y (MPa)
Shaft- Piles A and D	1.69E08	0.28	77	314
Shaft – Piles C and E	2E08	0.28	77	370
Helix and base plates welded connections	2E08	0.28	77	170

8.3.1.1 Pile-soil interface model

The pile-soil interface was modeled using the tangential behavior penalty-type Coulomb's frictional model, in which no relative tangential motion occurs until the surface traction reaches a critical shear stress value that is a fraction of the soil shear strength. The soil-pile interface adhesion factor α was set to 1 considering the assumed clay undrained shear strength values (CGS, 2006).

8.2.3 Loading sequence

The piles were wished in place for all the studied cases. An initial loading step of geostatic stresses and equilibrium was applied to consider the initial in-situ soil stresses. For both axial and lateral analysis, the geostatic step was followed by a displacement controlled analysis step whereby prescribed displacements were applied at reference points rigidly connected to the top loading plate.

8.2.4   Results and discussion

8.2.4.1   Axial performance

8.2.4.1.1 Load displacement curves

The load-displacement curves for compression and uplift loading cases are shown in Figure 8 - 5 (a) and (b), respectively. In both cases, the curves are characterized by an initial linear region where the resistance is derived from the developed shaft stresses, followed by a non-linear plastic zone and finally a global failure zone with an almost horizontal line (constant resistance). Comparing the results of Piles A and C to those of Piles D and E respectively, it is clear that the embedded depth has a profound effect on the pile stiffness and ultimate capacity. It is also noted that the initial linear parts of piles D and E are almost identical. This is because the tapered profile has small effect on the developed shaft stresses during the initial (linear) loading phase. This is further confirmed comparing the uplift and compressive results, where similar curve slopes (stiffness) were observed. The greater difference between Piles A and C in compression is mainly due to the different average diameters whereas in uplift the gapping effect discussed later for the tapered profile reduced that difference. Comparing the compression and uplift responses, it is noted that the maximum uplift resistance was less than the compressive one as expected.
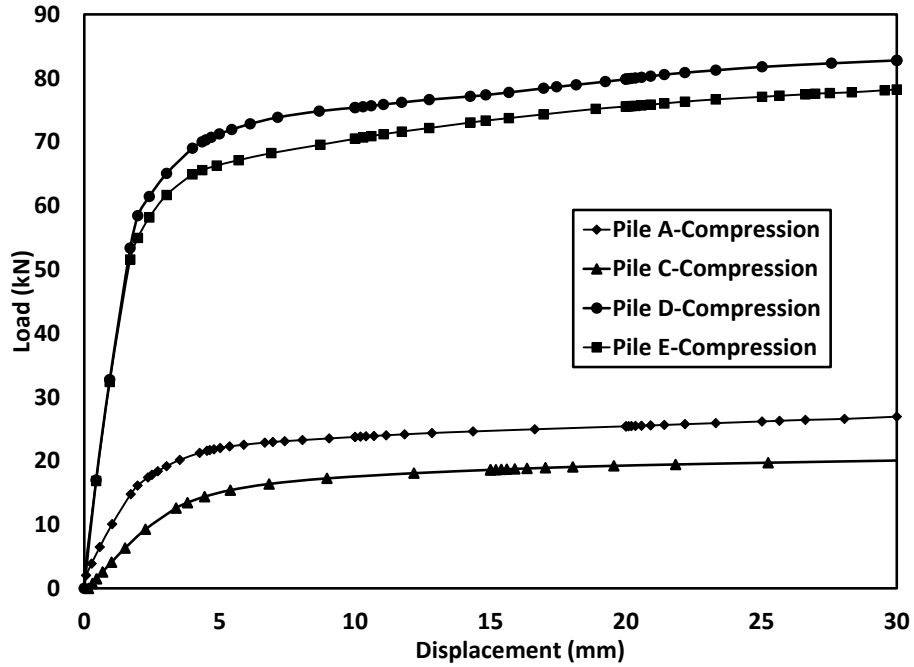
(a)
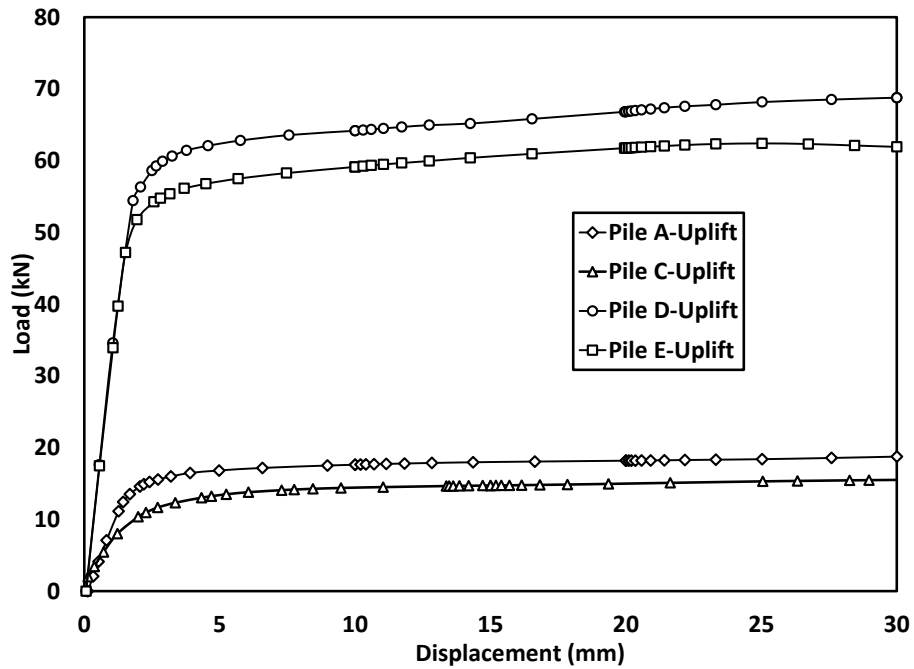
(b)

Figure 8 - 5: Load-displacement curves (a) Compression tests; (b) Uplift tests

8.2.4.1.2 Piles ultimate capacity

The piles ultimate capacity is determined using Chin's method instead of Fuller and Hoy method as was the case for piles installed in silty sand (Chapters 3 and 4). The Fuller and Hoy criterion may underestimate the capacity of long piles (Prakash and Sharma, 1990). The constructed chart to calculate the piles' capacities is shown in Figure 8 - 6. The calculated ultimate static capacities in uplift and compression are summarized in Table 8 - 2. To better compare the piles' efficiency, the capacity per unit volume of pile material was calculated and presented in the same table.
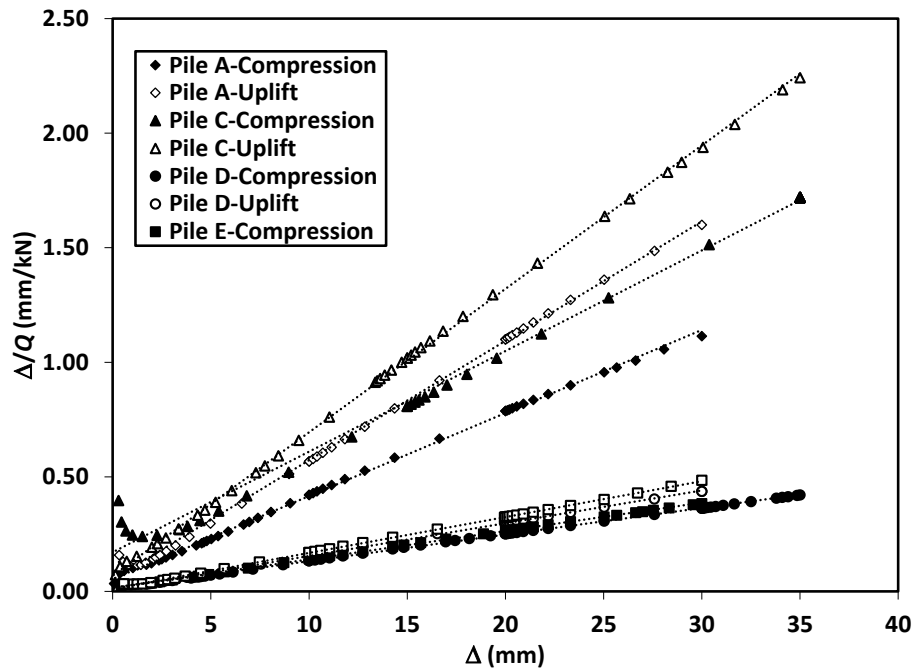
Figure 8 - 6: Chin analysis of pile load displacement curves

Table 8 - 2: Pile ultimate static axial capacity and capacity per unit material volume

Pile #	Ultimate axial capacity (kN)		Ultimate axial capacity/embedded volume (MN/m^3)	
	Compression	Uplift	Compression	Uplift
Pile A	27	19	2.23	1.57
Pile C	23	16	1.84	1.29
Pile D	86	70	3.68	3.00
Pile E	81	64	3.58	2.83

The ultimate capacities of Piles D and E (of the same length and average diameter) are comparable where no significant improvement resulted from the taper angle. The same findings were found comparing their capacities per unit volume. That was shown for both uplift and compression loadings. The slightly greater difference between the results of Piles A and C (of shorter length) is due to the greater average diameter of Pile A. The calculated uplift to compression capacity ratios were 70%, 70%,81% and 79% for Piles A, C, D and E, respectively.

Measuring the load transferred to the helix plate showed that, at the maximum applied displacement (30mm), the load was almost equally carried by the shaft resistance and the end bearing (helix and tip) for piles in compression. For the uplift case, 43% of the load was carried by the helix bearing and 57% by the shaft resistance.

The developed shaft stresses for Piles D and E under both compression and uplift loading were almost the same. This is further illustrated in Figure 8 - 7, which displays the variation of the shaft resistance with depth for both configurations in compression and uplift loading cases.

During uplift loading, soil-pile separation along the top of the piles. The separation increased with loading covering the top 0.25 m of Piles A and D. This separation had a minor effect on the pile capacity considering its short length and the low soil shear strength at the top. It was also noted that the normal (radial) stresses acting on the shaft decreased during uplift loading due to the taper effect. However, it had a minor effect on the pile capacity because the shaft resistance depended on the adhesion bond. The vertical stresses acting over the helix top surface during uplift loading were smaller near the pile wall reaching a minimum value along the pile-helix connection. This confirms that pile capacity is derived from helix bearing and shaft resistance and not the shear resistance along an equivalent cylindrical surface of diameter equal to the average of the helix and shaft diameter as might be the case for belled piles (Sharma *et al*., 1984).

During uplift loading, the developed shaft stresses just above the helix level (approximately 0.65 to $1D_{helix}$) decreased linearly until the helix level for all configurations as shown in

Figure 8 - 7. Similar observations were observed by Zhang (1999), which would be attributed to the bearing failure above the helix.
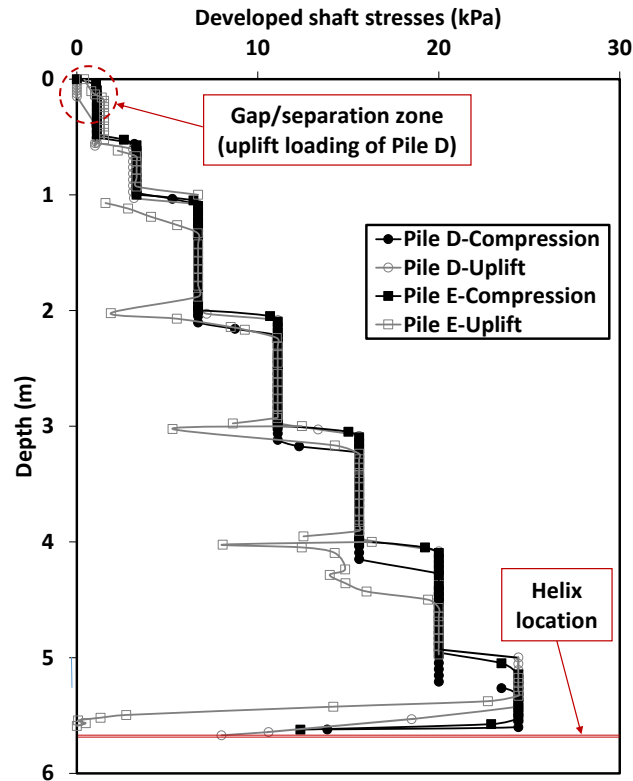
Figure 8 - 7: Variation of the developed shaft stresses with depth –Single piles in clay

The displacement fields around Pile D are shown in Figure 8 - 8 (a) and (b) for compression and uplift loading cases, respectively. The region of high strains around the helix plate extended radially to a distance equivalent to 0.9 and 1.4 times the helix diameter for uplift and compression loading cases, respectively.

For uplift loading cases, negligible heave was observed at the ground surface (less than 1mm). This small value was expected considering the deep helix plate behavior where the plastic zone does not extend to the ground surface.
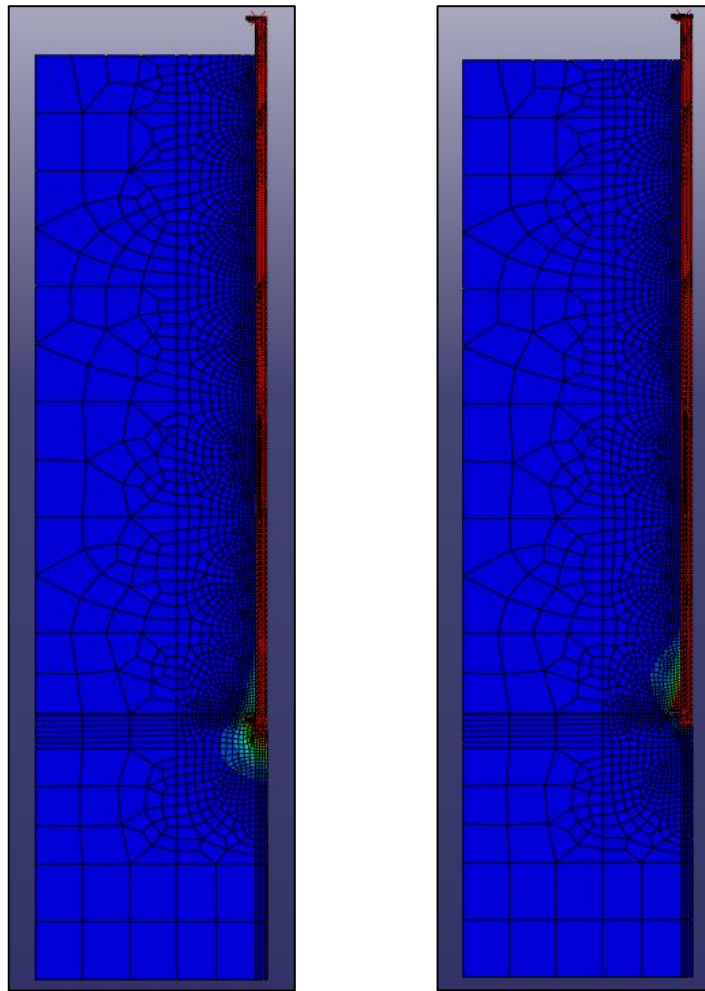
<div align="center">(a)   (b)</div>

Figure 8 - 8: Displacement fields around Pile D (a) Compression loading; (b) Uplift loading

8.2.4.2 Lateral performance

8.2.4.2.1 Load deflection curves

Lateral loading simulations of Piles A, C, D and E were performed considering free head condition. The computed load-deflection curves are presented in Figure 8 - 9.
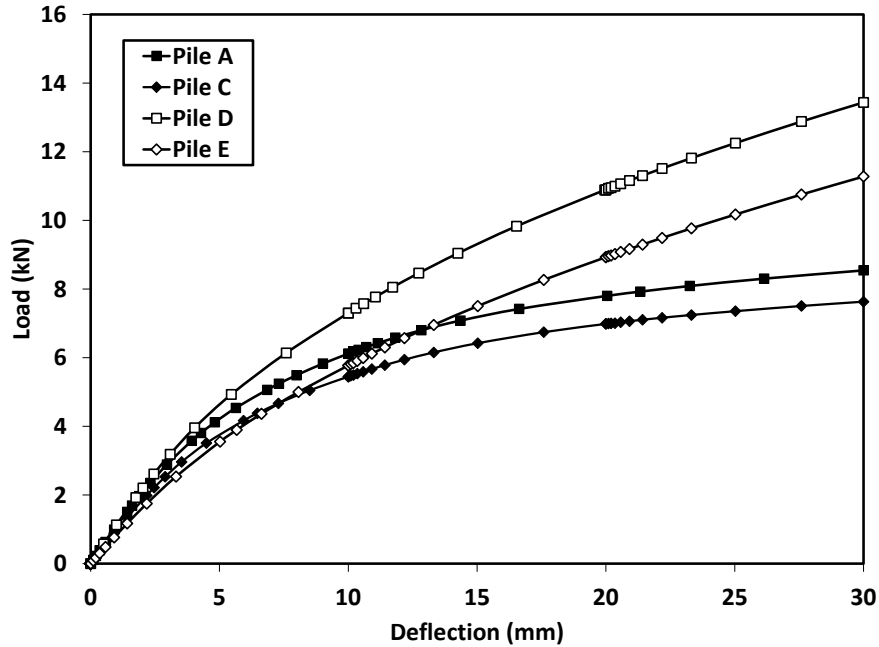
Figure 8 - 9: Load deflection curves-monotonic lateral loading- Piles A, C, D and E

The response curves are characterized by an initial linear part followed by a non-linear zone that extends to the end of the tests for Piles D and E. For Piles A and C, global failure region followed the non-linear zone. This difference in behavior is attributed to the different failure mechanisms (long vs short pile behavior). It should be noted that at smaller displacements, piles of the same shaft configuration (i.e. straight or tapered) acted similarly regardless of their length. This is due to the provided fixation by the helical plate restraining the bottom of the shorter piles resulting hence in a resembling behavior to that of long piles. This can be seen from the curved deflection profile of Pile A at 2mm head deflection as shown in Figure 8 - 10 (a). However at higher applied loads, as shown in Figure 8 - 10 (b), a rigid (short) behavior prevails where the entire pile rotates and the clay low passive resistance (lower K_p) is not sufficient to restrain the bottom of the pile.
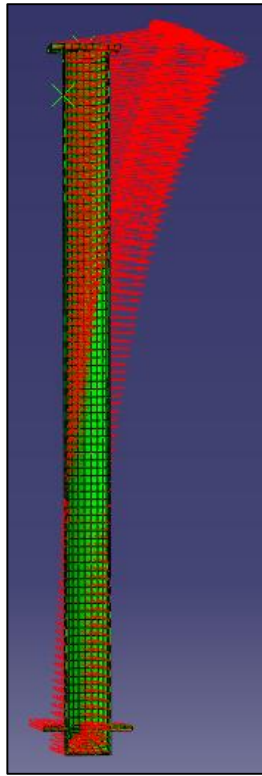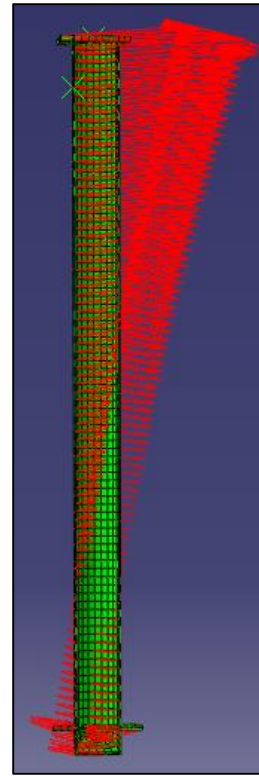
(a)   (b)

Figure 8 - 10: Pile A-pile deflected profile (a) 2mm head deflection; (b) 30mm head deflection

On the other hand, Piles D and E exhibited long (flexible) behavior where only the upper segment of the pile deflected and the lower section remained almost un-deformed as shown in Figure 8 - 11. Piles D and E showed similar deflection profiles with the top 3.3m controlling the displacement (i.e. approximately 16.5 times the average pile diameter).
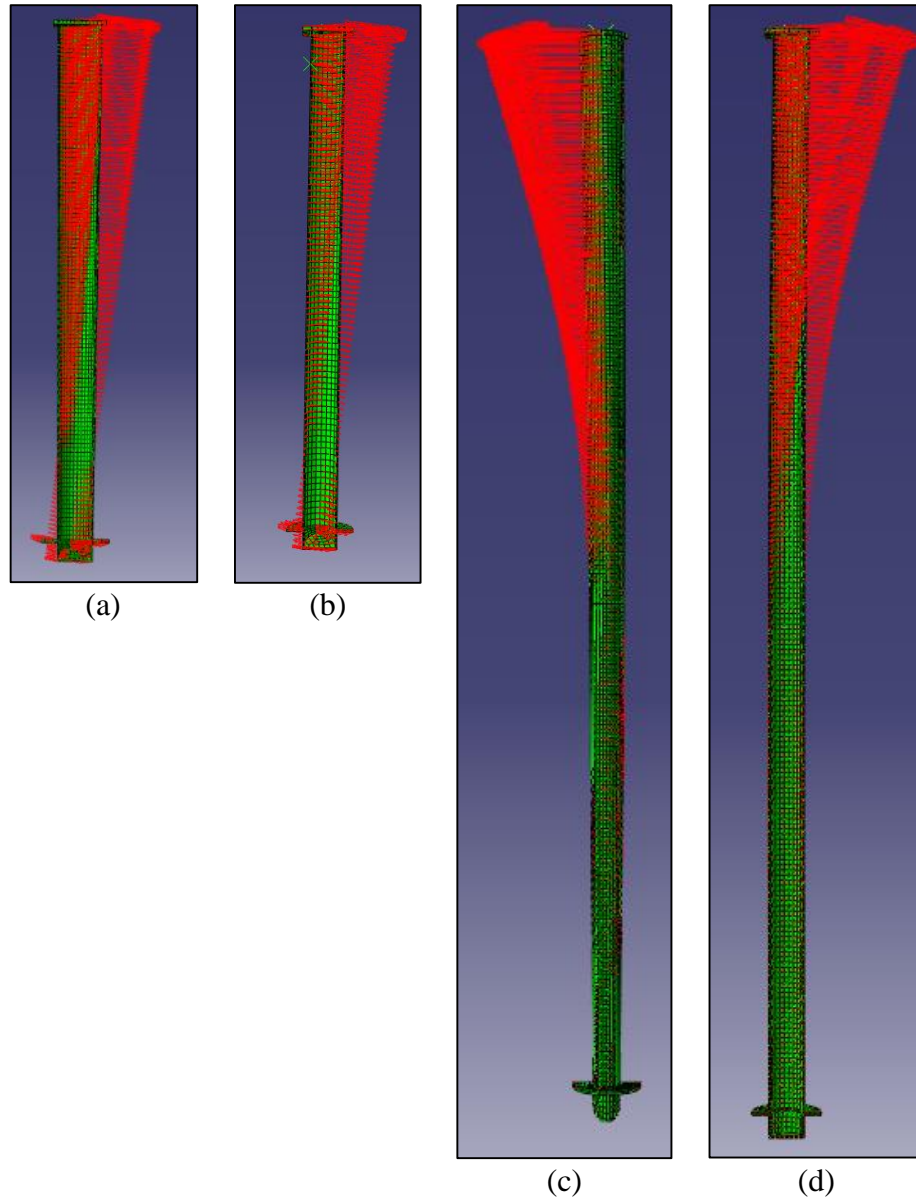
Figure 8 - 11: Pile lateral displacement at maximum applied load (a) Piles A; (b) Pile C; (c) Pile D; (d) Pile E

As expected, Piles A and D exhibited a stiffer response compared to Pile C and E respectively, due to greater cross-sectional inertia of the tapered pile at shallow depth, which governs the response of the pile to lateral load. It is noted that the helical plate did not improve the performance of longer piles similar to the observed performance of helical piles installed in sand.

The low earth pressure at shallow depths behind the pile prevented the soil from following the pile deflection and therefore a clear gap formed. While gapping can have significant effect on the pile cyclic performance, it is not believed to affect its static behavior.

8.2.4.2.2 Piles ultimate capacity

The definition of piles lateral capacity depends on many factors including the nature of the supported structure and the accepted displacement tolerance. Two criteria are generally adopted to define the ultimate pile lateral capacity: the load corresponding to the intersection of the 2 tangents to the load–deflection curve; and the load corresponding to a specific deflection value (typically 6.25mm or 12.5mm) (Prakash and Sharma, 1990). Since the plastic deformation/failure zone was not reached or well defined for all tested piles, the first criterion was not considered. The second criterion was employed herein and the loads corresponding to 6.25mm and 12.5mm head deflection were noted.

In order to account for the different average pile diameters (0.225m for pile A and 0.2m for piles C, D and E), the results are presented in terms of the pile capacity per average embedded diameters as shown in Table 8 - 4.

Table 8 - 3: Ultimate lateral static capacity

Pile #	Lateral capacity (kN)	
	Load at 6.25mm deflection	Load at 12.5mm deflection
Pile A	3.1	4.6
Pile C	2.7	4.2
Pile D	5.4	8.4
Pile E	4.2	6.6

Table 8 - 4: Ultimate lateral static capacity per average embedded diameters of the tested piles

Pile #	Capacity per diameter (kN/m)	
	Load at 6.25mm deflection	Load at 12.5mm deflection
Pile A	14.0	20.9
Pile C	13.5	21.0
Pile D	27.0	42.0
Pile E	21.0	33.0

The results of longer piles (D and E) showed that the taper angle increased the capacity per average embedded diameter by 28%, whereas comparing the results of Piles A and D showed that increasing the piles length, hence changing the behavior from rigid to flexible, almost doubled the lateral capacity per average embedded diameter. On the other hand, minor difference exists between the capacities of Piles A and C where short (rigid) behavior governs and the soil strength controls the lateral load resistance rather than the piles' cross section.

The soil lateral pressure along the pile length upon loading is shown in Figure 8 - 12. Comparable values were observed along the pile shaft for short piles (A and C) and for long piles (D and E). Greater passive resistance was developed by Piles D and E (flexible behavior) compared to Pile A and C (rigid behavior) as well as greater sustained bending moment by the pile cross-section as shown in Figure 8 - 13. For Piles A and C, the maximum bending moment occurred at a distance equivalent to 6 and 7.7 times the average shaft diameter D_{avg} below the ground surface. For longer piles, the maximum sustained bending moment occurred at 8.2 and 8.9 D_{avg} for Piles D and E, respectively. The slightly shallower location of maximum bending moment for the tapered piles is advantageous as the maximum bending moment is sustained by a section of higher inertia. The sustained bending moment by Pile D with head deflection is shown in Figure 8 - 14. The bending moment has shown to increase with head deflection and the location of the maximum value moves to a deeper location due to the excessive strains in the top soil.
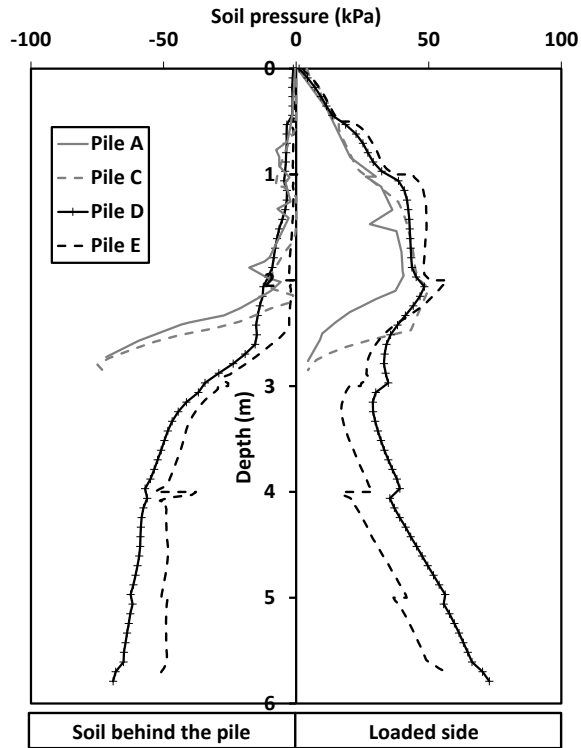
Figure 8 - 12: Soil pressure distribution at 3cm head deflection- Piles A, C, D and E
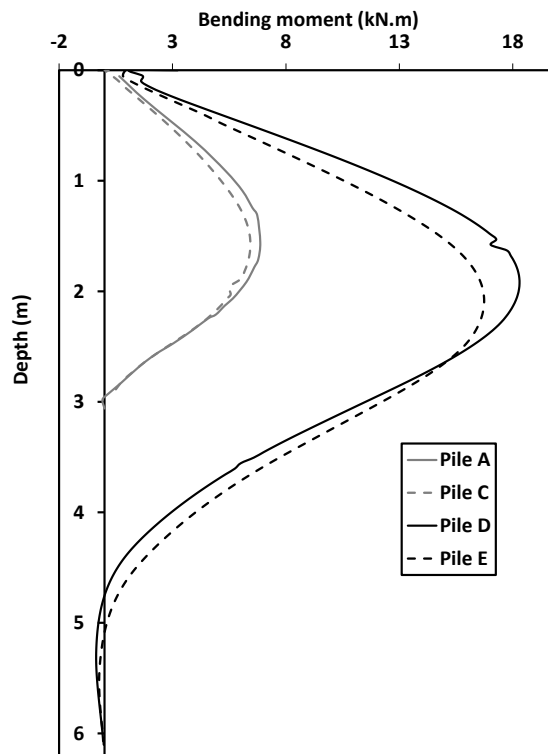
Figure 8 - 13: Sustained bending moment distribution at 3cm head deflection- Piles A, C, D and E
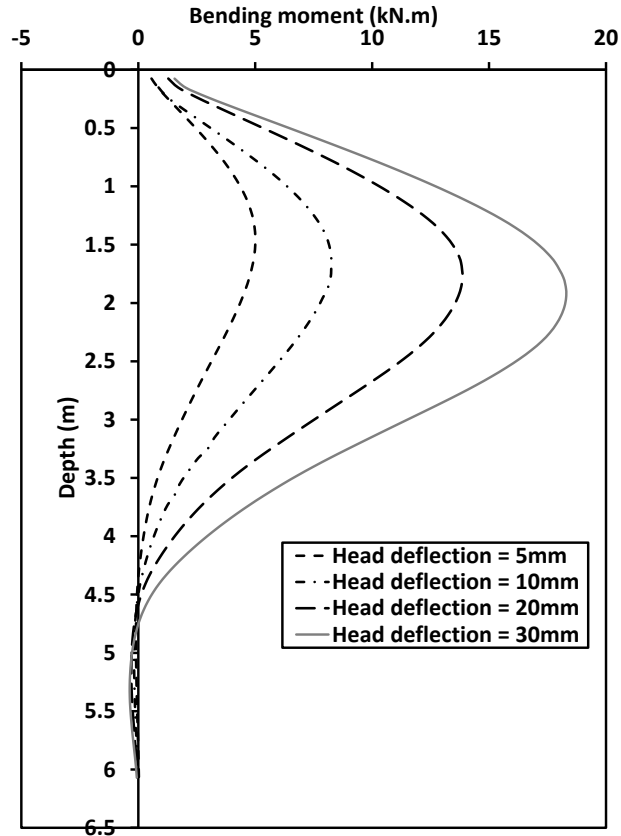
Figure 8 - 14: Variation of sustained bending moment distribution with pile head lateral deflection- Pile D

The loading scheme of many of the potential applications for the studied piles' configurations involves a combination of horizontal and moment loads. Accordingly, a number of numerical simulations were conducted considering Piles A, C, D and E subjected to different combinations of horizontal and moment loads. The determined interaction diagrams are shown in Figure 8 - 15.
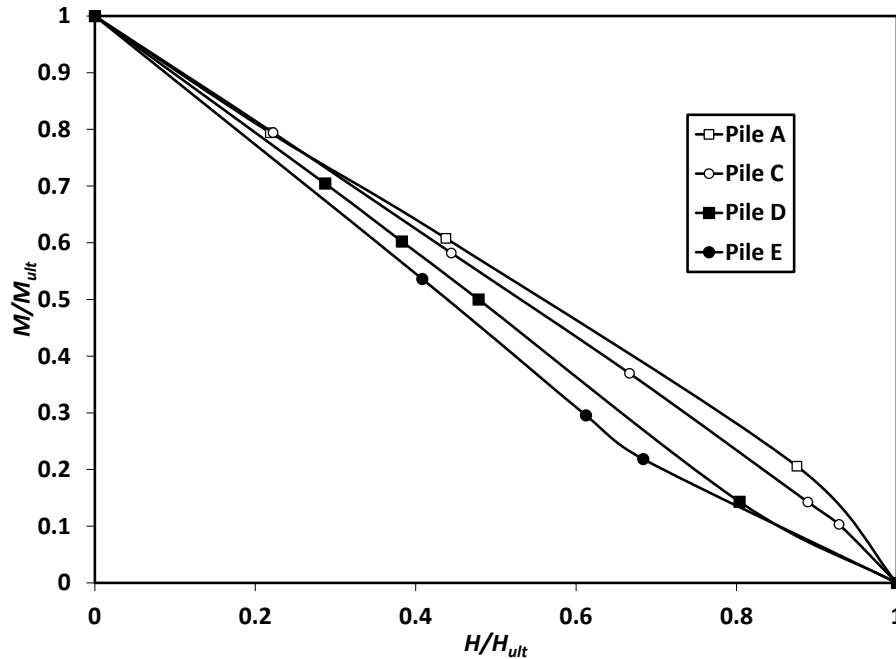
Figure 8 - 15: Moment – horizontal force interaction diagrams-Clay profile

The plot presents the variation of dimensionless applied moment $\overline{M}$ and horizontal forces $\overline{H}$ normalized by the values of the pure moment and horizontal loads resulting in 12.5mm head deflection respectively. This normalization technique was chosen to reflect the serviceability limits as previously used in determining the piles capacity as shown in Table 8 - 3. The curves show the stiffer performance of the tapered over straight sections of the same length. As well, shorter piles carried greater combinations of normalized moments and horizontal forces due to the provided fixation by the helical plates.

It should be noted that, while the actual tension tests results performed on specimens of configuration C and E piles showed the parameters presented in Table 8 - 1, the standard mechanical parameters for steel A53 grade B steel (ASTM A53/A53M, 2012) were considered for Piles C and E in calculating the interaction diagrams for a more generic design aid.

8.2.4.2.3 Effect of crust

The lateral performance of the four studied piles installed in the clay profile shown in Figure 8 - 16 was evaluated, where a top 0.5 m crust overlay the previously considered profile in Figure 8 - 4.
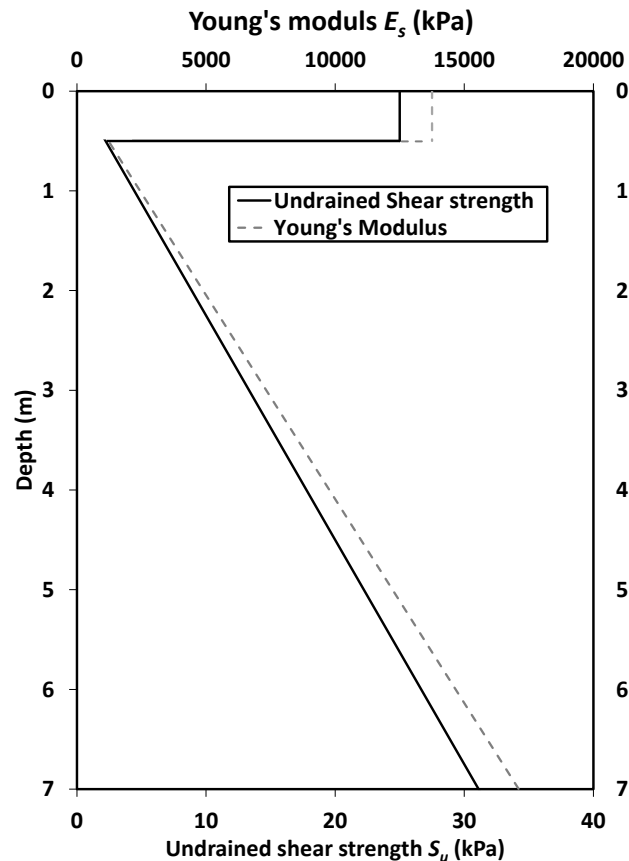
Figure 8 - 16: Considered soil profile-with crust

The resulting load-deflection curves are shown in Figure 8 - 17. The same trend was observed for both long and short piles compared to the case of no crust. It can be seen that the positive effect of the crust increasing the pile lateral resistance was more pronounced for the shorter piles (A and C) where the lateral capacity is mainly controlled by the soil yield, compared to the long piles (D and E) where the capacity is primarily controlled by the piles' cross section. Considering the pile capacity at 12.5mm head deflection, the results

showed that the presence of the crust increased the capacities of Piles A and C by 150% and 148% compared to 108% and 104% for Piles D and E respectively.

The stiffening effect of the crust was slightly more obvious for tapered piles (A and D) compared to the straight ones (C and E) since for the formers the pile along the crust zone has a greater section modulus and therefore results in greater capacity increase.
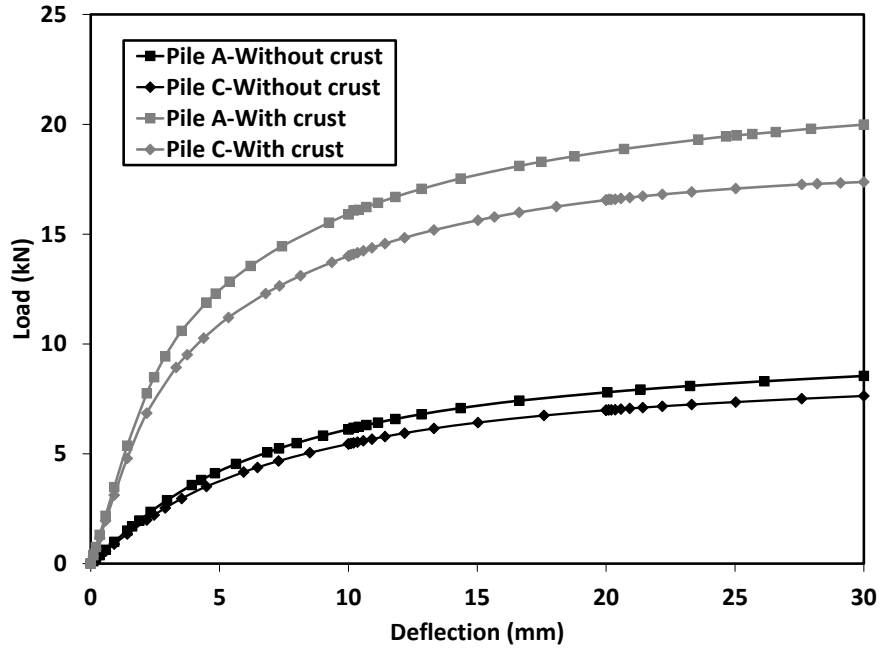
(a)
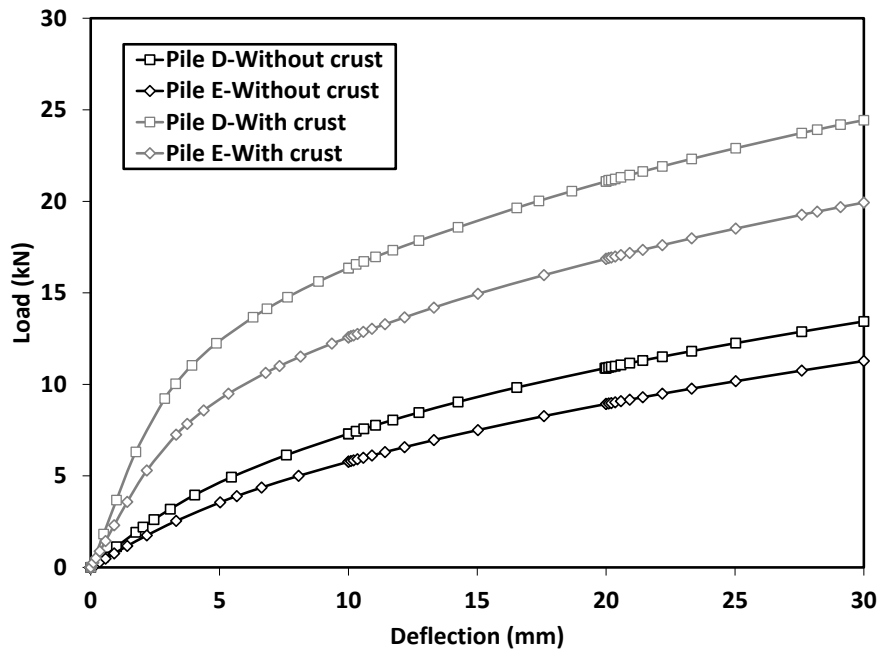
(b)

Figure 8 - 17: Load-deflection curves-clay profile with crust (a) Piles A and C; (b) Piles D and E

8.3 Conclusions

A novel ductile cast iron tapered helical pile system was investigated in this study. Finite element modeling of the proposed system in clay was developed along with a straight large diameter helical pile for comparison purposes. Compression, uplift and lateral monotonic loading cases were simulated. The main conclusions drawn from this study are as follows:

1. The proposed system represents an efficient piling option for both axial and lateral loading cases. It showed slightly improved axial capacity and a considerably enhanced lateral capacity compared to the straight helical pile.

2. The uplift capacity of the proposed pile in clay is approximately 80% of its axial compression capacity, which makes it suitable for applications that impose high uplift loading.

3. For long (flexible) piles, the sustained maximum bending moment occurred at a shallower depth for the tapered piles compared to the straight shafted one, i.e., at a section that has larger cross-sectional inertia.

4. Moment–horizontal force interaction diagrams are provided to aid in design of tapered and straight helical piles subjected to a combination of moment and horizontal loads.

5. The increase in the lateral capacity due to the presence of a top crust was more pronounced for shorter and tapered piles.

8.4 References

Abdelghany, Y. & El Naggar, M. H. Monotonic and cyclic behavior of helical piles under axial and lateral loading. Proceedings of the Fifth International Conference on Recent Advances in Geotechnical Earthquake Engineering and Soil Dynamics, 2010 San Diego, CA.

Briaud, J.-L. 2013. *Geotechnical Engineering: Unsaturated and Saturated Soils*, john Wiley and Sons.

CGS. 2006. *Canadian Foundation Engineering Manual*, 4th edition, Canadian Geotechnical Society.

Chin, F. K. Estimation of the ultimate load of piles from tests not carried to failure. 2nd Southeast Asian Conference on Soil Engineering, 1970, Singapore. 81-90.

Duncan, J. M. & Buchignani, A. L. 1976. An engineering manual for settlement studies. Berkeley: Department of Civil Engineering, University of California.

El Sharnouby, M. & El Naggar, M. H. 2012. Field investigation of axial monotonic and cyclic performance of reinforced helical pulldown micropiles. *Canadian Geotechnical Journal,* 49(5), 560-573.

Elkasabgy, M. & El Naggar, M. H. 2015. Axial compressive response of large capacity helical and driven steel piles in cohesive soils. *Canadian Geotechnical Journal,* 52(2), 224-243.

Elsherbiny, Z. H. & El Naggar, M. H. 2013. Axial compressive capacity of helical piles from field tests and numerical study. *Canadian Geotechnical Journal*, 50(12), 1191-1203.

Fleming, K., Weltman, A., Randolph, M. & Elson, K. 2009. *Piling engineering*, Taylor and Francis Group.

Fuller, F. M. & Hoy, H. E. 1970. Pile load tests including quick load test method, conventional methods and interpretations. HRB 333, 78-86.

Hibbitt, H. D., Karlsson, B. I. & Sorensen, E. P. 2008. ABAQUS Standard user's manual. Pawtucket, R. I.: Hibbitt, Karlsson & Sorensen Inc.

Hoyt, R. & Clemence, S. Uplift capacity of helical anchors in soil. 12th International Conference on Soil Mechanics and Foundation Engineering, 1989 Rio de Janeiro. 1019-1022.

Lambe, T. W. & Whitman, R. V. 1979. *Soil mechanics,* New York, John Willey and Sons Inc.

Lutenegger, A. J., Erikson, J. & Williams, N. Evaluating installation disturbance of helical anchors in clay from field vane tests. 39th Annual Conference on Deep Foundations, 2014, Atlanta, GA Deep Foundation Institute. 129-138.

Massarsch, K. R. Lateral earth pressure in normally consolidated clay. 7th European Conference on Soil Mechanics and Foundation Engineering, 1979 Brighton. 245-250.

Norlund, R. L. 1963. Bearing capacity of piles in cohesionless soils. *Journal of Soil Mechanics and Foundations Division,* 89(3), 1-36.

Perko, H. 2009. *Helical piles: A practical guide to design and installation,* New Jersey, John Willey and Sons Inc.

Prakash, S. & Sharma, H. D. 1990. *Pile foundation in engineering practice,* New York, John Wiley and Sons.

Prasad, Y. V. S. N. & Rao, S. N. 1996. Lateral capacity of helical piles in clay. *Journal of Geotechnical Engineering,* 122(11), 938-941.

Puri, V. K., Stephenson, R. W., Dziedzic, E. & Goen, L. 1984. Helical anchor piles under lateral loading. Laterally loaded deep foundations: Analysis and Performance. ASTM STP 835. Edited by J. A. Langer, E. T. Mosley, and C. D. Thompson. American Society for Testing and Materials, 194–213.

Sakr, M., El Naggar, M. H. & Nehdi, M. Lateral behaviour of composite tapered piles in dense sand. *Proceedings of the Institution of Civil Engineers-Geotechnical Engineering,* 2005, 158(3). 145-157.

Seamless Pole Inc 2010. Ductile iron poles. Birmingham, AL. (*http://www.seamlesspole.com/*)

Sharma, H. D., Sengupta, S. D. & Harron, G. 1984. Cast-In-Place bored piles on soft rock under artesian pressure. *Canadian Geotechnical Journal,* 21(4), 684-698.

Skempton, A. W. The planning and design of Hong Kong airport, discussion. Institution of Civil Engineers proceedings, 1957, London, 7. 305-307.

Wei, J. & El Naggar, M. H. 1998. Experimental study of axial behaviour of tapered piles. *Canadian Geotechnical Journal,* 35(4), 641-654.

Zhang, D. J. Y. 1999. Predicting capacity of helical screw piles in Alberta soils. *MSc thesis.* Edmonton, Alberta: University of Alberta.

Zil'berberg, S. D. & Sherstnev, A. D. 1990. Construction of compaction tapered pile foundation, (from the experience of the Vladspetsstroi Trust). *Soil Mechanics and Foundation Engineering,* 27(3), 96-101.

SUMMARY, CONCLUSIONS AND RECOMMENDATIONS

9.1 Summary

A novel piling system was proposed in this study: a spun-cast ductile iron (SCDI) tapered pile fitted with a lower helical plate to be installed by mechanical torque. The main objective of the study was to evaluate the efficiency of the proposed system under different loading cases.

A comprehensive investigation program was designed and implemented that included field tests and three dimensional finite element modelling.

The field testing program comprised installation and testing of seven instrumented piles including five SCDI tapered and two steel straight shafts. The piles were subjected to cyclic and monotonic compression, uplift and lateral load tests. Different loading sequences were adopted to assess the effect of prior loading on the piles' performance.

The commercial software ABAQUS (Hibbitt *et al.*, 2008) was then used to simulate the field tests in order to further understand the load transfer mechanism during loading and also to quantify the effects of the piles' geometry and installation technique on their behavior. Following the calibration and the validation of the created models with the field data, the FE model was used to analyze the performance of different pile configurations and to simulate the piles response to combined moment-horizontal loads. Finally, monotonic loading cases of the piles in a clay profile were numerically modelled. These includes monotonic compressive, uplift, lateral load tests simulations as well as when subjected to combined moment and horizontal loads.

9.2 Conclusions

Based on the results of the investigation program, the main conclusions drawn are:

Monotonic compression performance in silty sand

1. The proposed system showed a stiffer response and higher compressive resistance compared to the straight shaft piles thanks to the tapered profile and to the surface roughness resulting in a significantly higher shaft resistance.

2. Greater compressive efficiency is expected for longer versions of the proposed pile configuration.

3. The results showed that the soil along the tapered shaft recovered its stiffness and strength fully, hence counteracting the disturbance effect due to the helix rotation and shearing of the soil.

Monotonic uplift performance in silty sand

1. The addition of the helical plate enhanced the uplift resistance of tapered piles.

2. The proposed helical tapered piles showed stiffer response at lower displacements.

3. At higher displacements, reduction of the earth pressure coefficient of the soil surrounding the tapered shaft makes the straight piles a better alternative.

4. Longer versions of the tapered helical piles are expected to show more efficient uplift behavior. This was shown numerically and needs to be further confirmed experimentally.

Monotonic lateral performance in silty sand

1. The tapered piles exhibited a stiffer response and offered higher ultimate capacity compared to the straight-shaft piles owing to the greater flexural rigidity along the top portion of the pile.

2. The helical plate was found to significantly increase the lateral capacity of short piles due to the provided fixation to the bottom of the piles.

3. Moment–horizontal force interaction diagrams were developed and design equations were provided to aid in design of the proposed piling system subjected to a combination of significant moment and horizontal loads.

Cyclic axial performance in silty sand

1. The proposed piling system showed a better cyclic compressive performance compared to the straight large diameter helical piles.

2. The cyclic uplift performance of tapered piles strongly depends on the loading sequence.

Cyclic lateral performance in silty sand

1. Both large diameter straight shafted and tapered helical piles showed a satisfactorily performance under the cyclic lateral loading schemes applied in the current study.

2. The proposed system's lateral stiffness has almost remained unchanged through the lateral cyclic tests (negligible degradation effects were observed within the different studied loading amplitudes).

3. The application of the initial monotonic lateral test degraded the pile's cyclic performance. The resulting load deflection curves were shifted towards the direction of initial monotonic loading.

Monotonic performance in clay

1. Finite element analysis of the proposed system showed a slightly enhanced axial capacity and a considerably improved lateral capacity compared to the straight helical pile.

2. Uplift-to-compressive capacity was shown to be higher in clay than in sand since, for the former, the shaft resistance is not dependent on the lateral earth pressure.

3. For long (flexible) piles, the tapered profile had moved the location of the maximum sustained bending moment by the shaft to a shallower location, i.e., at a section that has larger cross-sectional inertia.

4. Moment–horizontal force interaction diagrams were provided for tapered and straight helical.

5. The lateral capacity increase resulting from the presence of a top crust was more obvious for tapered and shorter piles.

Loading sequence effects

1. The application of prior cyclic compression tests increased the monotonic compressive stiffness of the piles at lower displacements. At higher displacements however, those not tested in prior cyclic compression showed stiffer monotonic compressive response.

2. The application of cyclic uplift loading prior to the uplift monotonic tests eliminated the gapping-cave in effects resulting in increased developed shaft stresses at lower displacements during the latter tests.

3. The application of monotonic compression loading before cyclic uplift tests resulted in excessive total displacements especially during the initial static part before the start of load cycling. However, it reduced the cyclic uplift displacement (not the total) of the tapered helical piles compared to the straight shafted ones.

4. The application of a prior cyclic uplift test released the earth pressure surrounding the pile shaft and thus reduced the shaft resistance. For that loading sequence, large diameter helical straight shafted piles exhibited a better cyclic compressive performance.

5. The application of a prior monotonic lateral load degraded the pile's cyclic lateral performance.

6. The application of a prior cyclic lateral loading significantly reduced the monotonic lateral stiffness of the tested piles mainly due to the development of a gap along the upper portion of the pile and a zone of loose soil of the caved-in sand.

9.3   Recommendations for future research

The results of the present study revealed the improved performance of the proposed piling system in various loading conditions compared to the conventional piling alternatives. To further evaluate the system's efficiency and the possible enhancement of its configuration, the following are recommended for future research:

▪ Monotonic axial and lateral field testing of the proposed pile in clay.

- FE simulations and field testing of piles having different length, shaft taper angle, and helix diameter combinations.

- Field testing and FE simulations of tapered helical pile groups.

- Dynamic field testing of the suggested pile.

9.4 References

Hibbitt, H. D., Karlsson, B. I. & Sorensen, E. P. 2008. ABAQUS Standard user's manual. Pawtucket, R. I.: Hibbitt, Karlsson & Sorensen Inc.

APPENDIX A

This appendix summarizes the in-situ observations following the removal of the piles from the ground upon the completion of the field tests.

The seven tested piles were removed from the ground using a combined reversed torque and uplift technique. Due to the bearing pressure during the different axial tests, the retrieved piles of configurations A and C showed a slight deflection of the helical plates and the pile tip with more significant deformation for the latter configuration. On the other hand, the two tested configuration B piles had broken helix plates. For the first pile, the helix was detached but the shaft was left intact (suggesting a welding failure) whereas the shaft of the second pile was broken at the location of the helix. This failure occurred during uplift loading as discussed in Chapter 4. Images of the removed piles are shown in Figure A - 1.

(a)

(b)

Detached helix location

(c)

(d)

Figure A - 1: Retrieved piles from the ground (a) Configuration A deflected tip; (b) Configuration C deflected tip; (c) Configuration B broken helix and lower pile shaft; (d) Configuration B detached helix

APPENDIX B

Borehole Log:

- FILE NO: _____
- PROJECT: ASHLAND AVE.
- LOCATION: LONDON, ON
- DATE STARTED: July 12/11
- DATE COMPLETED: July 12/11
- WATER LEVEL: 11'
- CAVE IN: to 15' (wet) DATE: _____ TIME: _____
- WATER LEVEL: _____ CAVE IN: _____ DATE: _____ TIME: _____
- ENG: UWO
- DRILL RIG: 75 M
- HAMMER WT: 140 lb. auto
- VANE LENGTH: _____
- DRILLER: ADI
- METHOD: HSA (4¼")
- DROP: 30"
- DIA: _____
- BH/TP: 1
- pg 1 of 2

DESCRIPTION OF SOIL	DEPTH	SAMPLE TYPE	NO	REC	BLOW 6"	N CORR	PP TSF	VANE In-situ	VANE Re-mod	WT	DESCRIPTION
8" silt/sand fill					2						
8" topsoil		SS	1	24	2 / 2 / 2	4					
red/brown med. sand											
Sand ↓ SAA	13	SS	2	24	4 / 5 / 4 / 4	8					
~ to lt. brown — medium to fine		SS	3	24	2 / 4 / 5 / 5	10					
↓ SAA >> moisture		SS	4	24	4 / 4 / 4 / 4 / 5	9					
→ to saturated ⊽	11	SS	5	22	4 / 4 / 4 / 5	9					
↓ SAA		SS	6	18	0 / 3 / 3 / 3	6					
Saturated brown sand (med.) to coarse		SS	7	24	0 / 4 / 4 / 6	10					
↓		SS	8	14	2 / 4 / 4 / 5	9					
↓ SAA coarse		SS	9	24	3 / 5 / 7 / 6	13					

309

Figure B - 1: Drilled borehole log (performed by Aardvark drilling Inc.)

APPENDIX C

This appendix presents the types of the instrumentation devices used during the different field tests. Images of the different component are shown in Figure C - 1.

- **Load cell**

Interface high capacity standard precision lowprofile load cell model 1244 CLX-270K-B

- **Linear variable displacement transducers LVDT**

Measuring the pile head axial and lateral displacements: Penny and Giles HLP 190/FS1/100/4K

Measuring the lateral deflection at 0.92m below the pile head: LD Sensors LDS25

- **Hydraulic jack**

Enerpac double acting hollow plunger cylinder RRH 1006

- **Pump**

Enerpac ZE3 class hydraulic electric pump

- **Strain gauges**

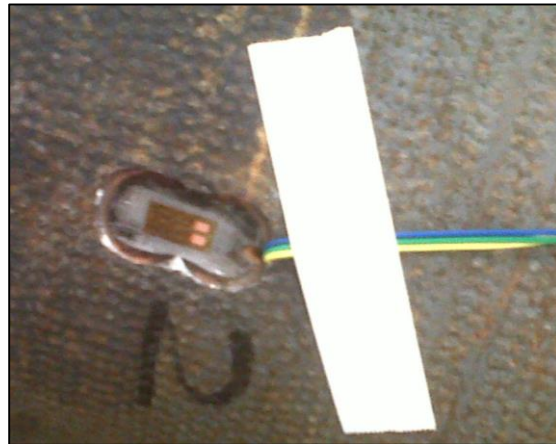Micro-Measurements general purpose strain gauges CEA-06-250UW-120

(a)

(b)

(c)

(d)

(e)

Figure C - 1: Used instrumentation devices (a) Load cell; (b) LVDTs; (c) Hydraulic jack; (d) Pump; (e) Strain gauge

CURRICULUM VITAE

Name: Ahmed Fahmy

Place of Birth: Egypt

**Post-Secondary   Master of Science
Education and   Civil and Environmental Engineering Department
Degrees:**   The University of Western Ontario
                       London, Ontario, Canada
                       2008-2010

                       Bachelor of Science
                       Civil and Environmental Engineering Department
                       Faculty of Engineering – Cairo University
                       Cairo, Egypt
                       2001-2006

**Academic   Research Assistant
Appointments:**   Civil and Environmental Engineering Department
                       The University of Western Ontario
                       London, Ontario, Canada
                       2008-2015

                       Teaching Assistant
                       Civil and Environmental Engineering Department
                       The University of Western Ontario
                       London, Ontario, Canada
                       2008-2015

                       Course Instructor
                       Civil and Environmental Engineering Department
                       The University of Western Ontario
                       London, Ontario, Canada
                       2013

**Professional   Full-time Geotechnical Engineer
Appointments:**   Dar Al-Handasah Consultants
                       Cairo, Egypt
                       2006-2008

                       Part-time Geotechnical Engineer
                       Geo-Consultants
                       Cairo, Egypt
                       2007-2008